

REPORT DOCUMENTATION PAGE

Form Approved
OMB No. 0704-0188

Public reporting burden for this collection of information is estimated to average 1 hour per response, including the time for reviewing instructions, searching existing data sources, gathering and maintaining the data needed, and completing and reviewing the collection of information. Send comments regarding this burden estimate or any other aspect of this collection of information, including suggestions for reducing this burden, to Washington Headquarters Services, Directorate for Information Operations and Reports, 1215 Jefferson Davis Highway, Suite 1204, Arlington, VA 22202-4302, and to the Office of Management and Budget, Paperwork Reduction Project (0704-0188), Washington, DC 20503.

1. AGENCY USE ONLY (Leave blank)	2. REPORT DATE	3. REPORT TYPE AND DATES COVERED	
	14.Aug.02	THESIS	
4. TITLE AND SUBTITLE		5. FUNDING NUMBERS	
MISSION AND MICRONELLE FLOW ANALYSIS OF A HIGH TEMPERATURE CHEMICAL PROPULSION SYSTEM			
6. AUTHOR(S)			
2D LT JONES JESSY R			
7. PERFORMING ORGANIZATION NAME(S) AND ADDRESS(ES)		8. PERFORMING ORGANIZATION REPORT NUMBER	
UNIVERSITY OF WASHINGTON		CI02-121	
9. SPONSORING/MONITORING AGENCY NAME(S) AND ADDRESS(ES)		10. SPONSORING/MONITORING AGENCY REPORT NUMBER	
THE DEPARTMENT OF THE AIR FORCE AFIT/CIA, BLDG 125 2950 P STREET WPAFB OH 45433			
11. SUPPLEMENTARY NOTES			
12a. DISTRIBUTION AVAILABILITY STATEMENT		12b. DISTRIBUTION CODE	
Unlimited distribution In Accordance With AFI 35-205/AFIT Sup 1			
13. ABSTRACT (Maximum 200 words)			

DISTRIBUTION STATEMENT A
Approved for Public Release
Distribution Unlimited

20020829 043

14. SUBJECT TERMS		15. NUMBER OF PAGES	
		255	
		16. PRICE CODE	
17. SECURITY CLASSIFICATION OF REPORT	18. SECURITY CLASSIFICATION OF THIS PAGE	19. SECURITY CLASSIFICATION OF ABSTRACT	20. LIMITATION OF ABSTRACT

AFMC/PA

University of Washington

Abstract

**Mission and Micronozzle Flow Analysis of a
High-Temperature Chemical Micropropulsion System**

Jessy R. Jones

Chair of Supervisory Committee:
Professor Arthur T. Mattick
Department of Aeronautics and Astronautics

Recent trends in small-scale satellites motivate the further development of the propulsion subsystem. Micro-electromechanical systems (MEMS) micronozzles provide sufficient geometries to produce impulse bits suitable for this scale of satellite. An area of concern with MEMS micronozzles is the inefficiency associated with viscous losses of the developing boundary layer. The University of Washington recently commenced research on a high-temperature propulsion system. An advantage of increased temperature levels is an increase in specific impulse. A disadvantage is an increase in viscous effects. The present research focuses on using numerical methods to determine an area of diminishing return for increased chamber temperature conditions. Initial focus is on the development of an optimum geometry which can be applied to these high-temperature gases. Using past research efforts, an expansion half angle of 30 degrees and expansion ratio of 10 are chosen. An interesting trend of the Reynolds number is observed for small to large aspect ratios. To determine optimum thrust and specific impulse efficiency, the aspect ratio is varied from 1, 5, 10, to 15. It is found that aspect ratios of 5, 10, and 15 for the same thrust level produce better results than an aspect ratio of 1. Using an aspect ratio of 10, a temperature analysis of Reynolds numbers is analyzed for chamber temperatures of 1000 to 3000 K. Although the viscous effects increase with the increase in temperature, the author proves that up to 3000 K, there is not an area of diminishing return for any of the aspect ratios in question. These results are applied to various missions for both the main and attitude-control propulsion subsystems.

This is a
SAF/PAS document

02 - - 0362

Call 697-3222/697-8932
for pickup or return to 5D227

AEROC 02 = 108

**Mission and Micronozzle Flow Analysis of a
High-Temperature Chemical Propulsion System**

Jessy R. Jones

A thesis submitted in partial fulfillment of the requirements for the degree of

Master of Science in Aeronautics and Astronautics

University of Washington

2002

Program Authorized to Offer Degree: Department of Aeronautics and Astronautics

**THE VIEWS EXPRESSED IN THIS ARTICLE
ARE THOSE OF THE AUTHOR AND DO NOT
REFLECT THE OFFICIAL POLICY OR
POSITION OF THE UNITED STATES,
DEPARTMENT OF DEFENSE, OR THE U.S.
GOVERNMENT**

University of Washington
Graduate School

This is to certify that I have examined this copy of a master's thesis by

Jessy R. Jones

and have found that it is complete and satisfactory in all respects,
and that any and all revisions required by final
examining committee have been made.

Committee Members:

Arthur T. Mattick

Arthur T. Mattick

Scott Eberhardt

Scott Eberhardt

Date:

3-19-02

In presenting this thesis in partial fulfillment of the requirements for a Master's degree at the University of Washington, I agree that the Library shall make its copies freely available for inspection. I further agree that extensive copying of this thesis is allowable only for scholarly purposes, consistent with "fair use" as prescribed in the U.S. Copyright Law. Any other reproduction for any purposes or by any means shall not be allowed without my written permission.

Signature Jessy R. Jones
Date 19 March 2002

University of Washington

Abstract

Mission and Micronozzle Flow Analysis of a
High-Temperature Chemical Micropropulsion System

Jessy R. Jones

Chair of Supervisory Committee:

Professor Arthur T. Mattick

Department of Aeronautics and Astronautics

Recent trends in small-scale satellites motivate the further development of the propulsion subsystem. Micro-electromechanical systems (MEMS) micronozzles provide sufficient geometries to produce impulse bits suitable for this scale of satellite. An area of concern with MEMS micronozzles is the inefficiency associated with viscous losses of the developing boundary layer. The University of Washington recently commenced research on a high-temperature propulsion system. An advantage of increased temperature levels is an increase in specific impulse. A disadvantage is an increase in viscous effects. The present research focuses on using numerical methods to determine an area of negative return for increased chamber temperature conditions. Initial focus is on the development of an optimum geometry which can be applied to these high-temperature gases. Using past research efforts, an expansion half angle of 30 degrees and expansion ratio of 10 are chosen. An interesting trend of the Reynolds number is observed for small to large aspect ratios. To determine optimum thrust and specific impulse efficiency, the aspect ratio is varied from 1, 5, 10, to 15. It is found that aspect ratios of 5, 10, and 15 for the same thrust level produce better results than an aspect ratio of 1. Using an aspect ratio of 10, a temperature analysis of Reynolds numbers is analyzed for chamber temperatures of 1000 to 3000 K. Although the viscous effects increase with the increase in temperature, the author proves that up to 3000 K, there is not an area of negative return for any of the aspect ratios in question. These results are applied to various missions for both the main and attitude-control propulsion subsystems.

TABLE OF CONTENTS

	Page
List of Figures	iv
List of Tables	viii
Glossary	xi
Introduction.....	1
Chapter 1: Micropulsion Overview	3
Chapter 2: Mission Overviews.....	5
Chapter 3: Mission Requirements.....	8
3.1 Stationkeeping.....	8
3.2 Formation Flying	15
3.3 Orbit Transfer / Maintenance.....	15
3.4 Interplanetary Transfer.....	18
Chapter 4: Micropulsion System Options.....	20
4.1 University of Washington Proposed Propulsion System	21
4.2 Monopropellant Comparisons.....	23
Chapter 5: Valve Technology	26
Chapter 6: Mission Application	23
Chapter 7: Mission Analysis Conclusion.....	44
Chapter 8: Background for Research of Micronozzle Flow Efficiencies	46
Chapter 9: Past/Present Research.....	60
9.1 DSMC vs Continuum(Navier-Stokes ‘NS’) Models.....	61
9.2 Nozzle Divergence Angle	65
9.3 Axisymmetric vs 3D Block Nozzle.....	67
9.4 2D vs 3D Simulations	70
9.5 Nozzle Throat Contour.....	71
9.6 High-Temperature Analysis.....	73
9.7 Truncated Nozzle	74
9.8 Wall Temperature	76
Chapter 10: Current Research Overview	78
Chapter 11: Physics of Micronozzle Flow	80
11.1 Frozen/Equilibrium Flow	83
11.2 Exit Expansion	84
11.3 Other Rarefied Effects	86

Chapter 12: Introduction to Aspect Ratio Analysis	87
Chapter 13: High-Temperature Effects	97
Chapter 14: Experimental Recommendation	102
Chapter 15: Numerical Modeling.....	105
15.1 Grid Setup (IMESH file).....	106
15.2 Numerical Setup (IDATA file)	115
15.2.1 Initial Conditions	115
15.2.2 Boundary Conditions	117
15.2.3 Chemistry Model	120
15.2.4 Numerical Code Setup	121
15.2.4.1 Flux Function.....	123
15.2.4.2 Flux Limiter	124
15.2.4.3 Explicit/Implicit Mode.....	125
15.2.4.4 Gauss-Seidel Relaxation Factor.....	125
15.2.4.5 Time Step Mode.....	126
15.2.4.6 Time Step Relax Factor	126
15.2.4.7 Order (Flux Phi I/J/K).....	126
15.2.4.8 Thermodynamic/Conductivity/Viscosity Models	127
15.2.4.9 CFL Number Range	129
15.2.4.10 Eigenvalue Smoothing Coefficients.....	129
Chapter 16: Output Post-processing of Converged Solutions.....	131
Chapter 17: Validation of Numerical Code and Mesh Refinement Studies.....	140
17.1 Inviscid/Viscid Results and Verification of Micronozzle with Aspect Ratio = 10	140
17.1.1 Inviscid Results.....	141
17.1.2 Viscous Results.....	144
17.1.3 Mesh Refinement Study of Aspect Ratio = 10	147
17.2 Y-Plus Reduction	150
17.3 Mesh Refinement Study of Aspect Ratio = 5.....	152
17.4 Mesh Refinement Study of Aspect Ratio = 1.....	154
17.5 Mesh Refinement Study of Aspect Ratio = 15.....	156
17.6 Results Comparison with Past Efforts.....	160
Chapter 18: Results of Aspect Ratio Analysis	162

Chapter 19: Results of High Temperature Analysis	178
Chapter 20: Conclusions of Micronozzle Flow Efficiencies	185
Chapter 21: Conclusions of Mission Application and Micronozzle Flow Analysis	187
Bibliography	190
Appendix A: Micropropulsion Technology Search	200
Appendix B: CEA Kinetics Code Input Example.....	205
Appendix C: Algorithm for Experimental Recommendation of Mass Flow Determination	206
Appendix D: Algorithm to Compute Grid Points Based on Expansion Ratio and Half-Angle	211
Appendix E: IMESH Input File for id118.....	213
Appendix F: Algorithm FISPCluster – Computes Scale, F, Isp, Re#, Kn#, mass flow, pressure force	227
Appendix G: Micronozzle Efficiency Results	240
Appendix H: IDATA Input File for id118	246

LIST OF FIGURES

#	Figure	Page
3-1	Surrey Small Spacecraft Predictions ¹⁶	8
3-2	Configuration for Slew Rate of Cylindrical Spacecraft	10
3-3	Mass Moment of Inertia Diagrams for Cylindrical/Cubic Spacecraft	10
3-4	Spacecraft Moment of Inertia with Extended Solar Panel	11
3-5	Slew Rates up to 180 degrees/minute	13
3-6	Slew Rates from 0 to 1 degree/minute	14
3-7	Hohmann and Low-Thrust Transfers ¹⁹	16
8-1	Ideal Thrust with Momentum Flux / Pressure Breakdown	47
8-2	Ideal Specific Impulse with Expansion Ratio Increase.....	48
8-3	Decrease in Specific Impulse / Thrust for Chamber Pressure Decrease 30 – 10 bar	48
8-4	Decrease in Isp with Decrease in Pressure of 30 – 0.01 bar	49
8-5	Increase of Isp with Increased Temperature	50
8-6	Reduction in Area Ratio Due to Viscous Effects ²⁰	51
8-7	Reynold's Number Variation with Geometry	53
8-8	Reynold's Number Variation with Geometry	54
8-9	Reynold's Number Variation with Geometry	54
8-10	Increased Isp with Chamber Temperature	56
8-11	Decrease in Reynolds Number with Increase in Chamber Temperature for Various Thrust Levels.....	57
8-12	Unknown Correlation of Efficiency to Reynolds Number	58
8-13	Unknown Correlation of Efficiency to Temperature	58
9-1	Reynolds Numbers 130 to 1300 NS(GASP), DSMC(SMILE) Comparison ²⁶	62
9-2	Difference Between NS and DSMC Codes at Nozzle Lip ³⁰	64
9-3	Differences in Velocity at the Wall ⁴²	65
9-4	Difference in Velocity Profiles of Various Half-Angles ²⁴	66
9-5	MEMS Nozzle	68
9-6	Surface Area to Volume Ratio for Various Nozzles	69
9-7	Boundary Thickness along End/Sidewalls ²⁷	70
9-8	Isp/Discharge Coefficient Values for Numerical/Experimental Test Cases ²⁷	71
9-9	Mach Contours for Smooth/Sharp Throat ²⁷	72

9-10	Axial Velocity Profile with Viscous Effects ²⁸	75
9-11	Reduction of Overall Thrust Due to Overextended Nozzle ³⁷	76
11-1	Shear Stress and Velocity Gradient ³¹	81
12-1	Results of Expansion Ratio/Aspect Ratio for Low Thrust Numbers ⁴⁷	87
12-2	Comparison of Aspect Ratio on Reynolds Number for F=125mN.....	89
12-3	Comparison of Aspect Ratio on Reynolds Number for F=10mN	90
12-4	Effects of Further Expansion Ratio on Reynolds Number.....	91
12-5	Reynolds Number Variable Breakdown @ Rt = 5, Eratio = 10.....	92
12-6	Reynolds Number Variable Breakdown @ Rt = 1, Eratio = 10.....	93
12-7	Reynolds/Knudsen Number vs Eratio	95
12-8	Axisymmetric Reynolds Number.....	96
13-1	Viscosity Variation With Increased Temperature.....	97
13-2	Weight Percentage of Products (H ₂ O/NH ₃ /N ₂ O).....	98
13-3	Throat Diameters for Various Thrust Levels	99
15-1	Graphic of Full Nozzle and ¼ Nozzle to be Analyzed	107
15-2	Points @ Junctions Used in Generating the Grid.....	108
15-3	Line Numbers Used in Generating the Grid	108
15-4	Surface Numbers Used in Generating the Grid.....	109
15-5	Zone Numbers Used in Generating the Grid.....	109
15-6	3D Micronozzle Mesh.....	113
15-7	Grid Clustering at Throat/Sidewalls	114
15-8	Grid Clustering at Endwalls	114
15-9	Mach Contours of Rt=5, Tc=3000 K	118
15-10	Mach Contours @ Endwall Lip	119
15-11	Mach Contours @ Sidewall Lip.....	119
15-12	Graphical Representation of Taylor Series Expansion ⁴⁰	127
15-13	Viscosity Values for Exact and Approximate Temperatures	129
15-14	Temperature Contour Plot for id149	130
15-15	Mach Contour Plot for id149	130
15-16	Temperature Contour Plot for id175	130
15-17	Mach Contour Plot for id175	130
16-1	Axial T, P, R Convergence	131
16-2	Axial Mach and Velocity Convergence	132
16-3	P, T, R Exit Plane Sidewall Symmetry Line Convergence.....	132

16-4	Mach, Axial Velocity Exit Plane Sidewall-Symmetry Line Convergence	133
16-5	P, T, R Exit Plane Endwall-Symmetry Line Convergence	133
16-6	Mach, Axial Velocity Exit Plane Endwall-Symmtery Line Convergence.....	134
16-7	Y-plus Values Along Nozzle Walls	136
16-8	Data Organization from Tecplot Output File.....	137
17-1	Inviscid Contour Plot of Axial Velocity	142
17-2	Inviscid Thrust Comparison of 1 st and 2 nd Order	143
17-3	Inviscid Isp Comparison of 1 st and 2 nd Order.....	143
17-4	Steps/Minute vs Cell Number	144
17-5	Contour Plot of Axial Velocity Including Viscosity.....	145
17-6	Viscous Thrust Comparison of 1 st and 2 nd Order	146
17-7	Viscous Isp Comparison of 1 st and 2 nd Order.....	146
17-8	Axial Contours of P, $\rho(R)$, and T for 2 nd Order Mesh Refinement	148
17-9	Thrust vs Eratio of 2 nd Order Mesh Refinement	149
17-10	Isp vs Eratio of 2 nd Order Mesh Refinement.....	149
17-11	Y-plus Values (1 / 1.1) of ID118 (Spacing = 0.002 @ endwalls).....	151
17-12	Mesh Analysis of Aspect Ratio = 5, Isp.....	153
17-13	Mesh Analysis of Aspect Ratio = 5, Thrust	153
17-14	Mesh Analysis of Aspect Ratio = 1, Isp.....	155
17-15	Mesh Analysis of Aspect Ratio = 5, Thrust	155
17-16	Mesh Analysis of Aspect Ratio = 15, Isp.....	157
17-17	Mesh Analysis of Aspect Ratio = 5, Thrust	157
17-18	Aspect Ratio Comparison of Mesh Refinement Study	159
18-1	T Plot of Rt=15, Tc=3000K	164
18-2	T Plot of Rt=10, Tc=3000K	164
18-3	T Plot of Rt=5, Tc=3000K	164
18-4	T Plot of Rt=1, Tc=3000K	164
18-5	Axial Velocity Plot of Rt=15, Tc=3000K, F=501mN	165
18-6	Axial Velocity Plot of Rt=10, Tc=3000K, F=501mN	165
18-7	Axial Velocity Plot of Rt=5, Tc=3000K, F=501mN	165
18-8	Axial Velocity Plot of Rt=1, Tc=3000K, F=501mN	165
18-9	Mach Plot of Rt=15, Tc=3000K, F=501mN.....	166
18-10	Mach Plot of Rt=15, Tc=3000K, F=501mN.....	166
18-11	Mach Plot of Rt=15, Tc=3000K, F=501mN.....	166

18-12	Mach Plot of Rt=15, Tc=3000K, F=501mN	166
18-13	T Plot of Rt=15, Tc=3000K	167
18-14	T Plot of Rt=10, Tc=3000K	167
18-15	T Plot of Rt=5, Tc=3000K	167
18-16	T Plot of Rt=1, Tc=3000K	167
18-17	Axial Velocity Plot of Rt=15, Tc=3000K, F=501mN	168
18-18	Axial Velocity Plot of Rt=10, Tc=3000K, F=501mN	168
18-19	Axial Velocity Plot of Rt=5, Tc=3000K, F=501mN	168
18-20	Axial Velocity Plot of Rt=1, Tc=3000K, F=501mN	168
18-21	Mach Plot of Rt=15, Tc=3000K, F=501mN	169
18-22	Mach Plot of Rt=15, Tc=3000K, F=501mN	169
18-23	Mach Plot of Rt=15, Tc=3000K, F=501mN	169
18-24	Mach Plot of Rt=15, Tc=3000K, F=501mN	169
18-25	Ideal/Computed Reynolds Number of Rt=1,5,10,15 @ F=501mN	170
18-26	Ideal/Computed Reynolds Number of Rt=1,5,10,15 @ F=31mN	171
18-27	Isp Efficiencies of Aspect Ratios 1,5,10,15 @ F=501mN	174
18-28	Thrust Efficiencies of Aspect Ratios 1,5,10,15 @ F=501mN	174
18-29	Isp Efficiencies of Aspect Ratios 1,5,10,15 @ F=501mN	175
18-30	Thrust Efficiencies of Aspect Ratios 1,5,10,15 @ F=501mN	175
18-31	Isp Levels of Aspect Ratios 1,5,10,15 @ F=501mN	176
18-32	Isp Levels of Aspect Ratios 1,5,10,15 @ F=31mN	176
19-1	Thrust Efficiency as a Function of Reynolds Number.....	179
19-2	Thrust Efficiency as a Function of Chamber Temperature.....	180
19-3	Isp Efficiency as a Function of Reynolds Number	181
19-4	Isp Efficiency as a Function of Chamber Temperature	182
19-5	Resultant Isp as a Function of Reynolds Number.....	183
19-6	Isp Levels of Isp vs Chamber Temperature for Various Re #.....	184

LIST OF TABLES

#	Table	Page
1-1	Small Satellite Classification ¹	3
1-2	Example of Spacecraft Cost and Development Time	3
3-1	Pointing Accuracy Requirements ¹⁷	9
3-2	Moment of Inertia for Selected Missons.....	12
3-3	MIB for Various Slew Rates of Selected Missions.....	12
3-4	ΔV of Orbital Tranfers.....	18
3-5	Interplanetary ΔV Requirements (Moon/Mars)	18
3-6	Interplanetary ΔV Requirements (Asteroid/Jupiter) ¹³	19
4-1	Micropropulsion Technology Summary	21
4-2	Monopropellant Propulsion Technologies	24
4-3	Density/Density-Isp for UW Fuel/Oxidizer	22
5-1	Valve Technology of General Dynamics (Primex Aerospace).....	19
6-1	Micropropulsion Technology Applied to SNAP-1 Mission	28
6-2	Micropropulsion Technology Applied to Main Propulsion System of NASA-GSFC Nanosatellite	30
6-3	Micropropulsion Technology Applied to Attitude Control System of NASA-GSFC Nanosatellite	31
6-4	Micropropulsion Technology Applied to GSFC SpartanLite	33
6-5	Micropropulsion Technology Applied to Main Propulsion System of LunARSat.....	35
6-6	Micropropulsion Technology Applied to Attitude Control System of LunARSat	36
6-7	Micropropulsion Technology Applied to TechSat21	38
6-8	Micropropulsion Technology Applied to ESA Geomagnetic Smallsatellite	40
6-9	Micropropulsion Technology Applied to Interplanetary Platform	42
7-1	Theoretical Isp Correlation to Chamber Temperature of NH ₃ /N ₂ O and H ₂ O diluent ..	44
9-1	Knudsen Number Categories ¹	61
9-2	DSMC (SMILE) & NS (GASP) Comparison ²⁶	63
9-3	Results of 2D / 1994 Computational Efforts of Various Geometries ²⁵	67
9-4	Results for High-Temperature Analysis of Axisymmetric Nozzles.....	68
9-5	Contoured Throat Results ²⁷	72
9-6	Wall Conditions for High-Temperature Analysis ²⁸	73

9-7	Results for Various Chamber/Wall Conditions of High-Temperature Analysis.....	73
9-8	3D Block Isp Efficiencies	74
9-9	Selected Nozzle Thrust Efficiencies for Truncated Nozzle	76
12-1	Throat diameters for thrust level = 125 mN at expansion ratio = 10	88
12-2	Throat diameters for thrust level = 10 mN at expansion ratio = 10	89
12-3	Limit of Continuum INCA Code	94
12-4	Aspect Ratio Test Cases.....	95
13-1	Test Cases for High-Temperature Analysis	101
13-2	Theoretical Isp Levels.....	101
14-1	Test Cases for Experimental Recommendation of Mass Flow	103
15-1	Grid Point Values.....	111
15-2	Grid Point Values for Different Expansion Ratios and Divergence Half-Angles....	112
15-3	Nozzle Initial Pressure Conditions.....	116
15-4	Initial Temperature/Species Conditions.....	116
15-5	Species Fractions for Approximate, Exact CEA Output and INCA Input.....	128
15-6	Comparison Results for Eigenvalue Smoothing Coefficients.....	130
16-1	Sample Output File Including Thrust and L2 Norm	135
17-1	Variation in Physical Dimensions for Aspect Ratios of 1,10.....	140
17-2	Conditions for Code Verification / Mesh Analysis of Rt = 10	141
17-3	Grid Data for Inviscid Mesh	142
17-4	Inviscid Results	143
17-5	Grid Data for Viscous Verification of Rt=10.....	145
17-6	Viscous Results	146
17-7	Grid Data of 2 nd Order Mesh Refinement, Rt=10	148
17-8	Results of Mesh Refinement, Rt=10	148
17-9	Mesh Refinement Verification of Tc = 3000 K, Rt = 10	150
17-10	F/Isp Variation of Re=2000 for Spacing from 0.005 to 0.001	150
17-11	F/Isp Variation of Re=2000 for Endwall Spacing of 0.001, 0.002, 0.005	151
17-12	Grid Data for Mesh Refinement Study of Aspect Ratio = 5	152
17-13	Results of Mesh Analysis of Aspect Ratio = 5	154
17-14	Grid Data for Aspect Ratio = 1	154
17-15	Results for Mesh Analysis of Aspect Ratio = 1	155
17-16	Grid Data for Mesh Study of Aspect Ratio = 15.....	156
17-17	Results for Mesh Analysis of Aspect Ratio = 15	157

17-18	Results Summary for Mesh Refinement Studies / Legend for Figure 17-18	158
17-19	Results Comparison with Past Efforts	160
18-1	Cause of Variation in Reynolds Number from Expected Results	172
18-2	Summary of Aspect Ratio Results	173
19-1	Operating Conditions for High-Temperature Analysis.....	178
19-2	Summary of Results for High-Temperature Analysis.....	178
19-3	Difference Trend in Isp For Each Temperature Increment.....	183
21-1	Small Thrust Levels with Impulse Bit Application.....	188

GLOSSARY

a.....	speed of sound (m/s)
ACS.....	attitude control system
A _e	exit area (m ²)
A _t	throat area (m ²)
b.....	base length (m)
B ₀	proportionality constant
C.....	mean molecular speed (m/s)
Cd.....	discharge coefficient
CG	cold gas
CP.....	chemical propulsion
DEAN	diethylhydroxylammonium nitrate
Del-v	delta-v (m/s)
DSMC	Direct Simulation Monte Carlo
D _t	throat diameter (m)
EP.....	electrical propulsion
Eratio (ϵ)	expansion ratio
F	thrust (N)
F_eff.....	thrust efficiency
FEEP	field emission electrical propulsion
FMMR.....	free molecule micro-resistojet
g.....	gravity (m/s ²)
GEO	geosynchronous orbit
GSFC.....	Goddard Space Flight Center
h.....	height (m)
HAN	hydroxylammonium nitrate
I	mass moment of inertia (kg-m ²)
Isp_eff	specific impulse efficiency
id #	test case identification number
Isp.....	specific impulse (sec)
k _B	Boltzmann's constant (1.38E-23 J/K)
Kn #.....	Knudsen Number
L.....	moment arm (m)

LEO.....	low-earth orbit
m (mdot).....	mass flux (kg/sec)
M.....	molecular mass (gm/mol)
MIB.....	minimum impulse bit (N-sec)
Minert	inert mass (kg)
MMH.....	monomethylhydrazine
MOI.....	mass moment of inertia (kg-m ²)
Mprop.....	propellant mass (kg)
Mprsys.....	propulsion system mass (kg)
n.....	# particles/unit volume
n_F	thrust efficiency
n_Isp.....	specific impulse efficiency
NS	Navier-Stokes Continuum Model
NTO	nitrous tetroxide
P	pressure (N/m ²)
P	power (W)
Pc.....	chamber pressure (N/m ²)
P _e	exit pressure (N/m ²)
PPT.....	pulsed-plasma thruster
R (ρ).....	density (kg/m ³)
Re #	Reynolds Number
Re_t.....	Reynolds Number @ throat
Re_e	Reynolds Number @ exit
RJ	resistojet
Rt (or AR).....	aspect ratio
SA/Vol	surface area to volume ratio (m ⁻¹)
s/c	spacecraft
SOI.....	sphere of influence
t	time (sec)
T	temperature (K)
Tc	chamber temperature (K)
T _e	exit temperature (K)
TEAN.....	triethanolammonium nitrate
TOF	time of flight (sec)

U	axial velocity (m/s)
V_{prsys}	propulsion system volume (kg)
V_{prop}	propellant volume (kg)
V_{inert}	inert system volume (kg)
τ	shear stress (N/m^2)
θ	divergence half-angle
λ	mean free path (m)
η	efficiency
$\rho\text{-Isp}$	density specific impulse ($\text{N}\cdot\text{s}/\text{ltr}$)
ΔV	delta-v (m/s)
μ	viscosity ($\text{kg}\cdot\text{m}/\text{s}$, poise)
σ	collision cross section
γ	gas constant
Ω_v	collision frequency

Acknowledgements

Thanks to the University of Washington Department of Aeronautics and Astronautics for the opportunity to study and perform this research.

Introduction

This thesis focuses on a new high-temperature chemical propulsion system under development at the University of Washington (UW). The chosen fuel/oxidizer combination is ammonia and nitrous oxide. With a stoichiometric reaction, the adiabatic flame temperature is around 3000 K. Advantages of this propellant combination are its non-toxicity and relatively high specific impulse. The disadvantage is finding a material of sufficient thermal resistivity to withstand the high temperatures. A brief mission analysis is performed to find if there exists an area of effective application for this propulsion system. One area of specific interest involves small spacecraft. Since this is a non-toxic propellant with high specific impulse, it has several advantages over other chemical propulsion systems. In order to maintain high levels of specific impulse for low thrust levels, it is necessary to decrease the physical dimensions of the nozzle. Reducing the scale and increasing the operating temperature magnifies the viscous effects associated with boundary layer growth. The second half of this thesis deals with finding a region of ‘negative return’ where the inefficiencies associated with viscous effects outweighs the increase of desired gain in specific impulse. Attention is given first to finding the optimum geometry for a MEMS nozzle using past research and a numerical study on the aspect ratio (height/width ratio at the throat). Aspect ratios of 5, 10 and 15 will show increased performance over an aspect ratio of 1. It will also be shown that while there is a definite trend towards an area of ‘negative return’, the maximum temperature level of 3000 K considered in this study still provides more increase in specific impulse than associated inefficiencies with viscous effects. Heat transfer is not taken into account in this study and may be an area of particular interest for further research efforts.

Following an overview of micropropulsion, several missions are outlined of different spacecraft mass and scope. The goal is to compare the use of the UW propulsion concept to other propulsion concepts already available or under research for application to these missions. Using criteria of specific impulse, propellant density and power requirements, it will be shown that the UW propulsion system is applicable to several different areas. Past research methods are reviewed to provide a background and basis for the current project. After an overview of the current research project, a review of the physics of micronozzle flow is given. Introduction to the aspect ratio and high-temperature cases are then given followed by an experimental

recommendation for calculating mass flux. Moving into the numerical methods section, a brief description of the commercially available INCA code is presented followed by detailed descriptions of the grid setup and numerics of the input file. The process of convergence and post-processing of results is summarized and then applied to a numerical validation and mesh refinement study of the four aspect ratios analyzed. Using the optimum aspect ratio from this study, an analysis of five temperature levels for five different Reynolds numbers is examined with the numerical code. The resultant thrust and Isp efficiencies are examined for trends and a possible area of ‘negative return’. From these results possible thrust levels are applied to the missions already presented.

Chapter 1: Micropulsion Overview

In recent years a greater push has been made to develop small-scale satellites. From manufacturing to launch, the development of such satellites provides increased savings of time and money. In terms of occupied weight and volume on launch vehicles, small spacecraft hold several advantages above large spacecraft. In the case of a failed launch or orbit insertion, the loss of small satellites is not as catastrophic as the loss of a single multi-million dollar satellite. For the purpose of this study and analysis, I will investigate satellites ranging from 5 to 500 kg. A rough classification of small satellites is provided below by AFRL¹ and Surrey University¹¹ in table 1-1.

Table 1-1. Small Satellite Classification¹

Classification	Spacecraft (s/c) Mass – kg
Mini-	100-1000
Micro-	10-100
Nano-	1-10
Pico-	< 1

Table 1-2 contains a broad summary of the mass/monetary/time budgets with respect to several different classifications of satellites.

Table 1-2. Example of Spacecraft Cost and Development Time

Spacecraft	Mass – kg	\$\$\$	Time
Nanosat ⁴	10	500K	9 years
SpartanLite ⁵	45	<10M	-
Deep Space I ²	486	149.7M	780 days

The budget required for each class of spacecraft generally increases proportionally with the mass. In case of a mission failure, the turn around time for building a new satellite is presumably going to be less for the small satellites than the larger.

The development of the subsystems necessary for these small-scale satellites has been an extensive area of emphasis. Several groups from the Air Force Research Lab at Edwards AFB to the civilian sector of Primex Aerospace (absorbed by General Dynamics) have investigated the broad spectrum of micropulsion technologies. The first section of this thesis is devoted to the

types of missions available for small-satellite exploitation, the types of propulsion technologies that will best accommodate these missions, and a case analysis of eight different missions to apply these concepts.

The University of Washington, in conjunction with Dr. Eckart Schmidt and Sienna Technologies, is investigating the development of a new high-performance chemical propulsion system²¹. Acting as either a bipropellant or ternary monopropellant system, it provides performance and further application in the micropropulsion market. In this thesis, particular attention is given to the application of this technology in the small-satellite category. An overview of applicable missions and advantages over other technologies is presented as either a main or attitude control system.

The second half of the thesis deals with efficiencies associated with micronozzles. Particular attention is given to the effects of the aspect ratio at the throat and increased chamber temperature levels. Increasing the chamber temperature ideally results in better specific impulse levels (fuel efficiency), but it also increases viscous losses associated with micronozzle flows. CFD techniques are employed to determine if there exists a region of ‘negative return’ for chamber temperature increase.

Chapter 2: Mission Overviews

Small satellite platforms can be applied to a variety of missions. Many missions are used as education platforms for universities and students at the graduate and undergraduate levels. Others are used as earth observing platforms and possibly for interplanetary scientific research and data collection.

In the past several years, engineers have proposed novel ideas for small spacecraft missions. In particular, an annual Small Satellite Conference is held at Utah State University. Missions suggested at the 1999 conference include: stereoscopic imaging, fire observation system, commercial communication, evaluation of damaged satellites, treaty enforcement, thruster attachment for deorbit burns, global change research, and remote sensing¹⁴. More recently, in August of 2001 the following mission concepts were presented:

A paper on formation flying missions was presented at the Joint Propulsion Conference held in Salt Lake City, Utah: 1) Space Technology : two formation flying satellites in a heliocentric orbit trailing the earth, mission designed to target 50 stars over 6 months; 2) Terrestrial Planet Finder : optical interferometer mission also in an earth-trailing heliocentric orbit, mission to find terrestrial planets; 3) Laser Interferometer Space Antenna : three spacecraft designed to ‘detect and observe gravitational waves’ in 1 AU orbit around the sun; 4) Micro-Arcsecond X-ray Imaging Mission : 32 separate spacecraft positioned to collect and assemble information on massive black hole event horizons; 5) Submillimeter Probe of the Evolution of Cosmic Structure : interferometer mission in the Earth-Sun Lagrangian neutrally stable orbit.¹²

At the Jet Propulsion Laboratory, requirements were calculated for a mission to Jupiter’s moon, Europa. It is possible that a larger spacecraft could carry several smaller spacecraft on ‘piggy-back’ to the moon. Once in orbit around the moon, the smaller spacecraft would perform the more hazardous mission of flying into the atmosphere. The mother spacecraft would release the spacecraft into the atmosphere of the moon to gather information and then the mother spacecraft would relay the information back to earth. The failure of a smaller spacecraft would not result in complete failure of the mission¹³.

In order to conduct a detailed plan of how the University of Washington can apply a new monopropellant system in the micropulsion arena, I will do a detailed analysis of several different missions. They include:

SNAP-1⁷ (6.5 kg) : Developed by Surrey University, this nanosatellite is believed to be the first nanosatellite to carry a cold-gas propulsion system. Launched in June of 2000, the mission of the satellite was to demonstrate new small satellite technologies by rendezvousing with another Surrey-built satellite in orbit thereby performing in-orbit formation flying. According to the website, this mission opens the door to future options of remote inspection and multi-point sensing.

NASA-GSFC Nanosatellite⁴ (10 kg) : This program is focused on producing a constellation of satellites that collect scientific data on the physical phenomena that occurs between the earth and the sun. In order to collect accurate data, different location data collection points are required. This is part of NASA's Space Science Sun-Earth Collection program. The first mission utilizing this technology will be a cluster of 100 nanosatellites that will perform remote sensing missions of the earth's magnetosphere. Launch of this mission is expected in 2007.

GSFC SpartanLite^{5,6} (45 kg) : This spacecraft supports a variety of scientific and technological experiments. It is deployed and retrieved from the space shuttle system in an orbit comparable to the International Space Station. A propulsion system is needed to increase the mission duration to one year.

LunARSat⁸ (100 kg) : Primarily an educational spacecraft, its mission is to orbit the moon and collect scientific data on the lunar environment. It will carry a camera and a plasma radar experiment. The propulsion system is needed for escape from the earth's gravity field and insertion into lunar orbit. It is also possible to use this system for the attitude control and pointing error corrections.

TechSat21⁹ (138 kg) : This constellation of satellites is designed by the AFRL and will fulfill a space-based surveillance mission by way of formation flying. The mission objective is to detect ground and airborne targets by way of Space Based Radar. In this system the aperture of surveillance is limited only by the distance of the constellation (in this case 100 km). In particular, the mission is designed to utilize 3 spacecraft in a technology demonstration in 2003 and then follow up with 12 spacecraft in 2007.

ESA Geomagnetic Smallsatellite¹⁰ (264 kg) : (a.k.a. Geometri) This is one of two satellites designed to study the earth's magnetic field. Two satellites at orbital heights of 200 and 600 km collectively gather data to investigate the lithosphere and ionosphere. A propulsion system is

needed for altitude maintenance and the attitude control system. Launch of the 200 km satellite is expected in 2003 and will last 6 months.

Interplanetary Platform¹¹ (590 kg) : (a.k.a. InterPlanet) Set up as a theoretical platform which can carry either payloads of 70 kg to the moon or 20 kg on interplanetary missions, Surrey University has developed this satellite with propulsion needed for both the main escape and insertion burns along with attitude control.

Chapter 3: Mission Requirements

Mission requirements of ΔV and impulse bit have varying values based on the type of mission, lifetime, slew rates, time of travel, and pointing accuracy needed. Below we will briefly investigate the requirements for stationkeeping, formation flying, orbit maintenance, orbit transfer, and interplanetary travel.

As an example of increasing needs for propulsion, figure 3-1 is taken from a report from the University of Surrey in the UK. It depicts the increasing need for propulsion systems of the University in the future.

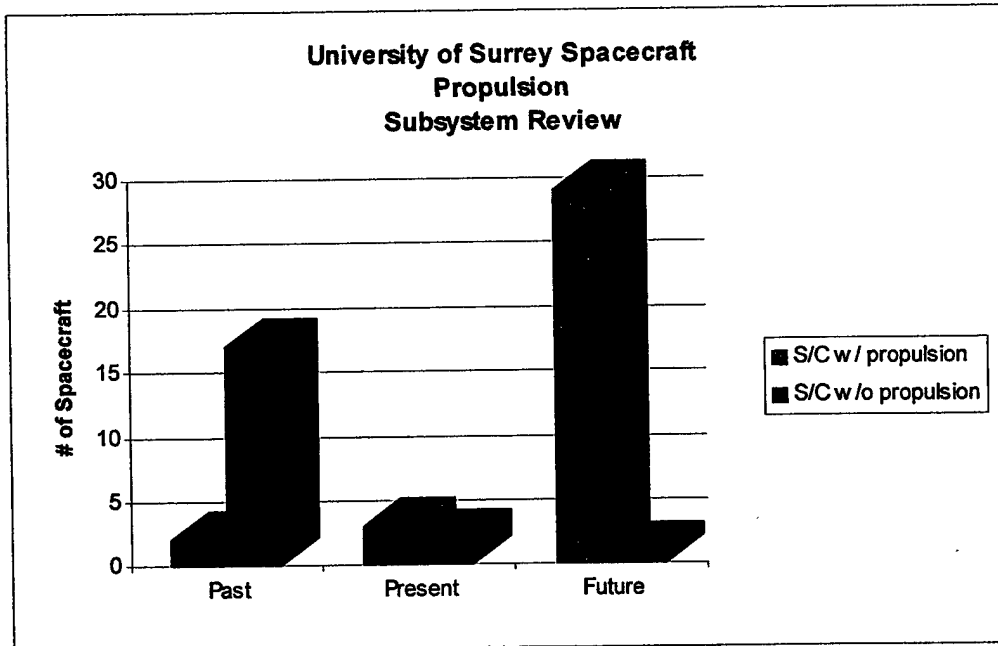


Figure 3-1. Surrey Small Spacecraft Predictions¹⁶

3.1 Stationkeeping

Traditionally, small spacecraft missions have been used to fly low-earth orbits and a large number of these missions have not used chemical or electric propulsion. The main source of an attitude control system has been gravity gradients, magnetic torquers, and reaction control wheels. These are proven and reliable sources of attitude control. Depending on the type of mission, they span a broad base of pointing requirements. Along with the reaction control

wheels, thrusters are needed to desaturate the wheels once they get moving too fast. Table 3-1 displays typical control systems required for desired levels of pointing accuracy:

Table 3-1. Pointing Accuracy Requirements¹⁷

Pointing Accuracy (deg)	Control System
> 5	Gravity Gradient
1 - 5	Thrusters/Dampers for Spinner Actuators
0.1 - 1	Reaction wheels/Thrusters
< 0.1	Reaction wheels/Thrusters (better ADS)

The ability to miniaturize the gravity gradient, reaction wheels, and magnetic torquers is much easier than chemical/electric propulsion (CP/EP) systems. There is also greater chance for failure of EP and CP subsystems. Assuming we can even meet the mass and volume limits of chemical/electric propulsion, the applicability and use of EP and CP requires further investigation and effort.

In order to reorient a spacecraft in orbit, a certain amount of force must be applied to the spacecraft along a moment arm perpendicular to the axis of rotation. This force results in an angular acceleration and slew rate corresponding to equations of (3-1):

$$F = \frac{I \ddot{\Theta}}{L} \xrightarrow{\Theta = \frac{\Theta}{\Delta t}} F = \frac{I \dot{\Theta}}{L \Delta t} \xrightarrow{MIB = F \Delta t} MIB = \frac{I \Theta}{L} \quad (3-1)$$

F = thrust (N)
 MIB = minimum impulse bit (N-s)
 I = mass moment of inertia ($\text{kg}\cdot\text{m}^2$)
 L = moment arm (m)
 t = time (s)
 $\dot{\Theta}$ = slew rate (rad/sec)
 $\ddot{\Theta}$ = angular acceleration (rad²/sec)

Figure 3-2 is a graphical representation of the two thrusters firing on a cylindrical spacecraft:

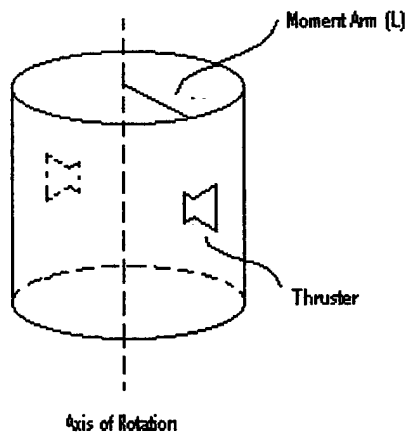


Figure 3-2. Configuration for Slew Rate of Cylindrical Spacecraft

The pointing accuracy is determined by the slew rate and ability to stop the spacecraft in a precise location. The slew rate is a function of thrust, burn time, mass moment of inertia and moment arm. Decreasing the thrust, burn time, or moment arm will decrease the slew rate. Increasing the mass moment of inertia will have the same effect. The mass moment of inertia for cylindrical and cubic shaped spacecraft is outlined in figure 3-3:

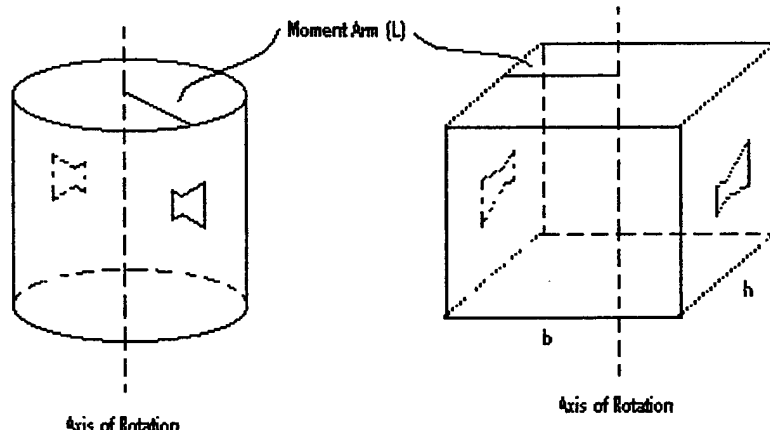


Figure 3-3. Mass Moment of Inertia Diagrams for Cylindrical/Cubic Spacecraft

The respective equations (3-2) for determining the mass moment of inertia (MOI) for a cylinder and cube/box are (assuming equally distributed mass):

Cylinder $I_{xx} = \frac{1}{2}mL^2$	Cube/Box $I_{xx} = \frac{1}{12}m(b^2 + h^2)$
---	--

(3-2)

In the case of extending solar panels, it is possible to compute a MOI based on separate components of the spacecraft.

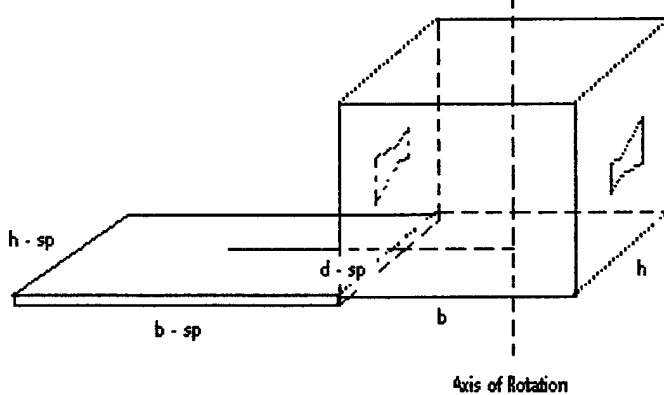


Figure 3-4. Spacecraft Moment of Inertia with Extended Solar Panel

We compute each separate MOI of the spacecraft components, but we add an additional term to account for the mass of the component and the distance from the axis of rotation. Assume we have four solar panels extending from four sides of the cubic spacecraft, the moment of inertia becomes (3-3):

$$\begin{aligned}
 I_{xx} &= I_{body(bd)} + I_{solarpanels(sp)} = \\
 &\frac{1}{12}m_{bd}(b_{bd}^2 + h_{bd}^2) + 4\left(\frac{1}{12}m_{sp}(b_{sp}^2 + h_{sp}^2) + m_{sp}d_{sp}\right)
 \end{aligned}
 \tag{3-3}$$

For the missions selected we assume a single body. In table 3-2 on the next page is a list of the mass moment of inertia properties of the eight spacecraft and applicable assumptions:

Table 3-2. Moment of Inertia for Selected Missions

Spacecraft	Shape	Mass (kg)	L (m)	b (m)	h (m)	MOI (kg-m^2)
SNAP-1	Cube	6.5	0.065			0.075
Nan sat	Cylinder	10	0.15	-	-	0.113
Spartanly	Cylinder	45	0.175	-	-	0.689
LunARSat	Box	100	-	0.6	0.8	8.333
TechSat21	Box	138	-	1.2	1.2	33.120
Geometri	Box	264	-	0.71	0.71	22.180
InterPlanet	Cube	576	-	1.1	1.1	116.160

Using these values for the MOI and moment arm, we can design a propulsion system for thrust and burn time (impulse bit) based on desired slew rates and pointing accuracy.

Table 3-3. MIB for Various Slew Rates of Selected Missions

Spacecraft	kg-m^2	(m)	Slew Rate (deg/min)												
			0.001	0.01	1	15	45	90	135	180	mN-s	N-s	N-s	N-s	N-s
SNAP-1	0.075	0.065	2.01E-02	2.01E-01	2.01E-02	3.02E-01	0.906	1.812	2.719	3.625					
Nanosat	0.113	0.15	1.31E-02	1.31E-01	1.31E-02	0.20	0.59	1.18	1.77	2.36					
SpartanLite	0.689	0.175	6.87E-02	6.87E-01	6.87E-02	1.03	3.09	6.19	9.28	12.37					
LunARSat	8.333	0.4	0.36	3.64	0.36	5.45	16.36	32.72	49.09	65.45					
TechSat21	33.120	0.6	0.96	9.63	0.96	14.45	43.35	86.71	130.06	173.42					
Geometri	22.180	0.355	1.09	10.90	1.09	16.36	49.07	98.14	147.22	196.29					
InterPlanet	116.160	0.55	3.69	36.86	3.69	55.29	165.88	331.75	497.63	663.50					

The following two pages depict graphically the MIB required for slew rates up to 180 degrees per minute.

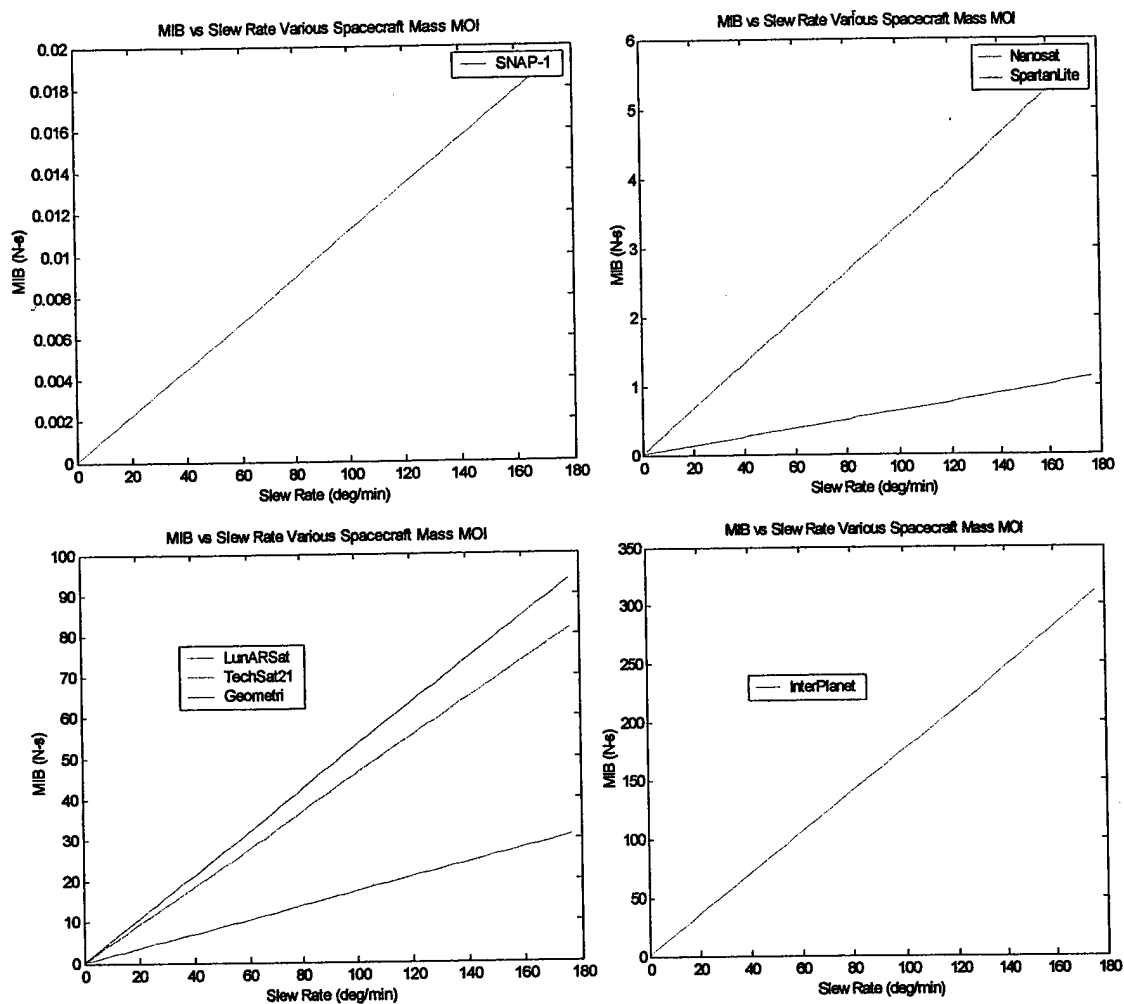


Figure 3-5. Slew Rates up to 180 degrees/minute

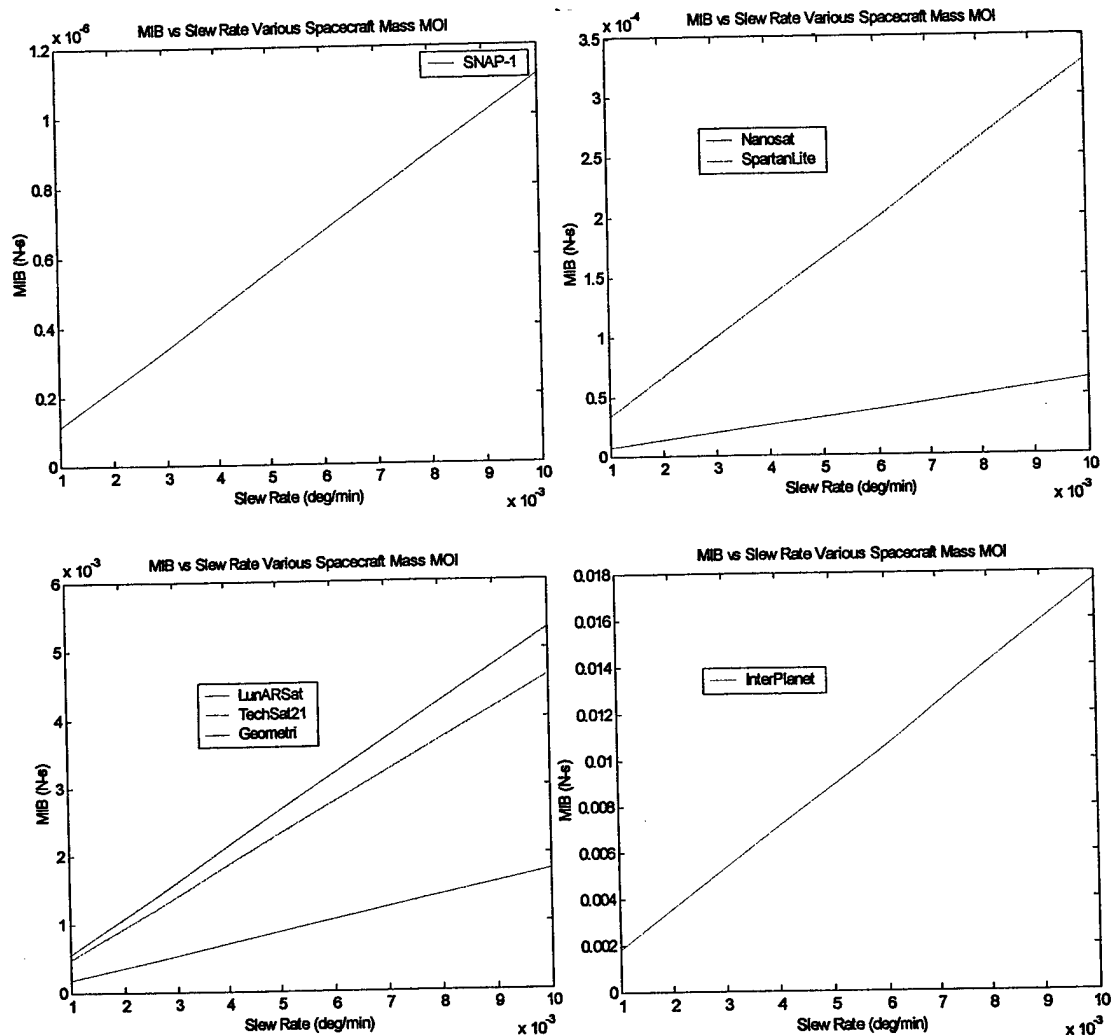


Figure 3-6. Slew Rates from 0 to 1 degree/minute

As mentioned before, impulse bits are a product of thrust and burn time. Therefore, by either decreasing the thrust or the burn time we can obtain the impulse bit level low enough for these small satellites. Electric propulsion (EP) can provide impulse bits small enough for highly precise attitude control. Chemical propulsion (CP) on the other hand, usually involves greater amounts of thrust, and therefore shorter firing times. The necessary thrust limits also depends on the valve technology available. In the next section we will look at the various technologies to fulfill the slew rate/pointing accuracy requirements of various missions.

3.2 Formation Flying

Impulse bits required for formation flying are generally accepted as being very small. For instance, the Dawgstar satellite developed by the University of Washington is using a pulsed-plasma thruster that is designed to produce impulse bits of only $65\mu\text{N}\cdot\text{sec}$ at 500 seconds of Isp²⁰. Of course, such small impulse bits require long transition periods for formation changes. If this is acceptable then electric propulsion may be the system of choice based on higher levels of Isp and precise maneuvering. The downside to electric propulsion is the need for a power supply unit which can add additional inert mass to the satellite. The need for chemical propulsion in this area will only be applicable for larger satellites which will still require small impulse bits for formation flying, just not in the μN range.

An example of formation flying using chemical propulsion is the SNAP-1 project from Surrey University. It uses a butane gas which is self-pressurizing to produce 45-120 mN of thrust. Therefore, although there are claims that the low thrust available from electric propulsion is ideal for formation flying, the limits are mission dependent and if this propulsion concept can produce thrust levels in the 50 mN range, it is likely that for specific missions this concept can also be used for formation flying.

3.3 Orbit Transfer/Maintenance

In order to increase the lifetime of missions, propulsion systems are used to boost the orbit of a satellite. Atmospheric drag gradually deteriorates the orbit of the satellite, therefore the ability to compensate for this opposing force is essential in LEO (low-earth orbit) missions. In addition, often times as a secondary payload, small satellites are placed in orbits which require

additional maneuvering upon release from the launch vehicle. This section will investigate the ΔV necessary for orbit maintenance/transfer for both impulsive and low-thrust maneuvers.

There are currently two methods of obtaining an altitude increase: For high thrust systems, the hohmann transfer is the most efficient use of fuel. A maneuver known as one-tangency burns can achieve an orbital transfer in a smaller amount of time, but at increased cost of fuel. For high thrust systems we will only consider the use of the Hohmann transfer.

For low thrust propulsion systems, the assumption of an impulsive burn necessary for a Hohmann transfer is not feasible, therefore it is necessary to perform a continuous burn over a longer period of time. David Vallado presents a summary of computations developed by Alfano to compute the time of flight necessary for these transfers¹⁸. Information from the propulsion division of General Dynamics gives information on the ΔV necessary for these burns¹⁹.

Hohmann transfers and low-thrust, continuous burns are illustrated below in figure 3-7:

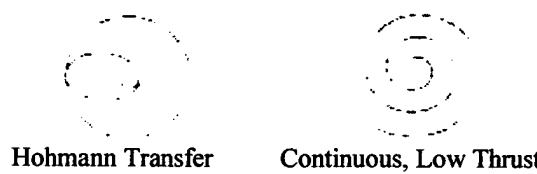


Figure 3-7. Hohmann and Low-Thrust Transfers¹⁹

The ΔV requirements for a Hohmann Transfer and Continuous-burn transfer are different due to the length of time involved between orbits. As will be seen below, low-thrust burns take longer and thus spend more time burning against forces of atmospheric drag and gravity on the way out. Below are equations used in computing the ΔV for both situations:

Hohmann Transfer¹⁵ (3-4)

$$V_2 = \sqrt{\frac{\mu}{R_2}}$$

$$\varepsilon = -\frac{\mu}{(R_1 + R_2)}$$

$$V_{T2} = \sqrt{2\left(\varepsilon + \frac{\mu}{R_2}\right)}$$

$$\Delta V_1 = |V_{T1} - V_1|$$

$$\Delta V_2 = \sqrt{[V_2^2 - V_{T2}^2 - 2V_2 V_{T2} \cos(\Delta\theta)]}$$

$$\Delta V_{TOTAL} = \Delta V_1 + \Delta V_2$$

Continuous, Low Thrust¹⁸ (3-5)

$$\Delta V_{TOTAL} = \sqrt{[V_1^2 + V_2^2 - 2V_1 V_2 \cos\left(\frac{\pi\theta}{2}\right)]}$$

R_1 = (m) altitude @ initial orbit (includes radius of earth)
 R_2 = (m) altitude @ final orbit (includes radius of earth)
 V_1 = (m/s) velocity @ initial orbit
 V_2 = (m/s) velocity @ final orbit
 V_{T2} = (m/s) velocity on transfer orbit
 ε = orbit energy
 μ = gravitational parameter of earth ... 398,600 km³/s²
 R_{earth} = 6,378 km
 R_{LEO} = 300 km
 R_{GEO} = 35,786 km
 θ = orbit inclination

Examples of ΔV orbital transfers are listed below in table 3-4. Note that there is not a significant difference between the Hohmann and low thrust transfers until at least a 300 km boost is needed.

Table 3-4. ΔV of Orbital Transfers

LEO to	ΔV (m/s)	ΔV (m/s)
	Hohmann Transfer	Continuous, Low Thrust
3 km boost	1.74	1.74
30 km boost	17.3	17.3
300 km boost	167.88	167.9
3000 km boost	1297	1308
30,000 km boost	3790	4429
GEO (35,486 km boost)	3,893	4,651

A greater difference is observed in the relative time of flight for each. The algorithm for the TOF of the Hohmann Transfer is a simple one-step process. The continuous burn is more involved and can be found in reference [18]. Generally the Hohmann transfer provides a faster and more fuel-efficient means of transferring between two orbits, therefore higher thrust propulsion systems are required.

3.4 Interplanetary Travel

Interplanetary travel is restricted to propulsions systems which can supply sufficient ΔV to escape earth's sphere of influence (SOI) and at the end of the journey, enough ΔV in a retroburn to be captured by the destination body's SOI. Table 3-5 contains requirements for typical interplanetary travel originating from LEO:

Table 3-5. Interplanetary ΔV Requirements (Moon/Mars)

Destination	Departure Burn	Arrival Insertion
Moon ¹¹	690 m/s	810 m/s
Mars ¹⁵	3590 m/s	2100 m/s

JPL has also done various calculations for interplanetary travel for both electrical and chemical systems. These missions take advantage of gravity assist trajectories to decrease the amount of ΔV the spacecraft must deliver.

Table 3-6. Interplanetary ΔV Requirements (Asteroid/Jupiter)¹³

Mission	Chemical ΔV (m/s)	Electrical ΔV (m/s)	Time of Travel (yrs)
Asteroid Rendezvous	3400 (Mars assist)		4.3
Asteroid Rendezvous		7000 (direct)	2.7
Jupiter-Europa	2500		4.8
Jupiter-Europa	945 (insertion)	5500 (Venus assist)	5.8

While gravity assist trajectories decrease the ΔV required, upon arrival at the planet, a burn is made to insert the spacecraft into the proper orbit. This burn must provide sufficient impulse along the approach trajectory to ensure that the satellite goes into orbit. Too little impulse and the spacecraft will continue past the body, too much and it will crash. This impulse must be delivered by a propulsion system capable of providing large amounts of thrust in relatively small periods of time. Making this clarification, while small-thrust systems such as electric propulsion can get you to the body in theoretically less time as seen above, chemical systems are essential to orbit insertion.

Chapter 4: Micropulsion System Options

With larger scale satellite systems, chemical propulsion systems have been the traditional choice for active attitude control. Electrical propulsion generally cannot supply a sufficient impulse bit for a given moment of inertia for larger spacecraft. With an increasing option for smaller spacecraft, electric propulsion technology has become a more viable option. On the other hand, certain missions require chemical propulsion for orbit insertion and shorter flight times as we have seen in the previous section.

Chemical propulsion systems generally operate anywhere between 50 and 300 seconds of specific impulse. Thus, for missions requiring large amounts of delta-v, large amounts of propellant must be stored on board. In contrast, electric propulsion systems range anywhere from 90 to 9000 seconds of specific impulse. Therefore, these systems are more suitable for large delta-v missions such as interplanetary travel (unless other means such as gravitational assist can be used). While electric propulsion has the upper hand in terms of specific impulse, chemical systems produce larger thrust levels. Thus, chemical systems are more suitable for large impulse burns such as orbit insertion and hohmann transfers. In order to produce larger amounts of thrust in electrical systems, it is necessary to increase the power input to the system. Table 4-1 is a summary table for chemical and electric propulsion technologies and their range of applicability (specifics and references of each technology can be found in Appendix A). Note that a comprehensive search of propulsion options has already been performed by Juergen Mueller and can be found in reference [57]. The technology search of this project extends his search and applies the data he already compiled.

The ρ -Isp (rho-Isp) listed in the following tables is a measure of the amount of Isp attainable for a given volume and is computed in equation (4-1) below:

$$\rho - Isp = .00981 * Isp * \rho \quad (4-1)$$

Table 4-1. Micropulsion Technology Summary

Technology	Isp (sec)	ρ -Isp (Ns/ltr)	Power (W)	Fmin(mN)	Fmax(mN)
Arcjet	90-1500	118-4974	4 - 30,000	5.40	2224
Bipropellant	260-313	2126-3659	-	100	-
Cold Gas	28-272	40-981	-	4.5	5 N
Colloid	450-1450	-	2.5 - 10,000	0.13	1
FEEP	9000	-	2.7 - 370	0.04	1.4
FMMR	70	-	15	4	6
Hall	576-5000	-	50 - 100,000	1.8	3 N
Hybrid	259-269	1982-3457	-	-	-
Ion	800-5000	-	50 - 100,000	1	890
Microwave	175-259	745-1500	-	187	654
Monopropellant	165-260	1480-3840	-	320	-
PPT	200-2580	-	1 - 750 Joules	0.002	2
Resistojet	127-304	745-1010	100 - 830	45	498
Solid	199-250	-	-	159 N	169 N
Subliming Solid	75-262	508-4781	100 - 2000 / N	0.01	10 N
Warm Gas	138	279	10 / N	10	10 N

The above technologies represent a wide range of research and resources. A large number of the above technologies are ideas and have not flown as of yet. In order to qualify the current system under development at the University of Washington, it is necessary to compare it with existing ideas and more fully understand the realm of opportunity and competition for mass and volume on the spacecraft itself and overall mission requirements.

4.1 University of Washington Ternary Propulsion System

The program underway at the University of Washington is designed to produce a green (non-toxic) propellant. It could take the form of either a bipropellant or monopropellant depending on the reaction properties of the fuel and oxidizer. Several gas mixtures were considered as candidates but the final consensus was a mixture of ammonia and nitrous oxide. The miscibility of these fuels is uncertain, therefore the practicality of its use as a monopropellant is largely unknown. In addition, whether or not the gases will combust in the presence of the other is also a question. It is possible that addition of a diluent such as nitrogen or water could stabilize a monopropellant mixture and then introduction to a catalyst would initiate combustion as is the case with Tridyne^{®106}. Other factors being investigated include the rate of combustion.

Applying this to a small-scale satellite requires fast reaction times so the most potential chemical energy can be converted into kinetic energy. Ideally it would be used as a simple blow-down system operating at chamber pressures of 30 bar. It could be used as a bipropellant system by separating the fuel and oxidizer, but the mixing time involved in small-scale devices is not sufficiently long to produce high efficiencies. In addition, bipropellant systems require additional inert mass and complexity. Therefore, with a ternary mixture (fuel/oxidizer/inert component to prevent premature combustion) we can store the propellant as a single liquid or gas. Not only is the combustion process a driving factor, but on board any satellite a reduction in the number of mechanical parts reduces the chance of catastrophic failure of the propulsions system. The blow down approach requires a holding tank for the ternary mixture, miniature valve for accurate impulse bit firings, nozzle, catalyst bed, and connections between the separate components.

For a stoichiometric mixture, the chamber temperature could reach temperature levels in excess of 3000 K. Ideally this temperature corresponds to ~280 seconds of specific impulse. Of course, this specific impulse level requires the ability to contain such high temperatures. Sienna Technologies Inc., of Woodinville, WA, is developing materials for high-level temperatures. Currently, they have a material which can be used for temperature levels of ~2000 K (corresponding to ~240 seconds of Isp for UW propulsion concept). Another material available, but currently not capable of use as a micronozzle, can withstand temperatures of 2500 K (Isp ~260 seconds). Other work is also being performed for materials that can withstand these high temperatures¹¹⁷.

In a preliminary analysis, Dr. Schmidt computed the density of this new propellant combination to be approximately 709 kg/m³ for stoichiometric oxidizer/fuel combination at 298 K. This gives the following:

Table 4-3. Density/Density-Isp for UW Fuel/Oxidizer²²

Propellant	Isp (sec)	Density (kg/m ³)	rho-Isp (Ns/ltr)
U of Wash.	~280	709	1967

4.2 Monopropellant Comparisons

A company local to the Seattle area has long specialized in small chemical propulsion systems. Primex (now absorbed into General Dynamics) has proven experience with hydrazine systems. The disadvantage of hydrazine is the toxicity and safe-handling procedures. Another possible popular monopropellant source is HAN and its derivatives. While this has the advantage of being a green propellant (non-toxic) the combustion process leaves behind a salt residue²². This residue can clog the throat and lead to failure of the entire propulsion system. The proposed propulsion system of the University of Washington incorporates advantages of being both green and residue free. Table 4-2 is a comprehensive table of the monopropellants found through a literature search.

Table 4-2. Monopropellant Propulsion Technologies

Propellant	Isp (sec)	Density (kg/m ³)	rho-Isp (Ns/ltr)	Fmin (mN)	Fmax (mN)	I-bit (mN-s)	Mass (kg)	Reference
Hydrazine	200-223	1010	2180	320	1000	14-43	.27-.28	82
Hydrazine	210-220	1010	2150	900			0.33	57 (79)
Hydrazine	213-224	1010	2150	2200			0.33	57 (79)
Hydrazine	226-229	1010	2217	4450			0.33	57 (79)
Hydrazine	175	1010	1734	20		< 50		83
Hydrazine	220	1010	2180	0.9	4.45			57 (100)
Hydrazine	220	1010	2180	5000			0.82	84
Hydrazine	222	1010	2200	250		23	0.376	57
Hydrazine	223	1010	2210	1000			.27-.28	57 (99)
Hydrazine	226	1010	2239	900			0.33	57 (99)
Hydrazine	230	1010	2279	4450			0.38	57 (100)
Hydrazine	230	1010	2279	18000			0.41	82
HAN - LPXM46	232.4	1435	3272					114
Hydrazine	234	1010	2318	1000		70	0.376	84
HAN - 20% H ₂ O	255	1435	3590					85
HAN - 15% H ₂ O	262	1435	3688					85
HAN - 15% H ₂ O	273	1435	3843					85
H ₂ O ₂ 85-92%	179	1347	2365	13345				115
H ₂ O ₂ 85-92%	179	1347	2365	26689				115
Hydrazine	150	1010	1486	20		50-100		83
HAN/Glycine	247	1500	3635					86
HAN/Glycine	225	1400	3090					86
HAN/Glycine	204	1400	2802					86
HAN/TEAN	247	1400	3392					85
HAN/TEAN	259.4	1450	3690					85
HAN/DEHAN	262.6	1390	3581					85
H ₂ O ₂	165	1390	2250	2000		20		63
Hydrazine	227	1010	2249	1000		10		63
HAN/TEAN	253		0	400	500000			63
N ₂ O	206	745	1506					101
Hydrazine	220	1010	2180	187	1121	4.45	0.33	19
Hydrazine	220	1010	2180	890	2001.7	71.2	0.319	19
Hydrazine	220	1010	2180	1334	5338	84.5	0.33	19
Hydrazine	220	1010	2180	9786	22241	334	0.68	19
Hydrazine	232	1010	2299		26689	1156	0.47	19
Hydrazine	228	1010	2259	16458	35586	503	0.39	19
Hydrazine	225	1010	2229	40034	111206	979	0.41	19
Hydrazine	220	1010	2180	48930	177929	3158	0.88	19
Hydrazine	228	1010	2259	71172	231308	2447	0.88	19
Hydrazine	229	1010	2269	346961	653889	26689	1.9	19
Hydrazine	231	1010	2289	222411	489304	5338	1.86	19
UW Proposal	~ 280	709	1967					23
MMH/NTO Biprop	280	1100	3021	4450			.43	57 (99)

Evident from above is the vast experience with hydrazine systems which makes their proven history a source of confidence for satellite engineers. HAN and the UW ternary systems offer higher levels of Isp and are non-toxic. Theoretically it should be possible to obtain the same thrust levels as the hydrazine system. The disadvantage is obviously the lower density compared to the other choices, but once again the non-toxicity and no-residue advantages may outweigh the density problem. For spacecraft where volume is not the main concern, the high specific impulse provides for mass savings over other choices. The UW ternary system will operate at higher temperature levels, therefore smaller physical dimensions will be required for the same thrust level resulting in greater inefficiencies due to viscous effects. Further details of the thrust levels and viscous losses will be explained further after the nozzle flow analysis.

Addition of a diluent in the UW system will reduce the adiabatic temperature and smaller thrust levels are expected. For example, reducing the chamber temperature from 3033 K to 2500 K produces a specific impulse drop of nearly 20 seconds. Even dropping down to a chamber temperature of 2000 K produces a specific impulse (~240 seconds) comparable with the HAN propellant.

Chapter 5: Valve Technology

Essential to providing small impulse bits for small satellites based on the available thrust for a given propulsion system is the valve. Two important design drivers when looking for a suitable valve are the weight and response time. Obviously for small spacecraft, the lower the weight the better. Theoretically, if it was possible to make the response time (the time the propellant is allowed to flow) as small as possible, we could operate at any thrust level and still achieve the desired impulse bit. In reality, since the response time is limited by physical movement of material, only finite levels are attainable. Therefore, in order to achieve a specific impulse bit, there must be a tradeoff between thrust and response time. Table 5-1 is a list of currently used valves at General Dynamics in their small satellite propulsion division.

Table 5-1. Valve Technology of General Dynamics (Primex Aerospace)¹⁹

Valve	Weight (gm)	Operating Pressure (bar)	Power (W)	Response Time (msec)
Primex	204.1	10.3	9	8
Primex	201.9	16.2	12	25
Primex	204.1	24.1	9	20
Primex	272.2	16.9	29	22
Primex	265.8	31.0	27	60
Primex	195.0	27.6	10	20
Primex	122.5	22.4	45	11
Primex	272.2	31.0	50	20
Primex	199.6	22.4	60	16
Primex	408.2	30.7	58	40
Primex	426.4	24.1	30	22

MEMS technology has also produced micro-isolation valves. Although these valves do not weigh very much, they can only be opened once, thereby negating any applicability to multiple burns. The application of these valves will be investigated further for specific thrust levels and mission application.

Chapter 6: Mission Application

Having identified several missions and possible propulsion system options, the following discussion applies the propulsion technologies to these separate missions. For each mission an evaluation is performed for each propulsion system. Specific areas of interest are density specific impulse, volume required for propellant storage, and thrust range. If available, attention is also given to the minimum impulse bit available and power required for valve operation. Since the valve is generally independent of the propulsion system, the minimum impulse bit will vary based on the type of valve chosen. Therefore, for this study these values are presented when data is available, but particular attention is given to the three areas mentioned previously.

The following tables use these acronyms: RJ – resistojet, CG – cold gas, W-gas – warm gas, M-prop – monopropellant, Biprop – bipropellant, FMMR – free molecule micro-resistojet, FEEP – field emission electric propulsion. The first three lines of each table represent the mission requirements and design limits. Items underlined represent a technology parameter which exceeds those limits. If an item is italicized in bold, this represents a parameter which is close to the requirements of the mission and may be used if the requirements are flexible. Following each table, a brief explanation of how the monopropellant of the University of Washington (hereafter referred to as UW ternary) could possibly fulfill the respective mission, if at all. The other propulsion system specifications are provided as a reference and comparison. Other acronyms are listed below:

Minert : inert mass
Mprsys : propulsion system mass
Vprsys : propulsion system volume
Del-v : delta-v
Mprop : propellant mass
Vprop : propellant volume
P : power
F : thrust
Vinert : inert system volume

Table 6-1. Micropulsion Technology Applied to SNAP-1 Mission⁷

(m/s)		(kg)	(g)		(g)	(kg)	(mN)		(cm3)	(cm3)	(W)
del-V		Ms/c	Mprsys		Minert	Mprop	F	MIB	Vinert	Vprsys	P
3		6.5	455		422		45-120	n/a	7.400	65.000	3.5-6
		(sec)	(kg)	(kg/m3)	(Ns/ltr)	(kg)	(mN)	(mN-s)	(cm3)	(cm3)	(W)
SYSTEM	Propellant(s)	Isp	Mprsys	rho	rho-Isp	Mprop	F	MIB	Vpr	Vprsys	P
* CG	Butane - C4H10 (l)	65	0.65	530	338	0.0305	45-120	n/a	57.6	65.000	3.5-6
Arcjet	N2	110		400	432	0.0180	5.4		45.1		4
Arcjet	NH3	787		609	4702	0.0025	1930		4.1		26 k
Biprop	MMH/CIF3	310		699	2126	0.0064	100	0.1	9.2		
Biprop	MMH/NTO	290	0.1	1100	3129	0.0069	156000		6.2		
CG	Water	100	0.4418	1000	981	0.0198	50	1000	19.8	27.2	0.3
CG	Ammonia	96	0.4427	609	574	0.0207	50	1000	33.9	41.3	0.3
Colloid	Nal/glycerol	450				0.0044	0.6				2.5
Colloid	Nal/glycerol	1540			0	0.0013	0.4				10
FEEP	Cs	9000	1.6 p			0.0002	0.04			1920	2.7
FEEP	Cs	9000	8.7 p		0	0.0002	1.4			23268	370
FMMR	H2O	70		1000	687	0.0283	5		28.3	35.7	15
Hall	MIT Mini	1600		n/a	n/a	0.0012	3		n/a		50
Hall	Texas Tech	3300		n/a	n/a	0.0006	3000		n/a		30 k
Hall	BHT-HD-60	1700	< 2.2	n/a	n/a	0.0012	45		n/a	2160	700
Ion	NASA Lewis	1760			0	0.0011	3.6				100
Ion	JPL	3900	2.5		0	0.0005	31				100
Ion	BBM1-MK1-2/Xe	3518	12.5		0	0.0006	150			184490	
M-prop	Hydrazine	234	0.376	1010	2318	0.0085	250	23	8.4		9.6
M-prop	HAN	250		1450	3556	0.0079				5.5	
M-prop	H2O2	179		1347	2365	0.0111				8.2	
M-prop	UW Term (g)	282		42.47	117	0.0070			165.9		
M-prop	UW Term (l)	282		709.5	1963	0.0070			9.9		
PPT	LES-6	200	2.5			0.0099	2.00E-03	10000			1.85 J
PPT	MIT Lab	2580	11.9			0.0008	6				300J?
PPT	DAWGSTAR	500	3.8								6.5
RJ	N2O	127	1.24			0.0156	125			3998	100
RJ	N2O	182	1.24			0.0109	270			3998	600
RJ	H2O	152	1.24			0.0131	45			3998	100
Solid	Marc 4D	199	0.34			0.0100	159000			530	
Solid	STAR 5A	250	4.7			0.0079	169000			11946	
Solid	Acetamide	75		1000	736	0.0264	.01-10		26.4		
W-Gas	Tridyne	138		206	279	0.0144	1		69.8		10
W-Gas	Tridyne	138		206	279	0.0144	10		69.8		100

The SNAP-1 mission developed by Surrey University made use of a butane cold gas propellant system. Since the Isp is only 65 seconds for the butane propellant, it has a ρ -Isp of only 338 N-s/ltr and occupies 57.6 cm³ of space. Each of the monopropellant options has a higher Isp level and greater density, therefore any of these options for the same volume would provide a much higher attainable delta-v for the mission. The advantage of the butane propellant is the self-pressurizing characteristic. Additional mass for a pressurant is therefore cut from the mass budget. The UW ternary system would require additional mass within the propellant storage tanks to account for the high storage pressure required for propulsion. The simplicity in the cold gas system is obviously an advantage for such a small satellite. The thrust range may be in question for higher performance systems, but this will be answered after the nozzle flow analysis of this thesis.

The electric propulsion options are not viable based on either insufficient thrust levels, excessive power requirements, propulsion system weight or a combination of any of these factors. Integration of the UW ternary system is feasible based solely on propellant mass required for the delta-v requirement of 3 m/s. It would have to be simple enough to contend with the cold gas system. Whether or not the entire propulsion system can fit within the weight limit of 455 g is an area of further research.

Table 6-2. Micropulsion Technology Applied to Main Propulsion System of NASA-GSFC Nanosatellite⁴

(m/s)		(kg)	(kg)		(kg)	(kg)	(N)	mN-s	(cm3)	(cm3)	(W)
del-V		Ms/c	Mprsys		Minert	Mprop	F	MIB	Vinert	Vprsys	P
700	Main	10	2.6			2.0785	445	n/a			< 1
0.024	ACS		0.45				n/a	44			0.3
		(sec)	(kg)	(kg/m3)		(kg)	(N)	(mN-s)	(cm3)	(cm3)	(W)
SYSTEM	Propellant	Isp	Mprsys	rho	rho-Isp	Mprop	F	MIB	Vpr	Vprsys	P
MAIN		280	2.81201		0	2.2496	445	n/a			< 1
Arcjet	N2	110		400	432	4.7727	0.0054		11932		4
Arcjet	NH3	787		609	4702	0.8668	1.93		1423		26 k
Arcjet	N2	90		400	353	5.4744	0.0083		13686		5
Biprop	MMH/CIF3	310		699	2126	2.0561	0.1	0.1	2941		
Biprop	MMH/NTO	290	0.1	1100	3129	2.1812	156		1983		
CG	Xenon	28	9.2179	1095	301	9.2179			8418	8418.2	3.5-6
CG	Methane	105	4.9317	163	168	4.9317			30256	30255.8	3.5-6
CG	?? 2868						250				
CG	Water	100		1000	981	5.1010	1				20-10
Colloid	Nal/glycerol	450				1.4664	0.0006				2.5
Colloid	Nal/glycerol	1540			0	0.4528	0.0004				10
FEEP	Cs	9000	1.6 p			0.0790	4E-05			1920	2.7
FEEP		9000	8.7 p		0	0.0790	0.001			23268	370
FMMR	H2O	70		1000	687	6.3918	0.005		6392	6391.8	15
Hall	MIT Mini	1600		n/a	n/a	0.4362	0.003		n/a		50
Hall	Texas Tech	3300		n/a	n/a	0.2139	3		n/a		30 k
Hall	BHT-HD-60	1700	< 2.2	n/a	n/a	0.4111	1		n/a	2160	700
Ion	NASA Lewis	1760			0	0.3973	0.0036				100
Ion	JPL	3900	2.5		0	0.1813	0.031				100
Ion	BBM1-MK1-2/Xe	3518	12.5		0	0.2008	0.15			184490	
M-prop	Hydrazine	234	0.376	1010	2318	2.6283			2602		9.6
M-prop	HAN	250		1450	3556	2.4830			1712		
M-prop	H2O2	179		1347	2365	3.2876			2441		
M-prop	UW Tern (g)	250		42.47	104	2.4830			58466		
M-prop	UW Tern (l)	282		709.5	1963	2.2356			3151		
PPT	LES-6	200	2.5		0	3.0007					1.85 J
PPT	MIT Lab	2580	11.9		0	0.2728	0.006				300J?
PPT	DAWGSTAR	500	3.8			1.3300		0.07			6.5
RJ	N2O	127	1.24	745	928	4.2985	0.125		5770	3998	100
RJ	N2O	182	1.24	745	1330	3.2434	0.27		4354	3998	600
RJ	H2O	152	1.24	1000	1491	3.7465	0.045		3747	3998	100
Solid	Marc 4D	199	0.34		0	3.0133	159				530
Solid	STAR 5A	250	4.7		0	2.4830	169			11946	
Solid	NASA	280			0	2.2496	445				
W-gas	Tridyne	138		206	279	4.0374	0.001		19599		10
W-gas	Tridyne	138		206	279	4.0374	0.01		19599		100

Table 6-3. Micropulsion Technology Applied to Attitude Control System of NASA-GSFC Nanosatellite⁴

(m/s)		(kg)	(kg)		(kg)	(kg)	(N)	(mN-s)	(cm3)	(cm3)	(W)
del-V		Ms/c	Mprsys		Minert	Mprop	F	MIB	Vinert	Vprsys	P
0.024	ACS		0.45				1	44			< 1
		(sec)	(kg)	(kg/m3)		(kg)	(mN)	(mN-s)	(cm3)	(cm3)	(W)
System	Propellant	Isp	Mprsys	rho	rho-Isp	Mprop	F	MIB	Vpr	Vprsys	P
ACS		280	0.00011		0	8.74E-05	1000	44			< 1
Arcjet	N2	110		400	432	2.22E-04	5.4		5.56E-01		4
Arcjet	NH3	787		609	4702	3.11E-05	1930		5.10E-02		26 k
Arcjet	N2	90		400	353	2.72E-04	8.3		6.80E-01		5
Biprop	MMH/CIF3	310		699	2126	7.89E-05	100	0.1	1.13E-01		
Biprop	MMH/NTO	290	0.1	1100	3129	8.44E-05	156000		7.67E-02		
Biprop	MMH/NTO	295		1100	3183	8.29E-05	500	5	7.54E-02		
CG	Xenon	28	0.0009	1095	301	8.74E-04			7.98E-01	0.8	3.5-6
CG	Methane	105	0.0002	163	168	2.33E-04			1.43E+00	1.4	3.5-6
CG	Water	100		1000	981	2.45E-04	1000		2.45E-01		20-10
Colloid	Nal/glycerol	450				5.44E-05	0.6				2.5
Colloid	Nal/glycerol	1540			0	1.59E-05	0.4				10
FEEP	Cs	9000	1.6 p			2.72E-06	0.04			1920	2.7
FEEP		9000	8.7 p		0	2.72E-06	1			23268	370
FMMR	H2O	70		1000	687	3.49E-04			3.49E-01	0.3	15
Hall	MIT Mini	1600		n/a	n/a	1.53E-05	3				50
Hall	Texas Tech	3300		n/a	n/a	7.41E-06	3000				30 k
Hall	BHT-HD-60	1700	< 2.2	n/a	n/a	1.44E-05	1000			2160	700
Ion	NASA Lewis	1760			0	1.39E-05	3.6				100
Ion	JPL	3900	2.5		0	6.27E-06	31				100
Ion	BBM1-MK1-2/Xe	3518	12.5		0	6.95E-06	150			184490	
M-prop	Hydrazine	234	0.376	1010	2318	1.05E-04	1000		1.04E-01		9.6
M-prop	HAN	250		1450	3556	9.79E-05	1000		6.75E-02		
M-prop	H2O2	179		1347	2365	1.37E-04	1000		1.01E-01		
M-prop	UW Tern (g)	282		42.47	117	8.68E-05	1000		2.04E+00		
M-prop	UW Tern (l)	282		709.5	1963	8.68E-05	1000		1.22E-01		
PPT	LES-6	200	2.5		0	1.22E-04		10000			1.85 J
PPT	MIT Lab	2580	11.9		0	9.48E-06	6				300J?
PPT	DAWGSTAR	500	3.8			4.89E-05		0.065			6.5
RJ	N2O	127	1.24	745	928	1.93E-04	125		2.59E-01	3998	100
RJ	N2O	182	1.24	745	1330	1.34E-04	270		1.80E-01	3998	600
Solid	Marc 4D	199	0.34		0	1.23E-04	159000				530
Solid	STAR 5A	250	4.7		0	9.79E-05	169000				11946
Solid	NASA	280			0	8.74E-05	445000				
W-gas	Tridyne	138		206	279	1.77E-04	1		8.61E-01		10
W-gas	Tridyne	138		206	279	1.77E-04	10		8.61E-01		100

The nanosatellite mission specified above is divided into a main and ACS propulsion system. Each of these systems will be analyzed separately. The main propulsion system requires a high level of thrust (445 N) for a delta-v of 700 m/s. The chosen system is a solid motor designed to deliver 280 seconds of Isp. The UW ternary system can deliver theoretically the same level of specific impulse and at the same time offer the advantages of a liquid propulsion system over a solid motor. The major disadvantage of the liquid propulsion system is the need for higher power requirements for operation of the valve than are available for this mission. A power requirement of less than one watt basically eliminates all other options except the solid motor unless a simple separation device such as a burst disk can be utilized to initiate propellant flow. This of course negates the possible advantage of being able to shut off a liquid system. Therefore, for the given missions specs the UW ternary system is probably not viable for the main propulsion system unless more power can be diverted to operating the thruster valve. The EP systems simply do not provide enough thrust for the required mission.

The ACS system requirement of 44 mN-s is a design driver for this system when considering monopropellant/bipropellant options. With a thrust of 1 N, it is necessary that a valve operate with a response time of 44 msec to provide the required MIB. Valves already considered from Primex operate at these levels. If the power availability is increased then the UW ternary system is a viable option for the ACS. EP systems are not good candidates based on low thrust levels and high power requirements.

It may be worth the time for designers of such a satellite to look for possible options in increasing the power availability for the propulsion system so that one technology can be used for both the main propulsion system and ACS.

Table 6-4. Micropulsion Technology Applied to GSFC SpartanLite^{5,6}

(m/s)		(kg)	(kg)		(kg)	(kg)	(N)	(mN-s)	(cm3)	(cm3)	(W)
del-V		Ms/c	Mprsys		Minert	Mprop	F	MIB.	Vinert	Vprsys	P
120	Main	45	22.7				31	n/a		24745	48
200	(Electric Prop)						0.0156				
		(sec)	(kg)	(kg/m3)		(kg)	(N)	(mN-s)	(cm3)	(cm3)	(W)
System	Propellant(s)	Isp	Mprsys	rho	rho-Isp	Mprop	F	MIB	Vpr	Vprsys	P
MAIN							31				
Arcjet	N2	110		400	432	7.6130	0.005		19033		4
Arcjet	NH3	787		609	4702	1.1508	1.93		1890		26k
Arcjet	N2	280		400	1099	3.1601	0.014		7900		32
Biprop	MMH/CIF3	310		699	2126	1.7411	0.1	0.1	2491		
Biprop	MMH/NTO	290	0.1	1100	3129	1.8587	156		1690		
Biprop	N2H4/NTO	287	1.9777	1100	3097	1.8777	30		1707		
CG	Xenon	28		1095	301	15.9276			14546		3.5-6
CG	Methane	105		163	168	4.9486			30360		3.5-6
CG	Nitrogen (g)	65		220	140	7.7195			35088		
CG	Ethylene	75		415	305	6.7722	1		16318		3.5-6
Colloid	Nal/glycerol	450			0	1.9932	0.0006				2.5
Colloid	Nal/glycerol	1540			0	0.5918	0.0004				10
FEEP	Cs	9000	1.6 p		0	0.1018	4E-05			1920	2.7
FEEP	Cs	9000	8.7 p		0	0.1018	0.001			23268	370
FMMR	H2O	70		1000	687	11.3701	0.005		11370	11370	15
Hall	MIT Mini	1600		n/a	n/a	0.5698	0.003		n/a		50
Hall	Texas Tech	3300		n/a	n/a	0.2772	3		n/a		30 k
Hall	BHT-HD-60	1700	< 2.2	n/a	n/a	0.5364	1		n/a	2160	700
Ion	NASA Lewis	1760			0	0.5183	0.0036				100
Ion	JPL	3900	2.5		0	0.2346	0.031				100
M-prop	Hydrazine	234	0.376	1010	2318	2.2920			2269		9.6
M-prop	HAN	250		1450	3556	2.1488			1482		
M-prop	H2O2	179		1347	2365	2.9725			2207		
M-prop	UW Term (g)	282		42.47	117	1.9103			44979		
M-prop	UW Term (l)	282		709.5	1963	1.9103			2692		
PPT	LES-6	200	2.5		0	4.3611					1.85 J
PPT	MIT Lab	2580	11.9		0	0.3542	0.006				300J?
PPT	DAWGSTAR	500	3.8			1.7980		0.07			6.5
RJ	N2O	127	1.24	745	928	6.6739	0.125		8958	3998	100
RJ	N2O	182	1.24	745	1330	4.7688	0.27		6401	3998	600
Solid	Marc 4D	199	0.34		0	2.6828	159			530	
Solid	STAR 5A	250	4.7		0	2.1488	169			11946	
W-gas	Tridyne	138		206	279	6.1803	0.001		30001		10
W-gas	Tridyne	138		206	279	6.1803	0.01		30001		100

Based on the thrust and delta-v requirements of this mission, any of the monopropellant options are viable candidates. With relatively high Isp levels, the ability to reach a thrust level of 31 mN and on/off capabilities, both bipropellants and monopropellants could fulfill this role. In addition, 48 watts of power are available for the propulsion system, thereby allowing sufficient power for the valve. The bipropellant combination of N2H4/NTO has better performance parameters, but the advantage of the UW ternary mixture is its non-toxicity. Since the mass of the propellant system is nearly half of the entire mass of the spacecraft, volume advantages of HAN and the toxic monopropellants (higher density Isp) may not outweigh the advantage of a higher Isp for the UW ternary system. In addition, the salt residue comes into play at these low thrust levels. For all of these systems, the fact that the greater volume requirements for lower density fuels may be offset by the extra tank mass to contain this extra volume. For this case, comparing HAN and the UW ternary system, if we were to use aluminum tanks with a density¹³⁴ of 2.7 g/cm³, the extra tank mass would be about 428 grams. Comparing propellant weights already computed, this puts the UW ternary mixture above the HAN system. Extensive studies of mass budgets are not performed in this thesis, but for future reference they must be taken into account.

Table 6-5. Micropulsion Technology Applied to Main Propulsion System of LunARSat⁸

(m/s)		(kg)	(kg)		(kg)	(kg)	(N)	(mN-s)	(cm3)	(cm3)	(W)
del-V		Ms/c	Mprsys		Minert	Mprop	F	MIB	Vinert	Vprsys	P
1370	Main	100									T 30
		(sec)	(kg)	(kg/m3)		(kg)	(N)	(mN-s)	(cm3)	(cm3)	(W)
SYSTEM	Propellant	Isp	Mprsys	rho	rho-Isp	Mprop	F	MIB	Vpr	Vprsys	P
MAIN		290	51.4	1100	3129	38.22	110	n/a			
Arcjet	N2	110		400	432	71.90	0.005		179762		4
Arcjet	NH3	787		609	4702	16.26	1.93		26699		26k
Arcjet	N2	280		400	1099	39.27	0.014		98180		32
Biprop	MMH/CIF3	310		699	2126	36.27	0.1	0.1	51887		
Biprop	MMH/NTO	290	0.1	1100	3129	38.22	156		34744		
CG	Xenon	28		1095	301	99.32			90701		3.5-6
CG	Methane	105		163	168	73.55			451246		3.5-6
CG	Nitrogen (g)	65		220	140	88.33			401519		
CG	Ethylene	75		415	305	84.46	1		203529		3.5-6
Colloid	Nal/glycerol	450				26.68	6E-04				2.5
Colloid	Nal/glycerol	1540			0	8.67	4E-04				10
FEEP	Cs	9000	1.6 p			1.54	4E-05			1920	2.7
FEEP		9000	8.7 p		0	1.54	0.001			23268	370
FMMR	H2O	70		1000	687	86.40	0.005		86399	86399	15
Hall	MIT Mini	1600		n/a	n/a	8.36	0.003				50
Hall	Texas Tech	3300		n/a	n/a	4.14	3				30 k
Hall	BHT-HD-60	1700	< 2.2	n/a	n/a	7.89	1			2160	700
Ion	NASA Lewis	1760			0	7.63	0.004				100
Ion	JPL	3900	2.5		0	3.52	0.031				100
Ion	BBM1-MK1-2/Xe	3518	12.5		0	3.89	0.15				
M-prop	Hydrazine	234	0.376	1010	2318	44.94			44498		9.6
M-prop	HAN	250		1450	3556	42.80			29517		
M-prop	H2O2	179		1347	2365	54.17			40214		
M-prop	UW Term (g)	282		42.47	117	39.06			919628		
M-prop	UW Term (l)	282		709.5	1963	39.06			55048		
PPT	LES-6	200	2.5		0	50.26					1.85 J
PPT	MIT Lab	2580	11.9		0	5.27	0.006				300J?
PPT	DAWGSTAR	500	3.8			24.37		0.07			6.5
RJ	N2O	127	1.24	745	928	66.70	0.125		89531	3998	100
RJ	N2O	182	1.24	745	1330	53.57	0.27		71912	3998	600
RJ	H2O	152	1.24	1000	1491	60.10	0.045		60099	3998	100
Solid	Marc 4D	199	0.34		0	50.43	159				530
Solid	STAR 5A	250	4.7		0	42.80	169			11946	
W-gas	Tridyne	138		206	279	63.65	0.001		308982		10
W-gas	Tridyne	138		206	279	63.65	0.01		308982		100

Table 6-6. Micropulsion Technology Applied to Attitude Control System of LunARSat⁸

(m/s)		(kg)	(kg)		(kg)	(kg)	(N)	(mN-s)	(cm3)	(cm3)	(W)
del-V		Ms/c	Mprsys		Minert	Mprop	F	MIB	Vinert	Vprsys	P
100		100					1.32				T 30
		(sec)	(kg)	kg/m3		(kg)	(N)	(mN-s)	(cm3)	(cm3)	(W)
System	Propellant	Isp	Mprsys	rho	rho-isP	Mprop	F	MIB	Vpr	Vprsys	P
ACS							1.32				
Arcjet	N2	110		400	432	8.85E+00	<u>0.0054</u>	x	2.21E+04		4
Arcjet	NH3	787		609	4702	1.29E+00	<u>1.93</u>	x	2.11E+03		26 k
Arcjet	N2	90		400	353	1.07E+01	<u>0.0083</u>	x	2.68E+04		5
Biprop	MMH/CIF3	310		699	2126	3.23E+00	<u>0.001</u>	0.1	4.63E+03		
Biprop	MMH/NTO	290	0.1	1100	3129	3.45E+00	<u>156</u>		3.14E+03		
Biprop	MMH/NTO	295		1100	3183	3.40E+00	<u>0.005</u>	5	3.09E+03		
CG	Xenon	28	30.52	1095	301	3.05E+01			2.79E+04	27867.6	3.5-6
CG	Methane	105	9.25	163	168	9.25E+00			5.68E+04	56760.1	3.5-6
CG	Nitrogen	65		220	140	1.45E+01	1		6.60E+04		20-10
Colloid	Nal/glycerol	450			0	2.24E+00	<u>0.0006</u>				2.5
Colloid	Nal/glycerol	1540			0	6.60E-01	<u>0.0004</u>				10
FEEP	Cs	9000	1.6 p	?		1.13E-01	<u>0.00004</u>			1920	2.7
FEEP		9000	8.7 p		0	1.13E-01	<u>0.001</u>			23268	370
FMMR	H2O	70		1000	687	1.36E+01	<u>0.005</u>		1.36E+04	13551.7	15
Hall	MIT Mini	1600		n/a	n/a	6.35E-01	<u>0.003</u>				50
Hall	Texas Tech	3300		n/a	n/a	3.08E-01	3				30 k
Hall	BHT-HD-60	1700	< 2.2	n/a	n/a	5.98E-01	1			2160	700
Ion	NASA Lewis	1760			0	5.78E-01	<u>0.0036</u>				100
Ion	JPL	3900	2.5		0	2.61E-01	<u>0.031</u>				100
M-prop	Hydrazine	234	0.376	1010	2318	4.26E+00	1000		4.22E+03		9.6
M-prop	HAN	250		1450	3556	4.00E+00	1000		2.76E+03		
M-prop	H2O2	179		1347	2365	5.54E+00	1000		4.11E+03		
M-prop	UW Tern (g)	282		42.47	117	3.55E+00	1000		8.36E+04		
M-prop	UW Tern (l)	282		709.5	1963	3.55E+00	1000		5.00E+03		
PPT	LES-6	200	2.5		0	4.97E+00		10000			<u>1.85 J</u>
PPT	MIT Lab	2580	11.9		0	3.94E-01	<u>0.006</u>				300J?
PPT	DAWGSTAR	500	3.8			2.02E+00		0.065			<u>6.5</u>
RJ	N2O	127	1.24	745	928	7.71E+00	<u>0.125</u>	x	1.04E+04	3998	100
RJ	N2O	182	1.24	745	1330	5.45E+00	<u>0.27</u>	x	7.31E+03	3998	600
RJ	H2O	152	1.24	1000	1491	6.49E+00	<u>0.045</u>	x	6.49E+03	3998	100
Solid	Marc 4D	199	0.34		0	4.99E+00	<u>159</u>			530	
Solid	STAR 5A	250	4.7		0	4.00E+00	<u>169</u>			11946	
W-gas	Tridyne	138		206	279	7.12E+00	<u>0.001</u>		3.46E+04		10
W-gas	Tridyne	138		206	279	7.12E+00	<u>0.01</u>		3.46E+04		100

The main propulsion of the LunARSat mission is required for the earth-moon orbit transfer and a retro burn for insertion upon arrival, therefore high levels of thrust are needed for 1370 m/s of delta-v. The technology of choice was a bipropellant fuel/oxidizer combination of MMH/NTO which provides an Isp level of 290 seconds and a ρ -Isp of 3129 Ns/ltr. The thrust is designed at 110 N. These parameters are hard to beat, but the disadvantage is the complexity of the bipropellant system. In addition, if the goal is to carry one propulsion system to serve the needs of both the main and ACS, the bipropellants may cause excessive inert mass. This also eliminates the possibility of using the solid kick motors.

Monopropellants may offer a viable solution based on reduced complexity at the cost of slightly degraded performance. Once again, the HAN propellants have a higher ρ -Isp, but the UW ternary mixture offers better levels of Isp. Therefore, although the HAN will occupy less volume for a given mission, the UW ternary mixture requires less mass. For a satellite of this size (100 kg), weight savings may possibly outweigh those of volume reduction.

The ACS requirements of 100 m/s at 1.32 N is within the range of the same monopropellant main system. Hydrazine systems have been produced by Primex to operate at thrust levels as low as 0.5 N. It is conceivable to think that the other monopropellant concepts could be used to operate at similar thrust levels. Once again, the low thrust levels will be addressed at the end of the nozzle flow analysis for the UW ternary system.

As far as the other propulsion concepts are concerned, electric systems do not have high enough thrust levels. Cold/warm gas require excessive mass and also do not produce high enough thrust levels to be used as both the main system and ACS.

Table 6-7. Micropulsion Technology Applied to TechSat21⁹

(m/s)		(kg)	(kg)		(kg)	(kg)	(mN)	(mN-s)	(cm3)	(cm3)	(W)
del-V		Ms/c	Mprsys		Minert	Mprop	F	MIB	Vinert	Vprsys	P
390	Main	138	10.7				0.2	2			350
		(sec)	(kg)	(kg/m3)		(kg)	(mN)	(mN-s)	(cm3)	(cm3)	(W)
SYSTEM	Propellant(s)	Isp	Mprsys	rho	rho-Isp	Mprop	F	MIB	Vpr	Vprsys	P
MAIN											
Arcjet	N2	110		400	432	<u>41.86</u>	5.4		104641		4
Arcjet	NH3	787		609	4702	<u>6.80</u>	<u>1930</u>		11162		<u>26k</u>
Arcjet	Hydrazine	440		1010	4360	<u>11.92</u>	<u>59</u>		11804		<u>370</u>
Biprop	MMH/CIF3	310		699	2126	<u>16.61</u>	<u>100</u>	0.1	23762		
Biprop	MMH/NTO	290	0.1	1100	3129	<u>17.68</u>	156000		16071		
Biprop	MMH/NTO	295		1100	3183	<u>17.40</u>	<u>500</u>	5	15817		
CG	Xenon	28		1095	301	<u>104.64</u>			95560		3.5-6
CG	Methane	105		163	168	<u>43.50</u>			<u>266853</u>		3.5-6
CG	Nitrogen (g)	65		220	140	<u>63.14</u>			<u>286996</u>		
Colloid	Nal/glycerol	450				<u>11.67</u>	0.6				2.5
Colloid	Nal/glycerol	1540			0	3.52	0.4				10
FEEP	Cs	9000	1.6 p			0.61	0.04			1920	2.7
FEEP	Cs	9000	8.7 p		0	0.61	1			23268	<u>370</u>
FMMR	H2O	70		1000	687	<u>59.80</u>	5		59796	59796	15
Hall	MIT Mini	1600		n/a	n/a	3.39	<u>3</u>		n/a		50
Hall	Texas Tech	3300		n/a	n/a	1.65	<u>3000</u>		n/a		<u>30 k</u>
Hall	MIT	865		n/a	n/a	6.20	1.8		n/a		126
Ion	NASA Lewis	1760			0	3.08	3.6				100
Ion	JPL	3900	2.5		0	1.40	<u>31</u>				100
Ion	DASA	3000			0	1.82	5			184490	240
M-prop	Hydrazine	234	0.376	1010	2318	<u>21.56</u>			21349		9.6
M-prop	HAN	250		1450	3556	<u>20.29</u>			13992		
M-prop	H2O2	179		1347	2365	<u>27.48</u>			20404		
M-prop	UW Tern (g)	282		42.47	117	<u>18.15</u>			<u>427258</u>		
M-prop	UW Tern (l)	282		709.5	1963	<u>18.15</u>			25575		
PPT	LES-6	200	2.5		0	<u>24.88</u>		<u>10000</u>			1.85 J
PPT	MIT Lab	2580	11.9		0	2.11	6				<u>300J?</u>
PPT	LES 8/9	1130	8.1			<u>4.77</u>		2.25			<u>750 J</u>
RJ	N2O	127	1.24	745	928	<u>37.09</u>	<u>12.5</u>		49787	3998	100
RJ	N2O	182	1.24	745	1330	<u>27.08</u>	<u>270</u>		36348	3998	<u>600</u>
RJ	H2O	152	1.24	1000	1491	<u>31.76</u>	<u>45</u>		31760	3998	100
Solid	Marc 4D	199	0.34		0	<u>24.99</u>	<u>2E+05</u>			530	
Solid	STAR 5A	250	<u>4.7</u>		0	<u>20.29</u>	<u>2E+05</u>			<u>11946</u>	
Solid	Acetamide	75		1000	736	<u>56.78</u>	<u>.01-10</u>		56778.3		
W-gas	Tridyne	138		206	279	<u>34.54</u>	<u>10</u>		167677		10
W-gas	Tridyne	138		206	279	<u>34.54</u>	<u>10</u>		167677		100

Although the spacecraft mass of TechSat21 is similar to that of the LunARSat mission, the delta-v (390 m/s) and thrust requirements (2 mN) are vastly different. In addition, the high power level available to the propulsion system (350 W) is conducive to an electric propulsion system. The allotted mass to the propulsion system is only 10.7 kg, therefore looking at only the propellant required for any of the chemical propulsion systems leads to the conclusion that chemical propulsion systems are not a viable option for this mission. It is foreseeable that the UW ternary system will possibly be able to provide thrust levels of 2 mN at a relatively high Isp level of around 250 seconds (after nozzle losses), but considering the other requirements it would not be a good choice for this mission.

Table 6-8. Micropropulsion Technology Applied to ESA Geomagnetic Smallsatellite¹⁰

(m/s)		(kg)	(kg)		(kg)	(kg)	(mN)	(mN-s)	(cm3)	(cm3)	(W)
del-V		Ms/c	Mprsys		Minert	Mprop	F	MIB	Vinert	Vprsys	P
798	Main	264	106.2		22.7	55.50					
	ACS					10.00	1000	10			
		(sec)	(kg)	(kg/m3)		(kg)	(mN)	(mN-s)	(cm3)	(cm3)	(W)
SYSTEM	Propellant	Isp	Mprsys	rho	rho-Isp	Mprop	F	MIB	Vpr	Vprsys	P
MAIN	Hydrazine	210	106.2	1010	2081	84.78			707000		
Arcjet	N2	110		400	432	137.98	5.4		344949		4
Arcjet	NH3	787		609	4702	25.92	1930		42569		26k
Arcjet	N2	90		400	353	157.08	0.0083	x	392692		5
Biprop	MMH/CIF3	310		699	2126	60.93	100	0.1	87169		
Biprop	MMH/NTO	290	0.1	1100	3129	64.57	156000		58703		
Biprop	MMH1/MON-1	285			0	65.55	3000	5			6
CG	Xenon	28		1095	301	249.55			227899		3.5-6
CG	Methane	105		163	168	142.34			873252		3.5-6
CG	Nitrogen (g)	65		220	140	188.47			856699		
CG	Ethylene	75		415	305	174.76	1000		421106		3.5-6
Colloid	Nal/glycerol	450				43.66	0.6				2.5
Colloid	Nal/glycerol	1540			0	13.58	0.4				10
FEEP	Cs	9000	1.6 p			2.38	0.04			1920	2.7
FEEP		9000	8.7 p		0	2.38	1			23268	370
FMMR	H2O	70		1000	687	181.41	5		181412	888412	15
Hall	MIT Mini	1600		n/a	n/a	13.09	3		n/a		50
Hall	Texas Tech	3300		n/a	n/a	6.43	3000		n/a		30 k
Ion	NASA Lewis	1760			0	11.92	3.6				100
Ion	JPL	3900	2.5		0	5.45	31				100
M-prop	Hydrazine	234	0.376	1010	2318	77.52			76753		9.6
M-prop	HAN	250		1450	3556	73.33			50569		
M-prop	H2O2	179		1347	2365	96.41			71576		
M-prop	UW Tern (g)	282		42.47	117	66.15			1557661		
M-prop	UW Tern (l)	282		709.5	1963	66.15			93240		
PPT	LES-6	200	2.5		0	88.22		10000			1.85 J
PPT	MIT Lab	2580	11.9		0	8.19	6				300J?
PPT	DAWGSTAR	500	3.8			39.64		0.065			6.5
RJ	N2O	127	1.24	745	928	124.87	12.5		167606	3998	100
RJ	N2O	182	1.24	745	1330	95.15	270		127722	3998	600
RJ	H2O	152	1.24	1000	1491	109.41	45		109409	3998	100
Solid	Marc 4D	199	0.34		0	88.58	159000			530	
Solid	STAR 5A	250	4.7		0	73.33	169000			11946	
Solid	Acetamide	75		1000	736	174.76	.01-10		174758.9		
W-gas	Tridyne	138		206	279	117.58	1		570770		10
W-gas	Tridyne	138		206	279	117.58	10		570770		100

At first glance this mission appears to be a prime candidate for both the main propulsion system (altitude maintenance) and ACS. Considering the main propulsion system first, the 264 kg satellite requires 798 m/s of delta-v and has an allotted propulsion mass budget of 106.2 kg. The satellite engineers chose the hydrazine monopropellant system. This is a reasonable choice based on its additional applicability to the ACS. It has a reasonably high level of Isp, but the disadvantage is the toxicity issues. Bipropellants have high levels of Isp and offer mass savings over the hydrazine system, but once again the complexity involved with a bipropellant system leads one the possibility of a monopropellant.

The UW ternary system has higher theoretical levels of Isp and therefore offers increased propellant savings of up to 11 kg. It is non-toxic and can possibly be applied to the ACS also. At a thrust level of 1 N for the ACS and MIB of 10 mN-s, a valve capable of a 10 msec response time is necessary. The same valve used for the hydrazine system could also be used for the other monopropellants.

Table 6-9. Micropropulsion Technology Applied to Interplanetary Platform¹¹

(m/s)		(kg)	(kg)		(kg)	(kg)	(mN)	(mN-s)	(cm3)	(cm3)	(W)
del-V		Ms/c	Mprsys		Minert	Mprop	F	MIB	Vinert	Vprsys	P
1700	Main	400	240			215.00				p 180000	T 100
100											
		(sec)	(kg)	(kg/m3)		(kg)	(mN)	(mN-s)	(cm3)	(cm3)	(W)
SYSTEM	Propellant	Isp	Mprsys	rho	rho-Isp	Mprop	F	MIB	Vpr	Vprsys	P
MAIN			240			215					
Arcjet	N2	110		400	432	317.23	5.4		793073		4
Arcjet	NH3	787		609	4702	79.05	1930		129811		26k
Arcjet	N2	90		400	353	341.68	0.0083		854193		5
Biprop	MMH/CIF3	310		699	2126	171.29	100	0.1	245050		
Biprop	MMH/NTO	290	0.1	1100	3129	179.94	156000		163581		
Biprop	HTP/Kerosene	290		1286	3659	179.94			139922		
CG	Xenon	28		1095	301	399.18			364547		3.5-6
CG	Methane	105		163	168	323.21			1982891		3.5-6
CG	Nitrogen (g)	65		220	140	372.19			1691769		
CG	Ethylene	75		415	305	360.32	1000		868236		3.5-6
Colloid	Nal/glycerol	450				127.85	0.6				2.5
Colloid	Nal/glycerol	1540			0	42.57	0.4				10
FEEP	Cs	9000	1.6 p			7.63	0.04			1920	2.7
FEEP	Cs	9000	8.7 p		0	7.63	1			23268	370
FMMR	H2O	70		1000	687	366.36	5		366355	506277	15
Hall	MIT Mini	1600		n/a	n/a	41.06	3		n/a		50
Hall	Texas Tech	3300		n/a	n/a	20.46	3000		n/a		30 k
Ion	NASA Lewis	1760			0	37.51	3.6				100
Ion	JPL	3900	2.5		0	17.38	31				100
M-prop	Hydrazine	234	0.376	1010	2318	209.26			207191		9.6
M-prop	HAN	250		1450	3556	200.00			137934		
M-prop	H2O2	179		1347	2365	248.08			184173		
M-prop	UW Tern (g)	280		42.47	117	184.59			4346264		
M-prop	UW Tern (l)	280		709.5	1949	184.59			260163		
PPT	LES-6	200	2.5		0	231.83		10000			1.85 J
PPT	MIT Lab	2580	11.9		0	25.98	6				300J?
PPT	Dawgstar	500	3.8			117.16		0.065			6.5
RJ	N2O	127	1.24	745	928	297.80	12.5		399728	3998	100
RJ	N2O	182	1.24	745	1330	245.64	270		329714	3998	600
RJ	H2O	152	1.24	1000	1491	272.08	45		272083	3998	100
Solid	Marc 4D	199	0.34		0	232.56	159000				530
Solid	STAR 5A	250	4.7		0	200.00	169000				11946
Solid	Acetamide	75		1000	736	360.32	.01-10				
Warm Gas	Tridyne	138		206	279	286.05	1		1388613		10
Warm Gas	Tridyne	138		206	279	286.05	10		1388613		100

This class of satellite is the largest mass wise (400 kg) of any other considered in this study. The allotted mass to the entire propulsion system (240 kg) is over 50% of the entire mass of the spacecraft. The delta-v of 1700 m/s is substantial for this size of spacecraft, therefore the propellant mass limit is set at 215 kg. While no thrust level is established for this system, an interplanetary spacecraft will require a substantial impulse burn at the rendezvous point for orbit insertion, therefore EP concepts are not considered. They may be used for substantial mass savings as a means for getting from earth to the desired planet.

The UW ternary system has the highest Isp, therefore it offers the best option for the monopropellant systems under consideration. Bipropellants become more of a viable option for spacecraft as they increase in size and mass. If the desire is to use the main propulsion system for the ACS then a monopropellant or bipropellant are possible options. The monopropellant would be the better choice considering the decreased complexity as already mentioned.

Chapter 7: Mission Analysis Conclusion

A brief mission analysis has been conducted on 7 different satellites with considerable different requirements and options in terms of propellant mass, power, propulsion system mass, delta-v and thrust range. The majority of satellites investigated could make use of the UW ternary system. In the cases where response time is not a major priority, electric propulsion systems offer the advantage of much higher specific impulse levels. They do require additional weight for the power supply unit, but it is possible that the increased savings of propellant for a given mission may offset this need. If the given situation does require higher thrust levels, the UW ternary system offers a theoretical maximum specific impulse of 283 seconds for an expansion ratio of 10. Of course, this is at a chamber temperature of 3033 K (stoichiometric combination of fuel/oxidizer). By reducing the chamber temperature, the following specific impulse levels of table 7-1 are expected.

Table 7-1. Theoretical Isp (eratio=10) for Chamber Temperature of NH₃/N₂O and H₂O diluent

Tc	Isp (sec)
1000	163.6
1500	202.3
2000	236.6
2500	262.4
3000	282.1

Reduction of the chamber temperature may be necessary in cases where the available material cannot support the high temperature levels expected. For MEMS nozzles, Sienna Technologies Inc., claims they can use an alumina ceramic to withstand temperatures up to 2000 K. Another material that could be developed into a micronozzle by Sienna Technologies can withstand 2500 K²³. Thrust levels attainable by such nozzles will be investigated in the following section. For higher thrust levels an alumina ceramic type nozzle may not be available due to the increased physical scale; therefore it is conceivable that the chamber temperature will have to be reduced for operation in a metallic chamber. Sienna does claim it can make conical nozzles based on the thickness of the material. Application of this technology is an area of possible further study.

Assuming the UW ternary system can provide the high thrust levels, it is a viable option for not only application to high thrust level missions such as orbit insertion and transfer, but also attitude corrections and possibly even formation flying. The ability of the system to provide impulse bits sufficiently small for such missions is dependent on the valve and lowest thrust attainable. The reduction in scale to achieve small thrust levels brings with it inherent inefficiencies due to viscous losses. The smallest attainable thrust level, coupled with the fastest response time for a given valve will determine which small satellite missions this propulsion system can be applied to.

If a material cannot be found to withstand the stoichiometric adiabatic flame temperature of the UW ternary system, it becomes a tradeoff between reducing Isp and the highest allowable temperature level. If other green propellants such as HAN provide improved performance over the UW ternary system as a result of material constraints, the UW ternary system is then restricted to operations with the MEMS nozzle range. In this range the UW ternary system has the advantage of no salt residues as a product of combustion. Such nozzles and their application to small satellite applications will be the focal point of investigation in the next section.

Chapter 8: Background for Research of Micronozzle Flow Efficiencies

In the past decade, engineers have researched and presented various ideas to use smaller spacecraft. An analysis of the use of small spacecraft was presented in the previous section of this thesis. Smaller spacecraft are cheaper to build, do not require as much space or weight on a launch vehicle, and in the case of failure, are easier to rebuild.

These smaller spacecraft require low thrust technology to avoid acceleration damage and fulfill necessary pointing accuracy. In addition, larger spacecraft can make use of small thrust technology for attitude control systems and possible course corrections. Operating a propulsion system designed for high thrust maneuvers at low thrust levels is possible, but doing so results in large losses in efficiency.

The equation for thrust in the vacuum of space is given below in equation (8-1):

$$F = \dot{m}U + P_e A_e \quad (8-1)$$

$$\begin{aligned} \dot{m} &= \text{mass flow (kg/s)} \\ U &= \text{exit velocity (m/s)} \\ P_e &= \text{exit pressure (N/m}^2\text{)} \\ A_e &= \text{exit area (m}^2\text{)} \end{aligned}$$

The two terms represent a momentum flux from the mass flow, and a pressure term. In a nozzle, a contained gas mixture passes through a converging/diverging nozzle. At the throat of this nozzle, the gas accelerates to mach 1. As the gas particles enter the diverging section after the throat, they accelerate past mach 1. In a vacuum, not considering boundary layer losses, we achieve maximum thrust and specific impulse efficiency from given chamber conditions by allowing the gases to infinitely expand. That is, we design for a maximum area ratio (exit area to throat area) based on weight and volume constraints. As we allow the gases to infinitely expand the axial velocity increases thereby decreasing the static pressure. This results in a greater amount of thrust from the momentum flux term than the pressure term as can be seen by the figure 8-1 ($T_c = 3000K$, $P_c = 30$ bar, $Eratio = 100$, molecular weight of propellant ~ 23 kg/kmol).

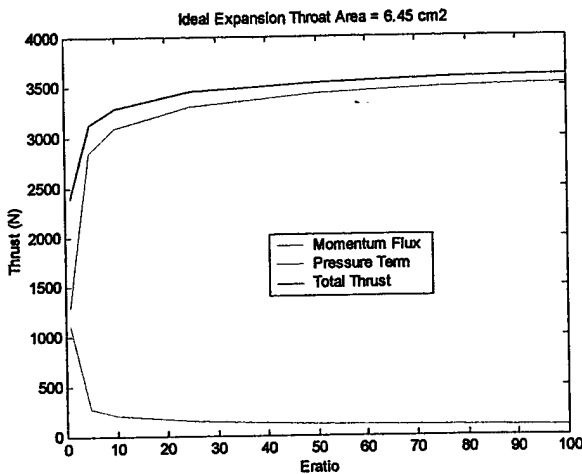


Figure 8-1. Ideal Thrust with Momentum Flux / Pressure Breakdown

As can be seen above, the increase in thrust begins to level out as we get further down the nozzle.

Another factor in the evaluation of a chemical propulsion system is the specific impulse. This is defined as the efficiency of the fuel to provide thrust. It compares to gas mileage in a car. The greater the amount of thrust for a given mass flow rate, the greater the ‘fuel efficiency’ as can be seen by equation (8-2):

$$Isp = \frac{F}{mg} \quad (8-2)$$

$$\begin{aligned} F &= \text{thrust (N)} \\ m &= \text{mass flow (kg/s)} \\ g &= \text{gravity (9.81 m/s}^2\text{)} \end{aligned}$$

As mentioned before, ideally the thrust continues to increase down the length of the nozzle and assuming the mass flow does not change, the Isp also continues to increase.

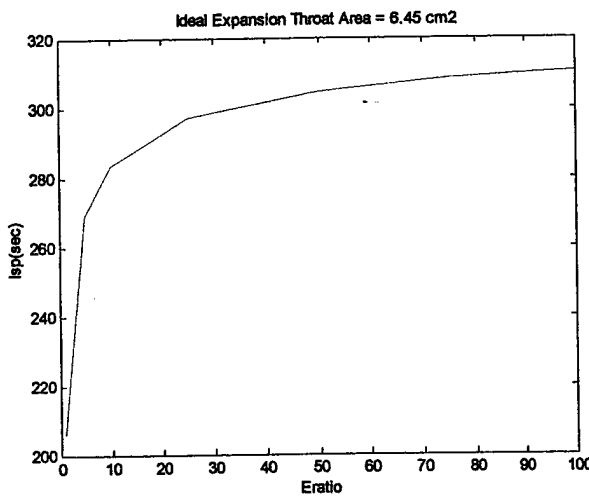


Figure 8-2. Ideal Specific Impulse with Expansion Ratio Increase

If a propulsion system was designed to operate at thrust levels seen above and yet we desired a lower thrust, then we could simply decrease the pressure in the combustion chamber. But, in doing so we decrease the specific impulse, or the efficiency with which we use the propellant gas. For instance, if we used the same propellant as above and the same physical parameters for the nozzle and reduce the operating chamber pressure from 30 bar to 10 bar, we get the results of figure (8-3):

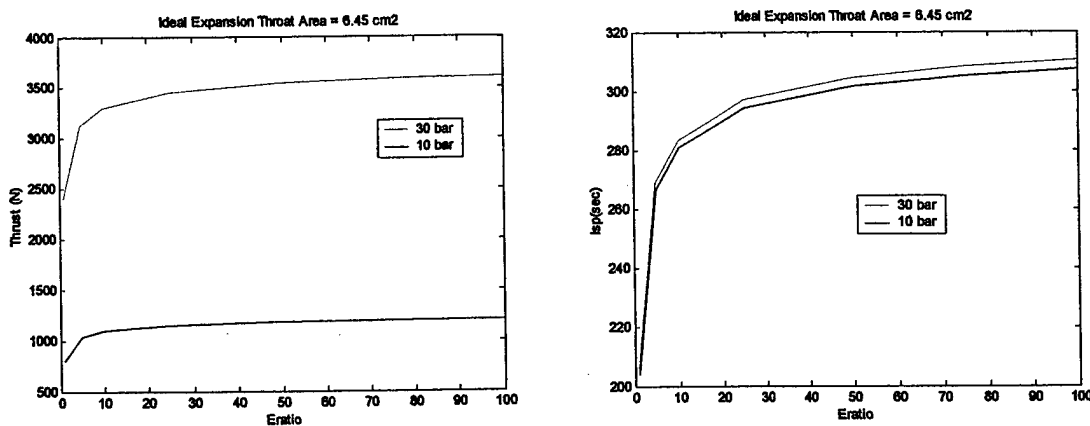


Figure 8-3. Decrease in Specific Impulse / Thrust for Chamber Pressure Decrease 30 – 10 bar

The decrease in specific impulse appears minimal for a decrease in thrust of nearly 300%, but a further decrease in thrust results in even greater inefficiencies. For example, we will be modeling

an expansion ratio of 10. If we were to decrease from a chamber pressure of 30 bar to 0.01 bar in order to decrease the thrust level from 3300N to 1.08N, the decrease in specific impulse would be over 20 seconds.

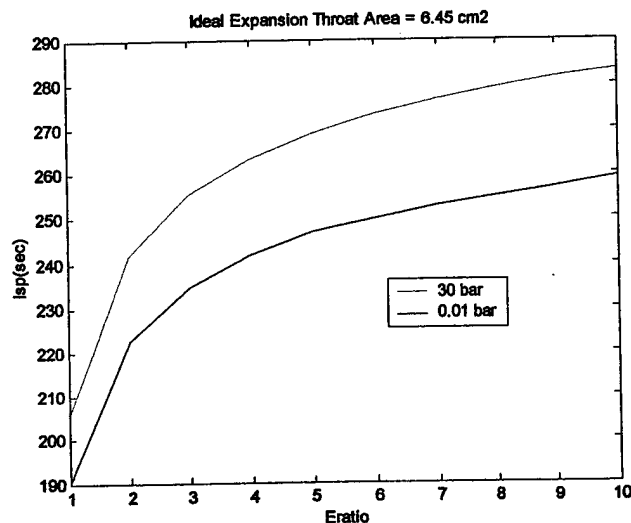


Figure 8-4. Decrease in Isp with Decrease in Pressure of 30 – 0.01 bar

In addition to varying the amount of thrust, engineers seek higher levels of efficiency. We have already discussed the effect of pressure on thrust and specific impulse. Temperature also plays a key role in the development of higher performance systems. As described before, temperature relates the amount of energy in a system. An increase in thermal energy results in a greater amount of kinetic energy leaving the nozzle. In the past the limiting factor for increased temperature systems has been the ability of the material to contain the thermal energy. As mentioned in the previous section, Sienna Technologies is developing a material capable of temperatures in excess of 2000 K. In the following graphic, the chamber pressure and physical geometry are constant. An increase in chamber temperature and expansion increases the specific impulse.

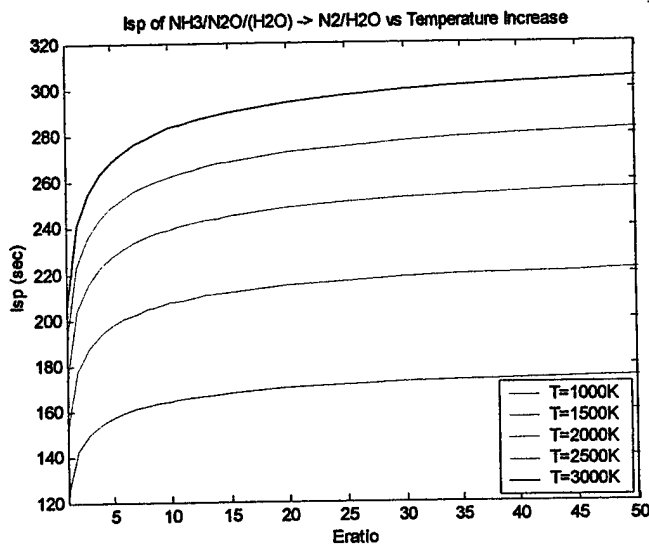


Figure 8-5. Increase of Isp with Increased Temperature

Another option in decreasing the thrust is to decrease the physical dimensions of the nozzle while operating at the same chamber pressure. For instance, in the above problem, if we had an expansion ratio of 50 and wanted a thrust level comparable to operating at 10 bar chamber pressure (1177.1 N), then instead of reducing our chamber pressure from 30 bar to 10 bar and losing specific impulse, we decrease the throat diameter from 2.54 cm to 1.48 cm.

On a macroscopic scale, scaling down the physical parameters is the solution to the efficiency problem. We attain smaller amounts of thrust and do not experience specific impulse inefficiencies. Yet, reducing the physical parameters on a microscopic scale results in a problem not encountered in the macroscopic case. For macroscopic nozzles an assumption is made about the boundary layer. Compared to the overall dimensions of the nozzle, the boundary layer occupies an extremely small portion of the exiting flow. Therefore, the associated viscous losses have a negligible effect on the efficiencies. For the purpose of this thesis, the term micronozzle will hereafter refer to those nozzles in which we cannot disregard this boundary layer.

A visual representation of the developing boundary is given in figure 8-6.

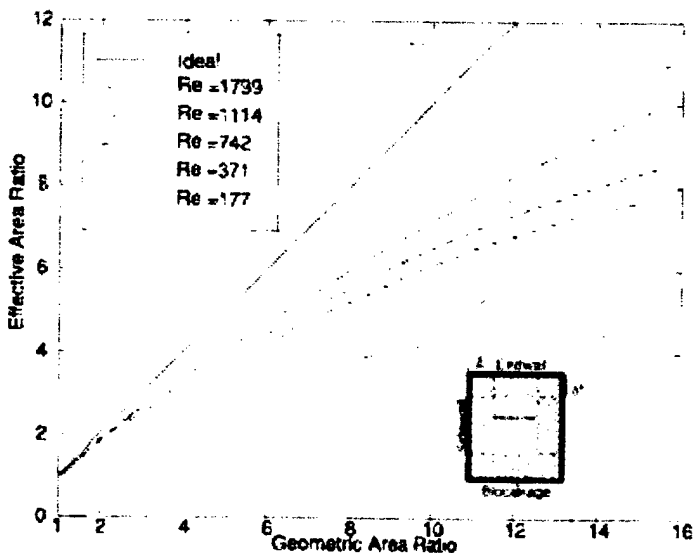


Figure 8-6. Reduction in Area Ratio Due to Viscous Effects²⁰

The graph above depicts a rectangular 3D nozzle. The physics of boundary layers will be discussed in detail later on. The x-axis in figure (8-6) is the geometric area ratio, and the y-axis depicts how much of the exit area is enveloped by the developing boundary layer. Ideally, the ratio of the geometric area ratio to the effective area ratio would be one. But, because of the boundary layer developing in the diverging nozzle region, the exit area unaffected by the viscous layer decreases thereby decreasing the effective area ratio. A way of quantifying the effects of this boundary layer is a dimensionless parameter known as the Reynolds number.

The development of the boundary layer is important for two reasons. First, as mentioned before, a gas expands in the diverging section of a nozzle proportional to the area ratio of the exit and the throat. If the area ratio decreases, the gases cannot fully expand and the overall velocity of the gas decreases. This decreases the momentum flux of the force expression and overall thrust magnitude. Note that although the momentum flux decreases, the pressure term should increase with a decrease in velocity, but the losses associated with the momentum flux decrease are greater than the pressure term increase as will be shown later on.

A second factor to consider is the boundary layer itself. Upon combustion in the chamber prior to entering the nozzle, separate chemical species undergo an exothermic reaction

which create large amounts of heat and energy. Based on the makeup of the molecules, this energy is stored in various modes of translation, rotation and vibration. The random thermal motion from the combustion process is then directed axially toward the nozzle throat. The thermal energy from combustion is gradually converted to kinetic energy as the species accelerate. In a macroscopic reference frame, the portion of the flow enveloped by the boundary layer actually decrease in velocity and the energy which could be converted to kinetic energy and thrust is converted back into thermal energy. Unlike the ideal assumption of uniform properties across the face of the exit plane, we must now deal with a region of supersonic expanding flow, which produces the majority of thrust, and a subsonic region caused by the boundary layer. A boundary layer reduces the thrust and specific impulse, thereby decreasing the efficiency of the nozzle. In macronozzles we generally make the assumption that this layer is insignificant when compared with the overall geometric dimensions of the nozzle. Instead, focus is given more generally to the contour of the nozzle to increase efficiency. For micronozzles, in addition to nozzle contour, we must also pay particular attention to losses from the boundary layer.

The effects of these nozzles are correlated to a dimensionless parameter called the Reynolds number. In general terms, the Reynolds number is a ratio of inertial forces to viscous forces. The greater the number, the more efficient a nozzle is going to be. Looking back at figure 8-6, it is evident that the larger the Reynolds number, or the smaller the viscous forces compared relative to the inertial forces, the closer we approach the ideal effective/geometric ratio of 1. The Reynolds number gives a general way of computing the effects a certain gas and physical nozzle is going to have on efficiency. Throughout the remainder of this thesis, specific attention is given to efficiency as a function of this parameter at the throat of our nozzles.

The Reynolds number is defined as:

$$Re = \frac{D_t U \rho}{\mu} \quad (8-3)$$

D_t = smallest characteristic parameter (m)
U = velocity (at the throat equivalent to local speed of sound) (m/s)
ρ = density (kg/m³)
μ = viscosity (m-s/kg)

The parameter μ also has units of poise or millipoise. The conversion from millipoise to metric units is $1E-4$ m-s/kg per millipoise. The viscosity increases roughly as the temperature to the 0.6 power. We will also calculate the Reynolds number at various locations in the diverging section of the nozzle to determine what the ratio of forces is.

In order to gain a desired thrust and specific impulse levels it is possible to vary any one of the three variables already mentioned: pressure, temperature or physical geometry. Below in figure 8-7 is a graphical representation of the Reynolds numbers associated with the independent variation of each of these three parameters.

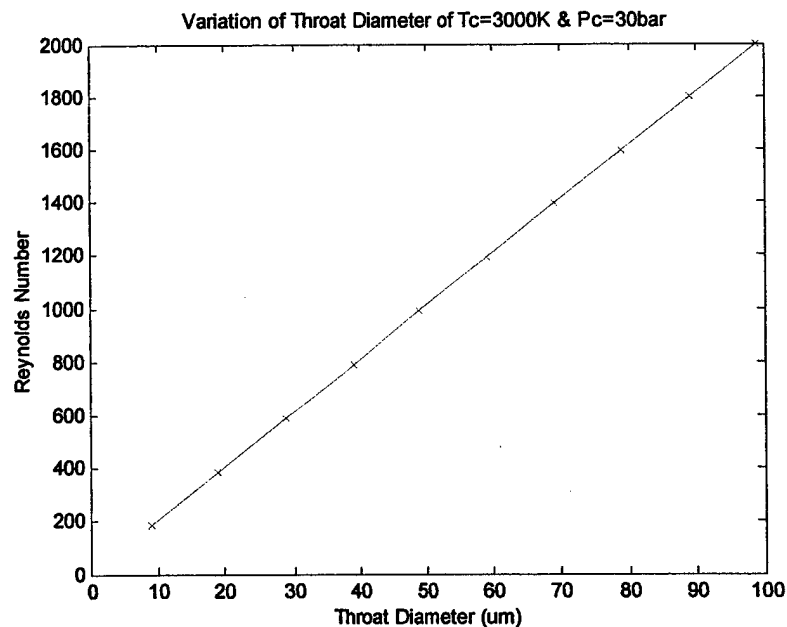


Figure 8-7. Reynolds Number Variation with Geometry

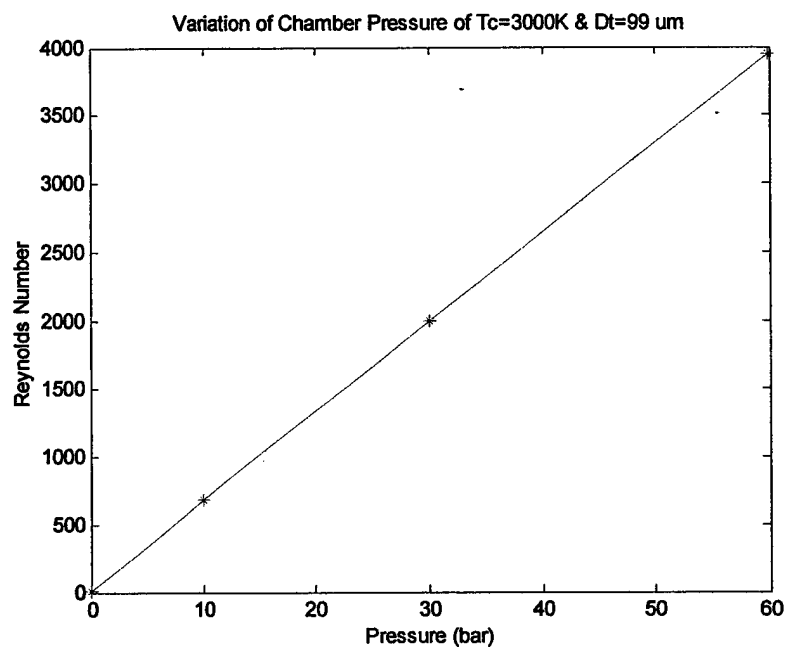


Figure 8-8. Reynolds Number Variation with Pressure

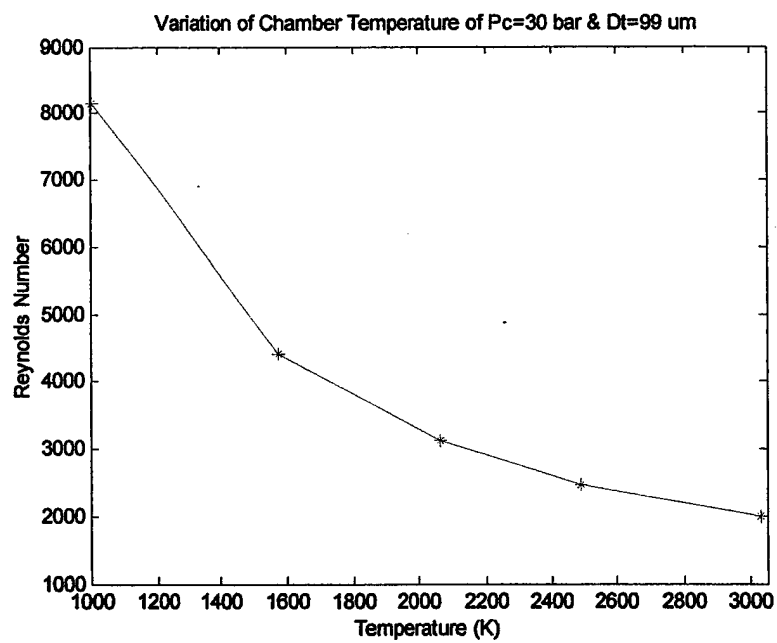


Figure 8-9. Reynolds Number Variation with Temperature

Pressure and physical geometry exhibit a linear relationship, but the temperature shows a power-law decrease due to the decrease in density and increase in velocity and viscosity. In order to understand the effects of temperature and pressure, we use the ideal gas law of equation (8-4).

$$P = \frac{\rho \hat{R} T}{M} \quad (8-4)$$

ρ = density (kg/m^3)
 R = gas constant (J/kmol-K)
 T = temperature (K)
 M = molecular mass (kg/kmol)

Increasing the temperature or decreasing the pressure decreases the density, thereby decreasing the Reynolds number and increasing the viscous effects. In addition, the viscosity term is primarily a function of temperature.

$$\mu \sim T^{0.6} \quad (8-5)$$

T = temperature (K)
 μ = viscosity (m-s/kg)

There is also a slight dependence on density, but it only plays a role when increasing to the point that real gas effects must be taken into consideration. This will be discussed in more detail later on. Increasing the temperature increases viscosity and decreases the Reynolds number. The degree of inefficiency as a function of Reynolds number is an area of intense research and the subject of this thesis.

The chamber pressure for this study will be held constant and geometry will be varied at specific temperature levels to evaluate the efficiencies at different Reynolds numbers. The question then is posed on whether or not there exists an optimum operating range for a desired thrust level based on an increase in chamber temperature as a function of Reynolds number. It is likely that as the temperature increases, the specific impulse will increase until it reaches a point where the inefficiencies associated with a growing viscous region outweigh the benefit gained from an increase in temperature. This process is defined graphically first by the increase of specific impulse with chamber temperature in figure 8-10.

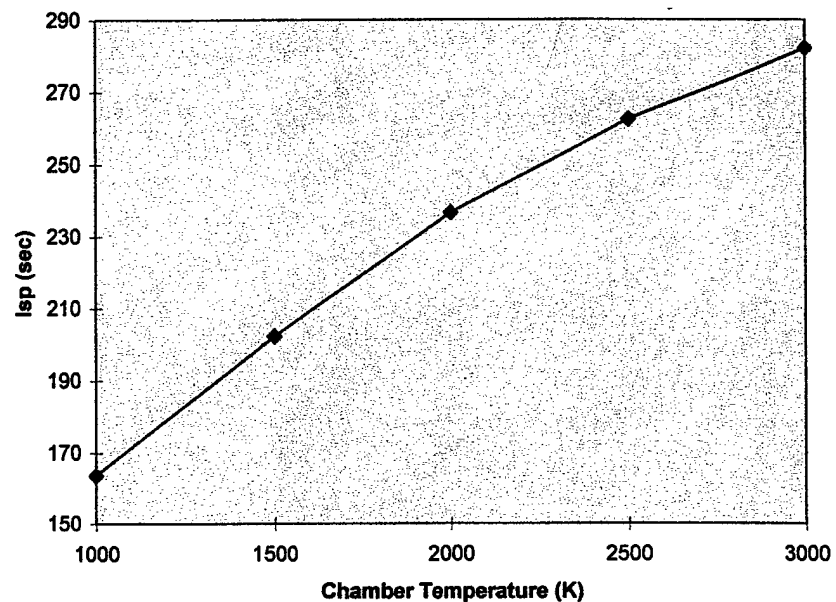
Increase Isp with Increase in Chamber Temperature

Figure 8-10. Increased Isp with Chamber Temperature

Designing for a specific thrust level corresponds to a finite Reynolds number (figure 8-11). The missing key is a correlation between the Reynolds number and Isp/thrust efficiency.

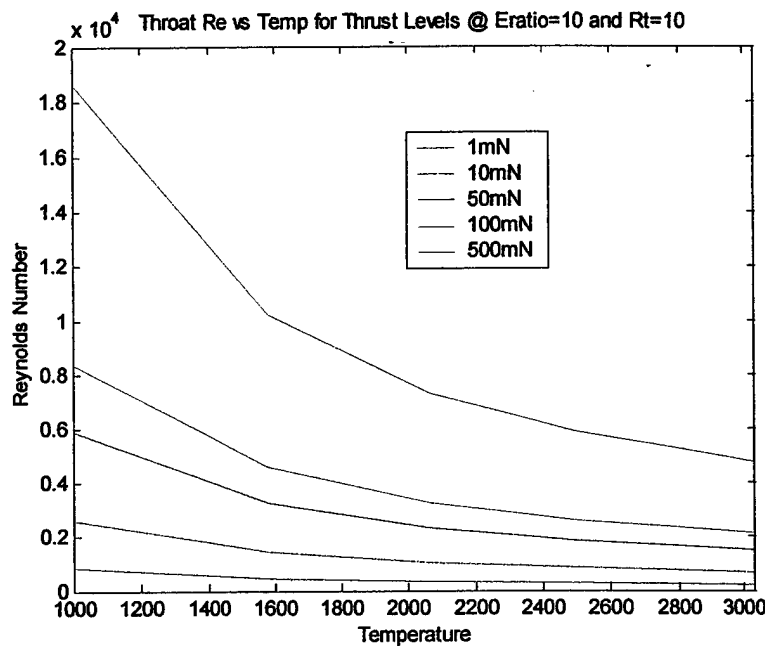


Figure 8-11. Decrease in Reynolds Number with Increase in Chamber Temperature for Various Thrust Levels

In the ideal situation, the specific impulse is independent of the Reynolds number, but taking into account the viscous effects there is a strong dependence on the Reynolds number. Studies have been performed on various nozzle geometries, but it is difficult to gain a correlation between efficiencies and the throat Reynolds number because the throat Reynolds predicts different results based on the geometry of the nozzle (divergence half-angle, aspect ratio, expansion ratio). The geometry determines the value of the Reynolds number downstream. Therefore, the initial goal of this study is to find an optimum nozzle geometry using results from past research efforts for the half-angle and expansion ratio. The aspect ratio will be analyzed through numerical methods in this thesis. Using this optimum nozzle geometry, a correlation will be obtained between throat Reynolds number and Isp/thrust efficiencies.

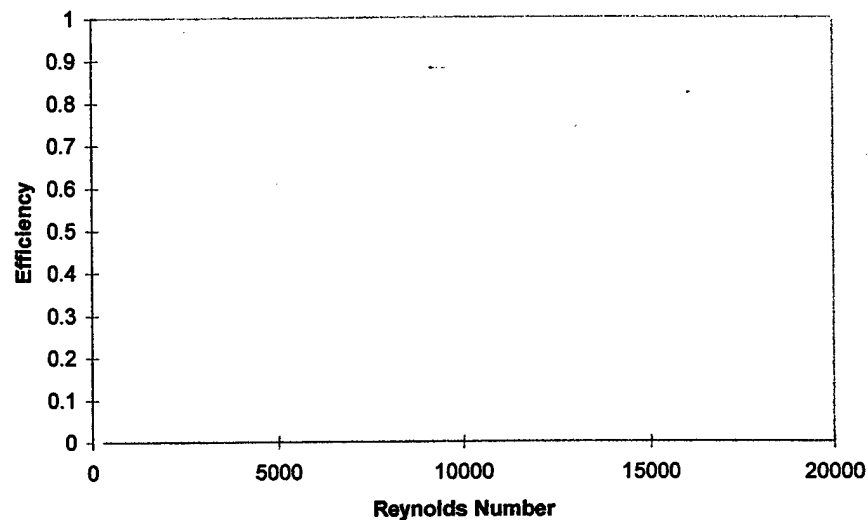


Figure 8-12. Unknown Correlation of Efficiency to Reynolds Number

With a correlation of efficiency to Reynolds number, it is then possible to plot the efficiency as a function of temperature for a given value of Reynolds number. Using this data (unknown graphically in figure 8-13) this data will then be applied back to figure (8-10).

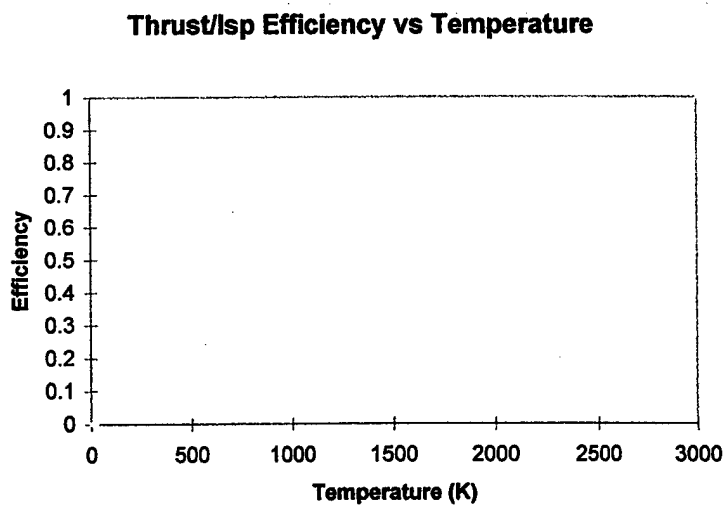


Figure 8-13. Unknown Correlation of Efficiency to Temperature

If the viscous effects overcome the increase in specific impulse from one temperature level to the next, the specific impulse will reach a maximum value and then begin to decrease instead of continually increasing. Hereafter it will be referred to as the region of 'negative return'. This thesis will be focused on finding an optimum nozzle geometry and then using this geometry, determine if an area of 'negative return' exists.

Chapter 9: Past/Present Research

In recent years advances in technology have paved the way for the development and application of small chemical thrusters. MEMS (microelectromechanical systems) technology has introduced the ability to etch small thrusters with micron-sized throats in flat sheets of silicon wafers. 3D rectangular nozzles can be mass fabricated by stacking several of these etched nozzles on top of each other and endwalls on the upper and lower sides. Due to the small scale of micronozzles it is difficult to perform empirical analyses. Therefore, the majority of published work has made use of a powerful numerical modeling tool known as computational fluid dynamics (CFD). Several papers have been published on what type of CFD tool is valid given the physics of the nozzle flow. This will be discussed in further detail later.

In order to limit the amount of analysis necessary for this thesis, the work of the aforementioned papers has been implemented into my computational efforts. To validate the assumptions, the general results of these papers are included below with reference to the full work and purpose for implementation into my computations. Areas of performed research include nozzle contour and expansion angle, high-temperature analysis (up to 2000K), direct-simulation monte carlo method (DSMC) vs continuum flow CFD techniques, truncated nozzle effects, rounded throat, and axisymmetric vs 3D block nozzle.

9.1 DSMC vs Continuum(NAVIER-STOKES 'NS') Models

There are two separate techniques currently available for analysis of MEMS micronozzles. One technique solves the traditional Navier-Stokes equations which model gas flow on a continuum level. The direct-simulation Monte Carlo (DSMC) uses statistical mechanics to track particles on a molecular level and in so doing develops the overall temperature, pressure and density profiles of the gas flow. The defining line between the DSMC and continuum models depends on a dimensionless parameter known as the Knudsen number. The Knudsen number is a ratio of the mean free path of each molecule to the characteristic dimension of the physical surroundings. The mean free path is defined as the distance each molecule travels between collisions.

$$Kn = \frac{1}{\sqrt{2\pi d^2 n L}} \quad (9-1)$$

$$n = \frac{P}{k_b T}; \quad n = \frac{\rho}{m}; \quad m = Ma$$

d = molecule diameter ($\sim 3.7E-10$ m)

L = characteristic physical dimension (m)

n = # particles / unit volume

P = pressure (N/m²)

k_b = Boltzmann's constant

T = temperature (K)

m = molecule mass (kg/kmol)

M = molecular weight / molecule

a = atomic mass unit (1.6603E-27 kg/particle)

The Knudsen number increases with a decrease in characteristic length, molecular weight, or decrease in density. Assuming other state properties are constant, decreasing the pressure or increasing the temperature will serve to decrease the density.

It is generally accepted that the continuum assumption fails for $Kn > 0.01$. A more specific breakdown for Knudsen numbers and flow category is given in table 9-1:

Table 9-1. Knudsen Number Categories¹

$Kn < 0.01$	Continuum flow
$0.01 < Kn < 0.1$	Slip flow
$0.1 < Kn < 3$	Transition flow
$Kn > 3$	Free molecular flow

It has been shown that attempting to use the continuum technique for high Knudsen number flows results in overprediction of Isp efficiencies. The following 2D results were presented in a 1999 paper by *et al Ketsdever*²⁶. The stagnation temperature was equal to 300 K, and the chamber pressure varied between 1 and 10 atm to gain throat Reynolds numbers of 130 to 1300.

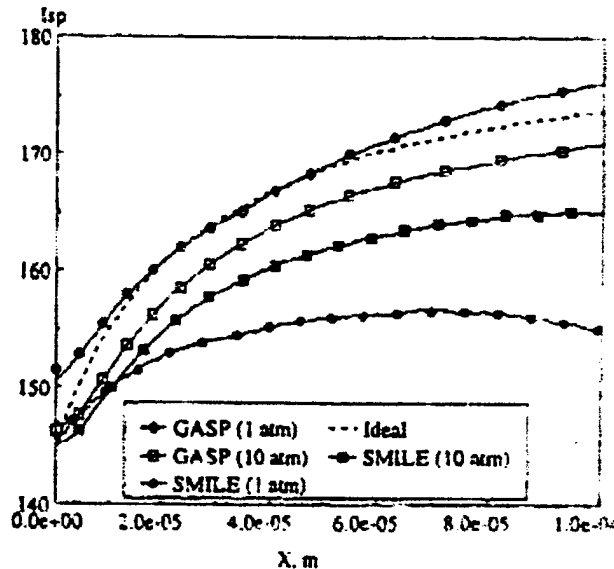


Figure 9-1. Reynolds Numbers 130 to 1300 NS(GASP), DSMC(SMILE) Comparison²⁶

At higher Reynolds numbers (1300, $P=10$ atm), there is a smaller difference between the results obtained for GASP and SMILE compared to the lower Reynolds number of 130 ($P=1$ atm). Obviously, at the lower Reynolds number the predicted results above the ideal Isp level are not viable. The value of the Knudsen number for $Re = 1300$ varied from 0.001 at the throat to around 0.2 at the exit. Therefore, according to the Knudsen number classification, the continuum model is only applicable to specific portions of the flow regime. In fact, the Knudsen numbers in these calculations are based on the 2D model, therefore, by adding endwalls (which have a characteristic length less than the diverging walls) the Knudsen number actually increases further allowing for greater deviation in the results for 3D calculations if they were performed. Another point is that the expansion ratio is at a very high value of 100. At such expansion levels, the density is going to decrease to values typical of rarefied effects. Therefore, according to these results, at higher Reynolds numbers, the NS model does predict Isp efficiencies greater than those of the DSMC code. According to the paper, this deviation in the results exhibits a direct correlation to the boundary conditions of the numerical algorithm. They suggested that first-order extrapolation conditions at the nozzle exit boundary led to the over prediction. They suggested making use of an expansion region outside of the nozzle would possibly reduce this error.

Also included in the paper was a verification run with experimental data from Rothe's electron beam measurements. The expansion ratio was only 3.7. The results for this analysis compare better with one another than the results presented above.

Table 9-2. DSMC (SMILE) & NS (GASP) Comparison²⁶

Code	Re	wall condition	$m, \text{kg/sec}$	thrust, N	I_{sp}, sec	m/m_{ideal}	$I_{sp}/I_{sp,\text{ideal}}$
GASP	270	adiabatic	1.995e-05	1.310e-02	67.03	0.9981	0.8663
SMILE	270	adiabatic	2.013e-05	1.298e-02	65.77	0.9062	0.4505
GASP	210	$T_w = 300K$	1.983e-05	1.331e-02	68.50	0.8927	0.8855
SMILE	210	$T_w = 300K$	2.014e-05	1.305e-02	66.08	0.9067	0.8843
GASP	120	adiabatic	8.364e-06	5.324e-03	64.96	0.8539	0.8400
SMILE	120	adiabatic	8.549e-06	5.120e-03	61.07	0.8728	0.7397
GASP	120	$T_w = 300K$	8.276e-06	5.429e-03	67.68	0.8450	0.8752
SMILE	120	$T_w = 300K$	8.550e-06	5.124e-03	61.39	0.8729	0.7935

For these small Reynolds numbers, there is a difference between the DSMC and NS calculations. In fact, the lower the Reynolds number, the greater the difference in the efficiencies. Although, where GASP predicts a greater I_{sp} efficiency, SMILE predicts a greater discharge coefficient ($m_{\text{actual}}/m_{\text{ideal}}$). I presume that the smaller expansion ratio keeps the Knudsen number at a minimum (although not presented in the paper), therefore allowing for greater applicability of the NS solver. This analysis is difficult to compare and draw conclusions on due to the different set up of an expansion region beyond the throat for the DSMC and NS method. The results just beyond the throat are the most viable, and they show a definite difference in the solutions of the two solvers, but only of a few percentage points for $Re = 1300$.

Following along these lines, another significant difference between these two codes in comparison studies is the characteristics of the gas flow near the nozzle lip. According to the study conducted by Alexeenko et al²⁸, at a Reynolds number of 200 ($Kn = 5E-3$), the flow within the nozzle between the two codes agreed fairly well. The largest difference occurred when looking at the nozzle lip. In this region the DSMC code predicts a rapid expansion of gases if the pressure gradient at the nozzle exit is sufficiently high. The result is that the sonic line intersects the nozzle lip and the subsonic boundary layer never exits the nozzle. This can be seen by the following nozzle mach contour lines produced in another study.

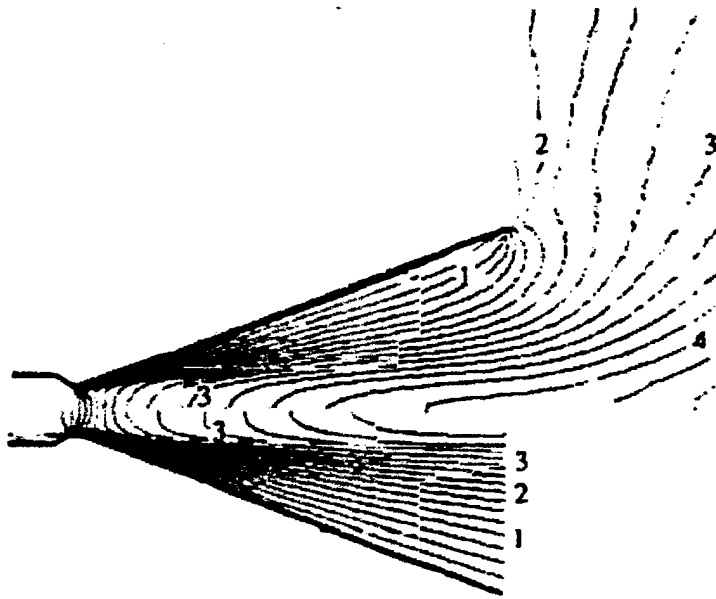


Figure 9-2. Difference Between NS and DSMC Codes at Nozzle Lip³⁰

The reason for this discrepancy is the use of extrapolation conditions from within the nozzle to model the outflow of the gas at the exit. As suggested in the study, by setting up an additional zone outside the nozzle exit as shown above in the diagram for not only the DSMC code, but also the NS code, it may be possible to capture the same effects at the nozzle lip.

The DSMC method also correctly captures the rarefied gas effects of gas slip at the nozzle wall. In continuum fluid mechanics the assumption is made that there is a region of no-slip at the nozzle wall, thus creating a decrease in velocity from the supersonic expanding divergent core to a magnitude of zero at the wall.

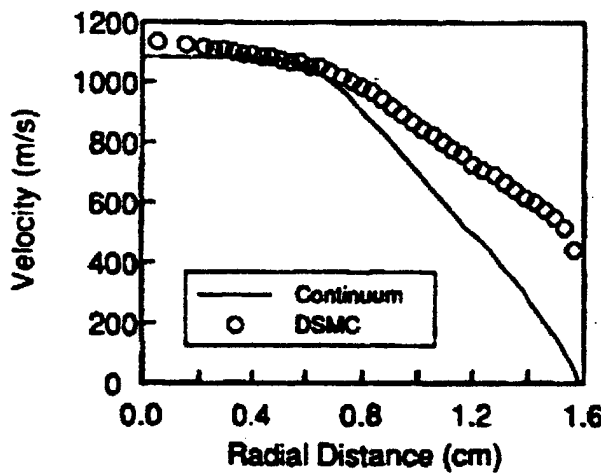


Figure 9-3. Differences in Velocity at the Wall⁴²

The INCA code allows for rarefied gas slip at the walls, thereby making it possible to sidestep this problem at the wall. Concerning the interior of the nozzle, it is not possible to model the rarefied effects with the INCA continuum code. Therefore, efforts will be made to stay within the continuum regime thereby negating the need for rarefied modeling.

9.2 Nozzle Divergence Angle

In macronozzles, engineers have found that bell-shaped nozzles prove to be the most efficient means of directing exiting particles along the primary thrust axis. In the case of divergent conical nozzles, Dr. Ron Humble published equation (9-2) to relate the divergence angle to thrust efficiency⁴⁴:

$$\lambda = \frac{1}{2}(1 + \cos \theta) \quad (9-2)$$

λ = thrust efficiency

θ = nozzle divergent half angle

Unlike macronozzles, design of micronozzles must take into consideration the inefficiencies associated with the developing viscous layer. As described earlier, the viscous layer impedes the expansion of high-temperature gases, thereby resulting in a subsonic boundary

layer gradually enveloping the supersonic core. In the macronozzle case, the smaller the divergent angle, the greater the inefficiency. For micronozzles, there is a trade off between the aforementioned divergent losses and those associated with the boundary layer absorbing the vital supersonic core. By using a larger expansion angle, we increase the area of the supersonic core while increasing divergent losses.

In 1993, Suk C. Kim produced a paper addressing this issue²⁴. Data produced was focused on Reynolds numbers of 1150; area ratio of 82 and chamber temperature of 1500 K. The walls are adiabatic and a no-slip condition is assumed. In figure 9-4 are the velocity profiles and Isp efficiency plots for the a 20, 30 degree conical nozzle and contour bell nozzle:

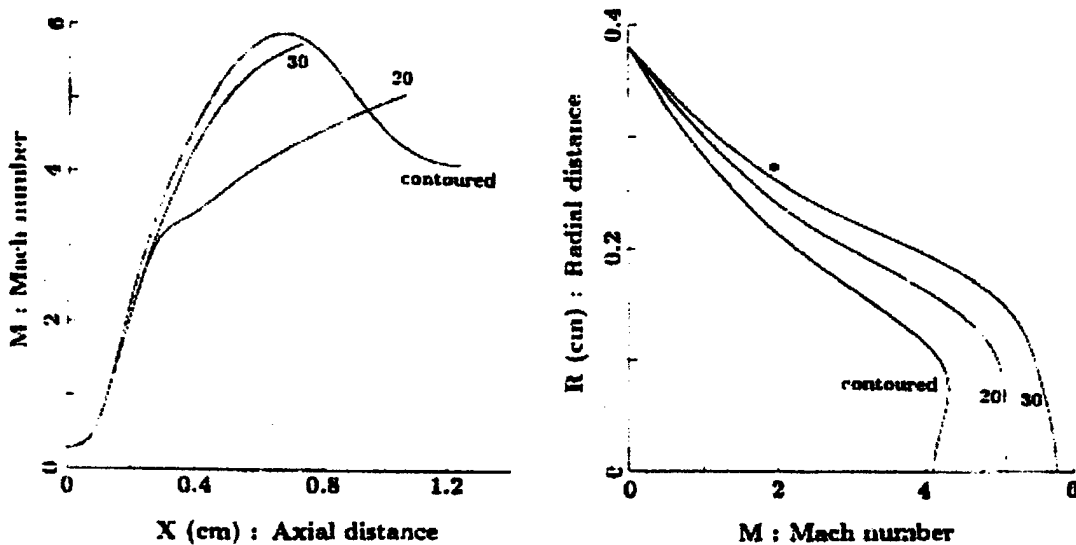


Figure 9-4. Difference in Velocity Profiles of Various Half-Angles²⁴

For this set of analyses, Kim made the assumption that the walls were adiabatic meaning there was no heat transfer in or out of the nozzle. He also assumed a no-slip velocity condition along the walls which is characteristic of gas flows in the continuum, high Reynolds number, low Knudsen number regime. The results of this paper indicate that at Reynolds numbers around 1000, it is advantageous to use higher divergence angles in order to increase the area available for supersonic expansion.

In 1994, researchers from Penn State University published a paper on 2D calculations of Reynolds numbers of 90 and 125 for stagnation temperatures of 300 and 1000 K; expansion ratio of 104²⁵. The goal of the research was to model viscous effects in 3 differently shaped nozzles: trumpet, conical and bell. The results of the numerical analysis are summarized below. The discharge coefficient is defined as ratio between the actual and ideal mass flow rate²⁵:

Table 9-3. Results of 2D / 1994 Computational Efforts of Various Geometries²⁵

Nozzle	Case (Re)	Isp Efficiency	Discharge Coefficient (Cd)
Trumpet	Unheated (117)	83	0.82
Bell	Unheated (117)	80	0.86
Conical	Unheated (117)	79	0.92
Trumpet	Heated (90)	49	0.82
Bell	Heated (90)	49	0.85
Conical	Heated (90)	46	0.92

At first glance, it appears that the two results contradict each other based on [ref 25], although we are looking at two separate conditions at the throat based on Reynolds numbers. For the greater Reynolds number, according to Kim the contoured nozzle attains the best performance (not considering the trumpet nozzle)²⁴. For the smaller Reynolds number at slightly lower temperatures (1000 K compared to 1500 K) the bell nozzle has better Isp efficiency than the contoured nozzle according to Penn State researchers.

For the purpose of this thesis, the goal is to determine the effect of increased temperature on Isp/thrust efficiency using a block nozzle configuration. Therefore, a 30 degree contoured nozzle will be used with constant endwall height for all Reynolds numbers examined from 250 to 2000.

9.3 Axisymmetric vs 3D Block Nozzle

Traditionally, axisymmetric nozzles have been used in all types of space/rocket propulsion. The small throat diameters required for small thrust levels are most feasible in a building block structure. Nozzles are etched in materials such as silicon or ceramics and can then be stacked together to gain the desired aspect ratio. On each end solid plates are attached and the result is a rectangular (square) nozzle and exit plane. The downside is that the endwalls do not

expand, rather there is a constant distance and the expansion occurs strictly as a function of the sidewall divergence.

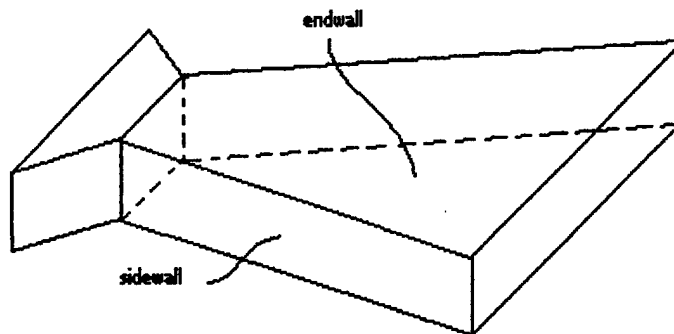


Figure 9-5. MEMS Nozzle

The surface area is directly proportional to shear forces along the walls. The combination of the shear stress and velocity gradient from the no-slip condition of the wall to the freestream is responsible for the build up of the boundary layer. The viscous layer expands into the volume normally occupied by the diverging section of the nozzle. If the divergent section is filled with a viscous layer, then the gas cannot fully expand. In a recent report of high-temperature gas flows, the following data of table 9-4 was reported for an expansion ratio of 100 for nozzles and an aspect ratio of 1 for the block nozzle (Reynolds number = 205)²⁸:

Table 9-4. Results for High-Temperature Analysis of Axisymmetric Nozzles²⁸

T _c (K)	Nozzle	F _{ideal} (mN)	F _{calc} (mN)	F _{eff} (%)	I _s p _{ideal}	I _s p _{calc}	I _s p _{eff}
300	Axi	1.24	1.03	83.1	76.5	65.5	85.6
1000	Axi	5.57	4.01	72.0	142.1	130.8	92.0
2000	Axi	12.9	9.14	70.9	201	141.3	70.3
300	3D				76.5	56.6	74.0
1000	3D				142.1	61.0	42.9

The results of the above analysis can be explained in part by the nozzle surface-volume ratios presented in figure 9-6.

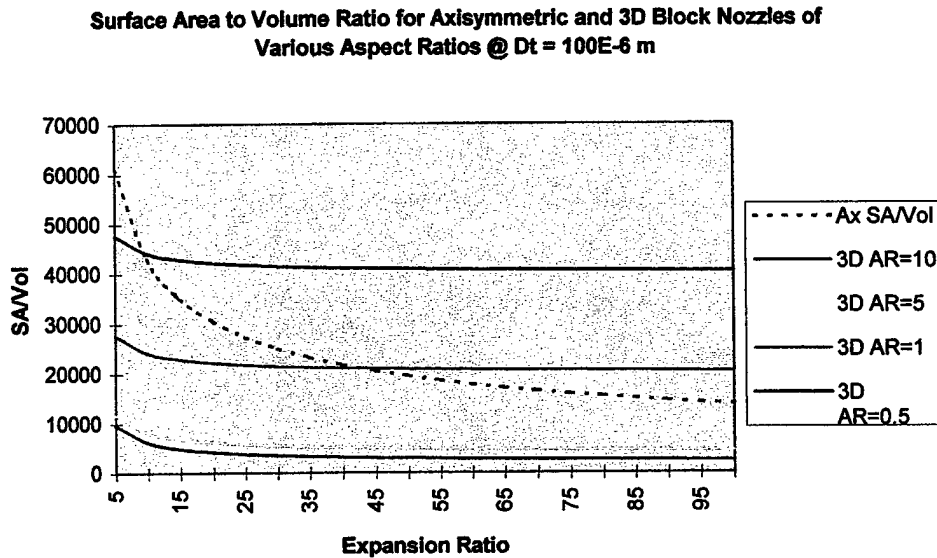


Figure 9-6. Surface Area to Volume Ratio for Various Nozzles

For an expansion ratio of 100 and aspect ratio of 1 for the block nozzle, the surface area/volume ratio of the 3D block nozzle is greater than that of the axisymmetric nozzle. For the limiting case of minimal heat transfer and increased viscosity as a result of higher temperatures, the 300 K case shows that efficiency reduces from 85.6 to 74.0 for the axisymmetric and 3D block nozzle, respectively.

In general, the surface area/volume ratio of an axisymmetric nozzle is greater than that of the 3D block nozzle, except at higher expansion ratios of the low aspect ratio nozzles. Therefore, based solely on the assumption that the boundary layer has more of an influence where the surface area/volume ratio is greatest, we could make the assumption that the 3D block nozzle is preferred over the axisymmetric nozzle at low expansion ratios. As it turns out, for a given thrust level the Reynolds number is always greater and decreases at a smaller rate down the axial length of the nozzle. In addition, for axisymmetric nozzles the expansion ratio goes as the square of the radius whereas the block nozzle is proportional to the nozzle width. For a given axial length the expansion ratio will be greater for axisymmetric nozzles over block nozzles. Therefore, conical nozzles will probably always produce greater efficiencies when considering viscous effects.

9.4 2D vs 3D Simulations

In his 1999 thesis⁴³, R.L. Bayt suggested the use of 2D simulations to obtain results of actual 3D nozzles. This assumption was pointed out by Markelov et al²⁷ as being viable for Reynolds numbers ≥ 1000 , but consideration must be given to the boundary layer development along the endwalls for smaller Reynolds numbers. One important factor to be considered is the aspect ratio, which is not pointed out in Markelov's paper²⁷ although the throat Reynolds number is below 1000, a large aspect ratio will reduce the effects of the boundary layer along the endwalls.

Nonetheless, the following data is reported with the missing aspect ratio in mind (we will assume it to be 1). The results presented were produced with the DSMC method. This first graph represents the displacement thickness both along the sidewalls for the 2D and 3D case, and along the endwalls for the 3D case. Bayt's assumption was that the boundary layer would have the same thickness for the sidewalls as well as along the endwalls. Figure 9-7 for a Reynolds number of 350 (Eratio of 7.1) contradicts his assumption:

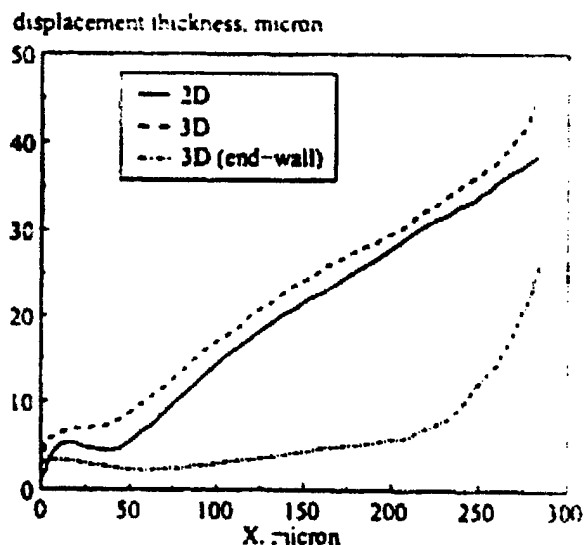


Figure 9-7. Boundary Thickness along End/Sidewalls²⁷

The expansion ratio in these cases is 7.1.

Figure 9-8 represents the Isp along the nozzle centerline and discharge coefficients for experimental and computational results.

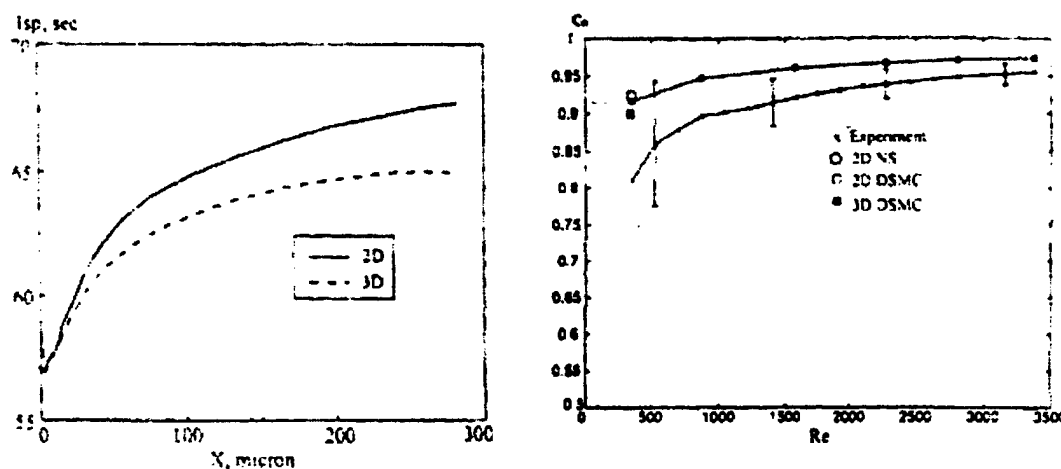


Figure 9-8. Isp/Discharge Coefficient Values for Numerical/Experimental Test Cases²⁷

As pointed out by Markelov et al²⁷, the error bars indicate that the computational results are within acceptable limits. The calculated 3D expected performance from 2D results is therefore not acceptable at these conditions (Re 350, Aspect Ratio ?).

For the purposes of our calculations, we will make use of the 3D simulations in as much as they do not require excess computational resources and time for convergence in order to produce the most accurate results for all simulations.

9.5 Nozzle Throat Contour

As reported by Ivanov et al²⁷ the contour of the throat can result in greater thrust performance by providing a smooth transition to the supersonic regime. In a recent study, the study of a smooth throat contour was compared with a sharp contour. The mach contours for the study are shown in figure 9-9.

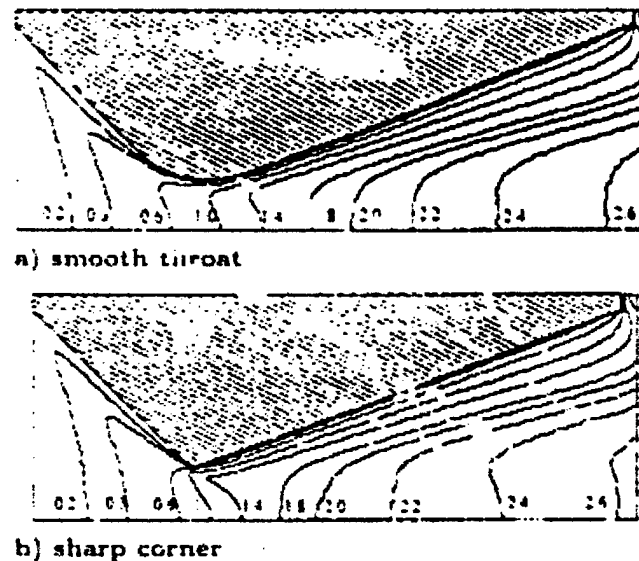


Figure 9-9. Mach Contours for Smooth/Sharp Throat²⁷

As reported by the study²⁷, “the presence of a sharp corner leads to a sharp peak of friction and rather complex behavior of pressure near the nozzle throat.” The results of the analysis are outlined in table 9-5 ($Re = 350$, $T_c=300K$) in table 9-5. Thrust and Isp efficiency is the ratio between the computed and ideal values.

Table 9-5. Contoured Throat Results²⁷

Contour	Eratio	mass flow (kg/sec)	F (mN)	Isp (sec)	Cd	F_eff	Isp_eff
Sharp	4	1.476	0.949	65.66	0.925	0.842	0.912
Smooth	4	1.472	0.943	65.47	0.922	0.837	0.909

Ivanov et al²⁷ explained the performance of the throat to better for the sharp case because of the extended axial distance required for the smooth case, thus allowing for an increase in viscous build up and boundary layer losses.

This study will use a sharp corner at the throat.

9.6 High-Temperature Analysis

Another recent study²⁸ focused on the effects of increasing temperature and viscous losses. While this study is most like the study this project is focused on, the highest temperature investigated was only 2000 K and the nozzle shape was axisymmetric instead of block. We are interested in temperatures as high as possibly 3000 K and block nozzles. In addition, the expansion ratio of 100 and nozzle-half angle of 15 will produce different results compared to the current study (expansion ratio of 10, half-angle of 30). The study broke down the various parameters that affect the loss of thrust and Isp. The conditions were outlined as follows in table 9-6 and 9-7 with the following properties in common ($Re = 205$, $Kn = 5.5E-3$, $Dt = 300 \mu m$, $Eratio = 100$, nozzle angle = 15°):

Table 9-6. Wall Conditions for High-Temperature Analysis²⁸

Case	Conditions
1	Smooth, no energy/momentum transfer to walls
2	Momentum transfer, adiabatic walls
3	Momentum and energy transfer to walls

Table 9-7. Results for Various Chamber/Wall Conditions of High-Temperature Analysis²⁸

Tc (K)	Conditions	F (mN)	F_eff	Isp (sec)	Isp_eff
300	1	1.21	97.8	74.8	97.8
300	2	0.99	79.8	64.2	83.9
300	3	1.03	83.1	65.5	85.6
1000	1	5.42	97.3	138.2	97.3
1000	2	4.51	82.7	117.6	82.8
1000	3	4.01	73.0	103.8	73.0
2000	1	12.5	96.7	194.5	96.8
2000	2	10.6	83.0	166.8	83.0
2000	3	9.14	70.3	141.3	70.3

For these axisymmetric nozzles, it is apparent from the results above that the transfer of energy to the walls has more of an impact for high temperature flows as would be expected. Note that the greater the temperature, the greater the overall reduction in efficiency due to the increased heat transfer losses. Yet, because they operated all three conditions at the same Reynolds number, the losses due to viscous losses are relatively the same (conditions = 2 : 83.9, 82.8 and 83.0).

In the current study, the losses due to viscous effects are expected to be the predominant source of inefficiency. The losses due to conduction heat transfer are not expected to significantly contribute to the overall performance due to poor conduction of the nozzle wall material (ceramic). Although, heat losses due to radiation must still be accounted for. For the current study, only the viscous losses will be modeled in order to generate a database of expected losses. Once more information is gained as to the reaction of the wall material to high-temperature gas flows, heat loss can also be modeled.

This study also briefly mentioned the modeling of a 3D block nozzle at 300 and 1000K. Using the same area ratio at an aspect ratio of 1, the results are in table 9-8.

Table 9-8. 3D Block Isp Efficiencies²⁸

Tc (K)	Ispideal	Ispcalc	Isp eff
300	76.5	56.6	74.0
1000	142.1	61.0	42.9

As indicated by the study, the greater loss in efficiencies for the block nozzle compared to the axisymmetric geometry is the greater surface area/volume ratio. As earlier indicated in the axisymmetric/3D comparison section, this is only the case at higher expansion ratios. As will be pointed out in the next section, truncation of the nozzle will produce greater efficiencies compared to high expansion ratios. The relation between axisymmetric and block nozzles is left for additional analysis, although it is the author's opinion that because axisymmetric nozzles have a greater expansion ratio for a given axial distance and divergence angle, it will outperform the block nozzles when considering viscous effects.

9.7 Truncated Nozzle

A majority of already published papers focused on expansion ratios greater than 50. In the case of a macronozzle, the further expansion of a nozzle in a vacuum leads to increased expansion of the gases and thus greater thrust and specific impulse. The limiting factor is the mass and volume occupied by the nozzle. In the micronozzle case, the limiting factor becomes the expansion ratio itself. The longer the axial distance, the greater the time for the viscous layers

to build and thus envelop the inviscid core flow. Given enough time and distance, the inviscid core will be completely absorbed by the boundary layers.

Alexeenko et al²⁸, produced the following results of thrust along a 3D block nozzle affected by viscous losses in figure 9-10.

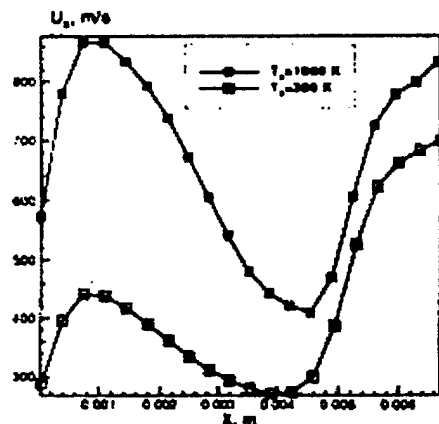


Figure 9-10. Axial Velocity Profile with Viscous Effects²⁸

Obviously, unlike the ideal condition where the velocity would progressively increase, the velocity actually peaks and then decreases due to viscous losses. As it approaches the nozzle exit, the gas speeds up again towards the vacuum conditions and some of the velocity is regained.

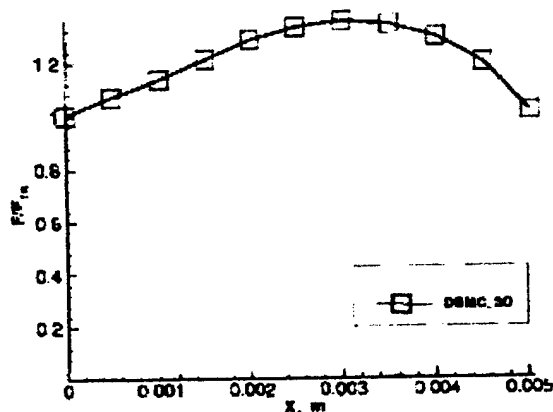
A recent study experimentally investigated the effect of truncating the nozzle by use of a cold gas setup by Reed et al²⁹. The study used nine separately fabricated silicon nozzles (area ratio from 1 to 24). The chamber temperature was 300 K and the aspect ratio was less than 1. Therefore, the endwall effects are expected to have a large impact in overall performance. The results of the analysis are below (Note, Reynolds numbers and Thrust Efficiencies listed in table 9-9 are approximate interpolations from exact values listed in the study):

Table 9-9. Selected Nozzle Thrust Efficiencies for Truncated Nozzle

Area Ratio	Re - 200	Re - 1000	Re - 2000
1.0	6.0	15.0	23.5
1.5	9.0	22.0	25.0
4.8	7.0	16.0	22.0
9.7	5.9	11.5	18.0
14.9	6.7	13.0	16.0
18.3	6.0	12.0	15.0
19.5	7.0	13.8	22.0
23.1	7.4	14.5	17.0
24.2	7.2	15.3	18.0

Although these values include experimental/interpolation error, the general idea is proven that at smaller area ratios produce greater thrust efficiencies.

Another paper showed a decrease in thrust level as a function of the axial distance³⁷.

Figure 9-11. Reduction of Overall Thrust Due to Overextended Nozzle³⁷

They suggested an increase in height or decrease in expansion ratio to reduce the effects. This suggestion was discovered after the current research was carried out, but the general idea is obvious that increasing the height decreases the effect of the endwall boundary layer on overall performance.

9.8 Wall Temperature

In order to correctly model the accurate flow of a physical problem it is necessary to properly set up the boundary conditions of the numerical code. The accurate convergence of a

numerical code is dependent upon the boundary and initial conditions. This topic has been the subject of a great deal of research in order to correctly validate numerical codes.

One area of interest is the temperature of the walls. In several studies the walls are set to be adiabatic. In a low temperature flow this does not present much of a difference in the final results because there is not a large gradient between the temperature within the nozzle flow and the ambient temperature on the other side of the nozzle wall. For higher temperature flows at long thrust times, the walls will heat up and a certain amount of energy will be lost through convection and conduction to the wall and eventually radiation into the surrounding ambient conditions. By assuming adiabatic walls, all energy is contained within the nozzle and eventually exits the nozzle producing thrust. For our specific case of high temperature flows, there is also the concern of viscosity which is a function of temperature. When energy is lost to through the nozzle walls, the viscosity decreases as the temperature decreases. This serves to increase the Reynolds number and decrease viscous losses. The question then remains which produces the greater difference in efficiency: the losses due to energy transfer to the wall or the gain due to decreased viscous effects? This is a question that will not be addressed in this thesis as we will be primarily focused on the viscous effects. Therefore, concerning the viscous effects an adiabatic wall will be the worst-case scenario for viscous losses. The loss of radiated energy and influence upon viscous effects and overall efficiency is left for another study.

Chapter 10: Current Research Overview

Previous studies have provided a foundation upon which to perform the following analysis. It is the goal of this current study to determine whether there exists an optimum operating range for a high-temperature chemical propulsion system. Since there are several parameters that affect the performance of a nozzle, ideally a research plan would cover each variable. Having obtained an ‘ideal’ geometry to include expansion angle, expansion ratio, aspect ratio, it would then be possible to determine if a high-temperature limit indeed exists for that ‘ideal’ geometry. While a limit may exist for less-efficient geometries, propulsion engineers would in theory use the ideal geometry if it allowed for use of higher performance chemical systems. Unfortunately time limits such an extensive study. Therefore, for reasons already reviewed, nozzles of this study are truncated to an expansion ratio of 10 with a nozzle half-angle of 30 degrees in a 3D block-nozzle configuration. Using this baseline physical geometry, the author found particular interest in the effects of varying the aspect ratio. For the given expansion ratio, aspect ratios of 1, 5 and 10 will be investigated and compared for thrust levels of 31 and 501 mN at chamber temperatures of 2000, 2500 and 3000 K.

Using the aspect ratio with the best performance and predefined geometric variables, the chamber temperature is varied for 1000, 1500, 2000, 2500 and 3000 K. At each temperature level, data is obtained for Reynolds numbers of 250, 500, 1000, 1500 and 2000. With this data it is then possible to determine the thrust/Isp efficiencies as a function of temperature and Reynolds number. Together with Isp as a function of temperature we will determine the preferred operating temperature range for the given propulsion system.

Data is obtained through a finite-volume numerical analysis of the computational fluid dynamics code INCA¹⁰⁹. Results will then be applied to missions already defined earlier in this thesis.

Based on the results of the aforementioned research programs, a research plan was developed to focus on developing an optimum nozzle for the high-temperature flows expected with the University’s developing chemical-propulsion system. Based on previous results, the nozzle has a divergent section of 30 degrees to minimize the effect of boundary layer growth and allow for greater expansion of the escaping gas. In addition, the throat has a sharp contour.

Analyses are performed at Reynolds numbers of 250 to 2000 for chamber temperatures between 1000 and 3000 K at aspect ratios (nozzle throat height to width) of 1, 5 and 10.

Chapter 11: Physics of Micronozzle Flow

As already mentioned, the motivation of this study is the development of higher-temperature propulsion systems which operate at higher levels of efficiency, or Isp. For a fixed expansion ratio and operating pressure, and assuming isentropic expansion, specific impulse varies directly with the square of the chamber temperature⁴⁴.

$$\begin{aligned} Isp &= \frac{F}{mg}; \quad F = A_e(\rho U_e^2 + P_e); \quad m = \rho A_e U_e \\ U_e &= \sqrt{\frac{2\gamma RT_o}{(\gamma - 1)} \left\{ 1 - \left(\frac{P_e}{P_o} \right)^{\frac{1}{\gamma-1}} \right\}}; \quad T_e = T_o \left(1 + \frac{\gamma-1}{2} M^2 \right)^{-1}; \\ Isp &\propto \sqrt{T_o} \end{aligned} \quad (11-1)$$

Isp = specific impulse (sec)

F = force (N)

m = mass flux (kg/sec)

A_e = exit area (m²)

ρ_e = exit density (kg/m³)

U_e = exit velocity (m/sec)

P_o = chamber pressure (N/m²)

P_e = chamber pressure (N/m²)

R = gas constant (8314.41 / molecular mass)

M = mach number

T_e = exit temperature (K)

T_o = chamber temperature (K)

For the proposed system, a propellant is accelerated through a MEMS nozzle. The oxidizer/fuel can be stored either as monopropellants or bipropellants. For a monopropellant, the oxidizer/fuel mixture is introduced to a catalyst which initiates decomposition and combustion. A bipropellant simply introduces the propellants and if hypergolic they will spontaneously combust, if not a spark is required. The choice of these two options requires further analysis and testing of the properties of the reactants in question.

In either case, combustion products enter a combustion chamber where they are channeled to the convergent part of the nozzle. The flow is accelerated to mach 1 at the throat and then ideally accelerated supersonically towards the exit plane. In the vacuum of space, ideal use of the gas requires an infinite nozzle to allow full expansion of the gas to near-zero static

pressure. An infinite nozzle is realistically not possible, and in our case it turns out that a truncated nozzle will produce better efficiencies due to viscous envelopment of the supersonic inviscid freestream.

We will now take a closer look at viscosity, exactly what it is, what causes it, and how it effects the overall flow of the system. According to White³³, three transport properties of viscosity, thermal conductivity, and diffusion describe the physics of fluidic flow. Each is related macroscopically to a nonuniformity (gradient) of flow velocity, temperature and composition¹². This study is primarily concerned with retarding viscous effects due to a velocity gradient on the overflow of the system. According to Cebeci³², there are three ways momentum is transferred: "transport by mean motion of the fluid, transfer by random molecular motion (represented by viscous stresses), and transfer by turbulent eddies (represented by the mean turbulent stresses)" (6). Acted upon by an outside force a particle gains a bulk kinetic energy. In nozzle flow, this is due to a pressure gradient and physical effects of a converging/diverging nozzle. Viscous effects at the wall begin at the onset of the flow and increase in magnitude as the fluid moves downstream.

To an outside observer, fluidic flow has a velocity of zero along a solid surface. This is the so-called 'no-slip' boundary condition at the wall. Moving away from the wall we witness a parabolic velocity profile until the freestream velocity of the inviscid core. This velocity gradient normal to the wall results in a shear stress (force/unit area) parallel to the wall. A fluid particle within this region of velocity gradient is distorted proportional to the shear stress acting upon it. This can be seen by figure 11-1.

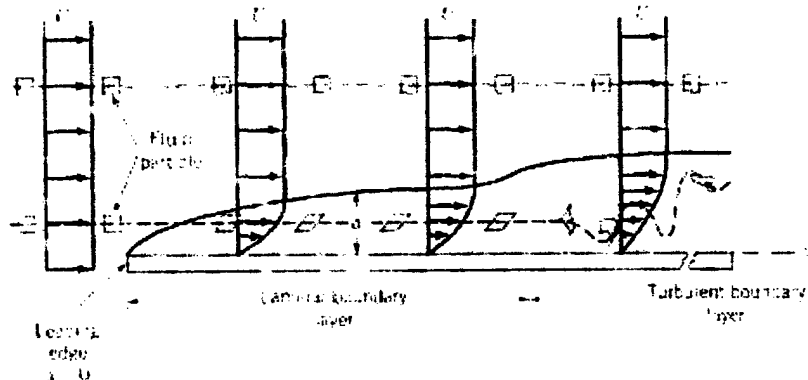


Figure 11-1. Shear Stress and Velocity Gradient³¹

In a quantitative sense, the shear stress is equal to the velocity gradient multiplied by some viscosity coefficient which is a dependent on the properties of the gas.

$$\tau = \mu \frac{du}{dy} \quad (11-2)$$

τ = shear stress (N/m^2)
 du/dy = velocity gradient

As already referenced to Cebeci³², viscosity is the transfer of momentum by random molecular motion. To fully understand how viscosity is working, it is necessary to look at it from a microscopic point of view. The no-slip boundary condition at the wall is due to the collision of particles with the wall and subsequent random deflection, the average of which gives an overall velocity of zero at the wall. The no-slip condition is observed at the initial onset of particle interaction with the solid surface. The gas particles already have a bulk kinetic energy parallel to the wall. In addition, they each have a degree of random thermal kinetic energy. The no-slip condition at the beginning results in the velocity gradient of the bulk kinetic energy. The thermal kinetic energy produced results in migration of the lower energy particles from the wall into the freestream. As a result of collisions between the lower/higher-energy particles, momentum is transferred away from the higher-energy particle and into the lower-energy particle. As the mass of particles collectively move downstream the thermal kinetic energy continues to create more collisions between the particles and in effect the boundary layer continues to grow (viscous effects increase). The viscosity coefficient of equation (11-2) is described microscopically by equation (11-3)³⁴:

$$\mu = \beta_\mu \rho \bar{C} \lambda \quad (11-3)$$

μ = viscosity coefficient
 B = proportionality constant
 ρ = density (kg/m^3)
 λ = mean free path (m)
 C = mean molecular speed (m/s)

Since λ goes as the inverse of the density, viscosity is independent of density. And the mean speed of a molecule through kinetic theory goes approximately as $T^{1/2}$. Realistically, the power is a little higher due to the ‘variation of intermolecular force with distance’³⁴. Therefore, it would seem valid to presume that viscosity is strictly a function of temperature. Generally this

assumption holds true except for circumstances in which we must take into account real gas effects. This only occurs when the density of the gas is high enough that the intermolecular spacing of separate molecules is on the order of the diameter of the molecules themselves.

According to Bird³⁵, pressures below 10 atmospheres result in viscosity dependence upon temperature only (reducing the pressure reduces the density and real gas effects thereby making viscosity a function of temperature only). For our case, we will be operating at a chamber pressure of 30 atmospheres within the chamber. The static pressure then rapidly decreases through the nozzle, albeit at a value still greater than 10 atmospheres. Still, the lowest chamber temperature is 1000 K which presumably provides a sufficient offset to warrant classification as a low-density gas. Therefore, the viscosity of our given mixture is solely a function of temperature.

As the boundary layer develops, the effective expansion ratio is reduced due to the increasing diffusion of the viscous effects into the inviscid supersonic core. If allowed to progress far enough, the viscosity will completely envelop the supersonic expansion, thereby negating the desired expulsion of high velocity particles from the nozzle exit plane. It is therefore conceived that there exists an optimum expansion ratio where the gas has had adequate time to expand and the boundary layer has not had enough time to adversely affect the expansion. For the present study, due to time constraints, a complete study on the expansion ratio will not to be attempted. Instead, an expansion ratio has been chosen which the author presumes is not large enough to enter the regime where the viscous effects actually begin to decrease the performance of thrust and Isp.

11.1 Frozen/Equilibrium Flow

Upon reaction within the combustion chamber, the products accelerate towards the throat of the nozzle and eventually exit into the vacuum of space. If the products continue to react with one another throughout the entire length of the nozzle, the gas is said to be in equilibrium. A new level of temperature corresponding to a decrease in temperature as the gas expands allows for further chemical interaction and the release of energy. Equilibrium simply means that the reaction time is much smaller than a characteristic flow time for a given temperature range. If the flow is frozen, the opposite is assumed. The reaction time is much larger than the flow time. Frozen flow produces smaller levels of specific impulse because energy that could be released with continued reactions (and thereby converted to kinetic energy by the nozzle contour) remains

within the separate species. Thus, potential reaction energy exits the nozzle without having been converted to kinetic energy.

The CEA chemical kinetics code¹³³ used for computing the ideal reaction product properties uses both equilibrium or frozen flow. An example of an input listing for the kinetics code is found in Appendix B. Due to the small physical dimensions of the nozzle and corresponding short characteristic flow time, I assumed the flow would be frozen. It is also possible to allow chemistry to occur within the flow with the INCA code. However, with the frozen flow assumption, the respective species were set to specific initial values in the combustion chamber. This is obviously the pessimistic approach to the amount of energy released throughout the combustion and acceleration process, but it provides a lower-level limit to expected results.

11.2 Exit Expansion

In recent papers, both continuum and DSMC models have been used to simulate the expansion of gases in micronozzles. The results of the two techniques have produced significant differences. In effect, the DSMC method has become the more preferred choice for valid numerical results when compared with limited experimental data. Many of these differences have to do with the differences between rarefied and continuum flows, while others deal with the problem numerically. One example of a numerical difference deals with the physics of the gas in the vicinity of the nozzle exit plane.

When a boundary layer gradually increases in thickness normal to the nozzle walls, the microscopic molecular collisions retard the flow and therefore we experience the velocity gradient described previously. Due to this decrease in velocity as we approach the wall, the pressure increases. A pressure gradient that would normally be used to expand gases is now trapped within the boundary layer. Due to the parabolic mathematical nature of boundary layers, information is propagated both upstream and downstream. This contrasts with the hyperbolic nature of supersonic flows which are dependent solely upon the characteristics of the upstream flow. Therefore, the parabolic, subsonic boundary layer not only 'sees' the favorable pressure gradient of the throat, it also 'sees' downstream the vacuum beyond the exit plane. At a certain point from the nozzle exit, it is expected that the substantial pressure gradient between the boundary layer flow and vacuum will result in supersonic expansion of the gases. We therefore

witness a difference between the struggle of the viscous effects in expanding the boundary layer and the pressure gradient in accelerating the flow towards the vacuum. Several papers have recently reported differences in modeling this effect. The continuum method has been used with simple extrapolation into the nozzle. This method does not accelerate the flow towards the vacuum, therefore the boundary layer continues to grow and develop leaving a substantial boundary layer at the nozzle exit. The DSMC method has been modeled with an additional region of points beyond the exit plane to take into account the vacuum of space. The result has been a predicted expansion of gases towards the nozzle lip. In effect, the mach line between the subsonic and supersonic regions produces a choking effect of the boundary layer, thereby accelerating the boundary layer to supersonic speeds at the nozzle lip. This physical result has been observed by several authors of recent reports studying differences^{26,30,37} between the continuum³⁶ and DSMC methods^{26,27,28,30,37}. By including an extra expansion region beyond the exit plane and setting the boundary conditions to supersonic flow, it is the hope that the use of the INCA continuum model can more correctly simulate the results of the DSMC method.

One question to be raised is at what point the flow will recognize the expansion region and begin to accelerate towards the nozzle lip. One method suggested by Prof Robert Breidenthal¹⁰⁸ considers the case that the exit / ambient pressures are matched at the nozzle exit. In this case, a pressure gradient would not induce expansion of the boundary layer towards the nozzle lip. If the flow were sufficiently rarefied, the mean free path would continue to increase towards the nozzle exit. In the molecular reference frame, collisions with the wall that create the no-slip condition and set up the velocity gradient essential for boundary layer development would cease to exist approximately one mean free path upstream of the nozzle. From this point, molecules that would normally hit the wall would actually accelerate pass the nozzle lip into the exit region beyond the nozzle. Since in our case we are only considering the case of vacuum ambient conditions, this hypothesis will be left for later study. For our case, one study²⁷ recently reported that for a nozzle geometry of aspect ratio of 1, throat diameter of 308 μm , and 7.1 expansion ratio, the “effect of vacuum conditions extends 20 μm inside the nozzle, which corresponds to 10-15 local mean free paths [2 μm] in the vicinity of the nozzle lip”. Therefore, it seems that for vacuum conditions the effect of the pressure gradient on the expansion of the gases extends much further upstream of the nozzle than would be expected for a mean-free-path explanation.

11.3 Other Rarefied Effects

Although we hope to stay within the limits of the continuum assumption with this study, further analysis would require investigation into the following variables. The DSMC method which focus on low-density flows takes into account the difference in both translational and vibrational modes within the gas. The continuum model on the other hand assumes the translational and vibrational modes to be in equilibrium with one another. Therefore, as the gas expands the temperature uniformly decreases in the continuum model. In comparison, the DSMC method even though the translational temperature decreases, the vibrational mode more slowly adapts to the expansion. The result is a decrease in expected Isp because of retained energy within the vibrational mode.

Another area of interest is the expected absence of the no-slip condition. This is the result of decreased collisions with the wall. Particles that collide with the wall retain a certain amount of energy and direction associated with the initial condition. This is modeled with a gas-surface interaction model which differentiates between specular and diffuse reflection (retains same incident energy and direction versus an inelastic collision with the wall). The main variable in numerical modeling is an accommodation coefficient ranging from 0 (diffusive) to 1 (specular). Investigation into these parameters will not be made in this study as a no-slip condition has been imposed. Further research should reference papers in the bibliography associated with DSMC modeling.

Chapter 12: Introduction to Aspect Ratio Analysis

Bayt *et al*⁴⁷ performed numerical and experimental analysis on a variety of micronozzles. The results of his analysis correspond in some degree to the analysis to be performed in reference to the aspect ratio. His work is the only one the author is aware of that is applied to nozzles of aspect ratios greater than one. For a constant thrust level, he reported values for three separate expansion ratios at different aspect ratios. The results indicated that an expansion ratio of 16.9 (aspect ratio of 8.2) outperformed an expansion ratio of 15.3 (aspect ratio of 17.1). This was the case until a thrust level of 2 mN where he claims the aspect ratio of 17.1 (expansion ratio = 15.3)

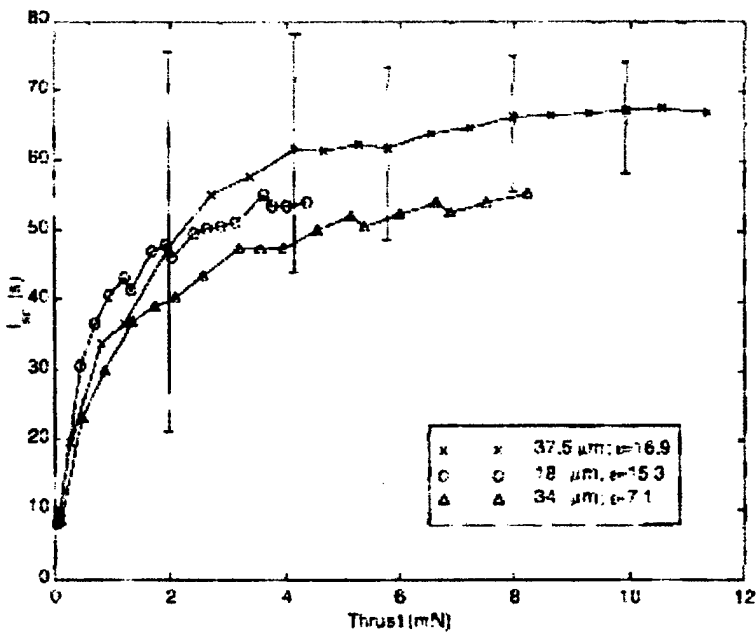


Figure 12-1. Results of Expansion Ratio/Aspect Ratio for Low Thrust Numbers⁴⁷

outperformed an aspect ratio of 8.2 (expansion ratio = 16.9) because the endwall boundary layer effects were more pronounced in the 8.2 case. The conclusions of this result are somewhat vague based on the variation of two parameters (expansion ratio and aspect ratio).

The goal of this portion of the thesis is to design for two separate thrust levels, then using different aspect ratios determine which aspect ratio (1, 5, 10 or 15) will produce better

efficiencies. Particular attention is given to the value of the Reynolds number throughout the nozzle and its correlation to performance.

The throat diameter necessary to achieve a desired thrust is given by the following equations:

$$\begin{aligned}
 F &= A_e (\rho V^2 + P) \\
 A_e &= \varepsilon A_t \\
 A_t &= D_t^2 R_t \\
 \therefore D_t &= \sqrt{\left(\frac{F}{R_t \varepsilon (\rho V^2 + P)} \right)}
 \end{aligned} \tag{12-1}$$

F = thrust (N)

ρ = density (kg/m^3)

U = velocity (m/s)

P = pressure (N/m^2)

A_e = exit area (m^2)

ε = expansion ratio

A_t = throat area (m^2)

D_t = throat width (m)

R_t = aspect ratio (throat height / throat width)

Using the derived equation (12-1) together with the output data of the CEA chemical kinetics code¹³³, the following throat diameters are calculated at a chamber temperature of 3033 K.

Table 12-1. Throat diameters for thrust level = 125 mN at expansion ratio = 10

Aspect Ratio	Throat Diameter (um)	Re throat	Re exit
1	156.4	3159	552
5	70.0	1413	1233
10	49.5	999	1754
15	40.4	816	1424
Conical	176.5	3564	1968

Table 12-2. Throat diameters for thrust level = 10 mN at expansion ratio = 10

Aspect Ratio	Throat Diameter (um)	Re throat	Re exit
1	44.2	893	156
5	19.8	400	349
10	14.0	283	493
15	114.2	231	403
Conical	49.9	1008	557

Reynolds numbers are graphically represented in figure 12-2 and 12-3 from the throat to the exit based on the physical conditions above.

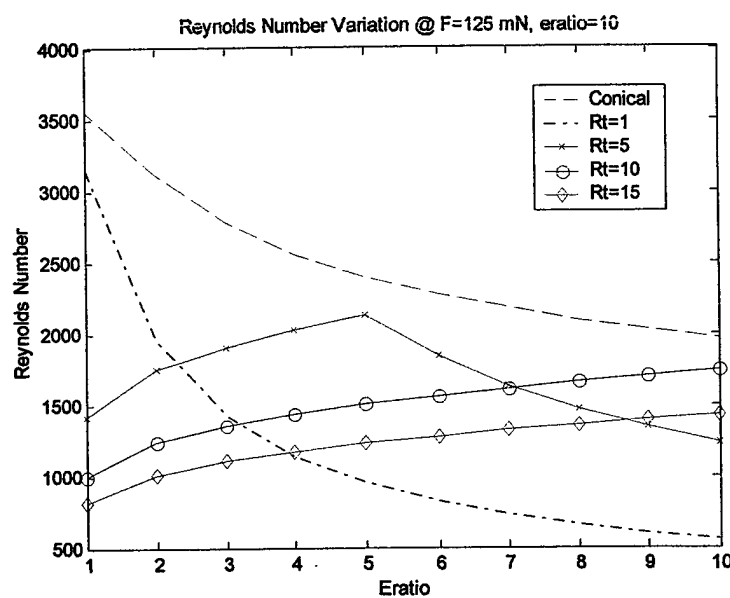


Figure 12-2. Comparison of Aspect Ratio on Reynolds Number for F=125mN

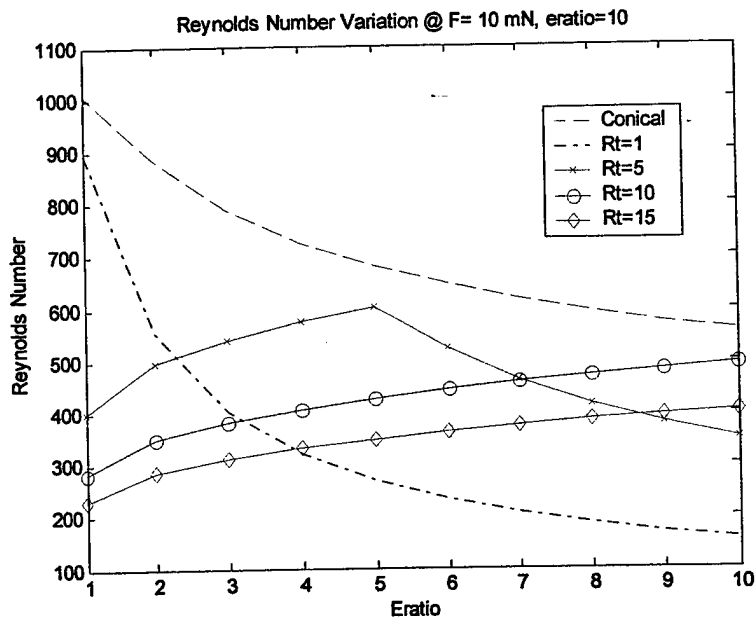


Figure 12-3. Comparison of Aspect Ratio on Reynolds Number for $F=10\text{mN}$

As seen above, the Reynolds number immediately begins a drastic decrease after the throat for an aspect ratio of 1, thereby signifying an immediate increase of the viscous effects compared to the inertial effects of the gas. For the higher aspect ratio of 10, the Reynolds number continues to increase until it reaches the expansion ratio equal to the aspect ratio. An aspect ratio of 5 exemplifies that once the limiting characteristic becomes the constant distance between the endwalls, the Reynolds number begins to decrease. We witness the same trend for an aspect ratio of 10 if we use an expansion ratio of 15.

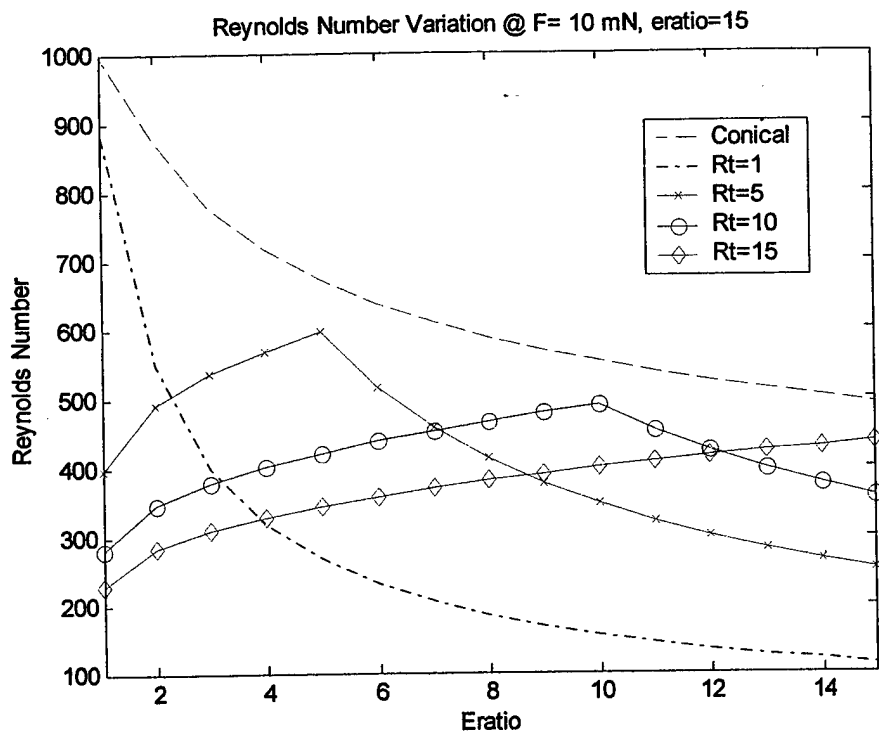


Figure 12-4. Effects of Further Expansion Ratio on Reynolds Number

Larger expansion ratios for the same thrust level decrease the throat diameter under ideal conditions because of expected further expansion of the gases. This serves to decrease the Reynolds number at the throat regardless of aspect ratio. From the previous analysis, for aspect ratios greater than one the Reynolds number is expected to increase until the nozzle height is equal to the width, from which point it will decrease. This raises an interesting question of which nozzle has the greater efficiency. For an expansion ratio of 10, an aspect ratio of one begins with a higher Reynolds numbers at the throat then immediately decreases to a smaller Reynolds number than the aspect ratio of 10 begins with. An aspect ratio of 5 ends with only a slightly smaller Reynolds number than it began with due to the increase / decrease trend. An aspect ratio of 15 starts even lower than for an aspect ratio of 10, but experiences the same increase in Reynolds number. We will perform analyses on these cases to determine which design is optimum.

In order to understand what is happening, the following graphs starting with figure 12-5 indicate the effect of each variable on the overall Reynolds number:

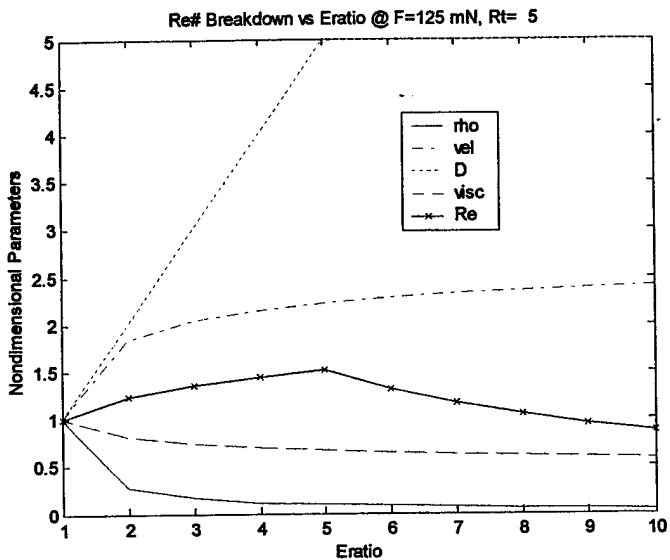


Figure 12-5. Reynolds Number Variable Breakdown @ Rt = 5, Eratio = 10

In this case, since the distance between the endwalls is greater than the increasing distance between the sidewalls, the product of this value with the increasing velocity and decreasing viscosity outweighs the decrease in density. The opposite is seen for the case of the aspect ratio equal to 1. Unlike the higher aspect ratio, the limiting physical dimension is the distance between the endwalls, therefore the characteristic dimension remains constant. Now, at a constant characteristic dimension, the increasing velocity and decreasing viscosity do not outweigh the decrease in density. Therefore, the overall Reynolds number immediately begins to decrease.

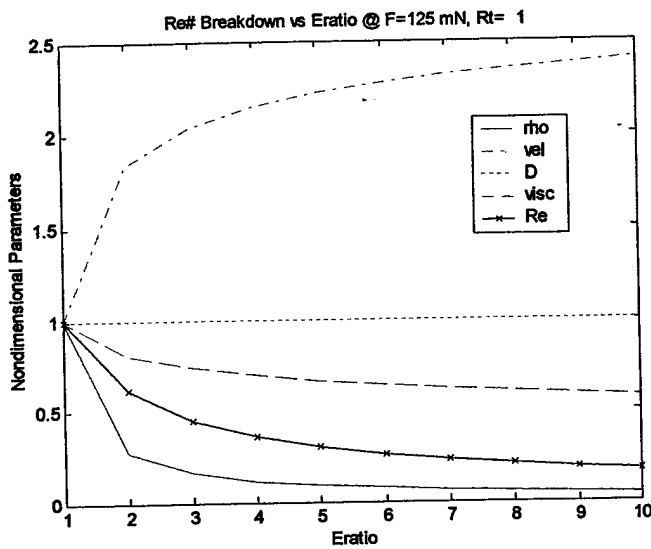


Figure 12-6. Reynolds Number Variable Breakdown @ Rt = 1, Eratio = 10

Due to the limit of the continuum flow model used by INCA, it is necessary to stay below the Knudsen number limit of 0.01. Using the CEA code as a basis, the following table depicts the lowest expected thrust level that can be modeled with INCA.

Table 12-3. Limit of Continuum INCA Code

Tc (K)	F (mN)	Dt (um)	Re (throat/exit)
Rt = 1			
1000	3.81	27.5	2281/586
1500	9.1	42.3	2006/435
2000	16.8	57.2	1864/356
2500	27.6	73.3	1823/323
3000	40.7	89.3	1822/318
Rt = 5			
1000	0.76	5.5	458/586
1500	1.82	8.5	401/435
2000	3.36	11.4	373/356
2500	5.52	14.7	365/323
3000	8.14	17.9	364/318
Rt = 10			
1000	0.38	2.7	229/586
1500	0.90	4.2	199/433
2000	1.68	5.7	186/356
2500	2.76	7.3	182/323
3000	4.06	8.9	182/317
Rt = 15			
1000	0.57	2.7	229/586
1500	1.37	4.2	201/436
2000	2.51	5.7	186/355
2500	4.11	7.3	181/321
3000	6.11	8.9	182/318

An example of the above analysis is given in figure 12-7 for the limiting thrust level of 40.7 mN for a chamber temperature of 3000 K and aspect ratio = 1.

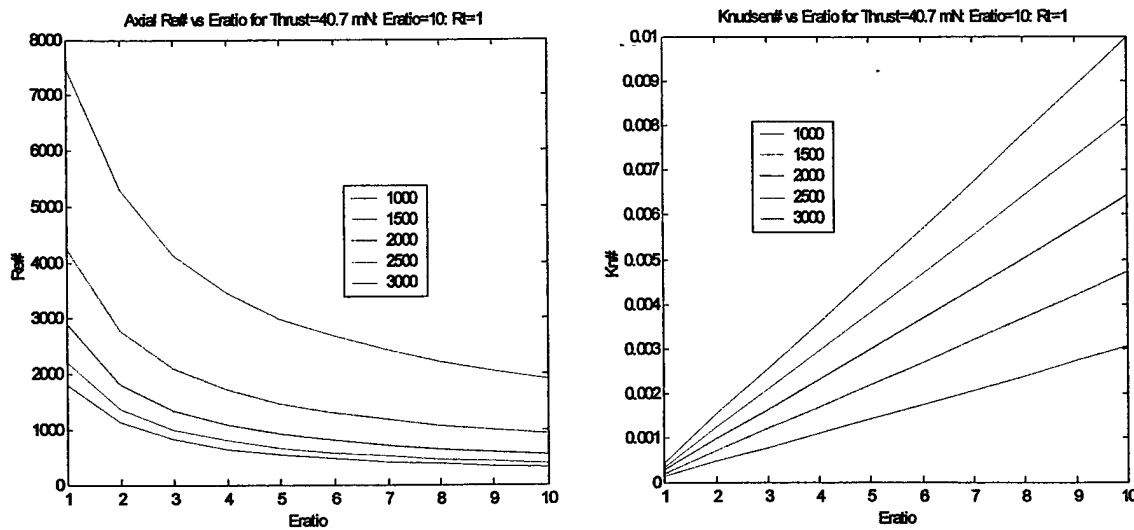


Figure 12-7. Reynolds/Knudsen Number vs Eratio

The following test cases of table 12-4 will be analyzed to determine which aspect ratio produces the greatest efficiency:

Table 12-4. Aspect Ratio Test Cases

id #	Design Thrust (mN)	Rt	Tc (K)	Throat Diameter (μm)	Re - ideal throat/exit	Ideal Thrust (mN)	Ideal Isp (sec)
118	501	10	3000	99.05	2021/3523	500.69	282.1
152	501	5	3000	138.4	2825/2631	489.27	282.1
149	501	1	3000	309.4	6315/1101	489.04	282.1
155	501	10	2500	98.7	2457/2262	500.95	262.4
156	501	5	2500	139.6	3474/3173	501.08	262.4
157	501	1	2500	312.1	7768/7081	500.91	262.4
158	501	10	2000	98.7	3217/2907	500.49	236.6
159	501	5	2000	139.6	4550/4096	500.62	236.6
160	501	1	2000	312.2	10176/1944	500.76	236.6
115	31	10	3000	24.76	505/881	31.32	282.1
169	31	5	3000	34.84	711/620	31.01	282.1
162	31	1	3000	77.9	1590/277	31.00	282.1
163	31	10	2500	24.6	432/765	31.01	262.4
164	31	5	2500	34.73	864/765	31.01	262.4
165	31	1	2500	77.64	1933/342	31.01	262.4
166	31	10	2000	24.56	801/1530	30.99	236.6
167	31	5	2000	34.73	1132/1025	30.98	236.6
168	31	1	2000	77.65	2531/2288	30.98	236.6

** Note, the design thrust is different than the ideal thrust in some cases because the throat diameter was computed for $T_c = 3032, 2492, 2076$ K instead of the exact value of 3000, 2500, 2000.

In comparison with axisymmetric nozzles, we take into consideration the surface area/volume ratio. As this value increases, the viscous effects will dominate the expansion of gases in a given volume. Reference back to figure 9-6.

Note that even for an aspect ratio of 1, the surface area/volume ratio is still greater at small expansion ratios and for a greater aspect ratio the axisymmetric is always greater up to an expansion ratio of 10. Looking again at our case of 125 mN, modeling the Reynolds number of the axisymmetric nozzle in an immediate decrease of the Reynolds number, although the decrease is not as drastic as an aspect ratio of 1.

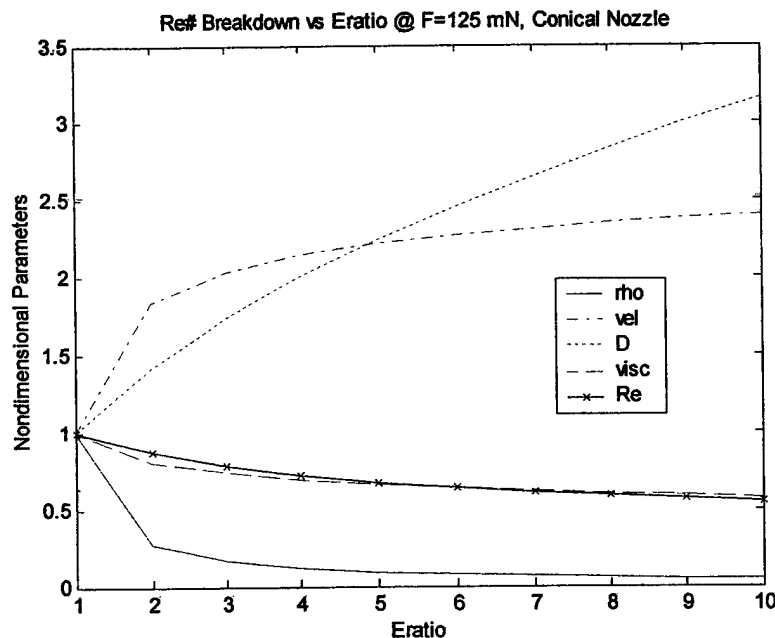


Figure 12-8. Axisymmetric Reynolds Number

Application of axisymmetric nozzles for low thrust applications is not nearly feasible as the use of MEMS nozzles, although investigation into the comparison of efficiencies would be of particular interest. The research of this project focuses primarily on the effect of the aspect ratio in 3D block nozzles.

Chapter 13: High-Temperature Effects

As we have already shown, by increasing temperature the efficiency of the exhaust products (figure 8-5), measured by Isp, increases:

In addition to an increase in Isp with an increase in temperature, the viscous effects also increase. Let's look more closely at the viscosity coefficient also increases due to its dependence upon temperature. According to Chapman and Cowling, low-density gases take have the relation of equation (13-1) to viscosity³³. Figure 13-1 graphically depicts the viscosity as a function of temperature from the output of the CEA code¹³³.

$$\mu = \frac{2.68E - 6\sqrt{MT}}{\sigma^2 \Omega_v} \quad (13-1)$$

σ = collision diameter, A°

M = molecular weight of gas

μ = viscosity (kg/m-s)

Ω_v = collision frequency (equal to unity for noninteraction)

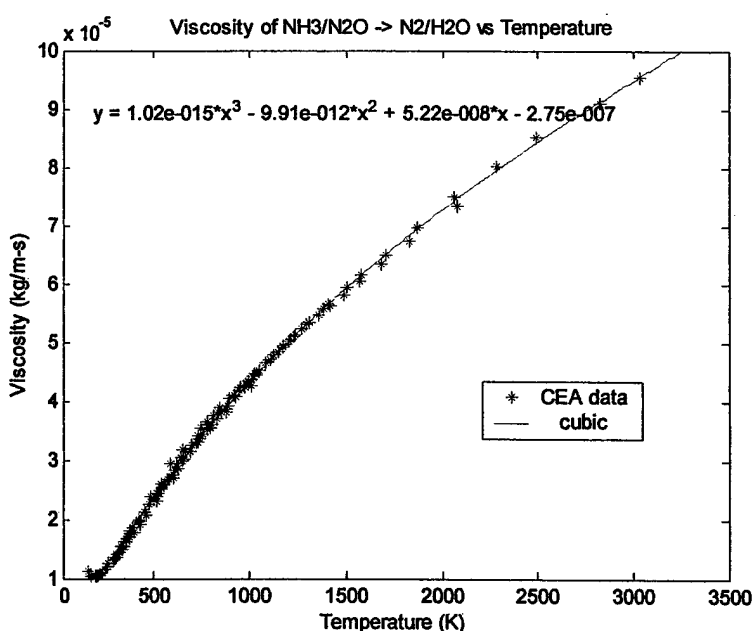


Figure 13-1. Viscosity Variation With Increased Temperature

We thus have an increase in efficiency with Isp and a suspected increase in viscous losses due to an increase in viscosity. The problem in question is whether or not the increased viscous

losses will outweigh the increased gain in Isp due to the temperature increase. In order to resolve this we perform the following analysis.

When designing for a specific mission, it is necessary to look at the thrust levels required. Based on the chamber pressure and temperature (along with already chosen value of expansion ratio) we calculate the necessary throat diameter. The data for these calculations was obtained from the CEA chemical kinetics code¹³³. By varying the amount of water combined with nitrous oxide and ammonia it is possible to reduce the adiabatic flame temperature of the reacting system. Figure 13-2 is an estimate of weight percentage for each component in order to obtain the desired chamber temperature. Exact tabulated values can be found in table 15-5.

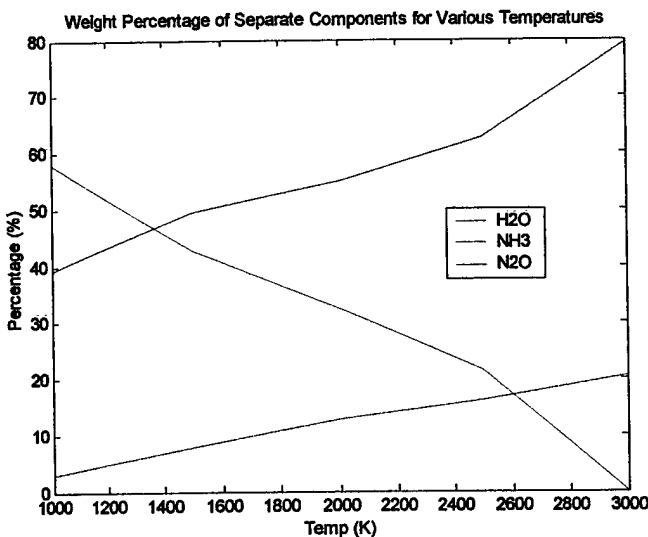


Figure 13-2. Weight Percentage of Products (H₂O/NH₃/N₂O)

With the output data, it is then possible to compute the throat diameters necessary given the expansion/aspect ratio of a given nozzle.

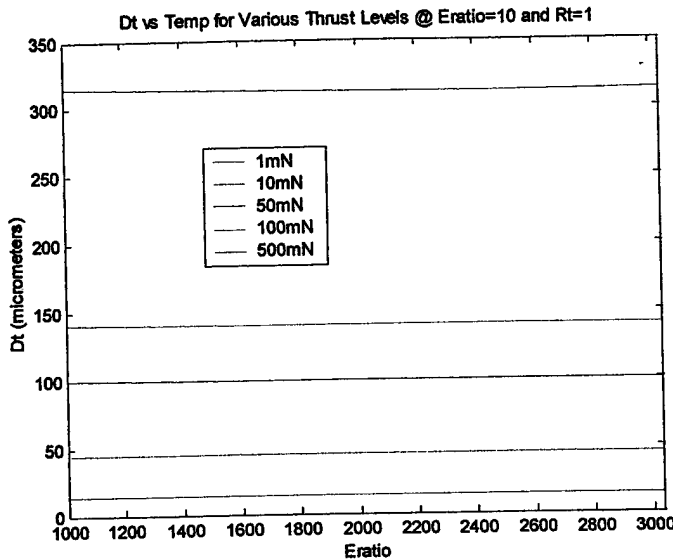


Figure 13-3. Throat Diameters for Various Thrust Levels

With the throat diameters, density, viscosity and sonic velocity at the throat we compute the values of Reynolds numbers at the throat as in figure 8-11. These dimensionless values will be the basis for the computation of Isp/thrust efficiency.

For the thrust levels indicated above, we will now investigate the value of the Reynolds and Knudsen numbers along the axial direction of the nozzle. As previously mentioned, the Knudsen number is another dimensionless parameter which quantifies the degree of gas rarefaction in the flow. Due to the restricted use of a continuum model employed by INCA, rarefied gas effects are not captured by the continuum method. When the Knudsen number is greater than 0.01, the gas enters the regime where accurate modeling by the particle kinetics code such as the direct simulation monte-carlo method is necessary. Therefore, using the following computations it is possible to determine which thrust levels we can accurately model using the continuum method.

Ideally, we would use this algorithm to analyze the efficiencies from micron to multi-newton thrust levels. Yet, as already discussed, the Navier-Stokes code we are using is restricted to only those fluid regimes where the continuum assumption is valid. These limits were set for the initial test runs are performed at aspect ratios of 1, 5, 10 and 15.

We will use the results of the aspect ratio analysis for evaluation of the high-temperature cases. The expansion ratio for this study is set at 10 in part to avoid problems with the loss of the

continuum assumption as the gas expands downstream. As already mentioned, further extension of the nozzle beyond where the expansion ratio equal the aspect ratio results in lower Reynolds number and an expected eventual decrease in efficiency.

Instead of focusing on the thrust level, we will design for Reynolds number. This will provide the thrust and Isp efficiencies as a function of Reynolds number. When designing for a mission, it will then be possible to solve with the physical dimensions of a required thrust to calculate the Reynolds number and expected efficiency at that thrust level.

Table 13-1 is a list of cases to be analyzed and assessed. For each case the thrust and Isp efficiency will be the desired output.

Table 13-1. Test Cases for High-Temperature Analysis

ID #	Tc (K)	Re	Dt (μm)	F (mN)	Isp (sec)	mdot (kg/s)
114	3032	250	12.38	7.3	283.3	2.818E-6
115	3032	500	24.76	31.3	283.3	1.127E-5
116	3032	1000	49.53	125.3	283.3	4.509E-5
117	3032	1500	74.29	281.9	283.3	1.015E-4
118	3032	2000	99.05	500.7	283.3	1.804E-4
119	2492	250	10.01	5.15	262.1	2.004E-6
120	2492	500	20.02	20.6	262.1	8.017E-6
121	2492	1000	40.05	82.5	262.1	3.207E-5
122	2492	1500	60.07	184.3	262.1	7.217E-5
123	2492	2000	80.09	330.0	262.1	1.283E-4
124	2062	250	7.94	3.24	239.3	1.381E-6
125	2062	500	15.88	12.97	239.3	5.524E-6
126	2062	1000	31.76	51.9	239.3	2.210E-5
127	2062	1500	47.65	116.7	239.3	4.971E-5
128	2062	2000	63.53	207.5	239.3	8.838E-5
129	1577	250	5.62	1.61	207.1	7.927E-7
130	1577	500	11.24	6.44	207.1	3.171E-6
131	1577	1000	22.47	25.77	207.1	1.268E-5
132	1577	1500	33.71	57.99	207.1	2.854E-5
133	1577	2000	44.94	103.09	207.1	5.073E-5
134	1008	250	3.03	0.465	164.4	2.881E-7
135	1008	500	6.07	1.86	164.4	1.153E-6
136	1008	1000	12.14	7.44	164.4	4.610E-6
137	1008	1500	18.21	16.73	164.4	1.037E-5
138	1008	2000	24.28	29.7	164.4	1.844E-5

** Note: Actual CFD runs are performed at exactly 3000K, 2500K, 2000K, 1500K, and 1000K. The temperatures above were used as an initial starting point for scaling parameters. The final data analysis will be done using the throat diameters above combined with output of the CEA code closer to 3000K, 2500K, 2000K, 1500K, and 1000K. This error was not recognized until late in the program, and although the differences are generally small, adjustments are nonetheless made for exact computation of the efficiencies.

Isp is strictly a function of initial chamber temperature and expansion ratio. Below are the ideal Isp values for the corrected chamber temperatures.

Table 13-2. Theoretical Isp Levels

Tc	Isp (sec)
1000	163.6
1500	202.3
2000	236.6
2500	262.4
3000	282.1

Chapter 14: Experimental Recommendation

Before continuing with the analysis of the 3D block nozzle described above, I would like to briefly mention an idea presented during analysis of these micronozzles. In the 1960s Rothe²⁹ used electron beam measurement techniques to measure the effects of boundary layers on small nozzle performance. By using the properties of gases, the electron beam technique obtained information on temperature and density (and thus pressure). This experimental data has been the basis of numerical method validation by many users of computational fluid dynamics in the research of micronozzles.

In a design similar to the method of Rothe, we thought of measuring the discharge coefficient (ratio of the actual mass flow rate / ideal mass flow rate) of a micronozzle. Using the CEA code¹³³ it is possible to obtain the Reynolds number and Knudsen number that would accurately describe the flow of the gas. Since it is not yet possible, and likewise dangerous, to produce the chemical products and temperatures for the gases under consideration, it was thought to use an inert gas and scale up the physical size of the micronozzle while keeping the Reynolds and Knudsen numbers constant, thereby correctly modeling the viscous effects of the micronozzle. This ‘macrosystem’ would then be inserted in a vacuum tank and fired until the pressure in the tank reached a pressure level similar to what would ideally be expected at the exit of the nozzle.

I wrote a computer algorithm that used the physical properties of several inert gases to obtain a suitable match for the CEA output of the gases under consideration. The following is a sample of results to model a throat Reynolds number of 1000 and Knudsen number of 0.0008 obtained from the algorithm of Appendix C.

Table 14-1. Test Cases for Experimental Recommendation of Mass Flow

Micronozzle $P_c = 20$ bar, $Re_{exact} = 949$, $Kn_{exact} = 0.00079914$
 1:Air 2:CO₂ 3:CO 4:He 5:H₂ 6:O₂ 7:N₂

Gas	Dt (m)	P_c (Pa)	Tc (K)	Rho (km/m ³)	Re_t	Kn_t
2	0.0005	10000	300	0.11183	965.06	0.0021481
3	0.0005	20000	400	0.10674	911.37	0.0014321
4	0.0005	60000	300	0.030498	924.33	0.00035802
4	0.0005	90000	400	0.034311	983.32	0.00031824
5	0.0005	40000	400	0.015249	981.5	0.00071603
7	0.0005	20000	400	0.10674	901.45	0.0014321
3	0.001	10000	400	0.053372	911.37	0.0014321
4	0.001	30000	300	0.015249	924.33	0.00035802
5	0.001	20000	400	0.0076246	981.5	0.00071603
7	0.001	10000	400	0.053372	901.45	0.0014321
4	0.0015	20000	300	0.010166	924.33	0.00035802
4	0.0015	30000	400	0.011437	983.32	0.00031824
5	0.002	10000	400	0.0038123	981.5	0.00071603
4	0.003	10000	300	0.005083	924.33	0.00035802
4	0.0045	10000	400	0.0038123	983.32	0.00031824

1:Air 2:CO₂ 3:CO 4:He 5:H₂ 6:O₂ 7:N₂

Gas	Dt (m)	P_c	Tc	Pe	mdot	Pdot	time
2	0.0005	10000	300	30.526	5.6468e-006	0.14565	209.58
3	0.0005	20000	400	61.051	7.8021e-006	0.31624	193.05
4	0.0005	60000	300	183.15	7.2234e-006	4.099	44.683
4	0.0005	90000	400	274.73	9.3834e-006	5.3247	51.595
5	0.0005	40000	400	122.1	4.1704e-006	2.3665	51.595
7	0.0005	20000	400	61.051	7.8021e-006	0.31624	193.05
3	0.001	10000	400	30.526	1.5604e-005	0.63248	48.263
4	0.001	30000	300	91.577	1.4447e-005	8.1979	11.171
5	0.001	20000	400	61.051	8.3408e-006	4.7331	12.899
7	0.001	10000	400	30.526	1.5604e-005	0.63248	48.263
4	0.0015	20000	300	61.051	2.167e-005	12.297	4.9648
4	0.0015	30000	400	91.577	2.815e-005	15.974	5.7328
5	0.002	10000	400	30.526	1.6682e-005	9.4662	3.2247
4	0.003	10000	300	30.526	4.334e-005	24.594	1.2412
4	0.0045	10000	400	30.526	8.4451e-005	47.922	0.63698

- D_t = throat diameter, T_c = chamber temperature, P_c/Pe = chamber/exit pressure, ρ = density
 $Mdot$ = mass flux, $Pdot$ = pressure increase

The time here represents the time it would take for the pressure in the experimental chamber to equal the pressure at the exit plane of the nozzle for ideal conditions. By computing the actual time for this to occur it is possible to compute the mass flow rate and thereby the

effects of viscosity on the discharge coefficient (ratio of actual/ideal mass flow rate). While this would not provide enough information to ascertain the effects of thrust/Isp efficiency, it would provide a basis for verifying a numerical code and provide a source of verification of the Rothe experiment.

Due to time constraints, research focused on numerical methods to estimate expected efficiencies.

Chapter 15: Numerical Method Modeling

Classically, the verification of an engineering system hinges on the qualification of experimental results. For the system under consideration it is difficult to obtain experimental data given the small scale of the physical parameters. In the past decade, significant advancements have been made in the area of numerical modeling. In general, this process uses numerical methods to converge to a desired solution by defining initial and boundary conditions for a physical geometry and mesh. This is a powerful tool especially for the case where we do not have the ability to perform complicated experiments. While intensive research is being made to qualify these methods, they are extremely case sensitive and particular attention must be given to the variables effecting the algorithm in order to ensure that the converged solution correctly models the physical phenomena.

The verification of numerical modeling is a difficult part of such analyses. Ideally, we would compare experimental data with the numerical results. Due to the small physical scale, little experimentation has been performed on MEMS nozzles. In particular, no experimental evidence is available for aspect ratio studies. A recent study produced by Reed et al⁷ analyzed aspect ratios less than 1 at various throat diameters for chamber conditions of 300 K. Yet, in order to model for specific thrust levels and various missions, it is necessary to gain a substantial database from which to choose the most efficient operating conditions. In addition to experimental data, it is possible to compare results from similar numerical modeling efforts. Once again, there is a lack of sufficient results at the physical geometries in question to validate the code. To the authors knowledge, no numerical work has been done at temperatures greater than 2000 K, and experiments have focused on cold gas flows of ~300 K.

Therefore, with lack of extensive experimental/numerical data, it is necessary to move to a numerical validation. This is done by validating first and second order schemes of the same physical geometry. In theory, for the same physical geometry, the accuracy of a 1st and 2nd order scheme should increase as the grid of the 1st order scheme is increased. If there are inconsistencies in the boundary conditions or grid setup, the solutions will not agree with one another and the result is not to be trusted.

Once the 1st and 2nd order schemes have converged, it is then necessary to do a grid refinement study of the 2nd order scheme. There exists a mesh density beyond which increasing

the mesh density will not produce a sufficient difference in successive results. The 2nd order scheme will produce more accurate results with a coarser mesh, therefore requiring less computational time and effort. In addition, for 2nd order modeling is necessary to capture viscous effects as 1st order adds additional numerical dissipation to the viscous terms.

Amtec Engineering has developed a commercially available CFD code known as INCA¹⁰⁹. It is a finite volume code that can model a variety of different flow problems. Specifics of using INCA will be discussed later on.

Along with INCA is a companion grid generator known as GRIDALL. For the purposes of this program, this grid generator is utilized to develop a model of the micronozzles in question. Once the grid is established the coordinates of all cells are then transported into INCA and the convergent process begins.

15.1 Grid Setup (IMESH file)

In order to reduce computational time, it is possible to use lines of symmetry within CFD code. For instance, 3D block micronozzles have a rectangular cross-section, therefore they have 2 lines of symmetry. This method was utilized in a recent paper by Ivanov *et al*²⁷. It is possible to analyze 2D micronozzles with one line of symmetry, but the current study is concerned with the effects of the endwall boundary layer and for accurate prediction of overall thrust it is necessary to model the endwall effects.

Figure 15-1 is a graphical representation of the lines of symmetry and physical depiction of the micronozzle. The shaded area will be modeled through numerical simulations. The overall thrust is then calculated by multiplying the thrust of the quarter area by four. The Isp is a weighted factor between thrust and mass flow rate, therefore this region is sufficient by itself to compute Isp.

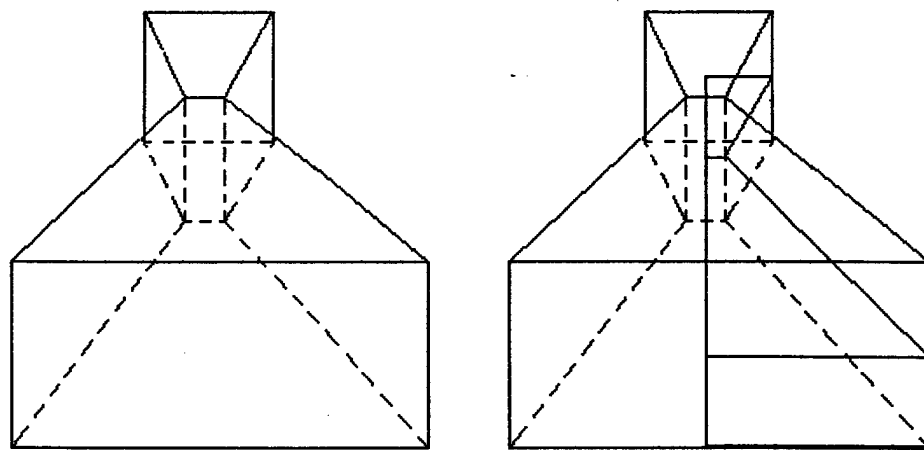


Figure 15-1. Graphic of Full Nozzle and $\frac{1}{4}$ Nozzle to be Analyzed

The next step is setting up a grid in the GRIDALL program. GRIDALL requires the input of each point, a definition of each line using those points, a definition of each surface using the lines, and then a definition of each zone using the surfaces. The input values for GRIDALL are in meters, therefore a scale factor is also available to size the physical dimensions to whatever size desired.

The following figures represent the points, lines, surfaces and zones of the micronozzle to be studied:

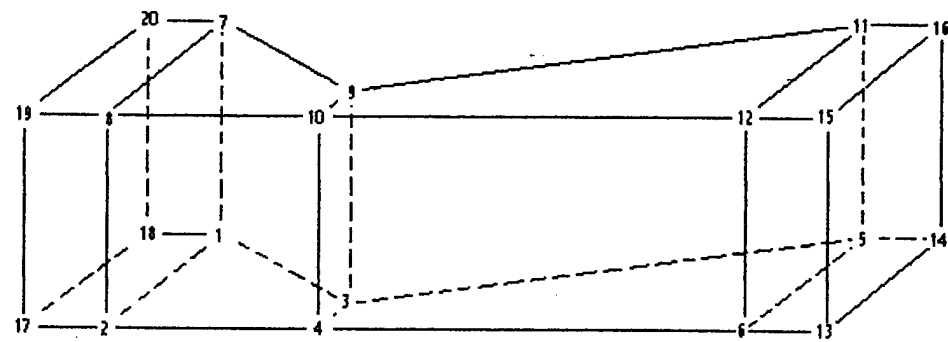


Figure 15-2. Points @ Junctions Used in Generating the Grid

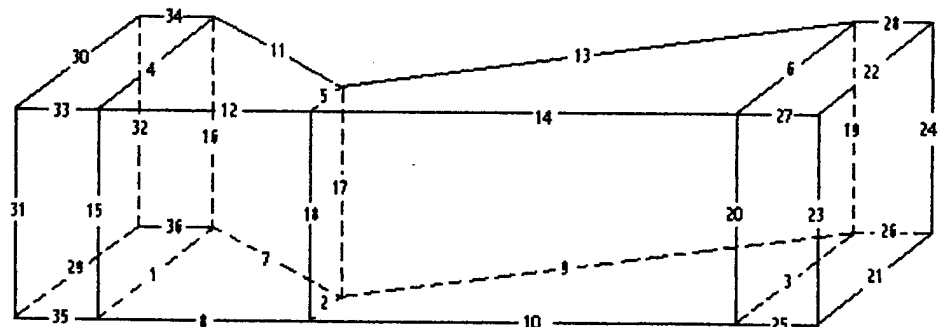


Figure 15-3. Line Numbers Used in Generating the Grid

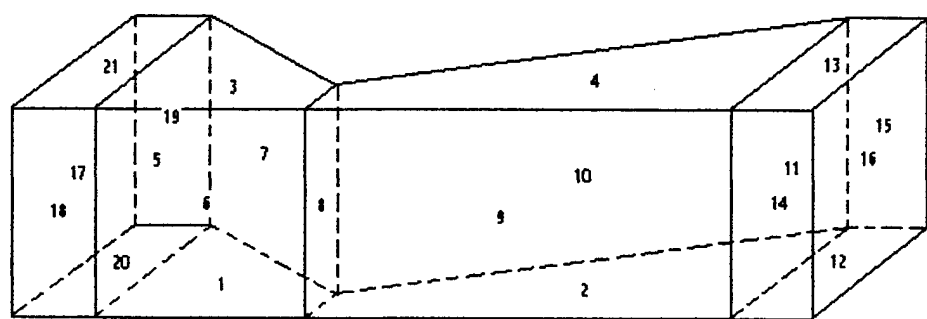


Figure 15-4. Surface Numbers Used in Generating the Grid

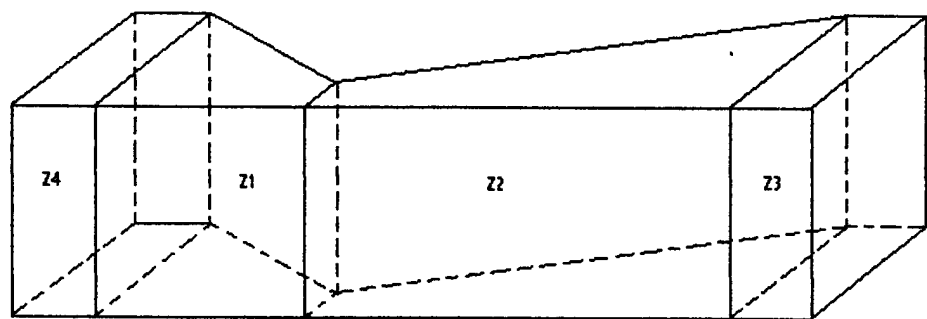


Figure 15-5. Zone Numbers Used in Generating the Grid

Each line is designated with a finite number of points. These points can be distributed evenly across the line, or they can be logarithmically weighted to one side. For this study, it is necessary to cluster grid points at the throat and along each of the walls (i.e., throat clustering along lines 2,5 ... endwall clustering along lines 15, 16, 17, 18, 19, 20, 23, 24, 31, 32 ... and sidewall clustering at 1, 2, 3, 21, 22, 29, 30). This is necessary to accurately capture the viscous effects across the wall. Whether or not the grid is close enough to the wall is determined by the y-plus value:

$$y_plus = \frac{y_normal * \sqrt{\frac{\tau}{\rho}}}{\nu} \quad (15-1)$$

y_normal = perpendicular spacing from nearest grid point to wall (m)

τ = shear stress (N/m^2)

ρ = density (kg/m^3)

ν = kinematic viscosity (m^2/s)

The grids currently analyzed were designed on a centimeter scale with the full throat width at 1 cm. In order to scale to micrometer dimensions, I used the scale factor of equation (15-2).

$$SF = \frac{X}{(0.5)(1E6)} \quad (15-2)$$

X = throat diameter (μm)

The following of table 15-1 and 15-2 are the grid coordinates in centimeters for a $\frac{1}{4}$ micronozzle section with expansion ratio of 10, aspect ratio of 10, throat diameter of 99 microns and expansion angle of 30 degrees:

Table 15-1. Grid Point Values

Points	x	y	z
1	5.5	1.5	0
2	5.5	0	0
3	6.60	0.25	0
4	6.60	0	0
5	10.497*	2.5*	0
6	10.497*	0	0
7	5.5	1.5	2.5**
8	5.5	0	2.5**
9	6.60	0.25	2.5**
10	6.60	0	2.5**
11	10.497*	2.5*	2.5**
12	10.497*	0	2.5**
13	11.5	0	0
14	11.5	2.5	0
15	11.5	0	2.5**
16	11.5	2.5	2.5**
17	4.5	0	0
18	4.5	1.5	0
19	4.5	0	2.5**
20	4.5	1.5	2.5**

* These numbers are changed to vary the expansion angle and expansion ratio.
 - pts 13 – 16 must also be changed for the exit region.

** These numbers vary the aspect ratio based on a half throat width of 0.25 (thus
 the current aspect ratio is 10 because half of the physical height is divided by
 half of the throat width, i.e. pt $7z/3y$). Using trigonometry, the algorithm found
 in Appendix D computes the x and y coordinates for various expansion ratios
 and angles. Below is a sample output:

Table 15-2. Grid Point Values for Different Expansion Ratios and Divergence Half-Angles

Eratio	Angle	x	y
3	20	7.9737	0.75
3	30	7.466	0.75
5	20	9.3475	1.25
5	30	8.3321	1.25
10	20	12.782	2.5
10	30	10.497	2.5
15	20	16.216	3.75
15	30	12.662	3.75
20	20	19.651	5
20	30	14.827	5
25	20	23.085	6.25
25	30	16.992	6.25
50	20	40.257	12.5
50	30	27.818	12.5
100	20	74.6	25
100	30	49.468	25

After specifying the number of points and distribution along each line, it is necessary to specify the surface and zones using these lines. Appendix E contains a complete setup for the following micronozzle. The physical geometry is an aspect ratio of 10, expansion ratio of 10, divergence half angle of 30 degrees, and throat diameter of 99 micrometers. Based on the chemical kinetics code, these dimensions should produce a Reynolds number of 2000 at the throat for a chamber temperature of 3000 K. At the given expansion ratio, the resulting thrust is expected to be 500 mN. This particular micronozzle has the following number of points: in the axial direction beginning with zone 1 30/100/4/5, along the endwalls 25 and the sidewalls 30. Hereafter the number of points in the mesh will be listed as '30/100/4/5 25/30'.

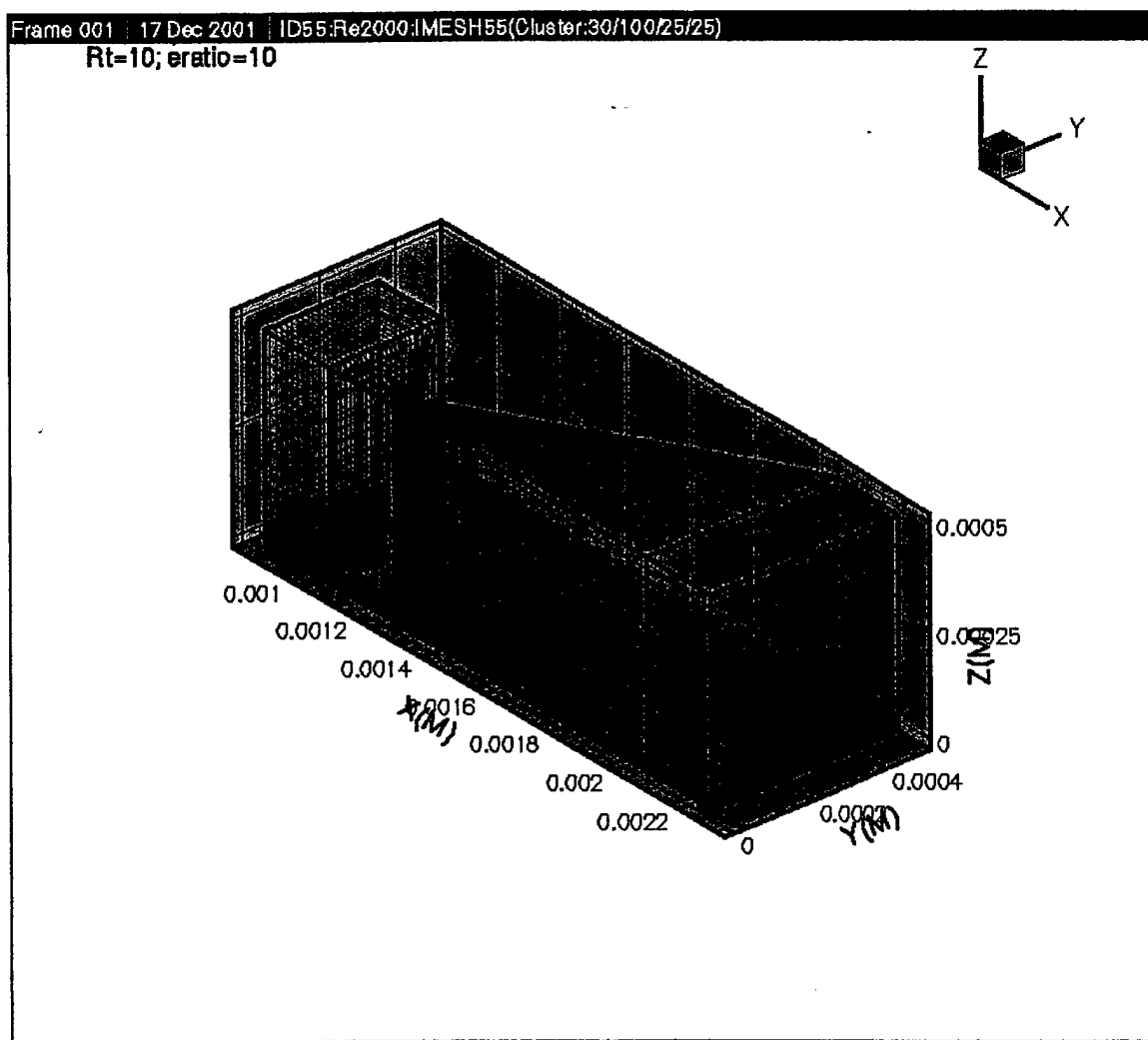


Figure 15-6. 3D Micronozzle Mesh

By zooming in at the throat we can see the clustering at the throat from the convergent/divergent sections and along the sidewalls:

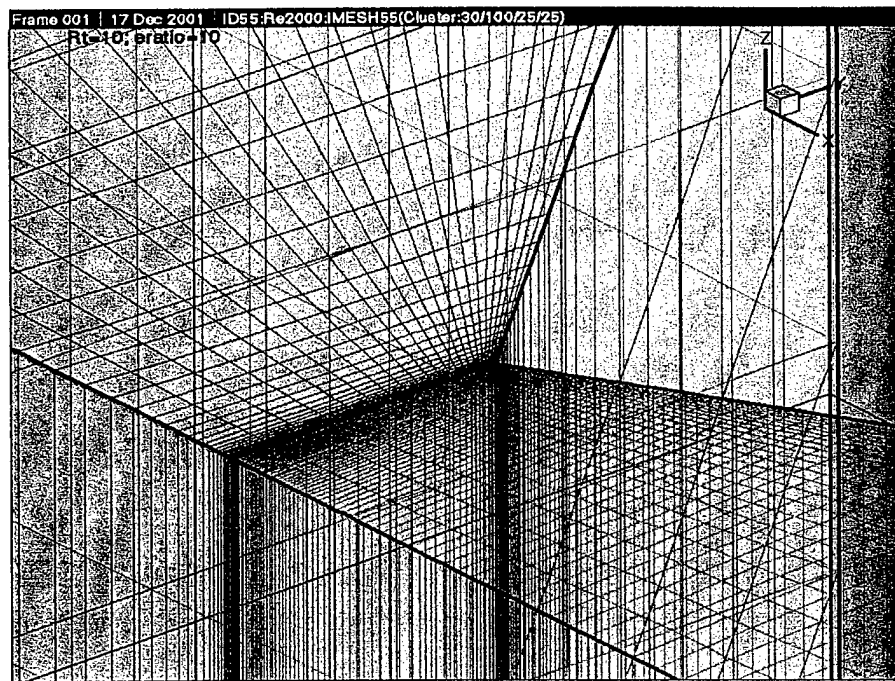


Figure 15-7. Grid Clustering at Throat/Sidewalls

This graphic depicts clustering along the endwalls:

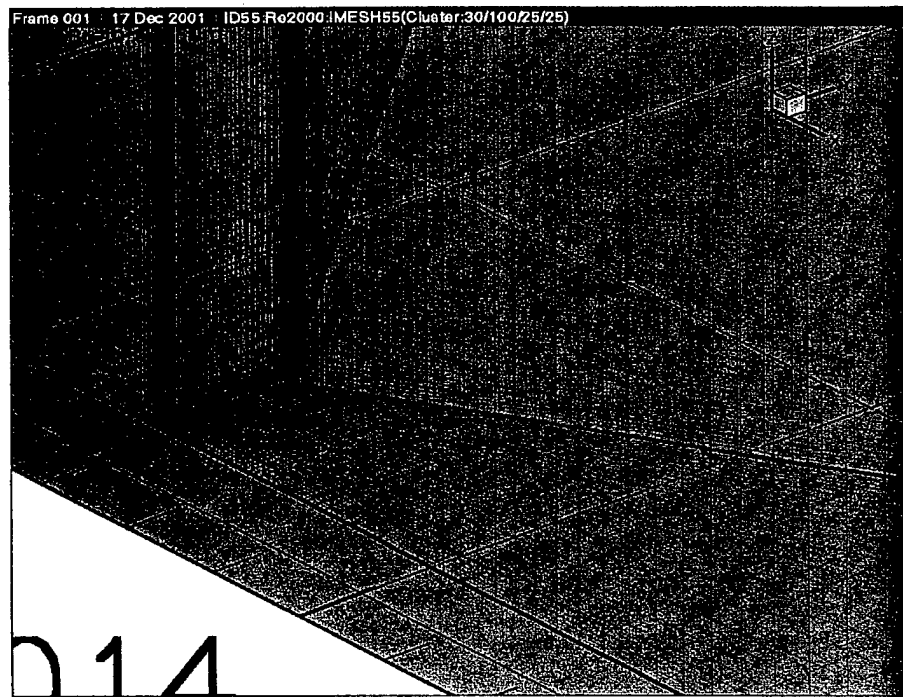


Figure 15-8. Grid Clustering at Endwalls

As mentioned previously, clustering is necessary at the walls and the throat to resolve strong gradients and properly capture the viscous effects. For 2nd order accuracy, the CFD code will not converge with an evenly spaced grid. Clustering is necessary to ensure convergence.

15.2 Numerical Setup (*IDATA* file)

Having established the desired grid, the INCA code mandates definition of the initial conditions, boundary conditions, and numerical variables such as the CFL number and order of spatial difference discretization. The following section will step through each of these areas.

15.2.1 Initial Conditions

First step is the initial conditions. Since the predefined mesh file has 4 separate blocks or regimes, it is necessary to specify initial conditions for each of those blocks. The physics of the flow also varies from one block to another, therefore in order to ensure to convergence of the solution it is necessary to guess the initial conditions as close to a best guess of the final solution as possible. The following is the direct code for INCA initial conditions and a complete example input file can be found in Appendix H:

```

$ NSIC.UNIFORM.FLOW
LABEL      = 'ENTRANCE'
NUMBER.OF.BLOCKS = 1,
X.VELOCITY.COMP   = 100,
PRESSURE        = 30E5,
TEMPERATURE     = 3000,
SPECIES.MASS.FRACTIONS = .41 .59,
$ END

$ NSIC.UNIFORM.FLOW
LABEL      = 'CONVERGENCE'
NUMBER.OF.BLOCKS = 1,
X.VELOCITY.COMP   = 1000,
PRESSURE        = 20E5,
TEMPERATURE     = 2500,
SPECIES.MASS.FRACTIONS = .41 .59,
$ END

$ NSIC.UNIFORM.FLOW
LABEL      = 'DIVERGENCE'
NUMBER.OF.BLOCKS = 1,
X.VELOCITY.COMP   = 2000,

```

```

PRESSURE      = 10E4,
TEMPERATURE   = 1000,
SPECIES.MASS.FRACTIONS = .42 .56,
$ END

```

```

$ NSIC.UNIFORM.FLOW
LABEL = 'EXIT IC'
NUMBER.OF.BLOCKS = 1,
X.VELOCITY.COMP = 2000,
PRESSURE = 5E3,
TEMPERATURE = 1000,
SPECIES.MASS.FRACTIONS = .42 .56,
$ END

```

When changing from one case to another, it is possible to use the restart file from a previous run, thereby reducing total computational time required for each successive case. But, in varying the chamber temperature it is necessary to start from new initial conditions without a restart file. Other parameters such as the species mass fractions must also be varied. Below is a table of the initial conditions used for each case.

Table 15-3. Nozzle Initial Pressure Conditions

Region	Pressure (bar)
Chamber	30
Convergence	20
Divergence	0.1
Exit	0.05

Table 15-4. Initial Temperature/Species Conditions

Condition					
Chamber T	3000	2500	2000	1500	1000
Convergence T	2500	2000	1500	1000	750
Divergence T	1000	1000	750	500	500
Exit T	1000	500	500	250	250
Species H2O	0.41	0.575	0.655	0.70	0.775
Species N2	0.59	0.425	0.345	0.30	0.225

** Initial conditions for the species mass fractions were obtained from the CEA kinetics code by introducing water as a diluent. There are other competing species, but these two are the most prevalent. The values reported here were increased slightly from the CEA output file in order to obtain a total of unity for the two species combined.

15.2.2 Boundary Conditions

The next objective was the definition of the boundary conditions on each side of the four blocks. Although the mesh sizes were predefined in the mesh setup, INCA automatically attaches an additional two cells to each side of the block. These are known as boundary cells and as the name suggests, contain the information predefined in the INCA code.

As already mentioned, the INCA code allows for use of lines of symmetry. The quarter section of nozzle of figure 9-5 has two lines of symmetry and therefore each of the four blocks has two sides defined with symmetry as the boundary condition. The interconnecting faces between each of the four blocks exchange information with each respective neighboring block at the end of each time step. INCA allows for automatic setup of the interconnecting regions, or it is possible to do it manually. The information is automatically transferred between the regions, therefore it is not necessary to define the conditions of interconnecting faces.

This leaves us with the inflow condition of the chamber, outflow conditions of the exit region, and wall properties of the nozzle itself. The inflow conditions, while seemingly simple, were not stable for a small subsonic influx of gas. The INCA code crashed during the convergence process because of an outflux condition which occurred during convergence of the solution. Therefore, it was necessary to set up a mixed inflow/outflow condition at the chamber inlet. The outflow static pressure was set to the stagnation pressure of the chamber. Without sufficient momentum, the flow not only accelerated to the throat, but also in the negative direction. By providing sufficient momentum to the influx of gas, the final solutions did not contain a negative flow and the solution smoothly converged.

The exit region ideally needs to model what would happen in a vacuum to underexpanded gases. Since we are using a small expansion ratio, there will be a sufficiently large pressure gradient at the exit plane of the nozzle. Previously I referred to work³⁰ that modeled the outflow with extrapolated boundary conditions into the divergent section of the nozzle and a kinetic approach (DSMC) that expanded into a vacuum. The kinetic modeling showed an expansion of gases towards the lip of the nozzle. The gases expanded in such a manner that the developing subsonic region of viscous flow never reaches the exit plane. Because of the parabolic nature of subsonic flow, it can ‘see’ downstream enough to recognize that a vacuum is approaching, therefore it will accelerate to supersonic speeds exiting the nozzle. This reasoning validated the use of simple supersonic boundary conditions at each of the exit regions (with exception to the

two sides of symmetry). As will be shown later, the subsonic viscous region does not entirely accelerate to mach one before exiting the nozzle, but unlike the extrapolated results, the use of supersonic boundary conditions more closely models and acceleration of the boundary layer to the exit. Below is a preview of the results that were seen throughout the computational process. Note that at the nozzle lip the flow begins to accelerate to supersonic speeds, although there is a thin passage of exiting subsonic flow at both the endwall and sidewall lip. According to Dr. Eberhardt, this is a result of the extrapolation of the supersonic boundary condition from the supersonic boundary layer and assumed acceptable.

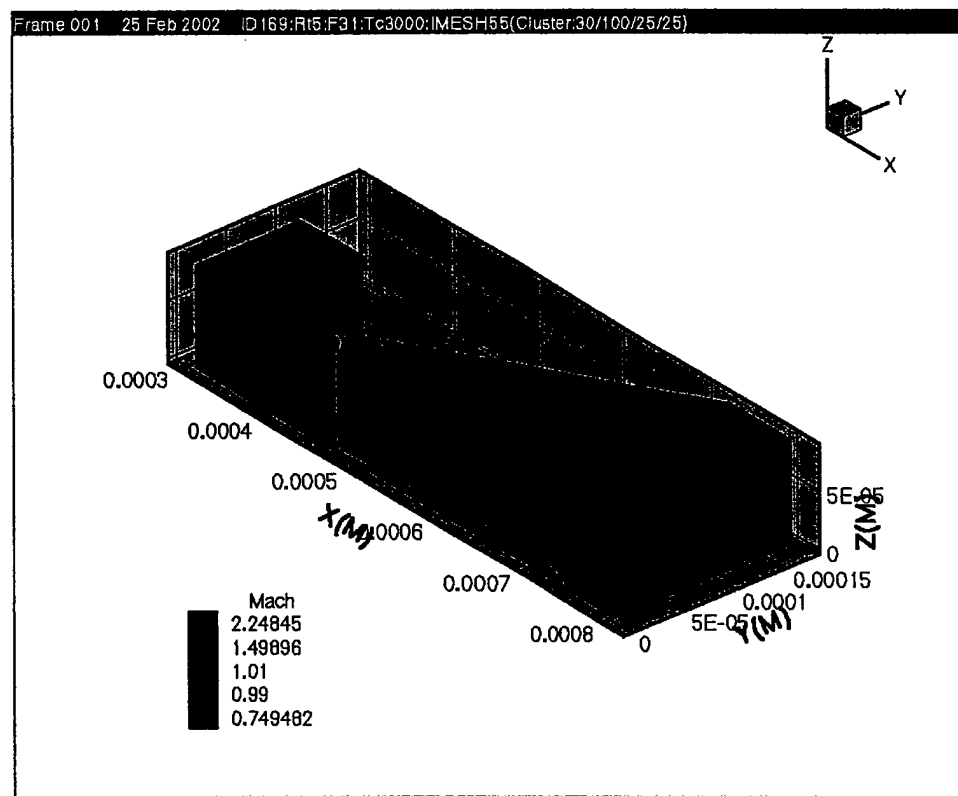


Figure 15-9. Mach Contours of $Rt=5$, $Tc=3000$ K

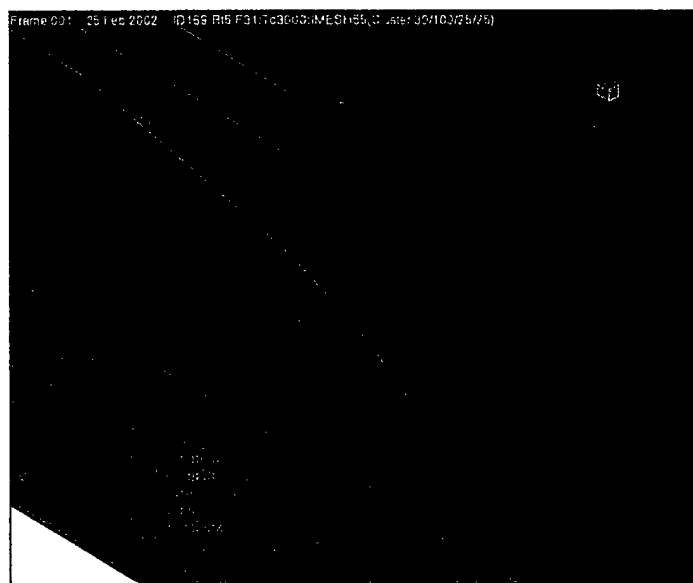


Figure 15-10. Mach Contours @ Endwall Lip

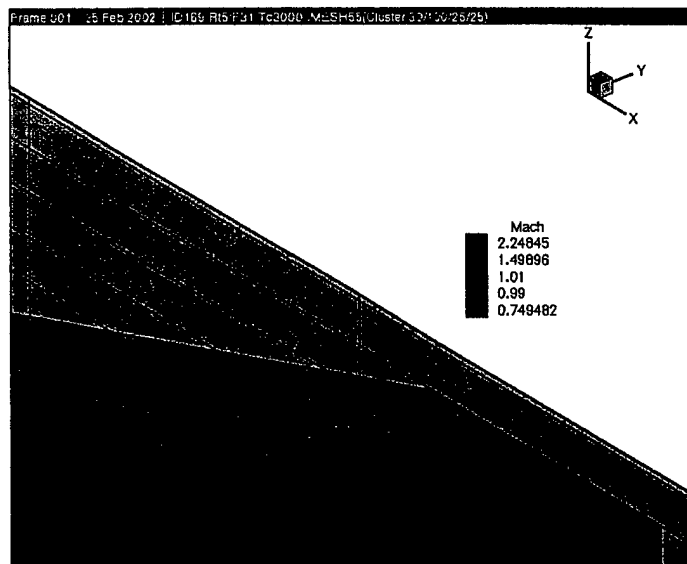


Figure 15-11. Mach Contours @ Sidewall Lip

In the vacuum of space the micronozzle will not be normally be in direct contact with heat from the sun. Therefore, the nozzle will most often be much colder than the ensuing flow of gas during a firing. Due to the high temperature gradient expected at the start of the flow between the gas and the nozzle wall material, there will be high losses of heat and energy, particularly for short impulse burns. For longer burns, the ceramic material of the micronozzle will not allow for high transfer of heat to the surroundings. A loss of heat and energy results in

losses of efficiency for the expanding gases. At the same time, it also reduces the effect of viscosity due to temperature decrease. Ideally we would like to model the radiation effects of the high temperature gases to the vacuum of space. Provided sufficient time, this will be a subject of interest. For initial calculations and verification of the code, the wall conditions will be set to be adiabatic. In addition, there is the option of setting the wall to model rarefied gas slip along the walls. It is expected that the flow will approach the rarefied gas regime, but in test runs it was observed that the use of the no-slip conditions did not vary greatly from the rarefied slip conditions. Once again, this would be a subject of interest, but for now the walls will be set to model no-slip conditions.

15.2.3 Chemistry Model

Within INCA it is possible to define finite-rate chemistry. Allowing for equilibrium flow, or maximum efficiency of expanding gases exiting a nozzle, would be overly optimistic, especially considering the extremely small scale of the micronozzles in question. Frozen flow is therefore predefined with set ratios between water and nitrogen. This is obviously the pessimistic approach to the recombination of gases and release of additional energy, but it does provide for a conservative estimate to nozzle performance. Therefore, the chemistry model is turned off for these cases. This too would be an area of further investigation.

Water and nitrogen are the products of ammonia and nitrous oxide. I obtained the coefficients of ranges 200 – 1000 K and 1000 K to 6000 K for calculation of specific heat, enthalpy and entropy from the NASA polynomial tables⁷⁵. In addition, the INCA¹⁰⁹ code uses the Blottner-Wilkes model of viscosity. Three coefficients for each species were obtained from Amtec Engineering¹¹⁰. Through experience it was noted that the viscosity output of the INCA code was slightly smaller than the viscosity output of the CEA kinetics code¹³³ for a given temperature. Since a CEA curve fit was utilized for post-processing of results, the viscosity values provided slightly smaller value for the Reynolds number than was experienced within the INCA code. The result is an effective built-on margin of error for efficiency when compared with the Reynolds number.

15.2.4 Numerical Code Setup

As stated in the INCA user's manual¹⁰⁹, the proper setup of the numerical code plays a significant role in the convergence and accuracy of the final solution. There are several different aspects of the numerics which we will step through in the following paragraphs. Before entering the setup of the program, equation (15-3) provides a general understanding of the bridge between the physical and numerical world. Numerical methods uses mathematical models, usually represented as partial differential equations, to model the physics of a particular situation. Generally we need as many equations as we have unknowns. For our case we need pressure, temperature, density, and three velocity vectors (u, v, w). The Navier-Stokes equations contain 5 equations: 3 momentum, 1 energy and 1 mass (continuity). Represented in conservative form, these equations are given on the next page⁴⁰:

P = pressure
T = temperature
 ρ = density
 μ = coefficient of viscosity
k = coefficient of thermal conductivity
 u, v, w = velocity
 x, y, z = 3D directions
B = body force
Q = conduction ($\delta Q / \delta T$)
 τ = shear stress

(15-3)

$$\frac{\partial Q}{\partial t} + \frac{\partial E_i}{\partial x} + \frac{\partial F_i}{\partial y} + \frac{\partial G_i}{\partial z} = H + \frac{\partial E_v}{\partial x} + \frac{\partial F_v}{\partial y} + \frac{\partial G_v}{\partial z}$$

where :

$$Q = \begin{bmatrix} \rho \\ \rho u \\ \rho v \\ \rho w \\ \rho e \end{bmatrix} \quad H = \begin{bmatrix} 0 \\ \rho B_x \\ \rho B_y \\ \rho B_z \\ q + \rho \bar{V} \cdot \bar{B} \end{bmatrix}$$

$$E_i = \begin{bmatrix} \rho u \\ \rho uu \\ \rho uv \\ \rho uw \\ (\rho e + P)u \end{bmatrix} \quad E_v = \begin{bmatrix} 0 \\ \tau_{xx} - P \\ \tau_{xy} \\ \tau_{xz} \\ u\tau_{xz} + v\tau_{xy} + w\tau_{xz} - q_x \end{bmatrix}$$

$$F_i = \begin{bmatrix} \rho v \\ \rho vu \\ \rho vv \\ \rho vw \\ (\rho e + P)v \end{bmatrix} \quad F_v = \begin{bmatrix} 0 \\ \tau_{yx} \\ \tau_{yy} - P \\ \tau_{yz} \\ u\tau_{yz} + v\tau_{yy} + w\tau_{yz} - q_y \end{bmatrix}$$

$$G_i = \begin{bmatrix} \rho w \\ \rho wu \\ \rho ww \\ \rho vw \\ (\rho e + P)w \end{bmatrix} \quad G_v = \begin{bmatrix} 0 \\ \tau_{zx} \\ \tau_{zy} \\ \tau_{zz} - P \\ u\tau_{zz} + v\tau_{zy} + w\tau_{zz} - q_z \end{bmatrix}$$

where :

$$\tau_{xx} = \frac{2}{3}\mu \left(2\frac{\partial u}{\partial x} - \frac{\partial v}{\partial y} - \frac{\partial w}{\partial z} \right) \quad \tau_{yy} = \frac{2}{3}\mu \left(2\frac{\partial v}{\partial y} - \frac{\partial u}{\partial x} - \frac{\partial w}{\partial z} \right) \quad \tau_{zz} = \frac{2}{3}\mu \left(2\frac{\partial w}{\partial z} - \frac{\partial v}{\partial y} - \frac{\partial u}{\partial x} \right)$$

$$\tau_{xy} = \tau_{yx} = \mu \left(\frac{\partial u}{\partial y} + \frac{\partial v}{\partial x} \right) \quad \tau_{xz} = \tau_{zx} = \mu \left(\frac{\partial u}{\partial z} + \frac{\partial w}{\partial x} \right) \quad \tau_{yz} = \tau_{zy} = \mu \left(\frac{\partial v}{\partial z} + \frac{\partial w}{\partial y} \right)$$

$$q_x = -k \frac{\partial T}{\partial x} \quad q_y = -k \frac{\partial T}{\partial y} \quad q_z = -k \frac{\partial T}{\partial z}$$

Because we have 5 equations and 6 unknowns, we use the ideal gas law from equation (8-4) to close the system.

In a general format, the momentum equations can be represented in the following form³⁵:

$$\begin{aligned} \rho \frac{\partial u}{\partial t} + \rho u \frac{\partial u}{\partial x} + \rho v \frac{\partial u}{\partial y} + \rho w \frac{\partial u}{\partial z} &= -\frac{\partial p}{\partial x} + \frac{\partial}{\partial x} \left(\mu \frac{\partial u}{\partial x} \right) + \frac{\partial}{\partial y} \left(\mu \frac{\partial u}{\partial y} \right) + \frac{\partial}{\partial z} \left(\mu \frac{\partial u}{\partial z} \right) \\ \rho \frac{\partial v}{\partial t} + \rho u \frac{\partial v}{\partial x} + \rho v \frac{\partial v}{\partial y} + \rho w \frac{\partial v}{\partial z} &= -\frac{\partial p}{\partial y} + \frac{\partial}{\partial x} \left(\mu \frac{\partial v}{\partial x} \right) + \frac{\partial}{\partial y} \left(\mu \frac{\partial v}{\partial y} \right) + \frac{\partial}{\partial z} \left(\mu \frac{\partial v}{\partial z} \right) \\ \rho \frac{\partial w}{\partial t} + \rho u \frac{\partial w}{\partial x} + \rho v \frac{\partial w}{\partial y} + \rho w \frac{\partial w}{\partial z} &= -\frac{\partial p}{\partial z} + \frac{\partial}{\partial x} \left(\mu \frac{\partial w}{\partial x} \right) + \frac{\partial}{\partial y} \left(\mu \frac{\partial w}{\partial y} \right) + \frac{\partial}{\partial z} \left(\mu \frac{\partial w}{\partial z} \right) \end{aligned} \quad (15-4)$$

The terms on the left describe the advection of momentum through bulk velocity from one location to another and are hyperbolic in nature. The pressure and viscosity terms on the right are known as diffusion terms and they model the transfer of momentum through viscosity and pressure gradients. They are parabolic in nature.

INCA uses another form of Navier Stokes equations known as the Reynolds averaged Navier Stokes equations. This form of the Navier Stokes equations uses a time-averaged solution of the equations of motion to correctly model turbulent flow⁴⁰. Since we are not particularly interested in turbulent flow for the physics of our problem, the time averaging does not directly affect the numerics of this problem. The reader is encouraged to reference the INCA user's manual for further instruction on the following terms¹⁰⁹.

15.2.4.1 Flux Function

One problem encountered in CFD is the evaluation of the advection terms on the left hand side of the Navier-Stokes equations. These are hyperbolic equations which describe the propagation of waves (information). Subsonic information can propagate both upstream and downstream. If supersonic, information propagates only downstream. Schemes have been developed to deal with the correct modeling of this information propagation. The first scheme is known as Steger-Warming. This scheme splits the eigenvalues of the F, G, H matrices into positive and negative components, so it takes on the following form of equation (15-5)³⁹:

$$F = M(\Lambda^+ + \Lambda^-)M^{-1}Q = (A^+ + A^-)Q = F^+ + F^- \quad (15-5)$$

F = convective terms of (x) direction on left-hand side of NS equations

M = matrix of eigenvectors

Λ = matrix of eigenvalues on the diagonal

A = flux jacobian of F with respect to vector matrix Q

Each of these vectors is then discretized with an upwind bias. Use of second order accuracy on the left-hand side requires additional numerical dissipation terms which are effective in modeling the propagation of waves, but by adding dissipation terms it also adds additional damping to the diffusion terms on the right hand side of the equation. Upwind biasing eliminates the information from the other direction. Since diffusion terms are parabolic in nature, they require information from both sides of the cell. Because each flux vector is represented with an upwind bias, the result is an inaccurate model of the viscosity. Therefore, this method of flux splitting is good for inviscid problems. For more information on the Steger-Warming scheme the reader should reference [39] and [45].

The other scheme available in INCA is the Roe, TVD scheme. This scheme introduces a parameter vector which can be used to represent both the Q and F,G,H matrices. The general approach is that it computes a numerical flux using an averaged computation of eigenvalues and eigenvectors to compute wave strengths which are in turn used to compute the flux at a given position between cells²⁷. Because information is taken from both sides of the cell the problem associated with upwind biasing is eliminated. Even when using 2nd order accuracy the Roe scheme only eliminates the oscillations associated with the propagation of waves and does not add excessive dissipation to the diffusion terms. Therefore, this method can accurately handle both the proper propagation of information and the diffusion terms. For more information on this scheme the reader is referred to ref [48] and [49].

15.2.4.2 Flux Limiter

Since the eventual goal is to obtain a second order solution to the flow field, a flux limiter is included to reduce the accuracy of the convective terms to first order in regions of shocks. This simply means that if the second order difference in pressure is sufficiently high (representative of a shock) then the accuracy reduces to first order thereby decreasing the oscillations typical of second order schemes and accurate capturing of the shock. The flux limiter coefficients are

values that determine the magnitude of the flux limiter. The greater the number, the more first order the scheme becomes. Values for this option were left at the default levels.

15.2.4.3 Explicit/Implicit Mode

The numerical convergence mode chosen was implicit. Although explicit allows for computation of a time accurate solution, the goal of this study is to compute a steady-state solution. Explicit methods generally require low values for the CFL number, often resulting in greater computational time and resources. The implicit mode on the other hand uses an iterative approach at each time level to solve for several unknowns at once. While it is not time accurate, it generally requires less computer resources depending on the number of iterations within each time step. The implicit method used for INCA is LU.SGS. A Gauss Seidel point relaxation technique is applied at each individual point of the flow field. This sets up a block diagonal matrix for three dimensions. The coefficient matrix is then broken up further into upper/lower diagonal matrices to ease the computational effort. An additional relaxation factor ω is used to speed up convergence.

15.2.4.4 Gauss-Seidel Relaxation Factor

This value is introduced by multiplying the residual of the sets of unknown equations from the Gauss-Seidel method by some factor between 1 and 2 (thereby becoming a successive overrelaxation method⁴¹). According to the INCA manual, at higher levels it helps to add stability to the algorithm, but lower values closer to 1 increases the convergence rate. A value of 1.5 was chosen as a safe operating zone and no attention was given as to the effect of varying this parameter on the convergence level.

15.2.4.5 Time Step Mode

While local time stepping may be used, the author did not experiment with this option. Instead a uniform time step was used across all grid cells. The INCA manual suggests using a uniform time step when using the implicit LU.SGS mode.

15.2.4.6 Time Step Relax Factor

This reduces the effective time step of each iteration if non-physical results such as negative pressures/energies are achieved through the evaluation process. INCA claims that the effective time step is reduced automatically, although it is the author's experience that this value must be reduced manually if the negative pressures/densities are experienced.

15.2.4.7 Order (Flux Phi I/J/K)

This variable determines the weight between first and second order. The goal is to eventually reach a second order scheme as this method more can use coarser grids to obtain more accurate results and 2nd order is more accurate in general for modeling viscosity. Second order accuracy is obtained through the process of spatial discretization of the Taylor Series expansion. In figure 15-12 below, pt3 represents a guess from the first term, point 4 includes the slope, and point 5 includes the curvature of some function $f(x)$. In addition, 1st order discretization of the convective terms tend to dominate the viscous terms, therefore the converged solution is not accurate in modeling viscous effects. 2nd order discretization is essential not only for using a coarser mesh, but also in obtaining correct models of the viscosity.

$$f(x + \Delta x) = f(x) + \underbrace{\frac{df}{dx} \Delta x}_{\text{First guess (not very good)}} + \underbrace{\frac{d^2f}{dx^2} \frac{(\Delta x)^2}{2}}_{\text{Add to capture slope}} + \dots$$

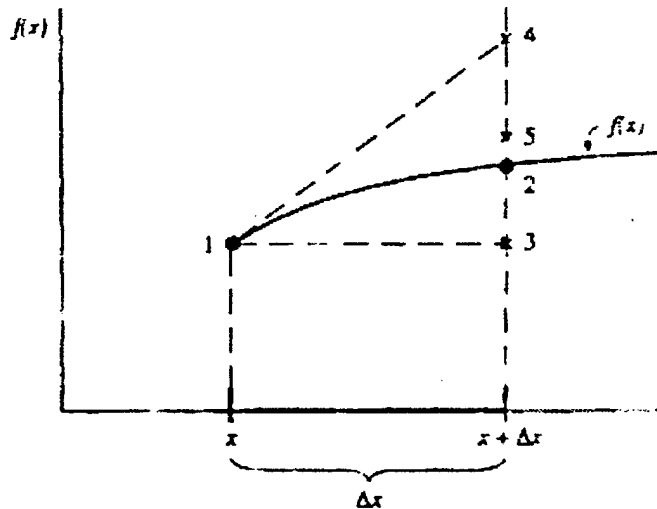


Figure 15-12. Graphical Representation of Taylor Series Expansion⁴⁰

Although second order does promise more accurate results with a coarser grid, it is also naturally unstable and requires additional artificial viscosity to reduce oscillations in regions of shocks. Initially, before understanding the need for a nonuniform mesh to capture viscous effects, I used a uniform mesh which readily converged for 1st order runs and did not converge for the second order case. Upon clustering of the grid cells at the walls and regions of high gradients the second order scheme readily converged.

15.2.4.8 Thermodynamic/Conductivity/Viscosity Models

Due to multiple species involved in the flow field, the Blottner-Wilkes method was chosen to model the viscous effects. It is used to calculate not only viscosity, but also conductivity properties of the gas. We are only concerned at this point with the viscous effects. Each gas is considered as a ‘thermally perfect species’ and therefore the equation $P=\rho RT$ applies. One area of mention involves the percentage of species defined in the input file. Originally, temperatures slightly off from 1000 (1008), 1500 (1467), 2000 (2076), 2500 (2492) and 3000

(3032) were used to calculate the initial species concentrations for each respective temperature level. Since the computational time involved exponentially increases for each species considered, only the dominant species, water and nitrogen, were included. Their concentrations were slightly altered from the actual output of the CEA code so that there would be a sum of unity for the fraction of species. In addition to the need for unity within the INCA code, the actual chamber temperatures were at an even 1000, 1500, 2000, 2500, and 3000K. Therefore, this also introduces some level of error in the calculations because the species concentrations are not exactly what the CEA chemical kinetics code claims they should be. Nonetheless, the species concentrations put the resultant viscosity in the ‘ballpark’ and from the original computations are within at least 5% of the CEA output for each temperature level and the error is assumed acceptable. Examples of exact and approximated levels are given below in table 15-5.

Table 15-5. Species Fractions for Approximate, Exact CEA Output and INCA Input

Species	3033	3000	INCA	2492	2500	INCA	2064	2000	INCA
H ₂ O	0.384	0.397	0.41	0.569	0.567	0.575	0.649	0.671	0.655
N ₂	0.557	0.548	0.59	0.419	0.421	0.425	0.337	0.32	0.345

Species	1577	1500	INCA	1008	1000	INCA
H ₂ O	0.68	0.695	0.70	0.748	0.747	0.77
N ₂	0.276	0.261	0.30	0.191	0.191	0.23

The values do not differ greatly from one another and the values for viscosity are for the most part a function of temperature and not species concentration. There is a slight deviation at the upper and lower limits of each curve as can be seen by the following figure:

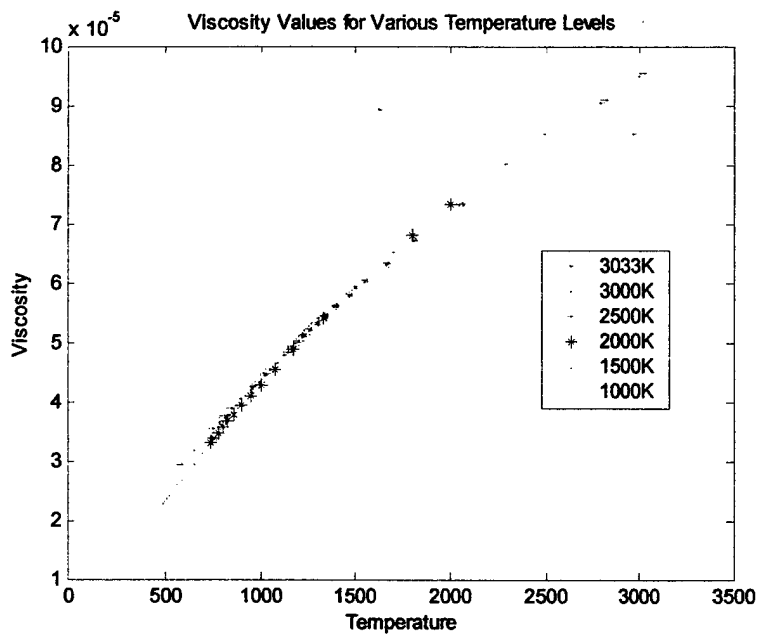


Figure 15-13. Viscosity Values for Exact and Approximate Temperatures¹³³

15.2.4.9 CFL Number Range

Once the mesh densities and spacings were sufficiently refined, the CFL number was set initially at 0.3 for the beginning of the simulation to help ‘mesh’ together the initial conditions of each separate block of data points. It was then increased incrementally by a factor of 1.05 or 1.01. In some cases it was increased only to 200 or 400 but by the end of the simulations when the mesh density and spacing were sufficiently refined, it was increased to the maximum value of 1E6.

15.2.4.10 Eigenvalue Smoothing Coefficients

Eigenvalue smoothing coefficients are used in Roe’s scheme for regions of high gradients such as at shock waves. Amtec Engineering claims that in regions of laminar flow, the eigenvalue coefficients will only effect specific parameters such as the shear stress¹¹⁰. Therefore, the overall solution should not be significantly altered when changing these values. Making use of results of the next section I verified this assumption. We see little error between the two

methods and therefore the smoothing coefficients of id149 used throughout the computations are deemed accurate.

Table 15-6. Comparison Results for Eigenvalue Smoothing Coefficients

id #	Smoothing Coefficients	Thrust (mN)	Isp (sec)	Mass flux (kg/m³)
149	.1, .1, .1, 1, 1, 1	396.2	254.5	3.97E-5
175	.01, .01, .01, 0, 0, 0	398	253.9	4.00E-5

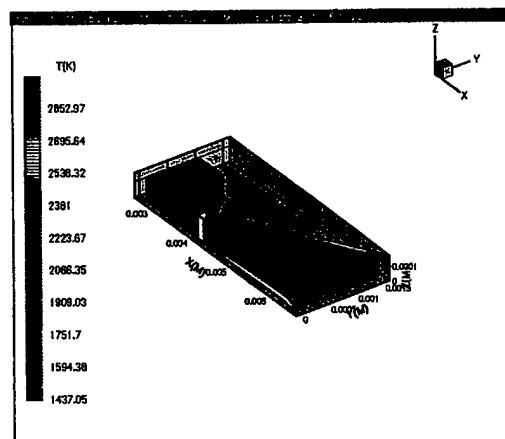


Figure 15-14. Temperature Contour Plot for id149

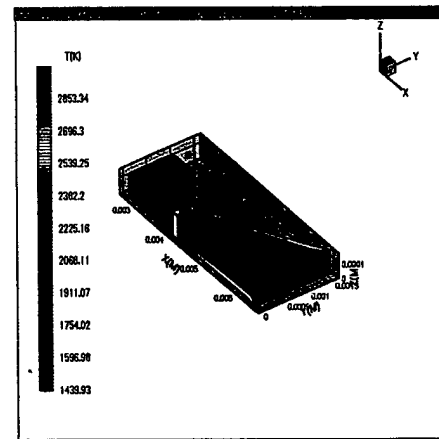


Figure 15-16. Temperature Contour Plot for id175

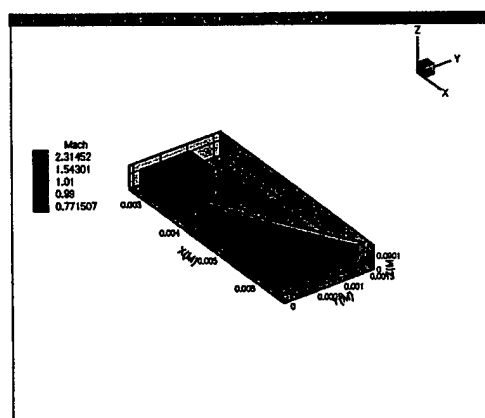


Figure 15-15. Mach Contour Plot of id149

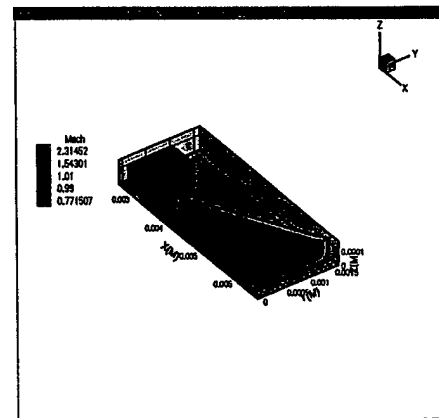


Figure 15.17. Mach Contour Plot of id175

Chapter 16: Output Post-processing of Converged Solutions

Upon sufficient convergence, INCA outputs results in a variety of files based upon the desired results. For our case, the desired outputs were defined as the 3D field and surface files. The field files contained the following variables : x (x-coordinate), y (y-coordinate), z (z-coordinate), u (axial velocity), v (radial 'y' velocity), w (radial 'z' velocity), P (pressure N/m²), T (temperature K), rho (density kg/m³), mach #, % H₂O, % N₂. Each grid point already set up in the IMESH file contains the physical data described above. The surface output file contains such variables as the y-plus value, viscosity, shear stress, etc.

There are three different methods to determine whether or not the solution is sufficiently converged to accept the results. The first involves the tracking of velocity, temperature, pressure and density profiles. Below is an example of a solution beginning from the initial values to a converged solution. The first two plot along the nozzle centerline, and the next four along the lines of symmetry of the nozzle exit. The numbers represent the number of iterations:

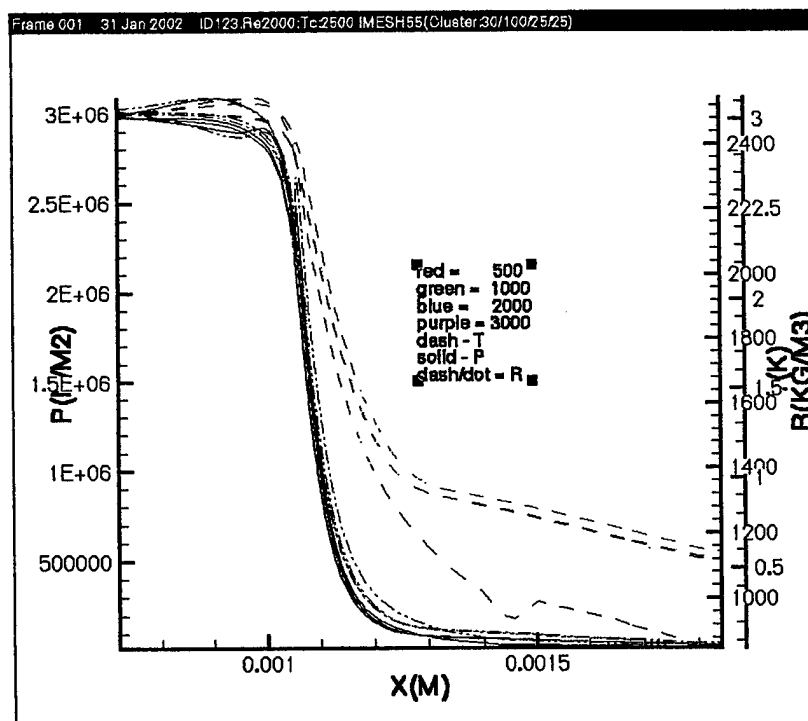


Figure 16-1. Axial T, P, R Convergence

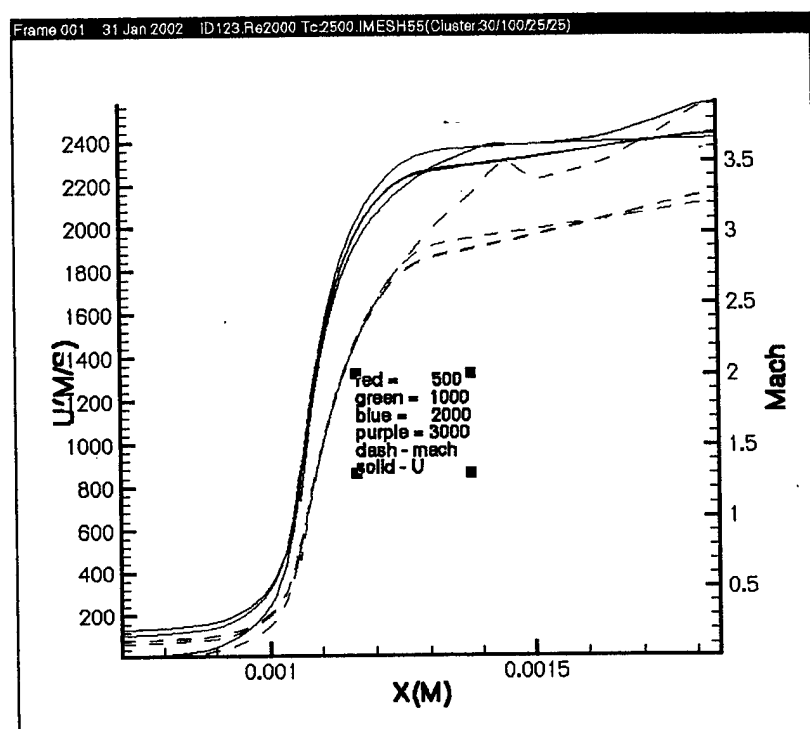


Figure 16-2. Axial Mach and Velocity Convergence

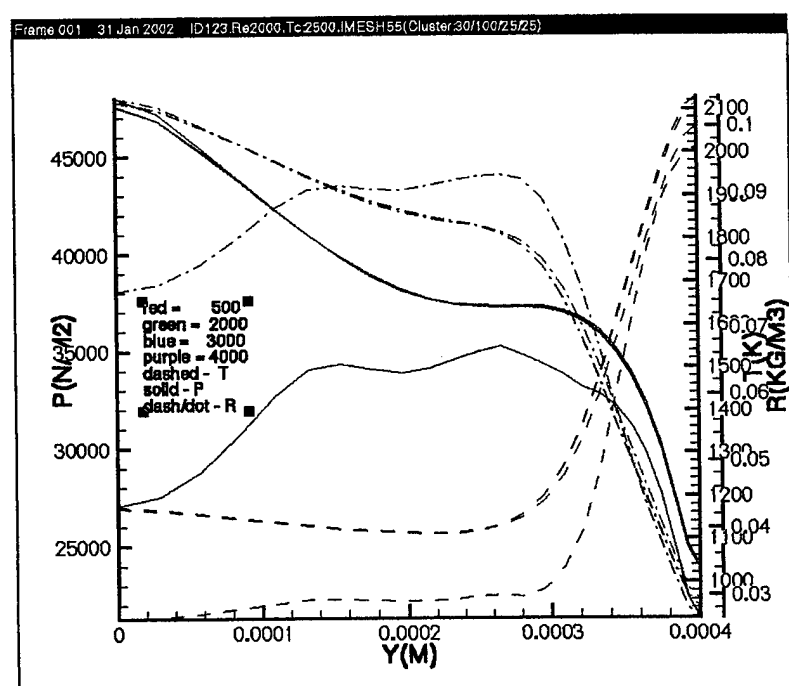


Figure 16-3. P, T, R Exit Plane Sidewall Symmetry Line Convergence

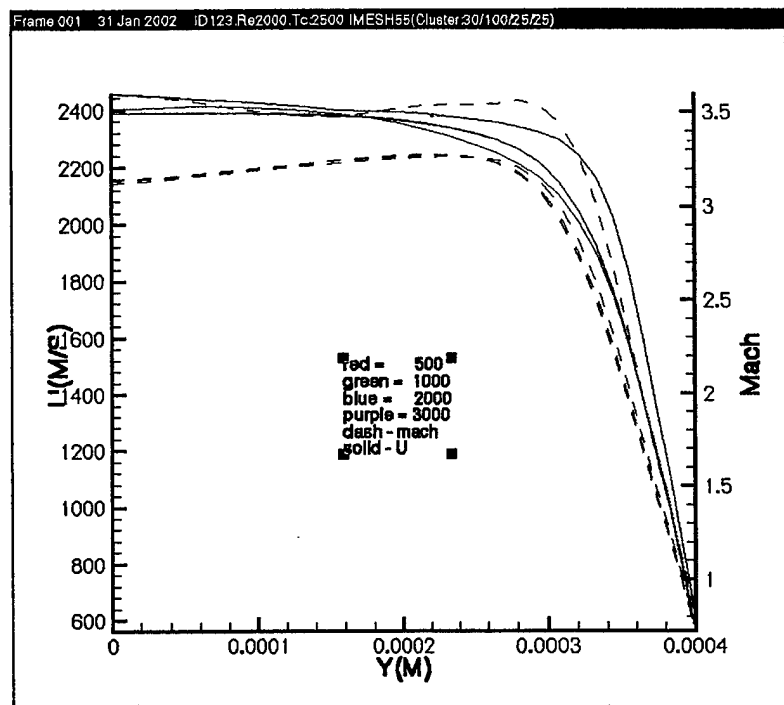


Figure 16-4. Mach, Axial Velocity Exit Plane Sidewall-Symmetry Line Convergence

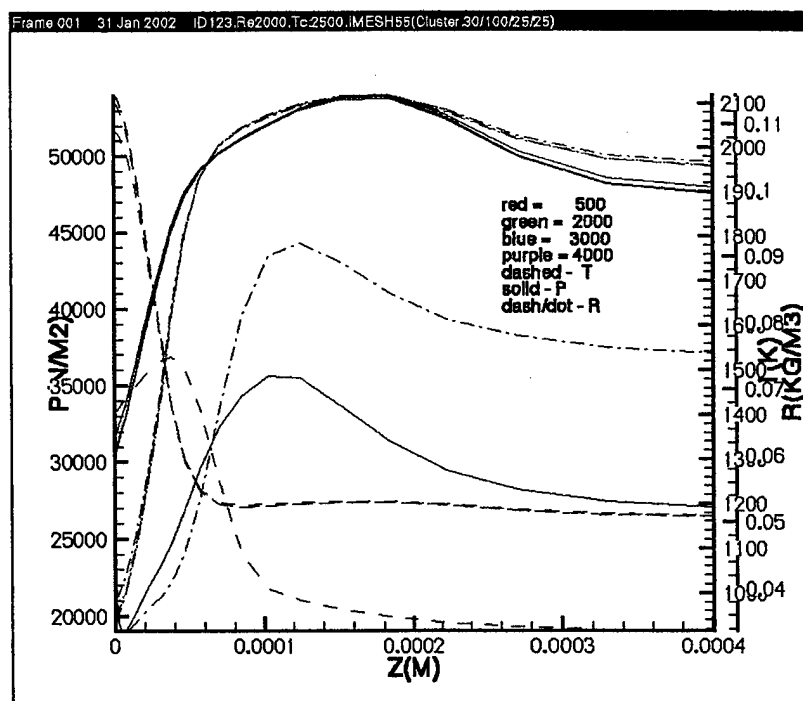


Figure 16-5. P, T, R Exit Plane Endwall-Symmetry Line Convergence

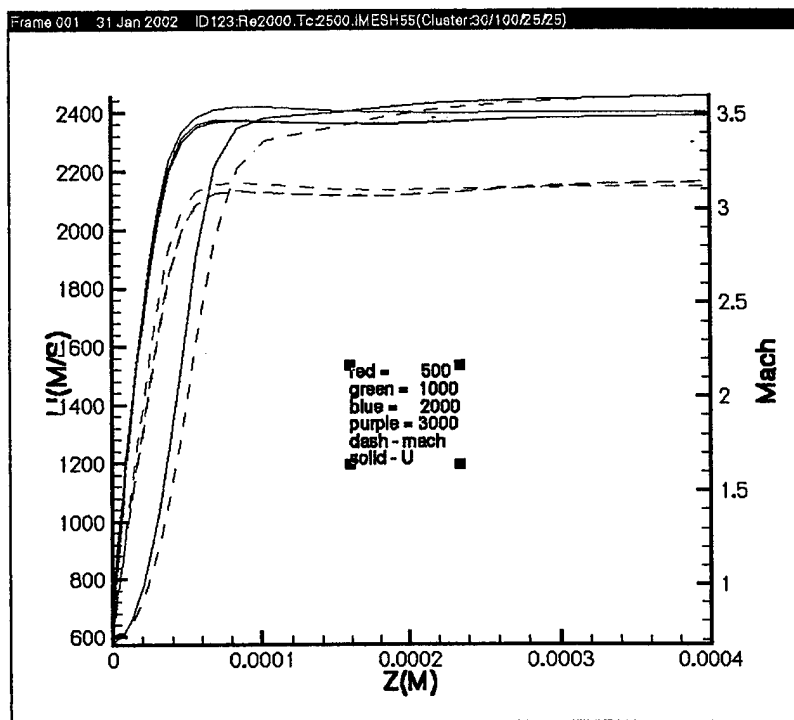


Figure 16-6. Mach, Axial Velocity Exit Plane Endwall-Symmetry Line Convergence

While this provides a general visual aid of the solution, it is not sufficient for the complete calculation of thrust and Isp. The second method involves the L2-norm of the speed of sound divided by the momentum. This value is computed for each block at the end of each time step. For machine-zero convergence the L2-norm should reduce to -12^{110} . For most cases investigated, an L2-norm of around -8 provided sufficient convergence.

The L2-norm of the solution is defined as the log of the sum of the change of a specified variable (X) from one time step to another as in equation (16-1).

$$L2 - norm = \ln \left(\sum_{ijk} (\Delta X)^2 \right) \quad (16-1)$$

The final method makes use of INCA's ability to compute the thrust across a given region of mesh points. In this case, I used the calculated thrust across the exit plane of the 2nd (divergence) block of points. I setup the INCA code to output the thrust every 50 time iterations. In the beginning of the thrust output would have large differences from time step to time step. As the solution converged, the difference would begin to decrease until finally it would oscillate

around the converged solution. Once the oscillations began during convergence, this signified that the answer was in the 'ballpark' of the final solution.

Table 16-1 is an example of an output file. Recall that the zones are numbered in the following sequence: convergent(1)/divergent(2)/exit(3)/chamber(4). This sequence was obtained through the grid development process.

Table 16-1. Sample Output File Including Thrust and L2 Norm

```

Z= 2 STEP= 700 Fx= 0.25150E-01 Fy= 0.45451E-02 Fz= 0.51200E-03
*****INCA/MAIN: STEP= 710, ZONE NO.= 1, CONVERGENCE.LEVEL= -10.092
*****INCA/MAIN: STEP= 710, ZONE NO.= 2, CONVERGENCE.LEVEL= -7.562
*****INCA/MAIN: STEP= 710, ZONE NO.= 3, CONVERGENCE.LEVEL= -7.331
*****INCA/MAIN: STEP= 710, ZONE NO.= 4, CONVERGENCE.LEVEL= -9.613
*****INCA/MAIN: STEP= 720, ZONE NO.= 1, CONVERGENCE.LEVEL= -10.097
*****INCA/MAIN: STEP= 720, ZONE NO.= 2, CONVERGENCE.LEVEL= -7.578
*****INCA/MAIN: STEP= 720, ZONE NO.= 3, CONVERGENCE.LEVEL= -7.343
*****INCA/MAIN: STEP= 720, ZONE NO.= 4, CONVERGENCE.LEVEL= -9.600
*****INCA/MAIN: STEP= 730, ZONE NO.= 1, CONVERGENCE.LEVEL= -10.100
*****INCA/MAIN: STEP= 730, ZONE NO.= 2, CONVERGENCE.LEVEL= -7.594
*****INCA/MAIN: STEP= 730, ZONE NO.= 3, CONVERGENCE.LEVEL= -7.355
*****INCA/MAIN: STEP= 730, ZONE NO.= 4, CONVERGENCE.LEVEL= -9.588
*****INCA/MAIN: STEP= 740, ZONE NO.= 1, CONVERGENCE.LEVEL= -10.100
*****INCA/MAIN: STEP= 740, ZONE NO.= 2, CONVERGENCE.LEVEL= -7.611
*****INCA/MAIN: STEP= 740, ZONE NO.= 3, CONVERGENCE.LEVEL= -7.366
*****INCA/MAIN: STEP= 740, ZONE NO.= 4, CONVERGENCE.LEVEL= -9.577
*****INCA/MAIN: STEP= 750, ZONE NO.= 1, CONVERGENCE.LEVEL= -10.097
*****INCA/MAIN: STEP= 750, ZONE NO.= 2, CONVERGENCE.LEVEL= -7.628
*****INCA/MAIN: STEP= 750, ZONE NO.= 3, CONVERGENCE.LEVEL= -7.376
*****INCA/MAIN: STEP= 750, ZONE NO.= 4, CONVERGENCE.LEVEL= -9.567
Z= 2 STEP= 750 Fx= 0.25167E-01 Fy= 0.45496E-02 Fz= 0.51337E-03

```

Zones 1 and 4 for the most part converge faster than zones 2 and 3. Therefore, in the validation process and data analyses sections, reference to the L2-norm will most often be to zones 2 (convergent section) and 3 (exit region). Often one region will appear to be converging (continual decrease of L2-norm value) while another zone will increase (increase of L2-norm). This is obviously a result of the convergent process as the solution over a longer period of time continues to converge.

Exceptions to the general trends noted above have been observed. On occasion the solution will appear to be oscillating around a specific point, but then jump to a different range of oscillation. While this has been observed, the jump only occurred once and the range did not vary drastically from one to another. Once the run is sufficiently converged, or I prematurely

stopped it with an EBRAKE file, the files are downloaded into Tecplot^{®52}. This program was also developed by Amtec Engineering and is used for visual processing of data.

Once the solution has sufficiently converged, it is necessary to check the y-plus values to ensure that the grid spacing is close enough to the walls to capture the viscous effects. This is accomplished through an additional data file in INCA. I set up INCA to collect the y-plus value at every point along the wall. Plotting this data in Tecplot^{®52} yields the graph of figure 16-7.

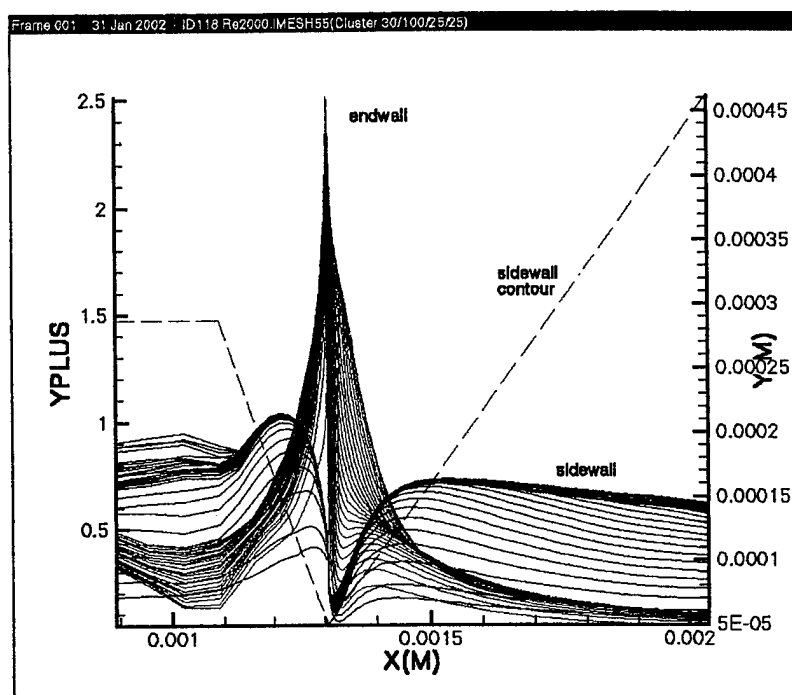


Figure 16-7. Y-plus Values Along Nozzle Walls

As previously mentioned, the y-plus value must be near unity for accurate modeling of viscous effects. As evident in this run, the y-plus value exceeds unity near the throat. Engineers at Amtec said y-plus values slightly greater than unity were acceptable due to the thinness of the boundary layer at the throat, and immediate drop to unity further downstream¹¹⁰. This will be analyzed further later on. Note that all y-plus values investigated will have the same general shape and contour as above. Therefore, from this point forward y-plus values will refer to the maximum values attained for both the sidewall and the endwall and will be presented in the following manner: max y-plus = sidewall/endwall (i.e., for case above $y_{max} = 1 / 2.5$).

In addition, it was possible to write additional data files which I downloaded into Matlab^{®64} for further analysis. By downloading the field data I wrote an algorithm to verify the physical dimensions of the nozzle, compute the mass flow rate, thrust, Isp, Reynolds and Knudsen numbers at different points along the divergent section of the nozzle. The algorithm itself (FISPCluster.m) can be found in Appendix F. Below is a brief description of each section.

The first step is to read in the data from the specified file. The output data is organized sequentially with each grid points as rows and physical data organized in columns. The first row of data represents the grid point at the throat on the bottom, physically in the middle of the nozzle. From there the y,z values remain the same and the grid point data sequentially follows down the axial distance of the nozzle. At the exit plane, the y grid point value is incremented by 1, the x-value returns to 1, and the z-value remains the same. Thus, we are still in the plane defining the bottom of the nozzle. Following this pattern, after the bottom x-y plane is finished, the grid point data increments to the next level. In short, first the x-value is incremented by one until the max x-value is reached (in this case 100), then the y-value increments to one and the x-value starts over again. Once the y value reaches its maximum (25 in this case) the z –value increments by one and the x and y values start over again. This process is repeated until the final z-value (representing the top plane of the grid (this case = 30), or physically speaking, the midpoint of the sidewall) is reached. Figure 16-8 visually represents the data organization:

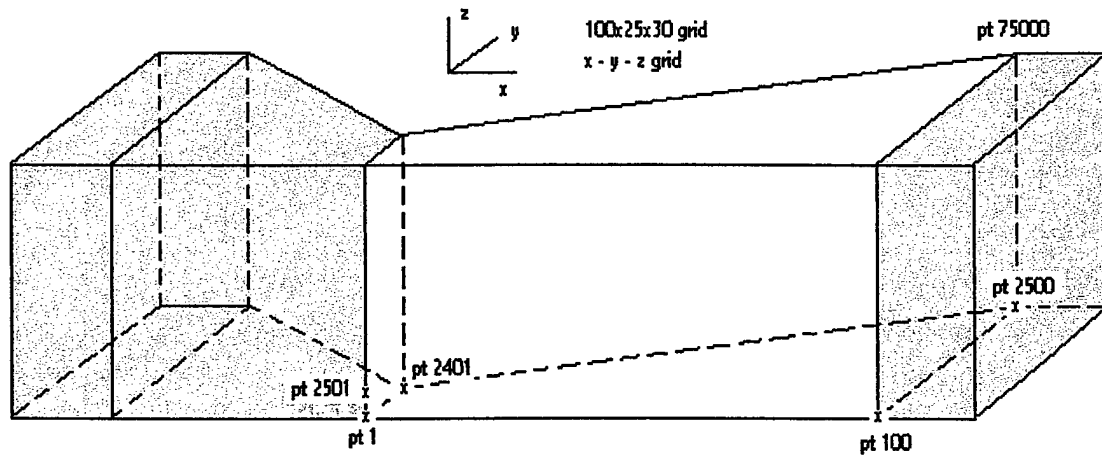


Figure 16-8. Data Organization from Tecplot^{®52} Output File

Due to the clustered grid points, the area of each cell (made up of 4 grid points) is not equal. Therefore, taking the physical data of the 4 surrounding grid points it is possible to determine the area of each cell. Since data was provided at each grid point, and not at the center of each cell, I took the average of the four surrounding grid points of velocity, temperature, pressure, density and mach number. Using these averaged values for each cell, it was then possible to compute the thrust and Isp of each cell.

I used the data from the grid points to verify the half-angle, expansion ratio, aspect ratio and physical dimensions. The cross-sectional area and overall mass flux for that area was calculated by summing across the cross-sectional face of each individual cell.

In the same manner, the thrust was calculated for each cell and summed across each cross-section along the axial direction of the nozzle. Since the result is only one-fourth of the entire nozzle, the final thrust was multiplied by 4 to achieve the overall thrust. The Isp was calculated using a mass-flux weighted average (16-3). Using the mass flux already calculated for each cross section and then calculating the percent mass flux of each cell, it is possible to determine the contribution of each individual cell to the overall cross-sectional mass flux. Due to the weighted average, inclusion of the other three sections of the overall nozzle is not necessary.

$$F = \sum A_{cell} (\rho U^2 + P) \quad (16-2)$$

F = thrust (N)

A_{cell} = cell area (m^2)

ρ = density (kg/m^3)

U = axial velocity (m/s^2)

P = pressure (N/m^2)

$$Isp = \sum \frac{F_{cell}}{g \cdot \rho A_{cell} U} \frac{m_{cell}}{m_{plane}} \quad (16-3)$$

Isp = specific impulse (sec)

F_{cell} = cell thrust (N)

m_{plane} = cross section mass flux (kg/sec)

m_{cell} = cell mass flux (kg/sec)

Therefore, if there are 100 axial points, the output file contains 100 separate values for thrust and Isp. In addition, at the corners of each cross section I calculated the Reynolds and Knudsen numbers to gain an overall understanding of how those values were changing along nozzle. As mentioned before, Knudsen numbers greater than 0.01 indicate transition into the

rarefied regime of gas dynamics where the continuum assumption begins to break down. Efforts were made to stay below 0.01, but on occasion they did rise slightly above this value.

Ideal values based on the expansion ratio were also computed using data from the CEA chemical kinetics code¹³³. These values were then compared with the output thrust and Isp to determine efficiency of the micronozzle.

Chapter 17: Validation of Numerical Code and Mesh Refinement Studies

Due to lack of experimental data of the geometries in question, it is necessary to perform a numerical validation of the CFD code and mesh refinement study. The numerical validation involves agreement between the 1st and 2nd order schemes within the IDATA file. The mesh refinement study requires increasing the number of grid points until changes in the desired output variables decrease to acceptable limits. In this case we are concerned with thrust and Isp.

Ideally, we would hope that validation of the code and mesh for one nozzle geometry would also do the same for other nozzle geometries. For example, if we were to verify the code and mesh for an aspect ratio of 10 and Reynolds number of 2000, and then setup an additional nozzle designed for the same thrust level, but at an aspect ratio of 1, the code and mesh would not require further validation. Unfortunately, this is not the case. When changing from one geometry to another, it is essential that an additional mesh analysis be performed to verify that the achieved solution would not change if additional grid points were added. This is due to the fact that a change in physical dimensions represents a change in the way the physics is played out throughout the nozzle. For example, consider the following micronozzles of table 17-1 designed for a thrust level of 500 mN:

Table 17-1. Variation in Physical Dimensions for Aspect Ratios of 1,10

Aspect Ratio	Eratio	Half Angle	Height (um) throat/exit	Width (um) throat/exit	Re Throat/exit
1	10	30	312.9	312.9/3.13 mm	6317/1103
10	10	30	989.9	98.9/989.9	1998/3488

Although the throat/exit height is smaller for an aspect ratio of 1, the throat/exit width is 300% larger. Therefore, for an aspect ratio of 10 we may need more grid points for the height over the width, than for an aspect ratio of 1.

17.1 Inviscid/Viscid Results and Verification of Micronozzle with Aspect Ratio = 10

The following code verification and mesh refinement analyses were performed for the conditions of table 17-2.

Table 17-2. Conditions for Code Verification / Mesh Analysis of $Rt = 10$

Chamber Temperature	3000 K
Chamber Pressure	30 bar (3E6 Pa)
Aspect Ratio	10
Expansion Ratio	10
Half Angle	30
Thrust	501 mN
Throat Diameter (Width)	99 micrometers

There is a large advantage to choosing this particular nozzle. Since we will be analyzing this chamber temperature (3000 K) at Reynolds numbers less than 2000 at the same aspect ratio, only the scale will decrease. In addition, analyzing the same Reynolds numbers at smaller chamber temperatures using the same geometry will also decrease the scale. (Reference back to table 13-1). Therefore, since the shape of the nozzle remains the same, it is expected that the code/grid verified for this nozzle will be valid for nozzles of the same shape, just at a smaller scale.

As previously mentioned, it is necessary that the 1st and 2nd order schemes agree with one another to verify the numerics of the code. I initially ran into problems with the viscous results, therefore with the suggestion of Prof Eberhardt^[11], I ran inviscid codes to find if the error was not a result of the viscous effects. From there it is possible to move on to the viscous validation. Generally, 1st order schemes do not capture viscous effects as described in the numerical modeling section. It is therefore essential that the 2nd order scheme be stable and converge. Using the 1st order scheme is simply a method to verify that the code overall is stable and converging.

17.1.1 Inviscid Results

Without the effects of viscosity, the expansion of gases produces the following velocity profile of figure 17-1. Recall that we are looking solely at the lower right hand quarter of a 3D block nozzle:

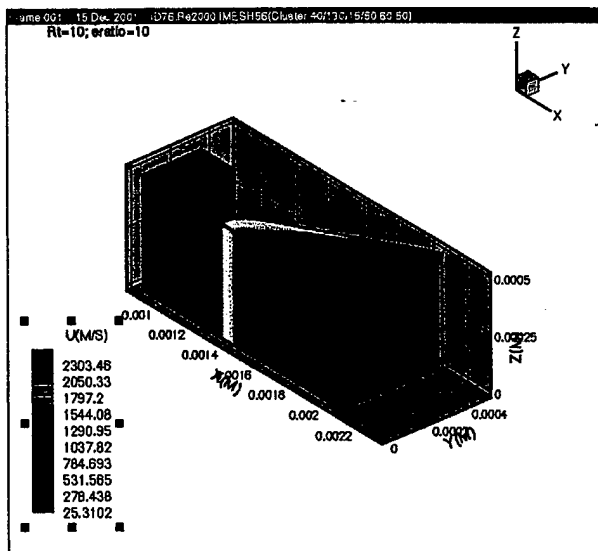


Figure 17-1. Inviscid Contour Plot of Axial Velocity

By going to the inviscid schemes and increasing the size of the mesh density, the hope was that the 1st and 2nd order difference would decrease. This would narrow the possible sources of error to the viscous effects. Table 17-3 contains the grid sizes for each respective mesh:

Table 17-3. Grid Data for Inviscid Mesh

Case	ID #	Total Cell #	Divergent Cells	Axial Points	Radial/Height
1 st – Coarse	69	277,095	208,299	30/110/5/4	50/40
1 st – Fine	76	638,911	372,939	40/130/15/40	60/50
2 nd – Coarse	70	93,960	68,904	30/100/5/4	25/30
2 nd – Fine	88	237,276	165,789	35/110/5/10	40/40

** axial points are from Z1, Z2, Z3, Z4 in order

By increasing the mesh density of the 1st and 2nd order schemes by 2.5x each, the following results of table 17-4 and figures 17-2 and 17-3 were obtained:

Table 17-4. Inviscid Results

Case	ID#	Z2 – Z3 L2-Norm	Re (throat/exit)	Kn (throat/exit)	F(mN): (% ideal)	Isp(sec): (% ideal)
1 st – Coarse	69		1890/3476	.0006/.001	428.5 (85.6)	270.1 (95.7)
1 st – Fine	76	8.1 – 7.9	1900/3600	.0006/.001	437.4 (87.4)	270.2 (95.8)
2 nd – Coarse	70	9.0 – 8.9	1871/3783	.0006/.001	445.0 (88.9)	271.9 (96.4)
2 nd – Fine	88	8.2 – 8.5	1878/3941	.0006/.001	446.0 (89.1)	271.8 (96.3)

** ID76 just started oscillations when the run was interrupted. It is currently at a max value, therefore I would expect the final thrust to decrease by an estimated 1-2 mN. The L2-norm is in a region where oscillations are generally within acceptable limits. The conclusions made below are therefore presumed valid.

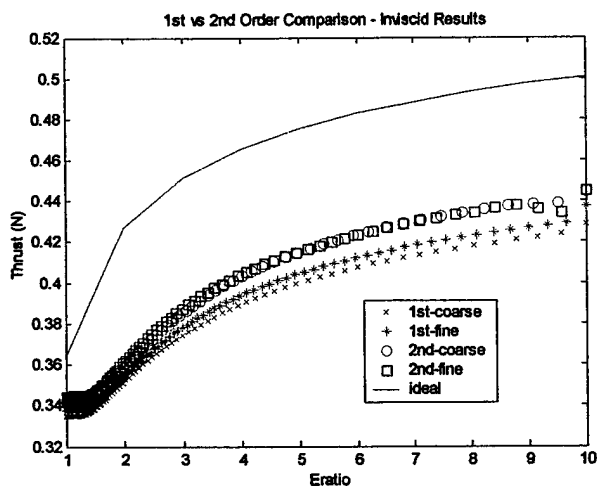


Figure 17-2. Inviscid Thrust Comparison of 1st and 2nd Order

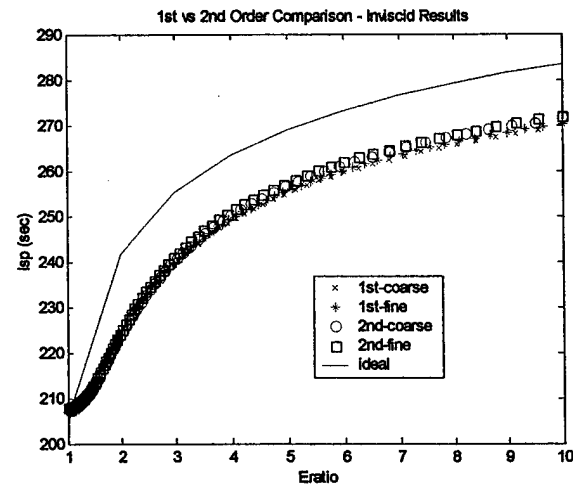


Figure 17-3. Inviscid Isp Comparison of 1st and 2nd Order

The results above indicate that an increase in mesh density for the 2nd order scheme changes only slightly the thrust at the exit plane. On the other hand, a change in the 1st order scheme produce a significant difference in the exit thrust. The convergence of the 1st and 2nd order schemes is therefore valid for the inviscid scenario.

The problem with increasing the mesh density is the increase in computational time. Experience with several mesh sizes has produced the following correlation of figure 17-4 between the number of cells in a given grid and the number of time steps accomplished each minute.

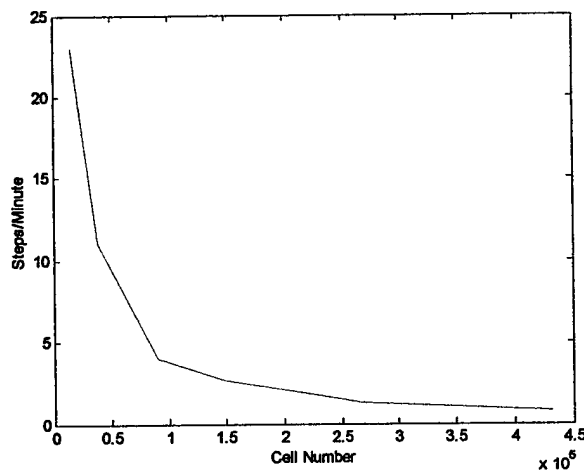


Figure 17-4. Steps/Minute vs Cell Number

Therefore, since the 1st order scheme showed an increase in exit thrust with the 250% increase in mesh density, and the 2nd order scheme stayed the same, I made the assumption that the problem was mesh dependent and with additional increases in mesh density the difference between the two schemes would continue to decrease. Using a mesh similar to id70 required about 24 hours to converge, starting from the initial conditions.

17.1.2 Viscous

From this point, I moved to the viscous effects. Figure 17-5 is a contour plot of the axial velocity similar to the previous inviscid contour plot.

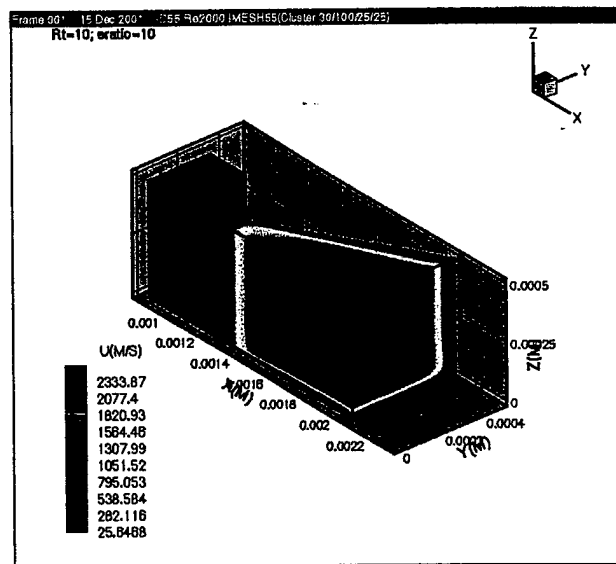


Figure 17-5. Contour Plot of Axial Velocity Including Viscosity

This physical geometry, at a chamber temperature of 3000 K (aspect ratio = 10), corresponds to a throat Reynolds number of ~2000. A further decrease in Reynolds number results in an increase in the viscous effects.

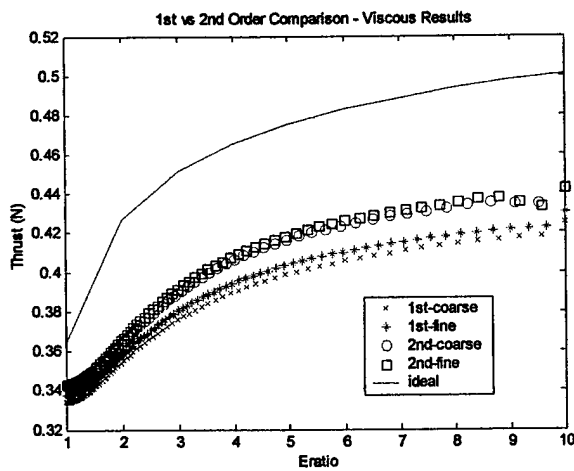
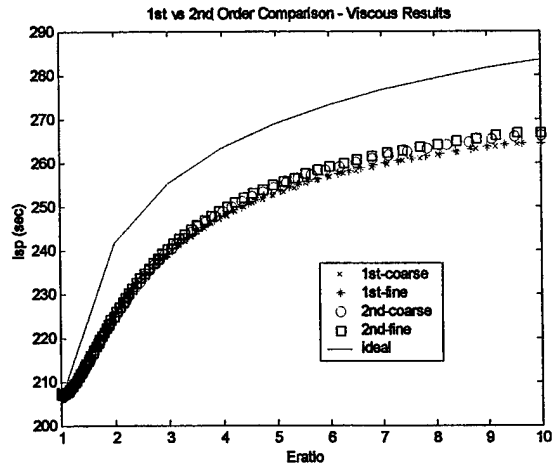
Similar to the mesh density analysis performed for the inviscid conditions, it is necessary to prove that the 1st and 2nd order schemes agree with one another to validate the setup of the grid and numerical algorithm. In addition to mesh density, viscous effects require the investigation of the y-plus value. This value links the grid size to the viscous effects. According to Amtec Engineering, for a laminar flow the y-plus value should be near unity¹¹⁰. Once this condition is satisfied, we can look at the thrust and Isp results to verify whether or not the 1st and 2nd order schemes are within sufficient limits to accept the validity of the code. Note that initially the error when compared with the ideal thrust value at these physical dimensions is about 2.8% between the 1st and 2nd order. By increasing the mesh density by approximately 250% in each case we decrease the error to approximately 0.6% as shown by the tables 17-5/17-6 and figures 17-6/17-7.

Table 17-5. Grid Data for Viscous Verification of Rt=10

Case	ID #	Total Cells	Divergence Cells	Axial Points	Radial/Height
1 st – Coarse	56	277,095	208,299	30/110/5/4	50/40
1 st – Fine	89	638,911	372,939	40/130/15/40	60/50
2 nd – Coarse	55	93,960	68,904	30/100/5/4	25/30
2 nd – Fine	79	237,276	165,789	35/110/5/10	40/40

Table 17-6. Viscous Results

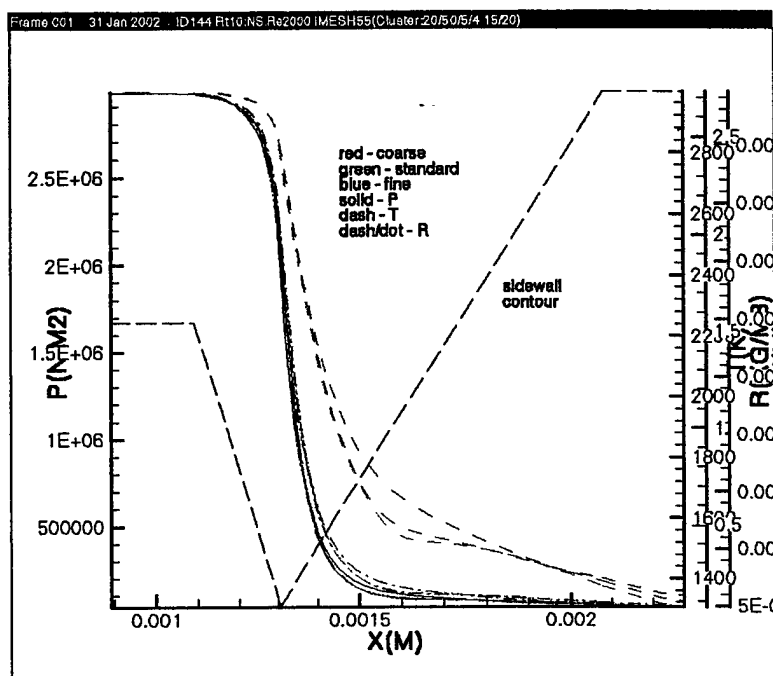
Case	ID #	Z2 - Z3 L2-norm	Re (throat/exit)	Kn (throat/exit)	F(mN): (% ideal)	Isp(sec): (%ideal)	M_dot(kg/s) (%ideal)
1 st - Coarse	56	8.3 - 8.4	1890/3839	.0006/.003	425.0 (84.9)	264.6 (93.8)	4.094E-5 (90.6)
1 st - Fine	89	7.9 - 8.4	1902/3969	.0006/.003	430.1 (85.9)	264.4 (93.7)	4.228E-5 (93.5)
2 nd - Coarse	55	8.7 - 8.8	1889/4151	.0007/.003	442.7 (88.4)	266.3 (94.4)	4.200E-5 (92.9)
2 nd - Fine	79	8.7 - 9.5	1888/4157	.0006/.003	442.3 (88.3)	266.6 (94.5)	4.146E-5 (91.7)

Figure 17-6. Viscous Thrust Comparison of 1st and 2nd OrderFigure 17-7. Viscous Isp Comparison of 1st and 2nd Order

As with the inviscid results, increasing the mesh density for the 2nd order scheme did not significantly change the exit thrust and yet the 1st order scheme increased by 6 mN, thereby decreasing the absolute difference (related to thrust) between the two schemes from 2.8% to 2.2%. The difference between the 1st and 2nd order schemes is as expected for the viscous calculations. Considering that in the 1st order case the spatial discretization of the convection terms in 1st order creates inaccuracies in modeling the viscous terms, even increasing the mesh density will not provide an accurate answer. This is verified by the fact that the same mesh for viscous and inviscid solutions produced different decreases in the difference between the 1st and 2nd order schemes. Therefore, the numerics of the code are assumed valid for all cases considered from this point forward.

17.1.3 Mesh Refinement Study of Aspect Ratio = 10

Having provided sufficient results that the 1st and 2nd order schemes agree with one another, the next step would naturally be a grid refinement study of the 2nd order scheme. Fortunately, the previous investigation between the 1st and 2nd order schemes verified that there was an insignificant difference between the 1st and 2nd meshes. In order to further validate the 2nd order scheme, it is necessary to do another analysis of an even coarser mesh. Therefore, redefining the previous coarse mesh as the standard mesh, we do another analysis of a '15/50/5/4 15/20' mesh. The results are below in figures 17-8 through 17-10 and tables 17-7/17-8.

Figure 17-8. Axial Contours of P , $\rho(R)$, and T for 2nd Order Mesh RefinementTable 17-7. Grid Data of 2nd Order Mesh Refinement, Rt=10

Case	ID #	Total Cell #	Divergence Cells	Axial Points	Radial/Height
2 nd – Coarse	144	675,000	15,000	15/50/5/4	15/20
2 nd – Standard	56	104,250	75,000	30/100/5/4	25/30
2 nd – Fine (1)	79	256,000	176,000	35/110/5/10	40/40
2 nd – Fine (2)	147	236,600	182,000	30/130/5/4	35/40

Table 17-8. Results of Mesh Refinement, Rt=10

Case	ID #	Z2 – Z3 L2-norm	Re (throat/ exit)	Kn (throat/ exit)	F(mN): (% ideal)	Isp(sec): (%ideal)	M_dot(kg/s) (%ideal)
2 nd – Coarse	144		1886/3829	.0006/.003	434.5 (86.8)	263.4 (93.4)	4.204E-5 (93.0)
2 nd – Standard	55	8.7 – 8.8	1889/4151	.0007/.003	442.7 (88.4)	266.3 (94.4)	4.200E-5 (92.9)
2 nd – Fine (1)	79	8.7 – 9.5	1888/4157	.0006/.003	442.3 (88.3)	266.6 (94.5)	4.146E-5 (91.7)
2 nd – Fine (2)	147	10.4 – 8.5	1887/4168	.0007/.004	442.8 (88.4)	266.9 (94.6)	4.2281E-5 (93.5)

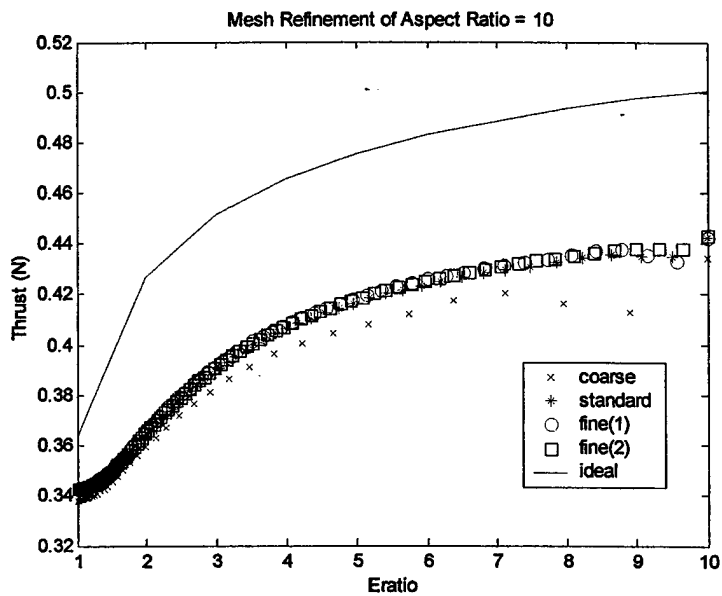


Figure 17-9. Thrust vs Eratio of 2nd Order Mesh Refinement

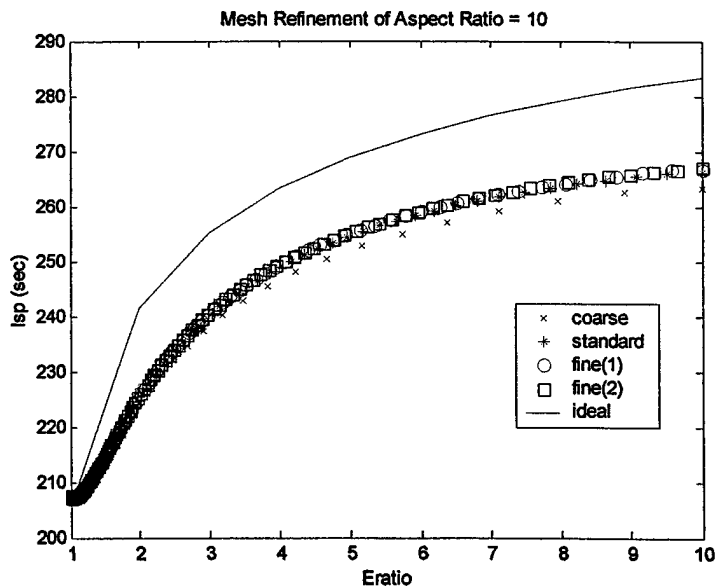


Figure 17-10. Isp vs Eratio of 2nd Order Mesh Refinement

Further validation was performed for the same chamber conditions but at smaller Reynolds numbers of 1500, 1000, and 500. The hope here is that by applying the coarse mesh to smaller scales of the same geometry, it is possible to verify the assumption that further grid

refinement studies are not necessary. The y-plus values tabulated model the same shape as the figure for Reynolds number of 2000, the max occurring as a sharp spike at the throat from the endwall. The results of table 17-9 validate this assumption:

Table 17-9. Mesh Refinement Verification of $T_c = 3000$ K, $R_t = 10$

ID #	Mesh	Max y+	Re	F (mN)	% Standard	Isp (sec)	% Standard
115	Standard	.54 / .9	500	26.7 ***	1.87	258.5	0.85
141	Coarse	.51 / .85	500	26.2	-	256.3	-
116	Standard	.8 / 1.5	1000	109.3	1.83	263.2	1.06
142	Coarse	.8 / 1.5	1000	107.3	-	260.4	-
117	Standard	.9 / 2	1500	248.1	1.85	265.2	1.06
143	Coarse	.9 / 2	1500	243.5	-	262.4	-
118	Standard	1 / 2.5	2000	442.7	1.89	266.3	1.09
144	Coarse	1.1 / 2.5	2000	434.5	-	263.4	-

17.2 Y-plus Reduction

Although engineers at Amtec¹¹⁰ seemed to think that a y-plus value at the throat of slightly greater than one would have little effect on the results, I decided to reduce the y-plus value to verify the recommendation. By reducing the normal spacing of the first point from 0.005 of the endwall points 15-20, 23-24, 31-32 to 0.001, the following results of table 17-10 were obtained:

Table 17-10. F/Isp Variation of $Re=2000$ for Spacing from 0.005 to 0.001

ID #	Mesh	1 st Spacing	Max y+	F (mN)	% Standard	Isp (sec)	% Standard
173	Standard	0.005	1/ 2.5	442.7	0.09	266.3	0.00
145	Standard	0.001	1/ 0.6	442.3	-	266.3	-
144	Coarse	0.005	1.1/2.5	434.5	1.15	263.4	0.04
146	Coarse	0.001	1/0.65	434.0	-	263.3	-

The above results validate the presumption that the y-plus value of the throat would not significantly change the end results at the exit plane. The y-plus values of the 1st/2nd order viscous study were not calculated explicitly, but based on the same mesh spacing and geometry as

id144, the expected y-plus values are assumed fairly consistent with those obtained for id144 (1.1/2.5). Therefore, the results previously obtained in the viscous sections by using a slightly higher number than unity for the y-plus value are still assumed valid. Nonetheless, in order to obtain the most accurate results possible, further calculations of data were performed using a y-plus value based on a first spacing of 0.002. The result was a reduction from a maximum y-plus value of 2.5 for spacing of 0.005 to near unity at 0.002. Below is the graphical depiction of y-plus data for ID118 (spacing = 0.002) in figure 17-11.

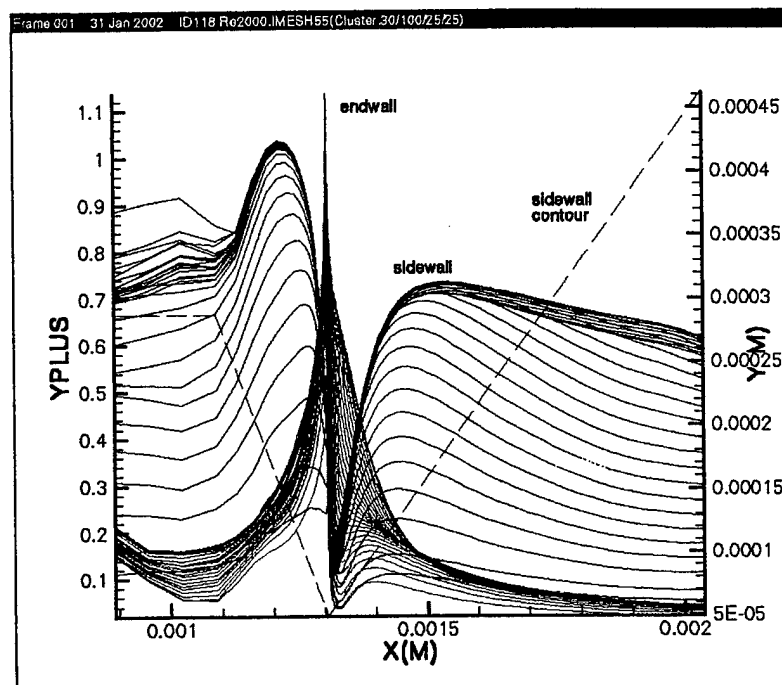


Figure 17-11. Y-plus Values (1 / 1.1) of ID118 (Spacing = 0.002 @ endwalls)

The overall effect on the exit plane is summarized below in table 17-11.

Table 17-11. F/Isp Variation of Re=2000 for Endwall Spacing of 0.001, 0.002, 0.005

ID #	Mesh	1 st Spacing	Max y+	F (mN)	% Standard	Isp (sec)	% Standard
173	Standard	0.005	.9 / 2.5	442.7	-	266.3	-
118	Standard	0.002	1.0 / 1.1	442.7	0	266.3	0
145	Standard	0.001	1.0 / .6	442.3	0.09	266.3	0
170	Standard	0.005	.54 / .9	26.8	-	258.5	-
115	Standard	0.002	.55 / .35	26.7	0.37	258.6	0.04

The reduction from the spacing used in the validation runs of 0.005 to 0.002 does not have a substantial effect on the results obtained with 0.005. A further reduction to 0.001 below unity shows a slight decrease in thrust, but not significant enough to warrant further investigation. Therefore, in further analysis, the first spacing is reduced to 0.002 to ensure that even at the spike of the throat, the y-plus value will be at or below unity.

One other note before full analysis of thrust/Isp runs was the discovery of a minor input error for the thermal coefficients of water within the chemical section of the INCA code. As described previously, the thermal coefficients are used from the NASA polynomial tables. The second value in the 1000 – 6000 K range was inputted as -2.3E-3 during the validation runs instead of -2.03E-3. While this is a seemingly insignificant error, two runs were initiated to ensure no unnecessary errors had been introduced. After 2000 time steps, the L2-norm values of 2 zones were off by only thousandths of a point and the thrust levels had not changed. This error made its way into some of the F/Isp results, but using the conclusion above it is deemed inconsequential.

In order to perform an aspect ratio analysis, it is necessary to perform a mesh refinement study of the aspect ratios in question. It is assumed that the 1st / 2nd order agreeance from the aspect ratio of 10 verifies the code, therefore further runs between 1st and 2nd order will not be carried out.

17.3 Mesh Refinement Study of Aspect Ratio = 5

Using the same analysis as before, a mesh analysis was performed on an aspect ratio of 5.

Table 17-12. Grid Data for Mesh Refinement Study of Aspect Ratio = 5

ID #	Case	Total Cell #	Divergence Cells	Axial Points	Radial/Height
151	Coarse	19,950	13,034	20/50/5/4	15/20
152	Standard	87,000	68,904	30/100/5/4	25/30
153	Fine (1)	218,790	171,054	30/130/5/4	35/40
154	Fine (2)	398,860	321,244	30/150/5/4	45/50

Graphical and tabulated values are listed below in figures 17-12/17-13 and table 17-13.

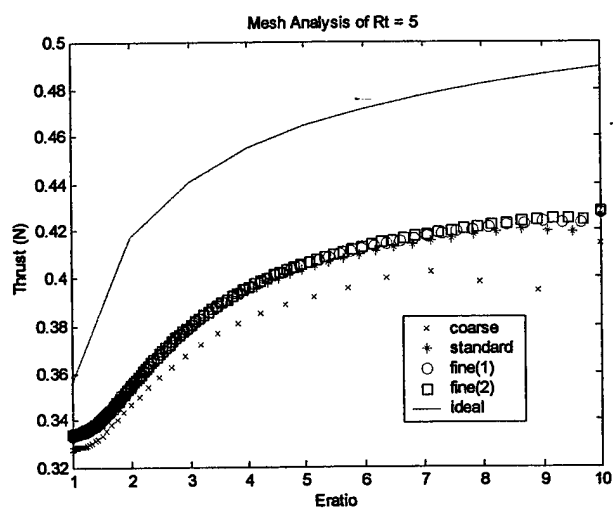


Figure 17-12. Mesh Analysis of Aspect Ratio = 5, Isp

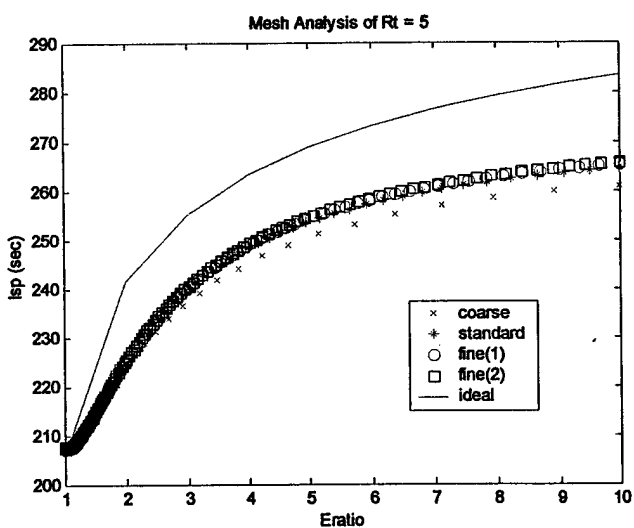


Figure 17-13. Mesh Analysis of Aspect Ratio = 5, Thrust

Table 17-13. Results of Mesh Analysis of Aspect Ratio = 5

Case	ID #	Y+ max	Re (throat/exit)	Kn (throat/exit)	F(mN): (%ideal)	Isp(sec): (%ideal)	M_dot(kg/s) (%ideal)
Coarse	151	.8 / 1.1	2607/2792	.0004/.004	414.7 (84.8)	260.9 (92.5)	4.051E-5 (91.7)
Standard	152	.7 / .8	2631/3159	.0004/.005	426.5 (87.2)	264.5 (93.8)	4.1089E-5 (93.0)
Fine (1)	153	.6 / .7	2629/3321	.0005/.005	427.9 (87.5)	265.4 (94.1)	4.1087E-5 (93.0)
Fine (2)	154		2628/3331	.0005/.006	428.1 (87.5)	265.7 (94.2)	4.107E-5 (92.9)

As noted above, the difference between fine (1) and fine (2) is negligible. In addition, the difference between the standard mesh results and fine results is only about 0.3% of thrust and Isp. Therefore, to reduce computational time the standard mesh will be used for further calculations accepting the error minimal error from above. Since the goal is a comparison with thrust and Isp efficiencies of different aspect ratios, we see that an aspect ratio of 10 has a thrust efficiency of 88.4 and Isp efficiency of 94.4. Using the standard mesh a measure of comparison does provide a small difference in the magnitude of the difference between the two aspect ratios, but the overall conclusion is still the same that an aspect ratio of 10 outperforms the aspect ratio of 5.

17.4 Mesh Refinement Study of Aspect Ratio = 1

Since a majority of numerical and experimental work has been performed for aspect ratios less than or equal to 1, this aspect ratio is included as a means of comparison with higher aspect ratios. The difference in the mesh size is solely a switch of the radial and height grid points compared with the aspect ratios of 5, 10.

Table 17-14. Grid Data for Aspect Ratio = 1

ID #	Case	Total Cell #	Divergence Cells	Axial Points	Radial/Height
148	Coarse	19,950	13,034	19/49/4/3	19/14
149	Standard	87,000	68,904	29/99/4/3	29/24
150	Fine	218,790	171,054	29/129/4/3	39/34

Results of an aspect ratio = 1 are in figures 17-14/17-15 and table 17-15.

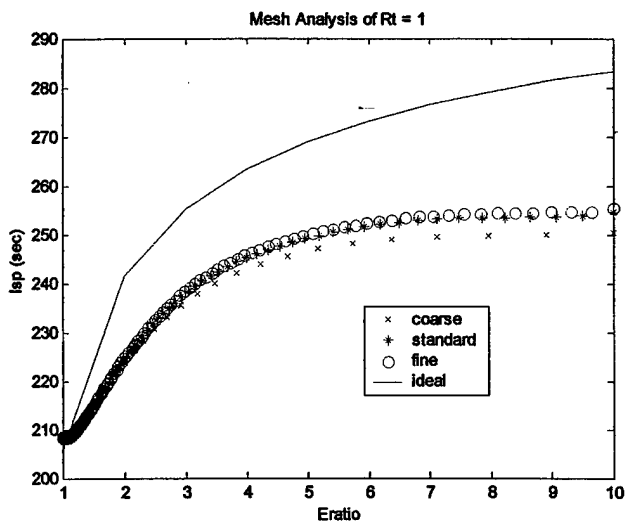


Figure 17-14. Mesh Analysis of Aspect Ratio = 1, Isp

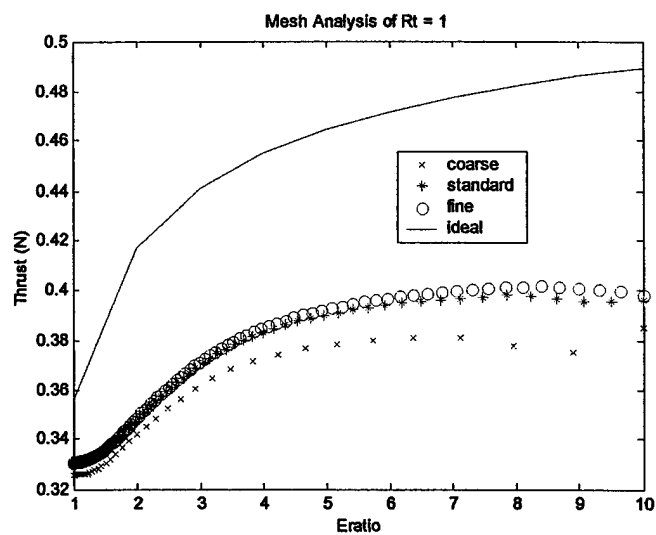


Figure 17-15. Mesh Analysis of Aspect Ratio = 1, Thrust

Table 17-15. Results for Mesh Analysis of Aspect Ratio = 1

Case	ID #	Y+ max	Re (throat/exit)	Kn (throat/exit)	F(mN): (%ideal)	Isp(sec): (%ideal)	M_dot(kg/s) (%ideal)
Coarse	148	.8 / 1.1	5817/1348	.0002/.006	384.8 (78.7)	250.4 (88.8)	3.916E-5 (88.6)
Standard	149	.8 / 1.2	5870/1491	.0002/.008	396.2 (81.0)	254.5 (90.2)	3.967E-5 (89.8)
Fine	150	.7 / 1.1	5871/1523	.0002/.008	398.1 (81.4)	255.4 (90.5)	3.973E-5 (89.9)

Because the difference between the standard and fine mesh sizes is roughly the same as the aspect ratio of 5, it is presumed that further refinement of the mesh will produce a negligible increase. Therefore, the standard mesh size will also be used for an aspect ratio of 1 accepting the small difference in increased thrust and Isp. Overall conclusions will not be affected by this assumption.

17.5 Mesh Refinement Study of Aspect Ratio = 15

An aspect ratio of 15 was analyzed for only two cases ($T_c = 3000\text{ K}$ @ $F = 501\text{mN}$ and 31mN) to see if a further increase would decrease the overall efficiency as the sidewall effects become more pronounced.

Table 17-16. Grid Data for Mesh Study of Aspect Ratio = 15

ID #	Case	Total Cell #	Divergence Cells	Axial Points	Radial/Height
176	Coarse	28,560	16,464	29/49/4/3	14/24
177	Standard	110,160	80,784	29/99/4/3	24/34
178	Fine	246,840	192,984	29/129/4/3	34/44

Results of an aspect ratio = 15 are in figures 17-16/17-17 and table 17-17.

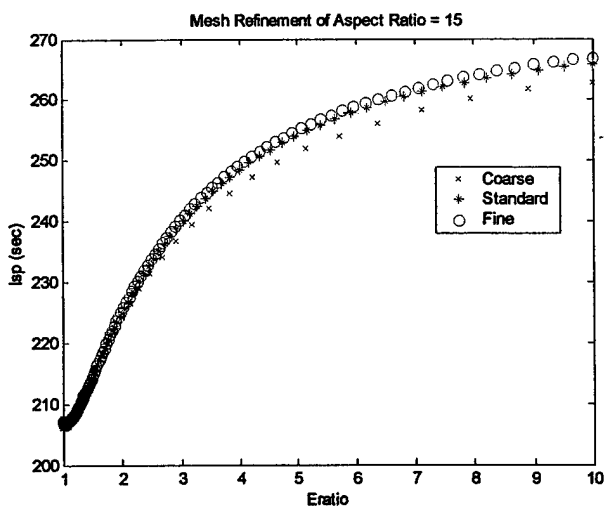


Figure 17-16. Mesh Analysis of Aspect Ratio = 15, Isp

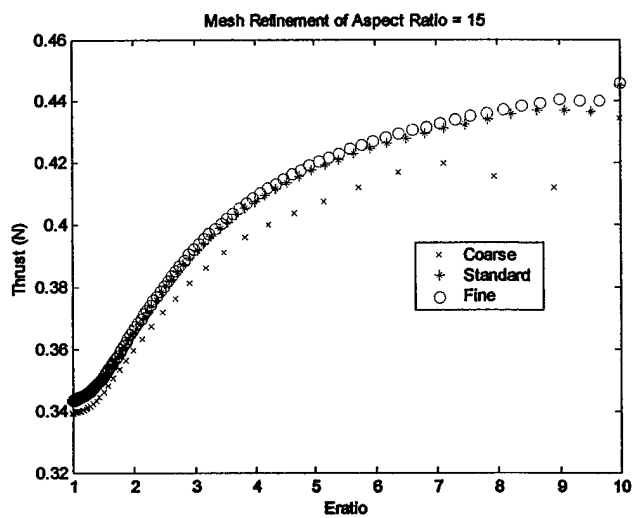


Figure 17-17. Mesh Analysis of Aspect Ratio = 15, Thrust

Table 17-17. Results for Mesh Analysis of Aspect Ratio = 15

Case	ID #	Y+ max	Re (throat/exit)	Kn (throat/exit)	F(mN): (% ideal)	Isp(sec): (%ideal)	M_dot(kg/s) (%ideal)
Coarse	176	.55 / .5	1537/3055	.0008/.003	434.4 (86.4)	262.8 (93.2)	4.213E-5 (92.7)
Standard	177	.55 / .55	1542/3326	.0008/.003	444.9 (88.5)	265.7 (94.2)	4.266E-5 (93.9)
Fine	178	.45 / .45	1542/3326	.0008/.003	445.9 (88.7)	266.8 (94.6)	4.258E-5 (93.7)

In this case, the difference in thrust for the three mesh sizes is actually smaller than for an aspect ratio of 5. The Isp difference is slightly higher (0.1%), but assumed negligible. Therefore, further mesh refinement is not necessary and the standard grid will be acceptable for further analysis.

Comparison of the four aspect ratios for a chamber temperature of 3000 K and thrust level of 501 mN results in the following:

Table 17-18. Results Summary for Mesh Refinement Studies / Legend for Figure 17-18

Mesh	Mesh id#	F-eff (%)	Isp-eff (%)	Legend
Rt,1 coarse	1	0.787	0.888	red square
Rt,1 stndrd	2	0.81	0.902	green circle
Rt,1 fine	3	0.814	0.905	blue triangle
Rt,5 coarse	4	0.848	0.925	red square
Rt,5 stndrd	5	0.872	0.938	green circle
Rt,5 fine (1)	6	0.875	0.941	blue triangle
Rt,5 fine (2)	7	0.875	0.942	black diamond
Rt,10 coarse	8	0.868	0.934	red square
Rt,10 stndrd	9	0.884	0.944	green circle
Rt,10 fine (1)	10	0.883	0.945	blue triangle
Rt,10 fine (2)	11	0.884	0.946	black diamond
Rt,15 coarse	12	0.864	0.932	red square
Rt,15 stndrd	13	0.885	0.942	green circle
Rt,15 fine	14	0.887	0.946	blue triangle

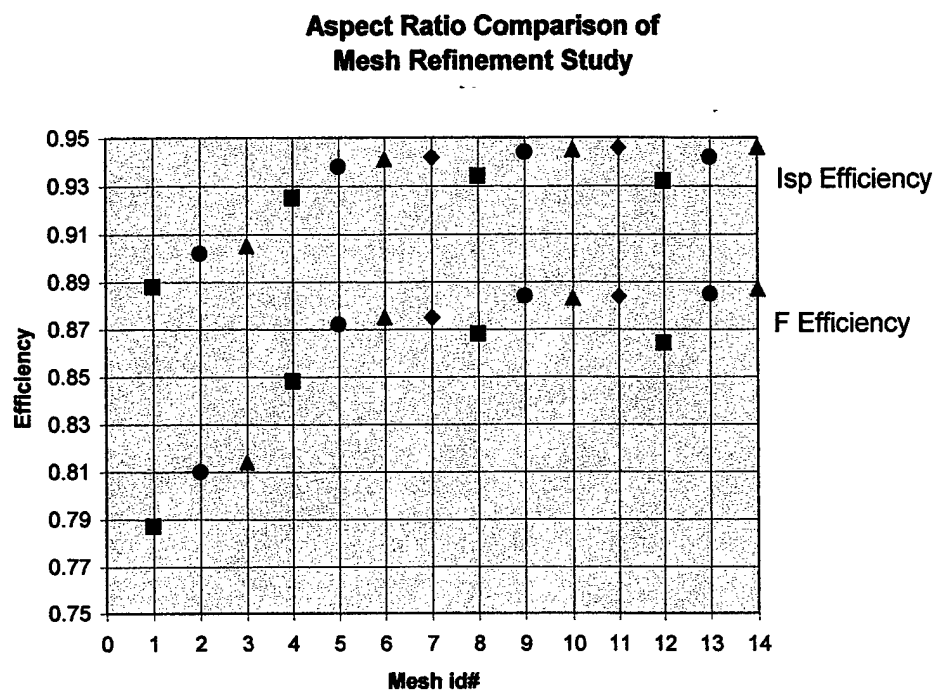


Figure 17-18. Aspect Ratio Comparison of Mesh Refinement Study
** Reference table 17-18 for legend

For the graph and table above, first note that the difference between the standard-fine(1)-fine(2) mesh results is minimal for each aspect ratio. Therefore, it is valid to assume that use of the standard mesh is sufficient. Another validation of this is the variation in efficiency as the aspect ratio increases. Whether comparing standard-standard, fine(1)-fine(1), or fine(2)-fine(2), the trend is generally the same. The only exception is between aspect ratios of 10 and 15. For the thrust trnd, a standard-standard comparison yields a slight decrease in efficiency from aspect ratio 10 to 15. Whereas, for the same aspect ratios, the fine(1)-fine(1) comparison yields a slight increase. Because the respective difference between the two methods is so small (-0.2% and +0.1%) respectively, they will be considered equal in the results discussion below. Investigation of further increase in aspect ratio is left for additional research.

17.6 Results Comparison with Past Efforts

While to the author's knowledge, no other attempts have been made to model the same physical geometry and gas conditions, a relative check of achieved efficiency levels in this section will provide confidence in the results.

Table 17-19. Results Comparison with Past Efforts

Case	Exp/ Num*	Eratio	Half- angle	Rt	Throat Re	Dt (μm)	Tc (K)	Pc (bar)	η_F	η_Isp
1	Num ³⁷	10	15	1	400	300	300	0.1	.05	.835
	INCA	10	30	1	1489	77.9	3000	30	.735	.839
2	Exp ^{47**}	8.2	20	4.7	1000	65	299		.755	
	INCA	10	30	5	1025	35	2000	30	.746	
3	Exp ^{47**}	8.2	20	4.7	2000	65	299		.825	
	INCA	10	30	5	2631	138	3000	30	.87	
4	Exp ^{47**}	16.9	20	8.2	1900	37.5	299		.86	
	INCA	10	30	10	1889	99.05	3000	30	.884	
5	Num ²⁸	100	15	1	205		1000			.429
	Num ²⁶	7.1	15	1	1300		297	10		.957
	INCA	10	30	1	1489	77.9	3000	30		.839

* Exp – experimental; Num – numerical

** these values for efficiency do not include divergence losses

Experimental data was obtained from Bayt *et al*⁴⁷ and is the closest source of verification to the runs conducted in INCA. Data could only be obtained for comparison with the thrust efficiencies. For case 2, the thrust efficiencies compare relatively well. In fact, there the INCA code predicts a slightly smaller performance level. This experimental efficiency must be corrected for nozzle divergence losses. According to Dr. Humble, a nozzle half-angle of 20 should only produce an error of 3%⁴⁴. Correcting for this puts the efficiency at around 72.5% which is still in the vicinity of what INCA predicts for this Reynolds number. The nozzle angle of 20 is expected to have a slightly smaller efficiency level as already suggested, so this may be the source of error. Case 4 shows for a larger expansion ratio and relatively same aspect ratio a slight difference in expected results for thrust efficiency. Including the 3% for divergence losses results in nearly 5% difference. This could be the result of both the nozzle half-angle difference and increased expansion ratio. Case 3 also shows a large difference, particularly when including the 3% for divergence losses. This can be accounted for in the large disparity between Reynolds numbers. Cases 1 and 5 are compared with other numerical results for an aspect ratio of 1. The

high difference in Isp of 95 compared to the INCA result of 84 is perplexing. The compared case only used a 2D analysis, so this may account for the difference since the endwall boundary layer played a significant role in this case of the aspect ratio being equal to 1. The case 1 difference in thrust efficiency is also a point of interest, although the smaller half angle and smaller Reynolds number indicates that the flow may be completely subsonic when exiting the nozzle plane. There is a disparity with between the thrust and Isp efficiencies of the flow nonetheless.

The results above, particularly with the experimental data of Bayt *et al*¹⁷, give confidence that the results in the following sections are accurate as far as the thrust is concerned. It will be shown that when considering thrust efficiencies, it is strictly a function of Reynolds number and has little dependence on temperature.

Chapter 18: Results of Aspect Ratio Analysis

Before considering the high-temperature effects, it is necessary to investigate the other variables contributing to micronozzle performance. Having gained an understanding of the optimum expansion ratio, aspect ratio and expansion angle, it is then feasible to investigate the performance of the high-temperature viscous effects. We have assumed that a truncated nozzle (smaller expansion ratio) will produce better results than an ideally expanding gas of an infinite nozzle due to the boundary layer envelopment of the supersonic core. This value has been set at 10, although further research may yield that an even larger expansion ratio will yield greater efficiencies (i.e., the gases will expand more than the boundary layer will decrease the core flow). The nozzle half-angle is set at 30 based on a previous study²⁴. Therefore, we are left with the aspect ratio.

Bayt⁴³ performed a 2D analysis assuming that the boundary layer growth along the sidewall would be the same as that along the endwalls. Another study showed that the growth along the endwalls is about half that of the growth along the sidewalls²⁷. In this study it was previously conceived to minimize the effect of the endwalls by increasing the aspect ratio. For a predetermined thrust level, increasing the aspect ratio will decrease the distance between the sidewalls while increasing the distance between the endwalls. As already noted, the Reynolds number has been shown to increase to the point where the distance between the sidewall equals that of the endwall. Increasing the aspect ratio decreases the smallest characteristic parameter used in determining the Reynolds number, but it also allows for the Reynolds number to increase further downstream. Whether or not there is an optimum range for the aspect ratio is the goal of the following section.

The increase of the aspect ratio is dependent upon the availability of the thickness of the material (i.e., ceramic or silicon), machining tolerances and ability to stack nozzles on top of one another. Ender Savrun⁴⁵, president of Sienna Technologies Inc., claims that an alumina ceramic material can produce micronozzles of 100 micron thickness and 80 micron throat diameters. Conceivably the throat diameter can be even further reduced. He suggested that going to silicon will reduce the minimum attainable thickness to 10 microns. Bayt *et al*³⁷ claims that silicon wafers should be at the most 300 μm thick due to ‘small feature distortion’. These tolerances are important when considering the desired thrust levels for given chamber conditions.

As described earlier, at a given thrust level, will a higher throat Reynolds number corresponding to a lower aspect ratio (Reynolds number continually decreasing from the throat to the exit) outperform a higher aspect ratio with a lower throat Reynolds number (increasing towards the exit)? Note that exact values can be found in the results table of Appendix G. Since the ideal thrust slightly varies from aspect ratio to aspect ratio, the comparison value will be the percent efficiency. The following pages of figures 18-1 through 18-24 are contour plots of temperature, velocity and mach number for 3000K of both 31/501mN.

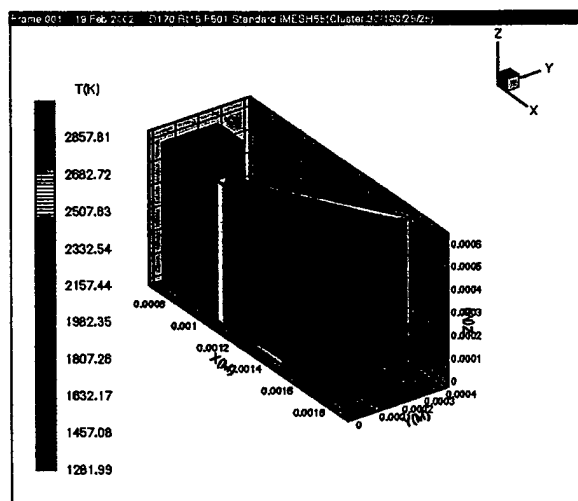


Figure 18-1. T Plot of Rt=15, Tc=3000K

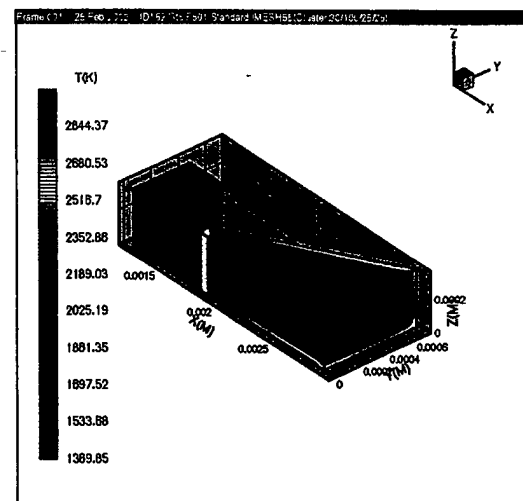


Figure 18-3. T Plot of Rt=5, Tc=3000K

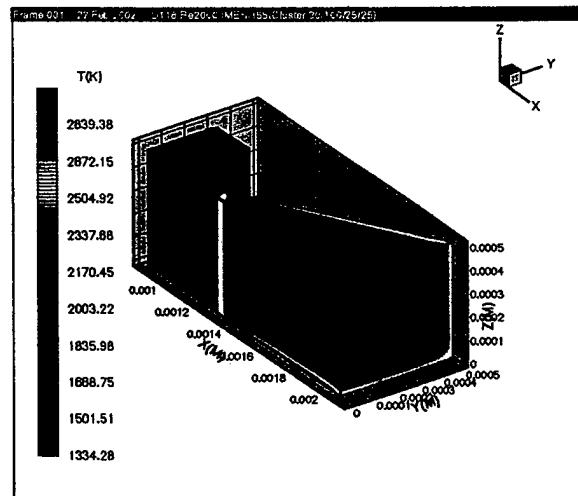


Figure 18-2. T Plot of Rt=10, Tc=3000K

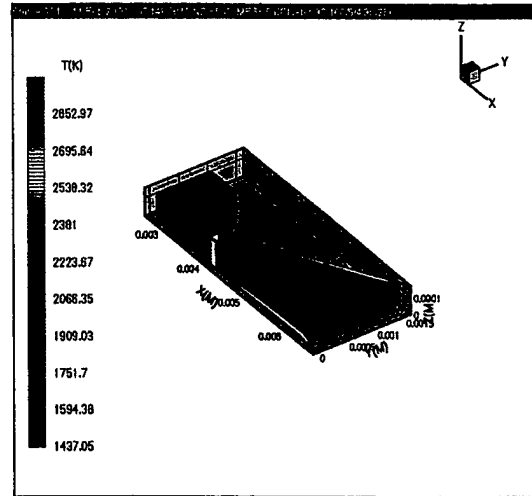


Figure 18-4. T Plot of Rt=1, Tc=3000

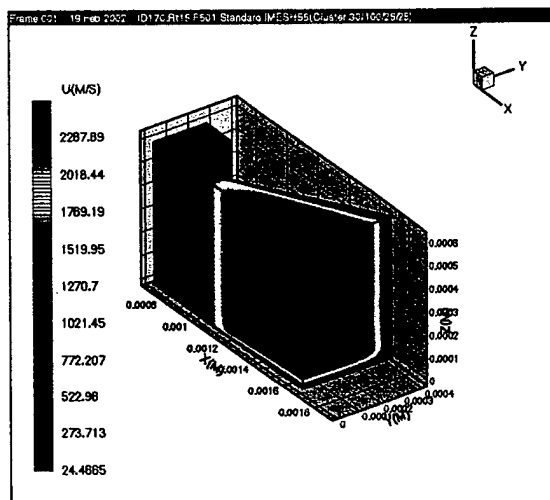


Figure 18-5. Axial Velocity Plot of $R_t=15$,
 $T_c=3000K$, $F=501mN$

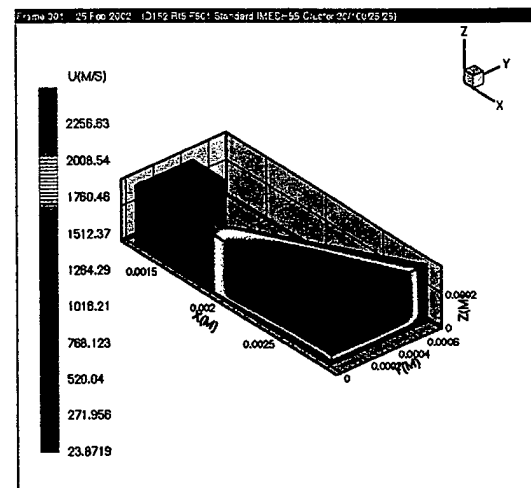


Figure 18-7. Axial Velocity Plot of $R_t=5$,
 $T_c=3000K$, $F=501mN$

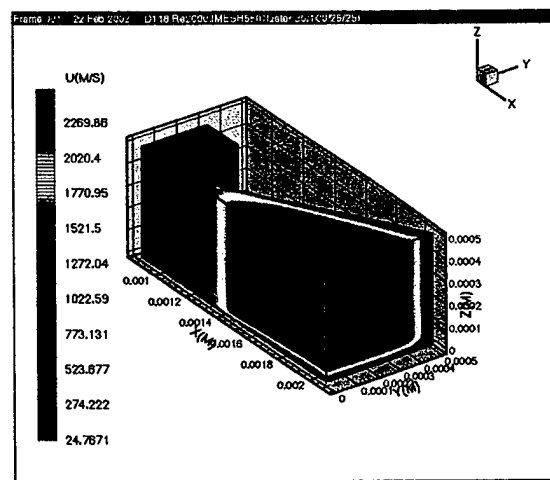


Figure 18-6. Axial Velocity Plot of $R_t=10$,
 $T_c=3000K$, $F=501mN$

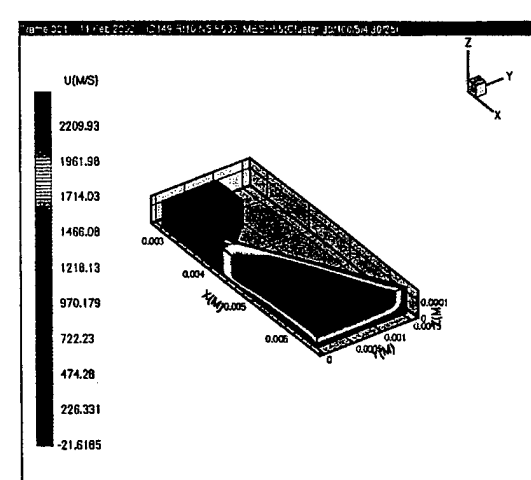


Figure 18-8. Axial Velocity Plot of $R_t=1$,
 $T_c=3000K$, $F=501mN$

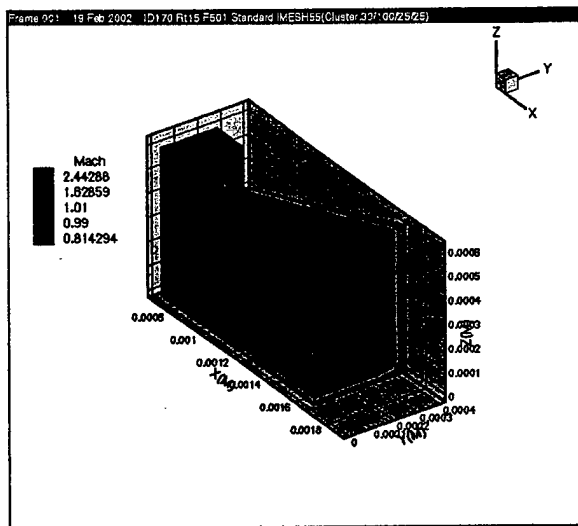


Figure 18-9. Mach Plot of $Rt=15$, $Tc=3000K$, $F=501mN$

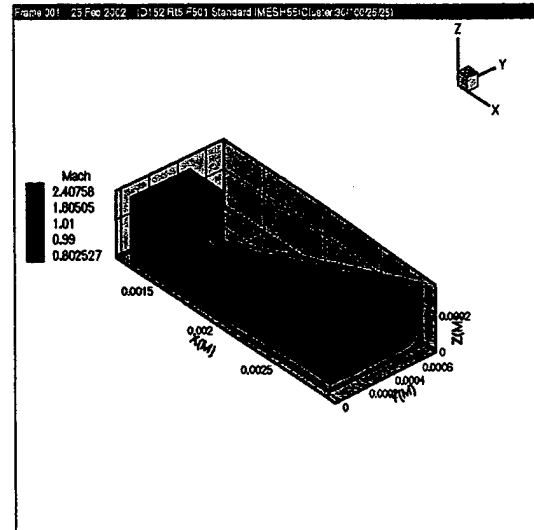


Figure 18-11. Mach Plot of $Rt=5$, $Tc=3000K$, $F=501mN$

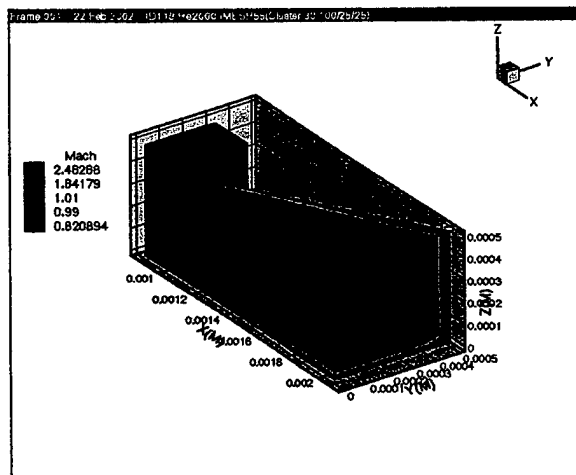


Figure 18-10. Mach Plot of $Rt=10$, $Tc=3000K$, $F=501mN$

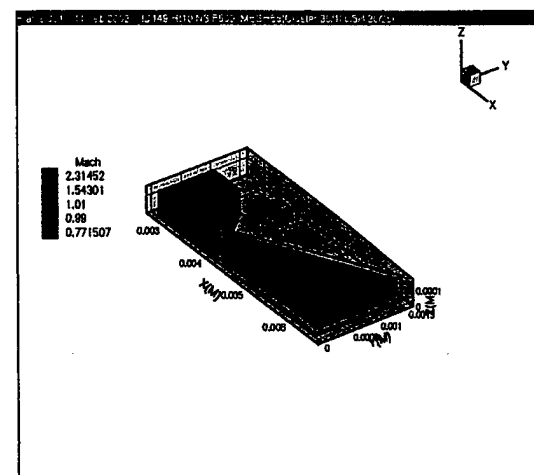


Figure 18-12. Mach Plot of $Rt=1$, $Tc=3000K$, $F=501mN$

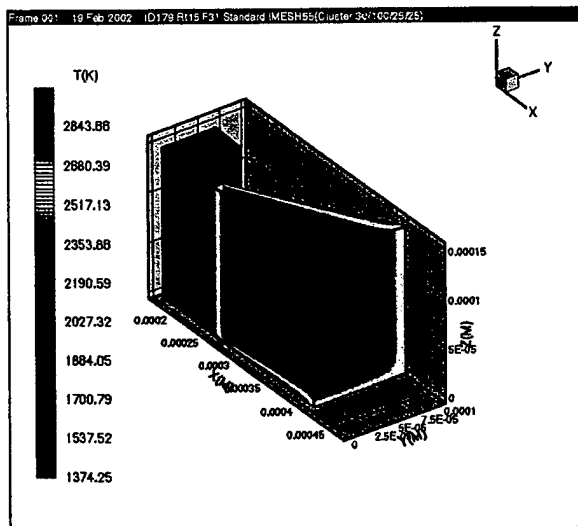


Figure 18-13. T Plot of $R_t=15$, $T_c=3000K$, $F=31mN$

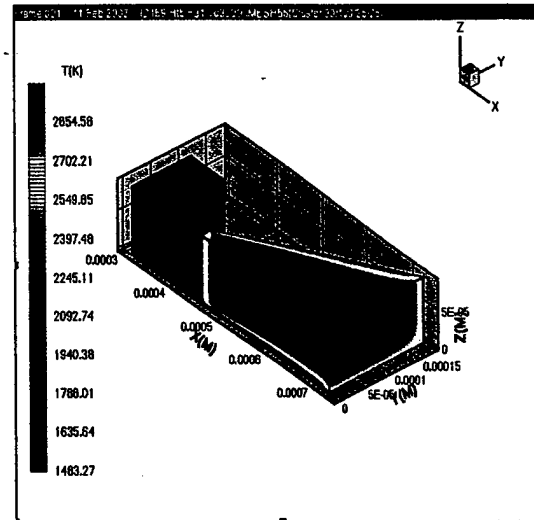


Figure 18-15. T Plot of $R_t=5$, $T_c=3000K$, $F=31mN$

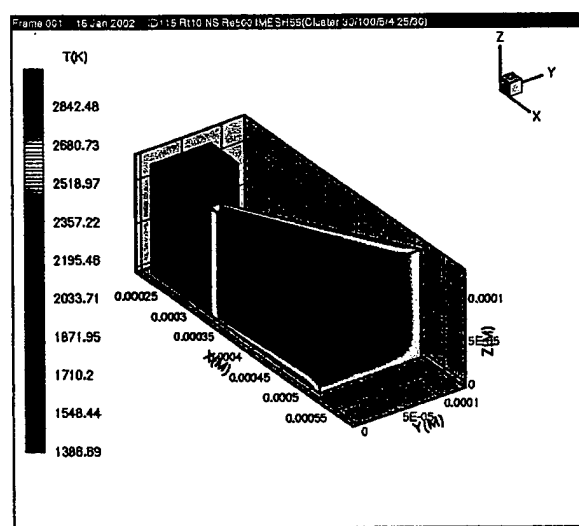


Figure 18-14. T Plot of $R_t=10$, $T_c=3000K$, $F=31mN$

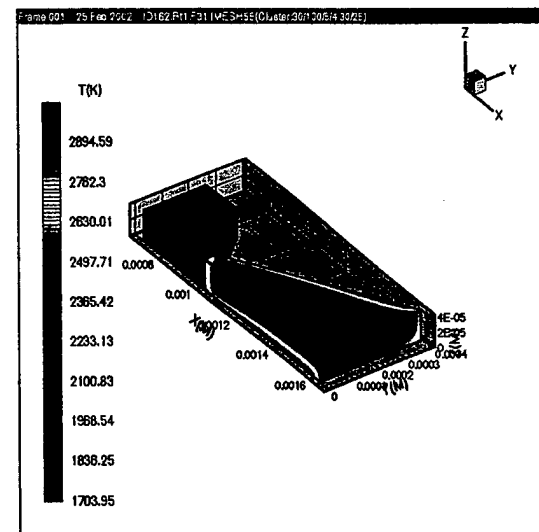


Figure 18-16. T Plot of $R_t=1$, $T_c=3000K$, $F=31mN$

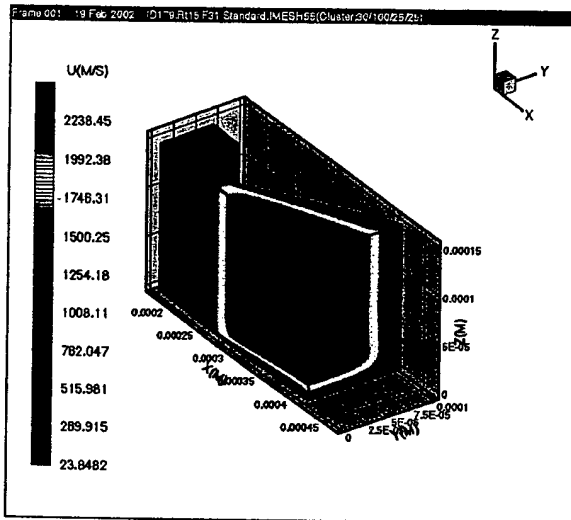


Figure 18-17. Axial Velocity Plot of $Rt=15$, $T_c=3000K$, $F=31mN$

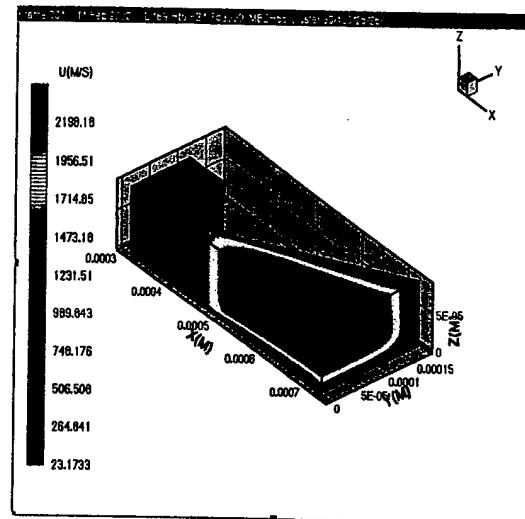


Figure 18-19. Axial Velocity Plot of $Rt=5$, $T_c=3000K$, $F=31mN$

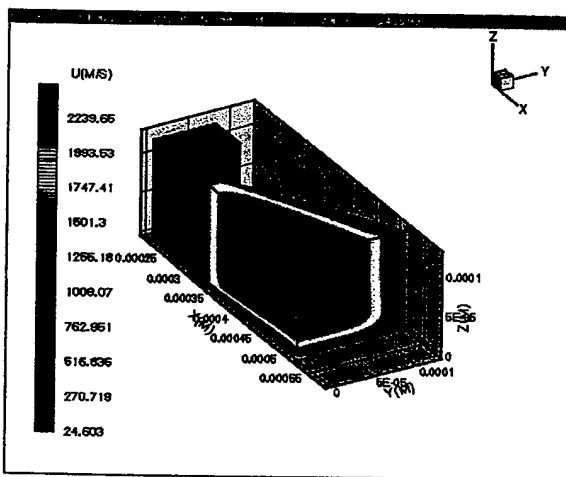


Figure 18-18. Axial Velocity Plot of $Rt=10$, $T_c=3000K$, $F=31mN$

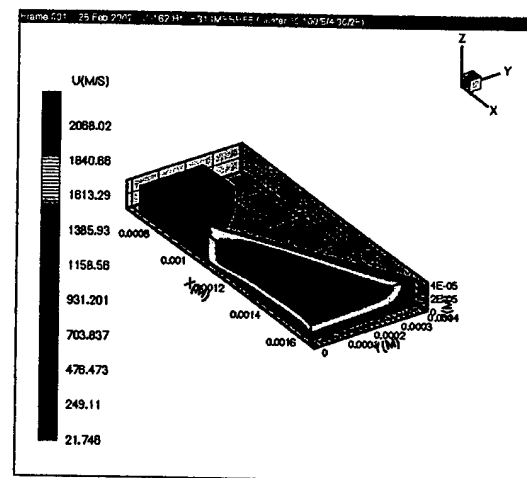


Figure 18-20. Axial Velocity Plot of $Rt=1$, $T_c=3000K$, $F=31mN$

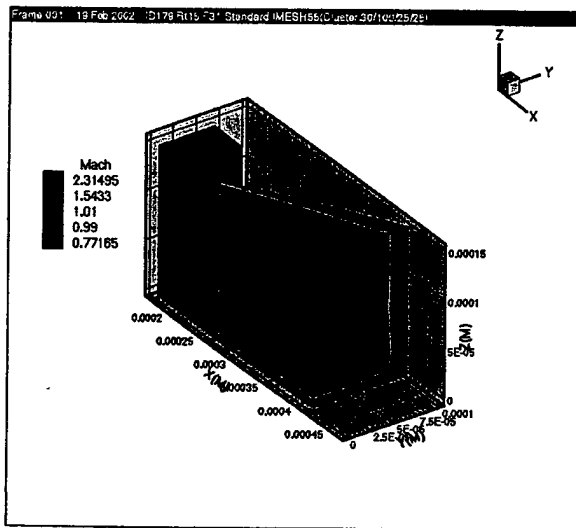


Figure 18-21. Mach Plot of $Rt=15$, $Tc=3000K$, $F=31mN$

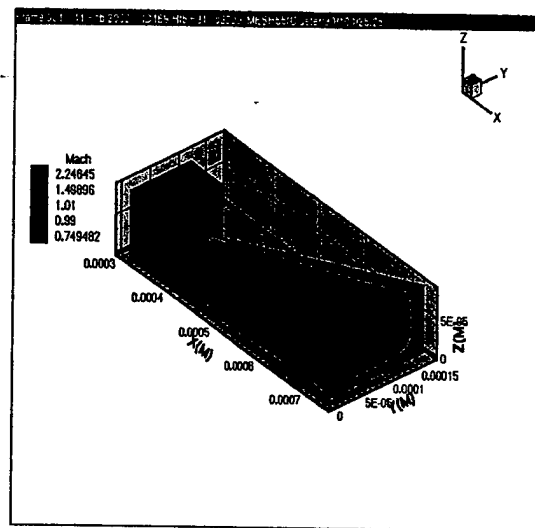


Figure 18-23. Mach Plot of $R_t=5$, $T_c=3000K$, $F=31mN$

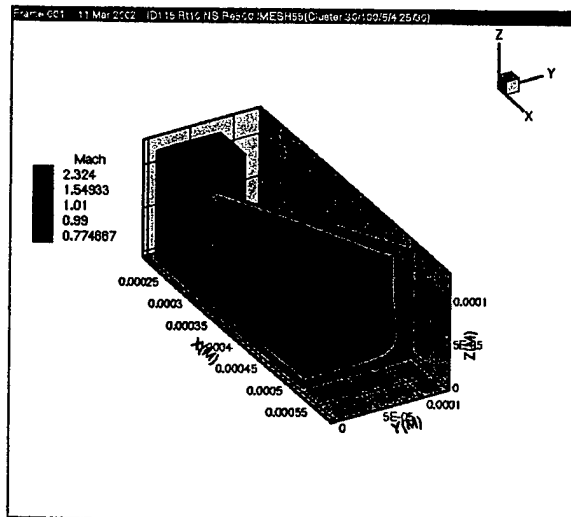


Figure 18-22. Mach Plot of $Rt=10$, $Tc=3000K$, $F=31mN$

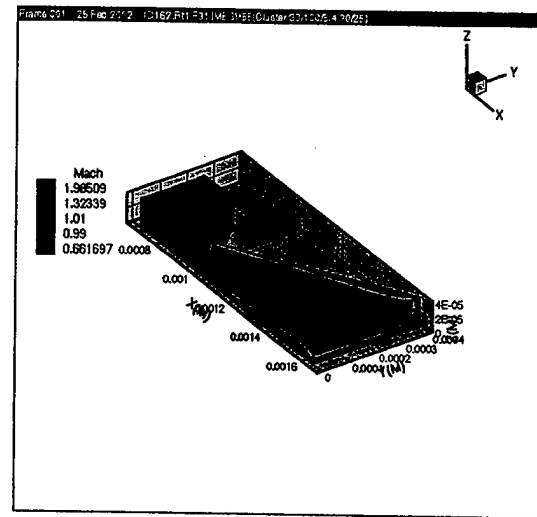


Figure 18-24. Mach Plot of $R_t=5$, $T_c=3000K$, $F=31mN$

The results below will verify the change in Reynolds number down the axial length of the nozzle for the various aspect ratios. This is done only for a chamber temperature of 3000 K and thrust level of 501mN and 31mN, although the same results are expected for the other temperature levels.

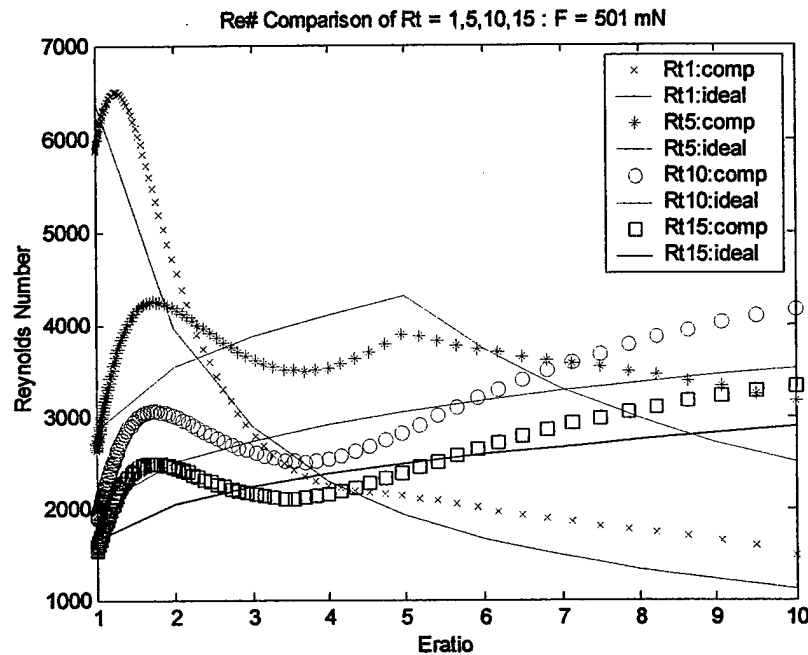


Figure 18-25. Ideal/Computed Reynolds Number of $Rt=1,5,10,15$ @ $F=501\text{mN}$

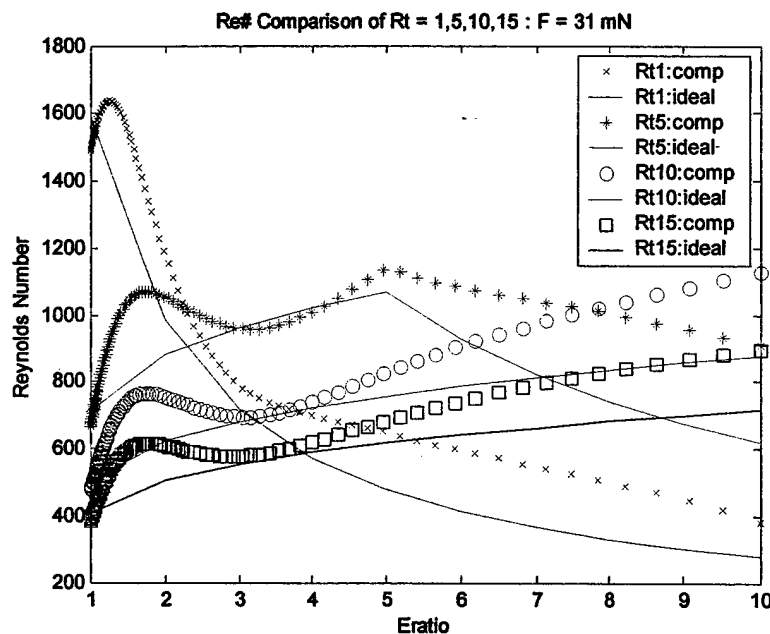


Figure 18-26. Ideal/Computed Reynolds Number of $Rt=1,5,10,15$ @ $F=31\text{mN}$

For both cases it is clear that along the axial centerline the Reynolds number from the numerical results model the general trend of the Reynolds number of ideal isentropic expansion. The numerical results are generally greater than the ideal results. This may be the result of several factors resulting from the decrease in the effective area ratio due to the boundary layer growth. Due to a decrease in expansion, the velocity will be lower and the viscosity higher than in the isentropic case (viscosity goes roughly as $T^{0.6}$). Therefore, the only other parameter is the density. The density increase must outweigh the combined velocity decrease and viscosity increase. Table 18-1 outlines the comparison between the ideal isentropic expansion of an expansion ratio of 10 and the numerically evaluated solutions at the center of the exit plane:

Table 18-1. Cause of Variation in Reynolds Number from Expected Results

Thrust (mN)	Rt	rho (kg/m ³)	U (m/s)	T (K)	visc (kg/m/s ²)	x factor
ideal		0.0694	2650	1390	5.199E-05	3537411
501	15	0.0913	2517	1388	5.568E-05	4127193
501	10	0.093	2518	1455	5.563E-05	4209491
501	5	0.108	2471	1477	5.751E-05	4640376
501	1	0.116	2455	1430	5.812E-05	4899862
31	15	0.1023	2484	1429	5.681E-05	4473036
31	10	0.1037	2485	1522	5.678E-05	4538473
31	5	0.129	2420	1725	5.936E-05	5259097
31	1	0.1417	2293	1262	6.481E-05	5013395

The 'x factor' signifies the factor that would be multiplied by the respective characteristic dimension to determine the Reynolds number. At the exit plane the 'x-factor' is greater than the isentropic expansion because the increased density outweighs the effect of velocity decrease and viscosity increase. Therefore, the Reynolds number along the centerline will be consistently greater than the isentropic value. This simply means that within the supersonic core the inertial effects are greater than the viscous effects. Within the boundary layer the values change significantly and the Reynolds number is significantly lower.

A data table of summarized results for the aspect ratio analysis is listed in table 18-2. For a more complete table reference Appendix G.

Table 18-2. Summary of Aspect Ratio Results

Id	Tc	Rt	Dt_pst	Re_t	Re_e	F_ideal	F_comp	n_F	Isp_ideal	Isp_comp	n_Isp
177	3000	15	81	1542	3326	502.78	444.9	88.5%	282.1	266.8	94.2%
118	3000	10	98.999	1889	4171	500.69	442.7	88.4%	282.09	266.3	94.4%
152	3000	5	138.4	2631	3159	489.27	426.5	87.2%	282.09	264.5	93.8%
149	3000	1	309.4	5870	1491	489.04	396.2	81.0%	282.09	254.5	90.2%
155	2500	10	98.7	2262	4947	500.95	441.6	88.2%	262.43	253	96.4%
156	2500	5	139.6	3173	3736	501.08	436.2	87.1%	262.43	251.6	95.9%
157	2500	1	312.1	7081	1767	500.91	406.9	81.2%	262.43	243	92.6%
158	2000	10	98.7	2907	6405	500.49	441.6	88.2%	236.61	229.9	97.2%
159	2000	5	139.6	4096	4776	500.62	436.2	87.1%	236.61	228.4	96.5%
160	2000	1	312.2	9139	2240	500.76	410.6	82.0%	236.61	221.6	93.7%
179	3000	15	20	345	712	30.65	26.1	85.2%	282.09	258.5	91.6%
115	3000	10	24.76	447	1128	31.318	26.7	85.3%	282.09	258.6	91.7%
169	3000	5	34.84	667	908	31.006	25.9	83.5%	282.09	255.9	90.7%
162	3000	1	77.9	1489	379	31.001	22.8	73.5%	282.09	236.8	83.9%
163	2500	10	17.363	565	1614	31.007	26.5	85.5%	262.43	246.7	94.0%
164	2500	5	34.725	795	1053	31.005	26	83.9%	262.43	244.4	93.1%
165	2500	1	77.65	1775	455	31.007	23	74.2%	262.43	227.7	86.8%
166	2000	10	24.56	729	1697	30.991	26.6	85.8%	236.61	224.7	95.0%
167	2000	5	34.73	1025	1326	30.984	23.1	74.6%	236.61	222.7	94.1%
168	2000	1	77.65	2288	618	30.978	23.5	75.9%	236.61	209.3	88.5%

The results exemplify the low Reynolds number within the boundary layers. For a thrust level of 501mN, we see the following results on thrust and Isp efficiency in figure 18-27/18-28.

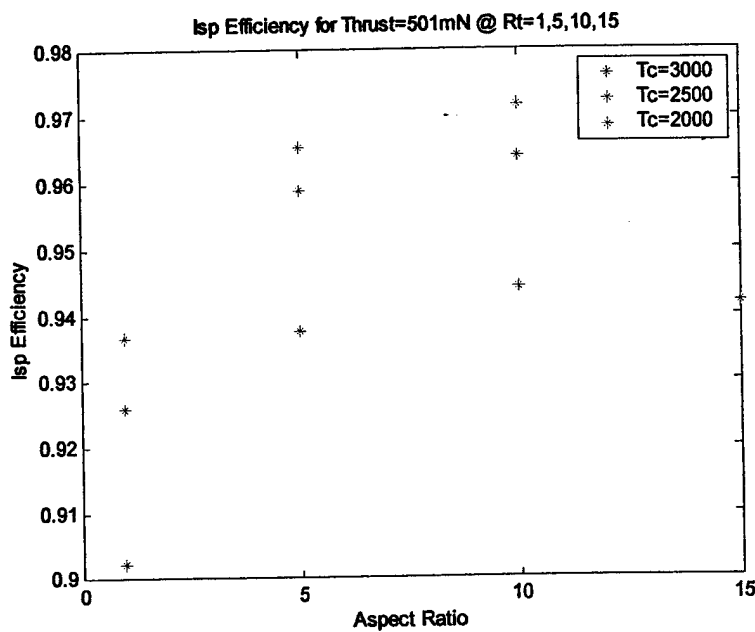


Figure 18-27. Isp Efficiencies of Aspect Ratios 1,5,10,15 @ F=501mN

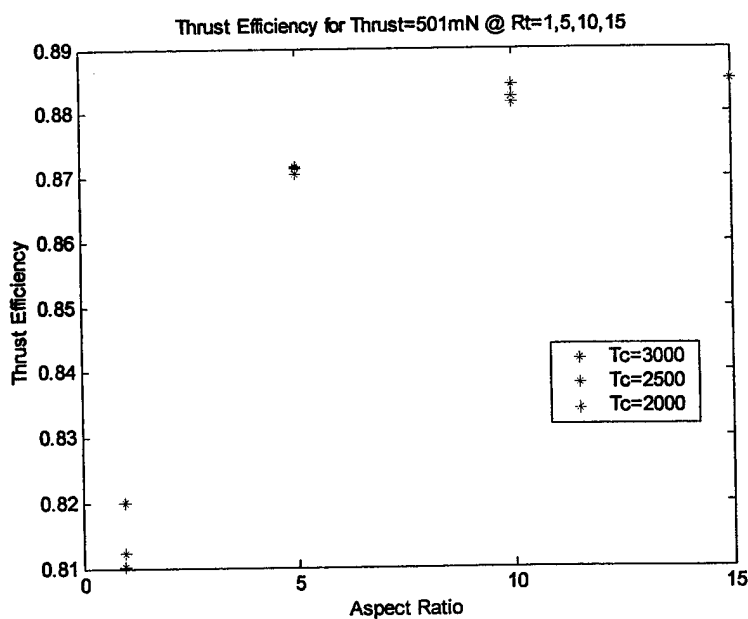


Figure 18-28. Thrust Efficiencies of Aspect Ratios 1,5,10,15 @ F=501mN

And for a thrust level of 31mN figures 18-29/18-30.

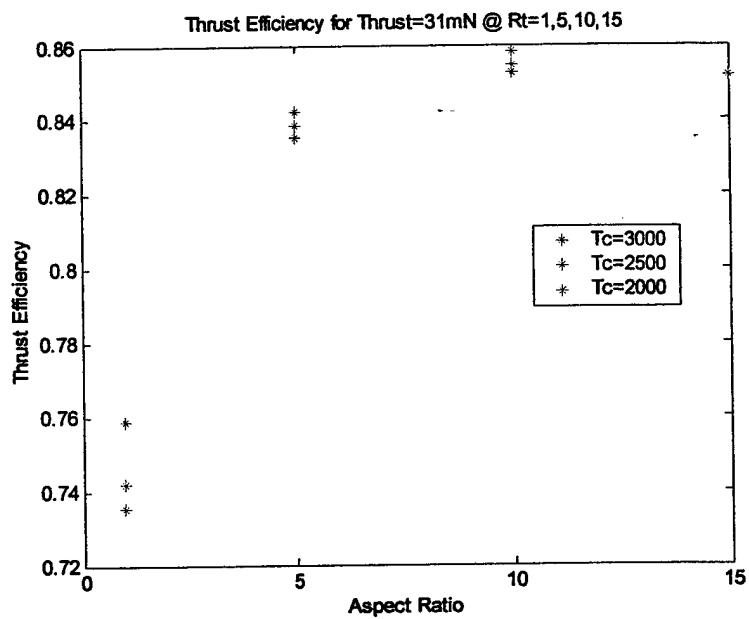


Figure 18-29. Thrust Efficiencies of Aspect Ratios 1,5,10,15 @ F=31mN

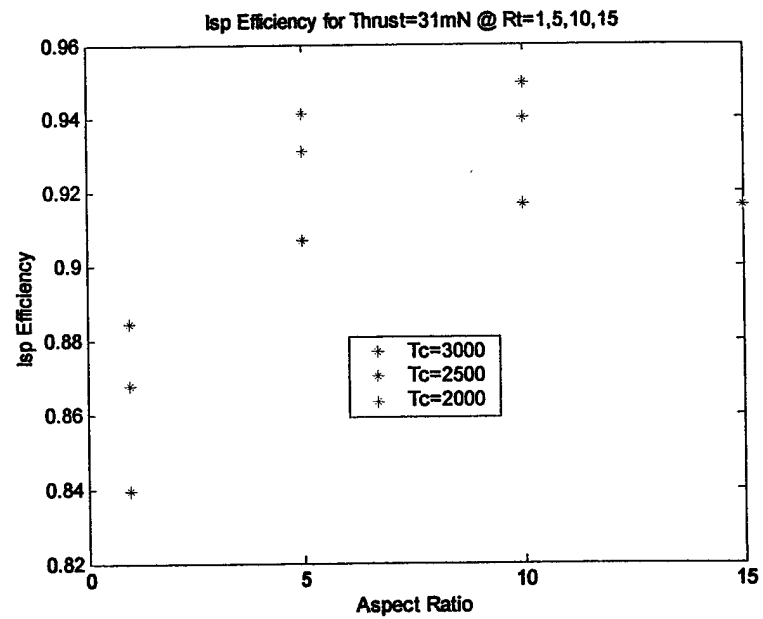


Figure 18-30. Thrust Efficiencies of Aspect Ratios 1,5,10,15 @ F=31mN

Using the values for Isp efficiency, we get a better idea of how the aspect ratios relate to one another by comparing the effective Isp levels of figures 18-31/18-32.

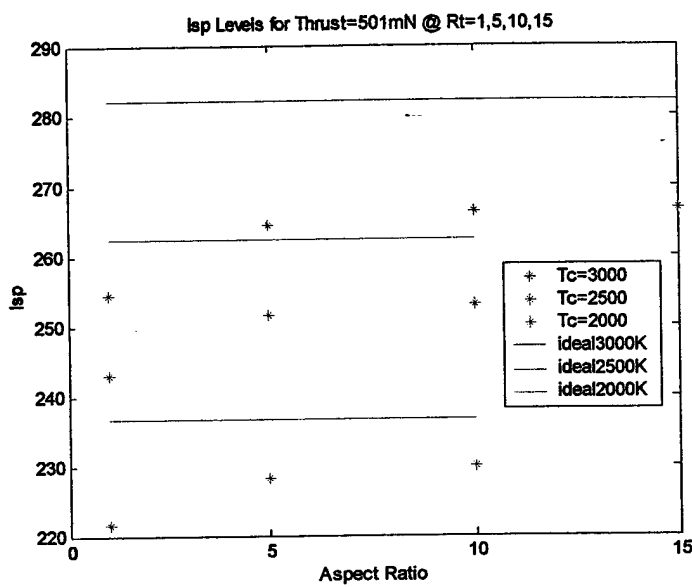


Figure 18-31. Isp Levels of Aspect Ratios 1,5,10,15 @ F=501mN

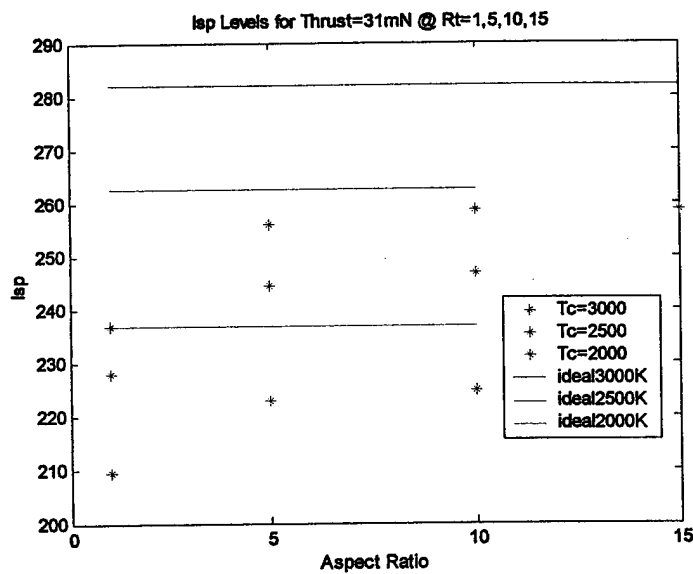


Figure 18-32. Isp Levels of Aspect Ratios 1,5,10,15 @ F=31mN

These results show that there is a definite advantage in using higher aspect ratios compared with an aspect ratio of 1. For instance, operating with an aspect ratio of 5 at 2500 K chamber temperature outperforms the effective Isp of an aspect ratio of 1 at 3000 K. The difference between the higher aspect ratios is small, therefore no substantial conclusions are made

between Isp levels of 5, 10, and 15. Although it does appear that the aspect ratio of 10 does produce the best results, the aspect ratio of 15 is expected to increase slightly with a further increase in mesh density. Therefore, the aspect ratio of 10 and 15 are presumed equal. These values both are greater than an aspect ratio of 5 by a small margin. Further increase in aspect ratio for the given geometry would more than likely produce results that would decrease the overall thrust level. It is therefore the author's suggestion to design a nozzle, if possible, around an aspect ratio equivalent to the expansion ratio.

The high-temperature analysis of the next section is therefore performed for an aspect ratio of 10, expansion ratio of 10, and expansion angle of 30.

Chapter 19: High-Temperature Analysis

This analysis was performed for a chamber temperature range of 1000 to 3000 K and Reynolds number range of 250 – 2000 at the throat. The other physical parameters are listed below in table 19-1.

Table 19-1. Operating Conditions for High-Temperature Analysis

Expansion Ratio	Expansion Half-angle	Aspect Ratio	Chamber Pressure
10	30	10	30 bar

A partial data summary is listed in table 19-2 although a complete table can be found in Appendix G.

Table 19-2. Summary of Results for High-Temperature Analysis

id	Tc	Rt	Dt (μm)	Re_t	Re_e	F_ideal	F_comp	n_F	Isp_ideal	Isp_comp	n_Isp
114	3000	10	12.38	240	609	7.8298	6.50	83.0%	282.09	252.1	89.37%
115	3000	10	24.76	447	1128	31.318	26.70	85.3%	282.09	258.6	91.67%
116	3000	10	49.53	949	2151	125.33	109.30	87.2%	282.09	263.2	93.30%
117	3000	10	74.30	1420	3165	282.02	248.10	88.0%	282.09	265.2	94.01%
118	3000	10	99.00	1889	4171	500.69	442.70	88.4%	282.09	266.3	94.40%
119	2500	10	10.01	233	588	5.1527	4.22	81.9%	262.43	239	91.07%
120	2500	10	20.02	462	1090	20.611	17.50	84.9%	262.43	245.3	93.47%
121	2500	10	40.05	918	2076	82.484	71.50	86.7%	262.43	249.7	95.15%
122	2500	10	60.07	1374	3053	185.56	162.30	87.5%	262.43	251.6	95.87%
123	2500	10	80.09	1829	4026	329.86	290.00	87.9%	262.43	252.7	96.29%
124	2000	10	7.94	238	16	3.239	2.66	82.1%	236.61	216.7	91.59%
125	2000	10	15.88	473	1156	12.956	10.98	84.7%	236.61	222.2	93.91%
126	2000	10	31.76	941	2203	51.823	44.80	86.4%	236.61	226	95.52%
127	2000	10	47.65	1408	3247	116.65	101.80	87.3%	236.61	227.6	96.19%
128	2000	10	63.55	1875	4166	207.5	182.00	87.7%	236.61	228.6	96.61%
129	1500	10	5.62	238	665	1.6097	1.33	82.6%	202.29	188.3	93.08%
130	1500	10	11.24	473	1247	6.4385	5.49	85.3%	202.29	192.7	95.26%
131	1500	10	22.47	940	2381	25.733	22.40	87.0%	202.29	195.8	96.79%
132	1500	10	33.71	1407	3507	57.913	50.80	87.7%	202.29	197.2	97.48%
133	1500	10	44.94	1873	4648	102.93	90.60	88.0%	202.29	198	97.88%
134	1000	10	3.03	212	683	0.46336	0.38	82.1%	163.6	152.6	93.28%
135	1000	10	6.07	420	1272	1.8596	1.58	85.0%	163.6	156.2	95.48%
136	1000	10	12.14	836	2425	7.4384	6.45	86.7%	163.6	158.5	96.88%
137	1000	10	18.21	1251	3562	16.736	14.60	87.2%	163.6	159.4	97.43%
138	1000	10	24.28	-	-	-	-	-	-	-	-

** id138 did not converge

The graphs below in figures 19-1/19-2 represent the Isp efficiency both as a function of Reynolds number and chamber temperature.

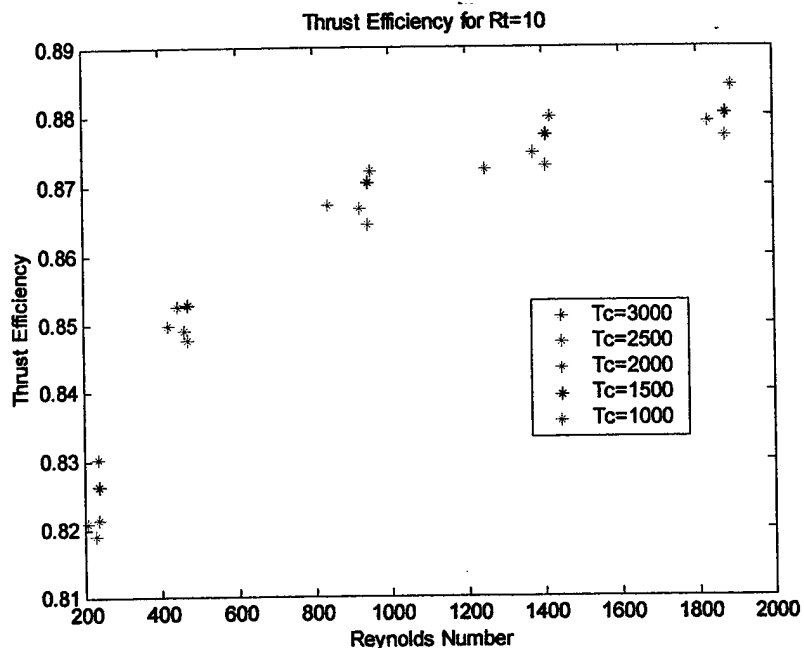


Figure 19-1. Thrust Efficiency as a Function of Reynolds Number

This graph depicts the thrust efficiency as we increase in Reynolds number. The efficiencies are roughly the same, although a temperature increase seems to increase the resultant efficiencies. This is a little counter-intuitive as we would expect the higher temperatures to result in greater viscous effects and thus smaller efficiencies. But, there does not seem to be a strong correlation between all temperature levels at each Reynolds number, and since the results are so close together, it is reasonable to conclude that at each temperature level the thrust efficiency is independent of operating temperature and strongly dependent upon the Reynolds number. Obviously, a decrease in Reynolds number results in an increasing rate of decreasing efficiency.

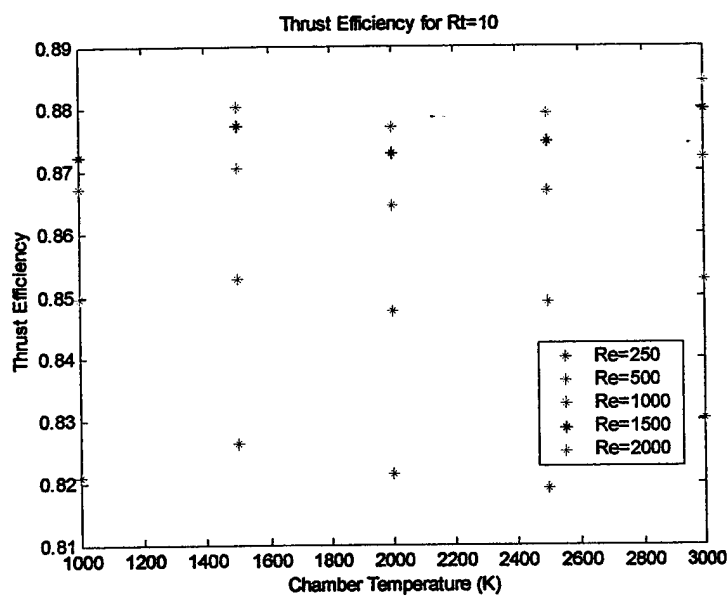


Figure 19-2. Thrust Efficiency as a Function of Chamber Temperature

Shown as a function of chamber temperature, it is once again evident that there are only small variations from one temperature level to the next for each Reynolds number. The same conclusions hold for this representation as for the previous figure. This is the unknown plot of figure 8-11.

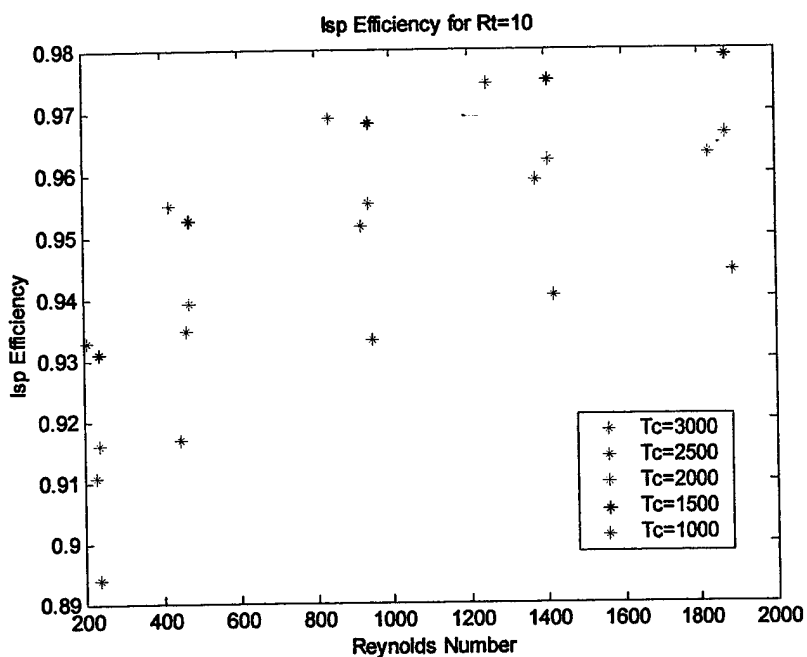


Figure 19-3. Isp Efficiency as a Function of Reynolds Number

The Isp graphs depict what was expected with an increase in temperature. The Isp efficiency of the higher temperatures is lower than that of the lower temperatures due to increased viscosity at the higher temperatures. The trend overall seems to be a leveling off at the higher Reynolds numbers and rapid decrease towards the smaller Reynolds numbers which means the lower the thrust level designing for (and thereby lower the Reynolds number) the more rapidly the efficiency drops. The difference between the temperature ranges does not vary from one Reynolds number to the next indicating that at each temperature level the viscosity increase due to temperature increase results in the same efficiency difference between temperature levels. This is the unknown plot of figure 8-12.

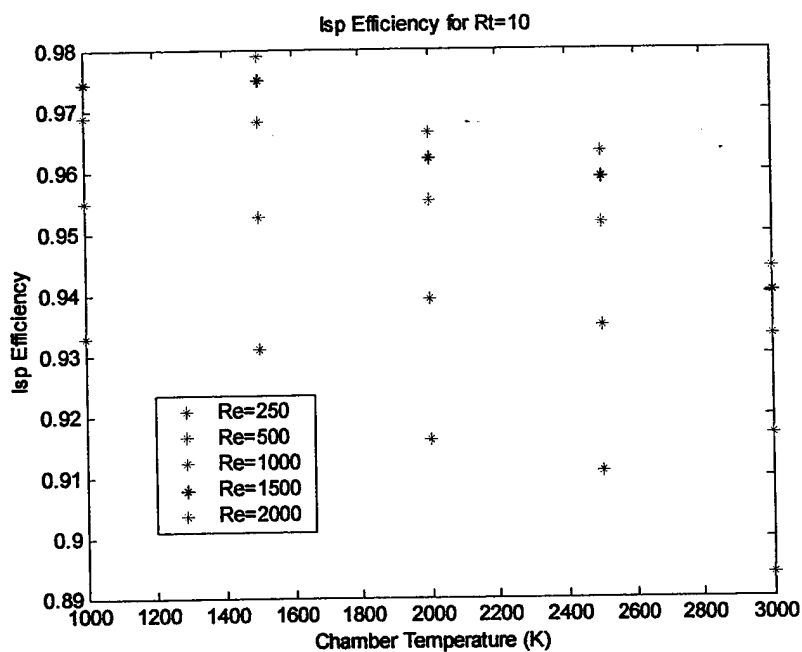


Figure 19-4. Isp Efficiency as a Function of Chamber Temperature

Looking at the results as a function of chamber temperature makes it plain that increasing the temperature results in a decrease in efficiency. Therefore, operating at higher temperatures verifies the assumption that the specific impulse will decrease. The remaining question is whether or not the resultant Isp of the higher temperatures is lower than that of the lower temperatures.

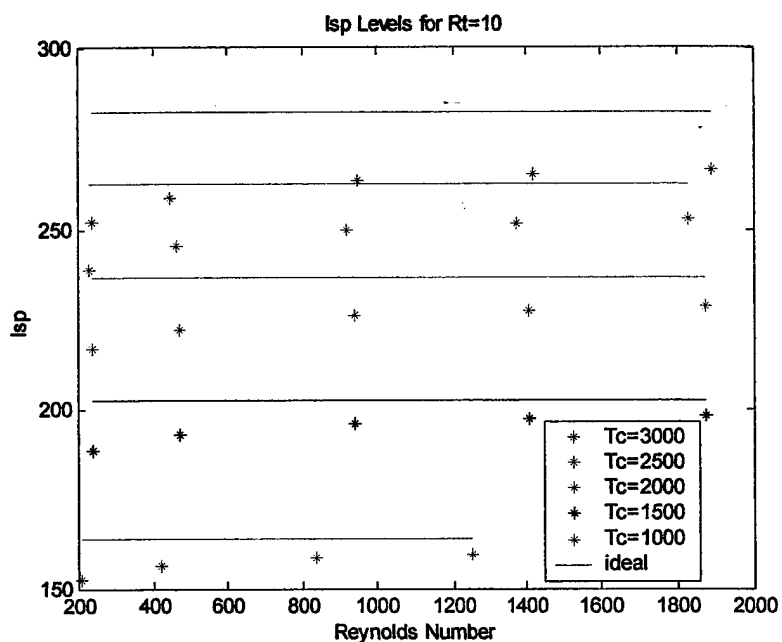


Figure 19-5. Resultant Isp as a Function of Reynolds Number

Applying the efficiencies from above to the ideal Isp levels previously established based on isentropic expansion, we see the resultant Isp levels. The question raised previously was whether the viscous effects of a higher temperature would outweigh the specific impulse gain of a lower temperature. From the above depiction, the author concludes that with an increase in temperature from one level to the next there is a decrease in the difference between the effective Isp levels. The table below depicts the difference which is nearly independent of the Reynolds number.

Table 19-3. Difference Trend in Isp For Each Temperature Increment

Temperature Range	Isp Difference (seconds)				
	Re = 2000	Re = 1500	Re = 1000	Re = 500	Re = 250
1000 - 1500	**	37.8	37.3	36.5	35.7
1500 - 2000	30.6	30.4	30.2	29.5	28.4
2000 - 2500	24.1	24.0	23.7	23.1	22.3
2500 - 3000	13.6	13.6	13.5	13.3	13.1

** id138 (Tc=1000K, Re=2000 did not fully converge to an accurate solution)

At 3000K, we have not yet reached an area of negative return where the viscous effects of increased temperature outweigh the increase in specific impulse. But, as evident by the graph and table above, with each 500K increment in temperature, not only is the difference between Isp levels decreasing, but the rate at which it is decreasing is increasing. Within the next 2000 K we should reach the area of negative return.

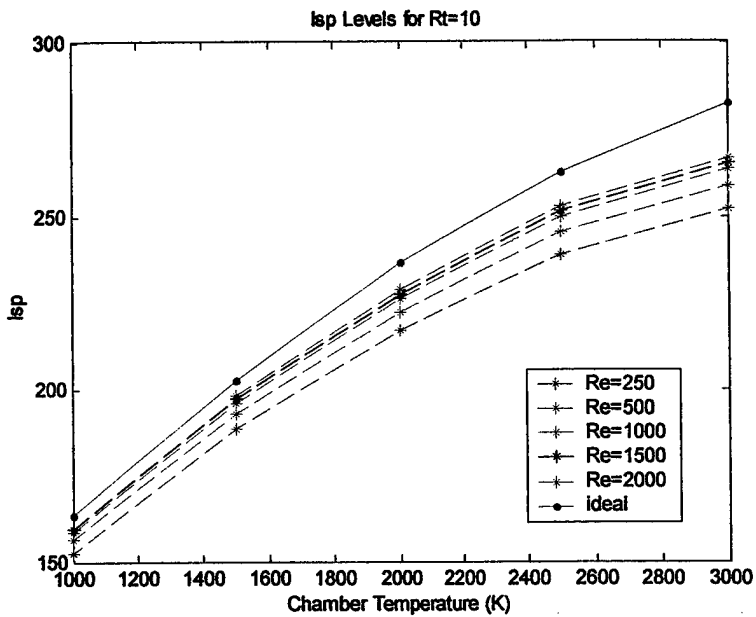


Figure 19-6. Isp Levels of Isp vs Chamber Temperature for Various Reynolds Numbers

Looking at the results as function of temperature displays the fixed difference between Reynolds numbers from one temperature level to the next. It also shows that as we increase in temperature there is an increasing difference between the ideal and computed solutions. Therefore, if it is possible in the future to produce propulsion systems of temperatures greater than 3000K, there appears to be an eventual maximum of achievable performance.

Chapter 20: Conclusions of Micronozzle Flow Efficiencies

The goal at the onset of this research project was to find an optimum range of chemical system performance where an increase in viscous effects because of an increase in temperature would outweigh the desired gain in specific impulse. Numerical simulations were used to analyze micronozzles with an expansion ratio of 10, expansion half-angle of 30, and chamber pressure of 30 bar. The results were modeled using a finite-volume numerical code produced by Amtec Engineering, commonly known as INCA.

Aspect ratios of 1, 5, 10 and 15 designed for two thrust levels of 31mN and 501mN were analyzed to determine the effect of increased aspect ratio. While there was a definite increase of efficiency from an aspect ratio of 1 to the three higher aspect ratios, the difference between 5, 10 and 15 was small. Generally, the higher the aspect ratio, the higher the efficiencies produced as the Reynolds number was decreased at the throat but increased towards the exit. It is assumed that there will be an eventual decrease in efficiency due to the sidewall boundary layer dominating the flow field, but for the cases considered, increasing the aspect ratio decreases the effect of the endwall boundary layer and increases overall efficiency. There is a strong correlation of efficiency to Reynolds number based on the aspect ratio. However, one must be careful when discussing efficiencies as a function of Reynolds number as each aspect ratio has its own efficiency connection to a given range of Reynolds numbers.

Using an aspect ratio of 10, high temperature cases were analyzed from 1000 to 3000 K to determine if there was an area of negative return. Although the viscosity effects did increase with an increase in temperature, the thrust efficiency was independent of the chamber temperature and dependent upon the Reynolds number. For the specific impulse efficiency, an area of negative returns was not found, although there was a decreasing difference between Isp levels as the temperatures were increased. Therefore, there is expected to be an area of negative return above 3000K. One may design for any temperature level up to 3000K with products of N₂ and H₂O without worrying about an overriding decrease in specific impulse due to viscous effects.

One should note that the study assumed adiabatic wall conditions. This variable may very well bring the level of negative return below 3000K. Upon contact with a hot gas, a certain amount of energy will be lost through conduction to the material of the nozzle wall. Generally, the hotter the gas, the greater the temperature gradient and the more energy will be lost upon

initial contact. Depending on the length of the burn, the nozzle material will heat up to a certain level and then establish a energy loss that may be modeled numerically as an isothermal wall. The losses expected in such conditions will be greater for the higher temperature cases. Whether or not it is enough to make up the additional 13 seconds of Isp from 2500K to 3000K is left for further investigation.

Further investigation into the physics behind micronozzle flows would be of particular interest. In particular, in the aspect ratio cases analyzed, a lower Reynolds number at the throat continually increasing towards the exit outperformed a high aspect ratio at the throat continually decreasing towards the exit. A simple explanation of these results is to conclude that the viscous effects play more of a role towards the exit plane of the nozzle. A similar result was seen with the high-temperature analysis. For a specific Reynolds number, theoretically a set Reynolds number would produce similar results independent of the temperature being analyzed. One correlation between the two cases is the density. At the exit plane and for higher temperatures the density is much less than at the throat and for lower temperature cases analyzed. Therefore, the viscous effects may play more of a predominant role in overall thrust and Isp efficiencies when at a lower density. Correlation between not only Reynolds number, but also density may be an area of further research.

Chapter 21: Conclusion of Mission Application and Micronozzle Flow Analysis

Application of the UW ternary system to macronozzles for high thrust missions does not encounter the inefficiencies associated with viscous losses as much as the micronozzles do. In fact, according to the above analysis, for operation at 0.5 N at near stoichiometric conditions (corresponding to throat diameter of ~99 μm and height of 990 μm) a throat Reynolds number of 2000 produced an Isp efficiency of ~94% (265.2 seconds) and a thrust efficiency of 88.4% (442.7 mN). Increasing the scale will further increase the Reynolds number and the expected efficiencies. As mentioned earlier in the mission analysis section, the application of this system to high thrust applications is dependent upon the availability of material capable of handling temperatures on the order of 3000 K. Nozzles of the 3D block type may be scaled up to provide higher levels of thrust which may be a viable option, but conical nozzles generally have higher levels of efficiency based on divergent effects. Further investigation into reduction of the nozzle half angle to reduce these losses for 3D block nozzles and comparison to conical efficiencies would be an area of interest. If the efficiencies gained from operating with a block nozzle capable of withstanding high temperatures outweighs the efficiencies gained from using a lower temperature conical nozzle, then application of this propulsion system to higher thrust applications is a viable option.

Using the UW ternary system for small thrust applications is promising based on the results of the flow analysis conducted above. Due to the limit of the INCA continuum code, the lowest thrust levels analyzed were on the order of ~8mN for a chamber temperature of 3000 K. Reduction of the chamber temperature allowed for calculation of efficiencies at thrust levels of ~5 mN. At these low thrust levels the Isp/F efficiency was around 90%/83% for a Reynolds number of 250 at the throat (aspect ratio of 10). Table 21-1 summarizes the lowest thrust levels analyzed for each temperature level. The minimum impulse bit is computed from the fastest response time valve of from table 5-1.

Table 21-1. Small Thrust Levels with Impulse Bit Application

id	Tc (K)	Rt	Re_t	Kn_e	F_ideal (mN)	F_comp (mN)	n_F	Isp_ideal (sec)	Isp_comp (sec)	n_Isp	MIB (μN·s)
114	3000	10	240	.03	7.8298	6.50	83.0%	282.09	252.1	89.37%	52.0
115	3000	10	447	.01	31.318	26.70	85.3%	282.09	258.6	91.67%	213.6
119	2500	10	233	.03	5.1527	4.22	81.9%	262.43	239	91.07%	33.6
120	2500	10	462	.02	20.611	17.50	84.9%	262.43	245.3	93.47%	140.0
124	2000	10	238	.03	3.239	2.66	82.1%	236.61	216.7	91.59%	18.6
125	2000	10	473	.02	12.956	10.98	84.7%	236.61	222.2	93.91%	87.8
129	1500	10	238	.04	1.6097	1.33	82.6%	202.29	188.3	93.08%	10.6
130	1500	10	473	.02	6.4385	5.49	85.3%	202.29	192.7	95.26%	43.9
134	1000	10	212	.05	0.46336	0.38	82.1%	163.6	152.6	93.28%	3.7
135	1000	10	420	.03	1.8596	1.58	85.0%	163.6	156.2	95.48%	14.9

The original goal was to stay within the limits of the continuum assumption. Referring back to table 9-1, the computed values from the runs above put us into the slip flow regime. Even though the original assumption is violated, the trends of decreased efficiency are consistent with what we would expect. Further investigation into application of INCA into larger Knudsen numbers would be an area of particular interest.

Using the MIB values from above, it is therefore conceivable to think that this high-temperature propulsion system could be applied to missions which require thrust levels on the order of a couple of millinewtons. The attainable MIB can be applied to nearly any desired slew rate of table 3-3. These small thrust levels are attainable, but the Isp levels when compared with electric propulsion systems are still much lower. Therefore, when power available and response time for maneuvers is not a question, electric propulsion systems are the more logical choice. If fast response times are needed for a mission where the delta-v requirements are not excessively high, the UW ternary system can provide relatively high Isp levels (compared with other chemical systems) for a relatively simple propulsion system setup.

Considering the technology currently available, Sienna Technologies Inc., can produce an alumina ceramic which withstands temperatures around 2000 K. They can etch a micronozzle of minimum dimensions, 100 μm height and 80 μm width. This is roughly an aspect ratio of 1 and looking in Appendix G, id162 shows that for an aspect ratio of 1 at 78 μm throat diameter, the thrust would be 23.5 mN of thrust corresponding to ~209 seconds of Isp. For a higher aspect ratio of 10, the minimum throat diameter of 80 μm would produce a thrust of about 250mN.

Corresponding impulse bits would be around $188\mu\text{m}\text{-sec}$ and $2\text{mN}\text{-sec}$. Referring back to table 3-3, such levels of impulse bit have a wide range of application.

Combining the use of the UW ternary system for both high/low thrust applications is an option to be considered and investigated further. Using a single system for both the main propulsion system and ACS provides advantages of a reduced complexity over separate subsystems. In addition, the non-toxicity and high performance of this system offers advantages over other monopropellant options. If further research concludes that the fuel/oxidizer/diluent combination can be contained in a monopropellant state, and a catalyst can be used to initiate combustion, the mission and flow analysis conducted above promise a broad range of application for a higher performance chemical propulsion system.

Bibliography

- ¹ **Micropropulsion for Small Spacecraft.** Michael M. Micci and Andrew D. Ketsdever, ed. American Institute of Aeronautics and Astronautics, 2000.
- ² http://nmp.jpl.nasa.gov/ds1/quick_facts.html
- ³ http://www.boeing.com/defense-space/space/delta/deltaPayload.htm#d2fairing_info
- ⁴ Vanetta P.P., "NASA-GSFC Nano-satellite Technology Development," Utah State University Small Satellite Conference, 1998. SSC98-VI-5.
- ⁵ Urban M., "Investigation of Propulsion System Requirements for Spartan Lite," Utah State University Small Satellite Conference, 1998. SSC98-VIII-5.
- ⁶ <http://spartans.gsfc.nasa.gov/>
- ⁷ http://www.sstl.co.uk/missions/subpage_missions.html
- ⁸ Eckart P., "LunARSat – European Orbiter Mission to the Moon," Utah State University Small Satellite Conference, 1998. SSC98-VI-3.
- ⁹ Schilling F., Spores R. and Spanjers G., "Micropropulsion Options for the TechSat21 Space-Based Radar Flight." **Micropropulsion for Small Spacecraft.** Michael M. Micci and Andrew D. Ketsdever, ed. American Institute of Aeronautics and Astronautics, 2000. pp 3 – 5.
- ¹⁰ Baren W.R., Schultz K.S. and Thomsen P.L., "A Geomagnetic Smallsat Observatory for Operation in a 200 KM Altitude Low Earth Orbit," W. R. Baren, K.S. Schultz, & P.L. Thomsen. Computer Resources International A/S (CRI A/S). Space Division, Denmark.
- ¹¹ Jason S. "Low Cost Planetary Exploration : Surrey Lunar Minisatellite and Interplanetary Platform Missions," Surrey Space Center. Utah State University Small Satellite Conference. 2000. SSC00-II-8.
- ¹² Reichbach J.G., "Micropulsion System Selection for Precision Formation Flying Satellites," AIAA Paper 2001-3646. 37th Joint Propulsion Conference. Salt Lake City, Utah. July 2001.
- ¹³ Mueller J. "Thruster Options for Microspacecraft: A Review and Evaluation of Existing Hardware and Emerging Technologies," AIAA Paper 97-3058. 33rd Joint Propulsion Conference. Seattle, WA. July 1997.
- ¹⁴ <http://www.sdl.usu.edu/conferences/smallsat/proceedings/13/>
- ¹⁵ **Understanding Space: An Introduction to Astronautics.** Jerry Jon Sellers. McGraw-Hill, Inc., New York. 1994. p 210.

- ¹⁶ Gibbon D., Paul M., Jolley P., Zakirov V., Haag G., Coxhill I., Sweeting M. and Eloirdi R., "Energetic Green Propulsion for Small Spacecraft" AIAA Paper 2001-3247. 37th Joint Propulsion Conference. Salt Lake City, Utah. July 2001.
- ¹⁷ Space Mission Analysis and Design. Wertz J.R. and Larson W.J. 3rd ed. Microcosm Press and Kluwer Academic Publishers. CA, 1999.
- ¹⁸ Fundamentals of Astrodynamics and Applications. Vallado, David A. McGraw-Hill, Inc., New York. 1997.
- ¹⁹ The Hydrazine Handbook. General Dynamics Company Information. Rocket Research Company. Redmond, WA. (206) 885-5000. Used also by Ref [57] and Ref [63].
- ²⁰ Rayburn C., Campbell M., Hoskins W. and Cassady R. "Development of a Micro-Pulsed Plasma Thruster for the Dawgstar Nanosatellite," AIAA Paper 2000-3256. 36th Joint Propulsion Conference. Huntsville, Alabama. July 2000.
- ²¹ Mattick A.T., "High Performance Microthrusters for Microsatellites," Final Report for AFOSR STTR Contract F49620-01-C-0010..
- ²² Personal Communication with Dr. Eckart Schmidt.
- ²³ Personal Communication with Ender Savrun, President, Sienna Technologies.
- ²⁴ Kim S.C., "Calculations of Low Reynolds Number Rocket Nozzles," AIAA Paper 93-0888. Monterey, CA. June 1993.
- ²⁵ Zelesnik D., Micci M. and Long L., "Direct Simulation Monte Carlo Model of Low Reynolds Number Nozzle Flows," Journal of Propulsion and Power. Vol 10, No 4, Jul-Aug 1994.
- ²⁶ Ivanov M., Markelov G., Ketsdever A. and Wadsworth D., "Numerical Study of Cold Gas Micronozzle Flows," AIAA Paper 99-0166. 35th Joint Propulsion Conference. Los Angeles, CA. June 1999.
- ²⁷ Markelov G. and Ivanov M., "A Comparative Analysis of 2D/3D Micronozzle Flows by the DSMC Method," AIAA 2001-1009. 37th Joint Propulsion Conference. Salt Lake City, Utah. July 2001.
- ²⁸ Alexeenko A., Levin D., Gimelshein S., Collins R. and Markelov G. "Numerical Simulation of High-Temperature Gas Flows in a Millimeter-Scale Thruster," AIAA 2001-1011. 37th Joint Propulsion Conference. Salt Lake City, Utah. July 2001.
- ²⁹ Reed B., de Groot W. and Dang L., "Experimental Evaluation of Cold Flow Micronozzles," AIAA Paper 2001-3521. 37th Joint Propulsion Conference. Salt Lake City, Utah. July 2001.

- ³⁰ Chung C., Kim S. and Stubbs R., "DSMC and Continuum Analyses of Los-Density Nozzle Flow," AIAA Paper 93-0727. Monterey, CA. June 1993.
- ³¹ Fundamentals of Fluid Mechanics. Munson B.R., Young D.F., Okiishi T.H. 3rd ed. John Wiley & Sons, Inc. New York, 1998.
- ³² Momentum Transfer in Boundary Layers. Cebeci T., Bradshaw P. McGraw-Hill, Inc. New York, 1977.
- ³³ Viscous Fluid Flow. White F.M. 2nd ed. McGraw-Hill, Inc. New York, 1991.
- ³⁴ Introduction to Physical Gas Dynamics. Vincenti W.G., Kruger C.H. Jr. Krieger Publishing Company. Florida, 1986.
- ³⁵ Transport Phenomena. Bird R.B., Stewart W.E., Lightfoot E.N. John Wiley & Sons, Inc. New York, 1960.
- ³⁶ Bayt R. L., Breuer K. S., "A Performance Evaluation of MEMS Based Micronozzles," AIAA 97-3169. 33rd Joint Propulsion Conference. Seattle, WA. July 1997.
- ³⁷ Alexeenko A.A., Gimelshein S.F., Levin D.A. and Collins R.J., "Numerical Modeling of Axisymmetric and Three-Dimensional Flows in MEMS Nozzles," AIAA 2000-3668. 36th Joint Propulsion Conference. Huntsville, Alabama. July 2000.
- ³⁸ Using Computational Fluid Dynamics. Shaw C.T., Prentice Hall. New York, 1992.
- ³⁹ Anderson W.K., Thomas J.L. and van Leer B., "A Comparison of Finite-Volume Flux Vector Splittings for the Euler Equations," AIAA Paper 85-0122. AIAA 23rd Aerospace Sciences Meeting. Reno, NV. January 1985.
- ⁴⁰ AA504 CFD I - Graduate Course Notes. University of Washington, Winter Quarter 2001. Instructor Paul Bernard.
- ⁴¹ Computational Fluid Dynamics: An Introduction for Engineers. Abbot M.B., Basco D.R. John Wiley & Sons, Inc. New York, 1989.
- ⁴² Boyd I.D., Penko P.E. and Carney T.M., "Efficient Monte-Carlo Simulation of Rarefied Flow in a Small Nozzle" AIAA Paper 90-1693. Orlando, FL. July 1990.
- ⁴³ Bayt, R.L. "Analysis, Fabrication and Testing of a MEMS-based Micropropulsion System," Ph.D. Thesis. June 1999.
- ⁴⁴ Space Propulsion Analysis and Design. Humble R.W., Henry G.N., Larson W.J. McGraw Hill Companies, Inc. New York, 1995.

- ⁴⁵ Steger J.L. and Warming R.F. "Flux Vector Splitting of the Inviscid Gasdynamic Equations with Application to Finite Difference Methods," *Journal of Computational Physics*, Vol. 40, No. 2, April 1981, pp. 263-293.
- ⁴⁶ Personal Communication with Ender Savrun, President Sienna Technologies Inc.
- ⁴⁷ Bayt R.L. and Breurer K.S., "Fabrication and Testing of Micron-Sized Cold-Gas Thrusters." Micropropulsion for Small Spacecraft. editors Ketsdever A.D., Micci M.M. pp 381-397.
- ⁴⁸ Riemann Solvers and Numerical Methods for Fluid Dynamics. Toro E.F. 2nd ed. Springer-Verling Berlin. New York, 1999..
- ⁴⁹ Roe P.L., "Approximate Riemann Solver, Parameter Vectors, and Difference Schemes," *Journal of Computational Physics* 135, pp 250-258. Article No. CP975705.
- ⁵⁰ Rothe, D.E., "Electron-Beam Studies of Viscous Flow in Supersonic Nozzles," *AIAA Journal* Vol. 9, No 5. May 1971.
- ⁵¹ Tahara H. and Nishida M., "Overview of Electric Propulsion Activity in Japan," *AIAA Paper 99-2159*. 35th Joint Propulsion Conference. Los Angeles, CA. June 1999.
- ⁵² Tecplot®. Amtec Engineering, Inc. Bellevue, WA.
- ⁵³ Schwende M.A., Schulte G., Dargies E., Gotzig U. and Scharli-Weinert E., "New Generation of Low-Thrust Bi-Propellant Engines in Qualification Process," *AIAA Paper 93-2120*. Monterery, CA. June 1993. From Ref [57].
- ⁵⁴ Hodge K.F., Allen K.A. and Hemmings B., "Development and Test of the ASAT Bipropellant Attitude Control System (ACS) Engine," *AIAA Paper 93-2587*. Monterery, CA. June 1993. From Ref [57].
- ⁵⁵ Loyan A.V. and Rulakov A.A., "Development and State of Arcjet Propulsion System for Orbit Correction and Automation of Low Power Satellites," *AIAA Paper 99-2434*. 35th Joint Propulsion Conference. Los Angeles, CA. June 1999.
- ⁵⁶ Randolph T., "Overview of Major U.S. Industrial Program in Electric Propulsion," *AIAA Paper 99-2160*. 35th Joint Propulsion Conference. Los Angeles, CA. June 1999.
- ⁵⁷ Mueller J., "Thruster Options for Microspacecraft: A Review and Evaluation of State-of-the-Art and Emerging Technologies." Micropropulsion for Small Spacecraft. Michael M. Micci and Andrew D. Ketsdever, ed. American Institute of Aeronautics and Astronautics, 2000. pp 45-137.
- ⁵⁸ "Design and Development of the Army KE ASAT ACS Thruster" *AIAA Paper 93-1959*. Monterey, CA. June 1993. From Ref [57].

- ⁵⁹ Wichmann H. and Fitzsimmons M., "Miniature High-Performance Delta V Engine," AIAA Paper 93-2582. Monterey, CA. June 1993. From Ref [57].
- ⁶⁰ Gotzig U., Shulte G., and Sowa A., "New Generation 10N Bipropellant MMH/NTO Thruster with Double Seat Valve," AIAA Paper 99-2594. 35th Joint Propulsion Conference. Los Angeles, CA. June 1999.
- ⁶¹ "New Generation of Low-Thrust Bi-Propellant Engines in Qualification Process," *Journal of Propulsion and Power*. Vol 10. No 1. 1994. pp. 40-46. From Ref [57].
- ⁶² Ruttle D. and Fitzsimmons M., "Development of Miniature 35-lbf Fast Response Bipropellant Divert Thruster," AIAA Paper 93-2585. Monterey, CA. June 1993. From Ref [57].
- ⁶³ deGroot W. and Oleson S., "Chemical Microthruster Options," AIAA Paper 96-2868. AIAA Paper 96-3292. Lake Buena Vista, FL. July 1996. From Ref [57].
- ⁶⁴ Matlab®. Matlab 6, Student Version. Release 12.
- ⁶⁵ Gibbon D., Paul M., Smith P., and McLellan R., "The Use of Liquified Gases in Small Satellite Propulsion Systems," AIAA Paper 2001-3246. 37th Joint Propulsion Conference. Salt Lake City, Utah. July 2001.
- ⁶⁶ Morash D.H. and Strand L., "Miniature Propulsion Components for the Pluto Fast Flyby Spacecraft," AIAA Paper 94-3374. Indianapolis, IN. June 1994. From Ref [57].
- ⁶⁷ Gross S.J. and Rhee M.S., "Low Power Draw, 44 mN-sec Cold Gas Micro-Thruster and Driver System," AIAA Paper 99-2694. 35th Joint Propulsion Conference. Los Angeles, CA. June 1999. From Ref [57].
- ⁶⁸ Hoskins W.A., Wilson J.M., Willey M.J., Meckel N.J., Campbell M. and Chung S., "PPT Development Efforts at Primex Aerospace Company," AIAA Paper 99-2291. . 35th Joint Propulsion Conference. Los Angeles, CA. June 1999.
- ⁶⁹ Bzibziak R., "Miniature Cold Gas Thrusters , " AIAA Paper 92-3256. Nashville, TN. June 1999. From Ref [57].
- ⁷⁰ Perel J., Bates T., Mahoney J., Moore R.D. and Yahiku A.Y., "Research on Charged Particle Bipolar Thrustor," AIAA Paper 67-728. Colorado Springs, CO. Sept. 1967. From Ref [57].
- ⁷¹ Kidd P.W. and Shelton K.H., "LifeTest (4350 Hours) of an Advanced Colloid Thruster Module," AIAA Paper 73-1078. 10th Electric Propulsion Conference. Lake Tahoe, NV. Oct/Nov 1973. From Ref [57].
- ⁷² Hurley V., Monheisen J., Pote B., Rostler P., Freeman C. and Kolencik J., "Development of Low Power Hall Thrusters," AIAA Paper 99-3534. 35th Joint Propulsion Conference. Los Angeles, CA. June 1999.

- ⁷³ Garkushka V., Lukashenko V., Semenkin A., Tverdokhlabov S., Kim V., Popov G., Masslenikov N. and Minashko V., "Modern Status of Hall Thruster Development in Russia," AIAA Paper 99-2157. 35th Joint Propulsion Conference. Los Angeles, CA. June 1999.
- ⁷⁴ Jacobson D and Jankovsky R., "Test Results of a 200 W Class Hall Effect Thruster," AIAA Paper 98-3792. 34th Joint Propulsion Conference. Cleveland, OH. July 1998. From Ref [57].
- ⁷⁵ NASA Thermochemical Datatables.
- ⁷⁶ Khaynes V. and Martinez-Sanchez M., "Design of Miniature Hall Thruster for Small Satellites," AIAA Paper 96-3291. AIAA Paper 96-3292. Lake Buena Vista, FL. July 1996.
- ⁷⁷ Spores R.A. and Mitat B., "The USAF Electric Propulsion Program," AIAA Paper 99-2162. 35th Joint Propulsion Conference. Los Angeles, CA. June 1999..
- ⁷⁸ Gorshkov O., "Low-Power Hall Type and Ion Electric Propulsion for the Small Sized Spacecraft," AIAA 98-3929. 34th Joint Propulsion Conf. Cleveland, OH. July 1998. From Ref [57].
- ⁷⁹ Primex (now General Dynamics), Company Information. From Ref [57].
- ⁸⁰ Bassner H.F., Berg H.P., Kukies R. and Bocchiola C., "The Design of RITA Electric Propulsion System for Sat 2 (Artemis)," AIAA Paper 90-2539. Orlando, FL. July 1990. From Ref [57].
- ⁸¹ Satori S., Okamoto H., Sugiki T.M., Aoki Y., Nagata A. and Kizaki T., "Development of Low Power Electric Propulsion Aiming at Small Satellite Applications," AIAA Paper 2001-3794. 37th Joint Propulsion Conference. Salt Lake City, Utah. July 2001.
- ⁸² Fick M. and Muetsch T., "Low Thrust and Low Cost Monopropellant Thruster for Satellites and Satellite Constellations," AIAA Paper 99-2592. 35th Joint Propulsion Conference. Los Angeles, CA. June 1999..
- ⁸³ Parker J.M., Thunnissen D.P., Blandino J.J. and Ganapathi G.B., "Preliminary Design and Status of a Hydrazine milliNewton Thruster Development," AIAA Paper 99-2596. 35th Joint Propulsion Conference. Los Angeles, CA. June 1999..
- ⁸⁴ Koelen O and Viertal Y., "Development and Qualification of a Low-cost, Long-life 1N Monopropellant Hydrazine Thruster," AIAA Paper 96-2867. Lake Buena Vista, FL. July 1996.

- ⁸⁵ Jankovsky R.S., "HAN-based Monopropellant Assessment for Spacecraft," AIAA Paper 96-2863. Lake Buena Vista, FL. July 1996.
- ⁸⁶ Meinhardt D., Brewster G., Christofferson S. and Wucherer E.J., "Development and Testing of New, HAN-based Monopropellant in Small Rocket Thrusters," AIAA Paper 98-4006. 34th Joint Propulsion Conference. Cleveland, OH. July 1998.
- ⁸⁷ Ziener J.K., Cubbin E.A., Choueiri E.Y., Dokukin V. and Oraevsky V., "Pulsed Plasma Propulsion for a Small Satellite Mission: COMPASS P3OINT. ," AIAA Paper 96-3292. Lake Buena Vista, FL. July 1996.
- ⁸⁸ Gulczynski F.S.III, Dulligan M.J., Lake P.J. and Spanjers M., "Micropropulsion Research at AFRL," AIAA Paper 2000-3255. 36th Joint Propulsion Conference. Huntsville, Alabama.
- ⁸⁹ Gatsonis N.A. and Martinez-Sanchez M., "Overview of US Academic Programs in Electric Propulsion," AIAA Paper 2000-3148. 36th Joint Propulsion Conference. Huntsville, Alabama. July 2000.
- ⁹⁰ AIAA Paper 91-2406. "Design of Tridyne Pressurization Systems for Liquid Oxygen polybutadiene Hybrid Rocket Motors," Sacramento, CA. June 1991. From Ref [57].
- ⁹¹ Zakirov V., Sweeting M., Lawrence T. and Sellers J., "Nitrous Oxide as a Rocket Propellant," IAF Paper 2000 – 51st International Astronautical Congress. Rio de Janeiro.
- ⁹² Grossman I., Jones I.R. Lee D.H., "Auxiliary Propulsion Survey, Part III: Survey of Secondary Propulsion and Passive Attitude Control Systems for Spacecraft," AFAPL-TR-6-867 Part III. From Ref [57].
- ⁹³ Pranajaya F.M., "Progress on Micro-Thruster Research and Flight Testing.," Utah State University Small Satellite Conference. 1999. SSC9-VIII-6. From Ref [57].
- ⁹⁴ "Micro-Electric Propulsion Technology," Final Report for Contract NAS8-98176, NASA, Marshall Space Flight Center. Oct, 1998. From Ref [57].
- ⁹⁵ "Advanced High-Thrust Colloid Sources," Journal of Spacecraft. Vol. 11, No. 7, 1974. pp 475-480. From Ref [57].
- ⁹⁶ Referenced from [57]. Personal Communication of Juergen Mueller with Marcuccio S., Centrospazio. Fall 1999/ Spring 2000.
- ⁹⁷ Patterson M., "Low Power Ion Thruster Development Status," AIAA 98-3347. 34th Joint Propulsion Conf. Cleveland, OH. July 1998. From Ref [57].
- ⁹⁸ Atlantic Research Corp., Company Information. From Ref [57].
- ⁹⁹ Kaiser-Marquardt, Company Information. From Ref [57].

- ¹⁰⁰ TRW, Company Information. From Ref [57].
- ¹⁰¹ Zakirov V., Lawrence T., Sellers J. and Sweeting M., "Nitrous Oxide as a Rocket Propellant for Small Satellites," CNES Space Propulsion Conference 2000.
- ¹⁰² Martinez-Sanchez M. and Pollard J.E., "Spacecraft Electric Propulsion: An Overview," Journal of Propulsion and Power. Vol 14. No 5. 1998.
- ¹⁰³ Lawrence T., Sweeting M., Paul M., Humble R., Drum J. and Sellers J., "Results of Cold Gas and Resistojet Research for Small Satellite Applications," Utah State University Small Satellite Conference. 1997.
- ¹⁰⁴ Thiokol Space Motors Catalog. From Ref [57].
- ¹⁰⁵ Boughers W.L., Can C.E., Rauscher R.A. and Slack W.J., "Prototype Development of a Solid Rocket Motor and an Electronic Safin and Arming Device for Nanosatellite (NANOSAT) Missions," Utah State University Small Satellite Conference. 2000. SSC00-X-1.
- ¹⁰⁶ "Microthrusters Employing Catalytically Reacted N₂-O₂-H₂ Gas Mixtures, Tridyne," Journal of Spacecraft and Rockets. Vol 8. No 2. 1971. pp 111-116. From Ref [57].
- ¹⁰⁷ Ketsdever A.D. and Mueller J., "Systems Considerations and Design Options for Microspacecraft Propulsion Systems," AIAA 99-2723. 35th Joint Propulsion Conference. Los Angeles, CA. June 1999.
- ¹⁰⁸ Personal Communication with Robert Breidenthal, Aeronautics/Astronautics Department. University of Washington.
- ¹⁰⁹ INCA : 3D Multi-Zone Navier-Stokes Flow Analysis with Finite-Rate Chemistry. Version 2.- Amtec Engineering, Inc. Bellevue, WA. INCA User's Manual.
- ¹¹⁰ Personal Communication with Scott Imlay and Dave Taflin. Engineers at Amtec Engineering.
- ¹¹¹ Personal Communication with Scott Eberhardt. Professor, Astronautics/Aeronautics Dept. University of Washington.
- ¹¹² Sutherland G.S. and Maes M.E., "A Review of Microrocket Technology: 10⁻⁶ to 1 lbf Thrust," Journal of Spacecraft and Rockets. Vol 3. No 8. August, 1966. From Ref [63].
- ¹¹³ University of Surrey, United Kingdom. Website. <http://www.sstl.co.uk/>
- ¹¹⁴ Stoeckle T., Anweten-Kurtz M. and Fasoulas S., "Heterogeneous Recombustion Reactions Including Energy Accommodation Considerations in High Enthalpy Gas Flows," AIAA Paper 97-2591. 33rd Joint Propulsion Conference. Seattle, WA. July 1997.

- ¹¹⁵ Wernimont E.J. and Mullens P., "Recent Developments in Hydrogen Peroxide Monopropellant Devices," AIAA Paper 99-2741. 35th Joint Propulsion Conference. Los Angeles, CA. June 1999..
- ¹¹⁶ Benson S.W., Arrington L.A., Hoskins W.A. and Meckel N.J., "Development of a PPT for the EO-1 Spacecraft," AIAA Paper 99-2276. 35th Joint Propulsion Conference. Los Angeles, CA. June 1999..
- ¹¹⁷ Schoenman L., "4000°F Materials for Low Thrust Rocket Engines," AIAA Paper 93-2406. Monterey, CA. June 1993.
- ¹¹⁸ Horisawa H. and Kimura I., "Study of Very Low-Power Arcjets." Micropropulsion for Small Spacecraft. Michael M. Micci and Andrew D. Ketsdever, ed. American Institute of Aeronautics and Astronautics, 2000. pp 185-197.
- ¹¹⁹ Aerojet, Company Information. From Ref [57].
- ¹²⁰ Royal Ordnance, Company Information. From Ref [57].
- ¹²¹ Moog Space Products Division, Company Information. From Ref [57].
- ¹²² Marotta Scientific Controls, Inc., Company Information. From Ref [57].
- ¹²³ Perel J, Mahoney J. and Sujo C., "Micro-Electric Propulsion Using Charged Clusters," Proceedings, Formation Flying and Micro-Propulsion Workshop, Air Force Research Laboratory. Lancaster, CA. Oct, 1998. From Ref [57].
- ¹²⁴ Wong J., Reed H. and Ketsdever A., "University Micro-/Nanosatellite as a Micropropulsion Testbed." Micropropulsion for Small Spacecraft. Michael M. Micci and Andrew D. Ketsdever, ed. American Institute of Aeronautics and Astronautics, 2000. pp 25-44. From Ref [57].
- ¹²⁵ Monheiser J., Hruby V., Freeman C., Connolly W. and Pote B., "Development and Testing of a Low-Power Hall Thruster System." Micropropulsion for Small Spacecraft. Michael M. Micci and Andrew D. Ketsdever, ed. American Institute of Aeronautics and Astronautics, 2000. pp 255-270.
- ¹²⁶ Khayms V. and Martinez-Sanchez M., "Fifty-Watt Hall Thruster for Microsatellites." Micropropulsion for Small Spacecraft. Michael M. Micci and Andrew D. Ketsdever, ed. American Institute of Aeronautics and Astronautics, 2000. pp 233-254.
- ¹²⁷ Brophy J.R., Pless L.C., Mueller J. and Anderson J.R., "Operating Characteristics of a 15-cm-dia. Ion Engine for Small Planetary Spacecraft," IEPC Paper 93-110. International Electric, Propulsion Conf. Seattle, WA. Sept 1993. From Ref [57]
- ¹²⁸ Beaettie J.R., Williams J.D. and Robson R.R., "Flight Qualification of an 18-mN Xenon Ion Thruster," IEPC Paper 93-106. Seattle, WA. Sept 1993. From Ref [57]

- ¹²⁹ Mueller J., Chakraborty I., Bame D. and Tang W., "Vaporizing Liquid Microthruster Concept: Preliminary Results of Initial Feasibility Studies." Micropropulsion for Small Spacecraft. Michael M. Micci and Andrew D. Ketsdever, ed. American Institute of Aeronautics and Astronautics, 2000. pp 215-230.
- ¹³⁰ Burton R.L., Rysanek F., Antonsen E.A., Wilson M.J. and Bushman S.S., "Pulsed Plasma Thruster Performance for Microspacecraft Propulsion." Micropropulsion for Small Spacecraft. Michael M. Micci and Andrew D. Ketsdever, ed. American Institute of Aeronautics and Astronautics, 2000. pp 337-352.
- ¹³¹ Atlantic Research Co. Solid Motor Catalog. From Ref [57].
- ¹³² RITA Ion Thruster Assembly. DASA Company Brochure. From Ref [57].
- ¹³³ NASA-Glenn Chemical Equilibrium Program CEA, October 17, 2000. McBride B. and Sanford G. REFS: NASA RP-1311, Part I, 1994 and NASA RP-1311, Part II, 1996.
- ¹³⁴ The Science and Engineering of Materials. Askeland D.R. 3rd ed. PWS Publishing Company, Boston. 1994.

APPENDIX A

	Technology	Prop	Ref.	Isp (s)	Density	p-Isp (Ns/ft ²)	P (W)	Fmin (mN)	Fmax (mN)	Ibit (uN-s)	M (kg)	V (cm ³)
1	Arcjet	N2	118	110	400	432	4.0	5.40	13.70			
2	Arcjet	N2	118	280	400	1099	32.0	5.40	13.70			
3	Arcjet	Argon	55	300	0	0	1k?	25.00	30.00			
4	Arcjet	Ammonia	55	400	609	2390	1k?					
5	Arcjet	Ammonia	55	900	609	5377	1k?					
6	Arcjet	N2	118	90-220	400	0	5-32	8.83	21.60			
7	Arcjet	Ammonia	56	787	609	4702	26 k	1920.00				
8	Arcjet	Hydrazine	56	440	1010	4360	370.0	59.00	74.00			
9	Arcjet	Hydrazine	56	440	1010	4360	1.8 k	250.00				
10	Arcjet	Hydrazine	19	465	1010	4607	1400.0	156.00	222.00	n/a	6	4465.00
11	Arcjet	Hydrazine	19	502	1010	4974	1800.0	200.00	231.00	n/a	5.56	5895.00
12	Arcjet	NH3	19	625	609	3734	2k - 5k	222.00	687.00			
13	Arcjet	NH3	19	725	609	4331	10k - 30k	667.00	2224.00			
14	Arcjet	H2	19	800-1500	ERR	ERR	1k - 50k	133.00	2224.00			
15	Biprop	HTP/Kerosene	16	260	0	0						
16	Biprop	MMH/INTO	57 (99)	280	1100	3021		4450.00		0.43	6641.00	
17	Biprop	MMH/INTO	57 (119)	280	1100	3021		22000.00		0.59	2767.00	
18	Biprop	MMH/MON-1	57 (53)	285	0	0		4000.00		0.27	0.27	
19	Biprop	MMH/INTO	57 (120)	285	1100	3075		22000.00		0.85	2860.00	
20	Biprop	N2H4/INTO	57 (54/58)	287	1100	3097		30000.00		0.1		
21	Biprop	MMH/INTO	57 (59)	289	1100	3119		22000.00		0.67	13273.00	
22	Biprop	MMH/MON-1	57 (53)	290	0	0		10000.00		0.3		
23	Biprop	MMH/INTO	57 (99)	290	1100	3129		10000.00		0.4	1296.00	
24	Biprop	MMH/INTO	57 (98)	290	1100	3129		22000.00		0.55	1988.00	
25	Biprop	MMH11/MON-1/3	60	291	0	0		7500.00	12000.00	0.65	15.9 L	
26	Biprop	MMH/INTO	57 (61)	313	1100	3378		22000.00				
27	Biprop	N2H4/INTO	57 (62)	290	1100	3129		156000.00		0.1		
28	Biprop	ClF3/MonoMeth	63 (112)	310	699	2126		100.00		100		5 mN
29	Biprop	N2O4/MMH	63 (19)	295	1100	3183		500.00				
30	Biprop	HTP/Kerosene	11	290	1286	3659						
31	Biprop	N2O/Kerosene	11	290	750	2134						
32	CG / Spark	H2O	65	250	1019	2500						
33	Cold Gas	Xenon	57 (92)	28	1095	333						
34	Cold Gas	Xe	65	31	1095	333						
35	Cold Gas	Krypton	57 (92)	37	4	1						
36	Cold Gas	Freon 12	57 (92)	37	0	0						
37	Cold Gas	Freon 14	57 (92)	45	0	0						
38	Cold Gas	Argon	57 (92)	52	2	1						
39	Cold Gas	N2O (1)	57 (92)	61	745	446						
40	Cold Gas	CO2 (1)	57 (92)	61	758	454						
41	Cold Gas	N2 (1)	57 (66)	65	400	255	2.4	4.50		100	7.34	
42	Cold Gas	N2 (1)	57 (121)	65	255	16.0	6.30		5.5			
43	Cold Gas	N2 (g)	57 (67/122)	65	220	140	0.3	50.00	1000.00	44000	<50	
44	Cold Gas	CO2 (1)	65	758	485							

Technology	Prop	Ref.	Isp (s)	Density	p-Isp (Ns/lr)	P (W)	Fmin (mN)	Fmax (mN)	Ibit (uN-s)	M (kg)	V (cm^3)
45 Cold Gas	N2 (l)	68	65	400	255	10.1	4.50	100	4.58		
46 Cold Gas	N2O (l)	113	68	745	482					1.24	3997.75
47 Cold Gas	N2O (l)	65	68	735	476						
48 Cold Gas	Butane (l)	65	70	527	362						
49 Cold Gas	N2 (l)	57 (92)	73	400	286						
50 Cold Gas	Neon	57 (92)	75	1	1						
51 Cold Gas	N2 (l)	65	76	400	165						
52 Cold Gas	Propane (l)	65	76	431	321						
53 Cold Gas	N2 (l)	57 (124)	80	400	315						
54 Cold Gas	Ammonia (l)	57 (92)	96	609	574						
55 Cold Gas	NH3 (l)	65	105	609	627						
56 Cold Gas	Methane (g)	57 (92)	105	163	168						
57 Cold Gas	He (g)	57 (92)	165	30	48						
58 Cold Gas	H2 (g)	57 (92)	272	15	40						
59 Cold Gas		57 (69)		ERR	ERR	30.0	2890.00			13	
60 Cold Gas		57 (99)		ERR	ERR	4500.00				5.4	
61 Cold Gas	N2 (g)	63	76	225	168	30 N	100.00	5000.00			
62 Cold Gas	H2O (l)	63 (112)	100	1000	981	0.10	500.00				
63 Cold Gas	NH3 (l)	63 (112)	100	611	599	0.10	500.00				
64 Cold Gas	C3H8 (l)	63 (112)	100	585	574	0.10	500.00				
65 Cold Gas		63	45-75	ERR	ERR	5.00	250000.00				
66 Cold Gas	Ethylene (g)	91	75	415	305						
67 Colloid	Nai/glycerol	57 (70)	450-700	ERR	ERR	2.5	0.60				
68 Colloid	Nai/glycerol	57 (93)	500	0	0	10.0	1.00			0.5	2000.00
69 Colloid	NH3acetate/glyc	57 (94/123)	529	0	0						
70 Colloid		57 (95)	1029	0	0					1.30	
71 Colloid		57 (95)	1382	0	0					0.16	
72 Colloid		57 (95)	1405	0	0					0.13	
73 Colloid	Nai/glycerol	57 (71)	1450	0	0					0.40	
74 FEEP	Cs	57 (96)	9000	0	0	2.7	0.04			1.6 p	1920.00
75 FEEP	Cs	57 (96)	9000	0	0	13.0	0.10			3 p	6214.00
76 FEEP	Cs	57 (96)	9000	0	0	9.3	1.40			2.4 p	2867.00
77 FEEP	Cs	57 (96)	9000	0	0	370.0	1.40			8.7 p	23268.00
78 FMMR	H2O	57 (124)	70	0	0	15.0	4.00	6.00		< 1	4750.00
79 Hall	BHT-200-X2B	72	1200-1600	ERR	ERR	100-300	4.00	17.00			
80 Hall	TAL D-38, D-55	73	1300-1500	ERR	ERR	.7-1.35 k					
81 Hall	SPT M70, M100	73	1300-1500	ERR	ERR	.7-1.35 k				10 D	
82 Hall	TAL D100 D150	73	1500-1800	ERR	ERR	5-10 k					
83 Hall	SPT M100 M140	73	1500-1800	ERR	ERR	5-10 k				13	
84 Hall	TAL D100 D55	73	1500-1900	ERR	ERR	1-5 k					
85 Hall	SPT M115 M100	73	1500-1900	ERR	ERR	1-5 k					
86 Hall	T 220	56	164-2392	ERR	ERR	10 k	278.00	524.00			
87 Hall	TAL TM 50	73	3000-5000	ERR	ERR	25-100 k					
88 Hall	SPT M290	73	3000-5000	ERR	ERR	25-100 k					

Technology	Prop	Ref.	Isp (s)	Density	p-Isp (Ns/ltr)	P (W)	Fmin (mN)	Fmax (mN)	Ibit (uNs/s)	M (kg)	V (cm^3)
89 Hall	SPT30	57 (74)	576-1300	ERR	99-258	5.60	13.00				
90 Hall	X40	57 (78)	800-1750	ERR	80-540	5.00	35.00				
91 Hall	K15	57 (78)	830-1718	ERR	70-400	5.00	16.00				
92 Hall	BHC-1500-025	125	800	0	0	100.0	4.00				
93 Hall	MIT	126	865	0	0	126.0	1.80				
94 Hall	BHT-RT-150	72	1250	0	0	150.0	7.00				
95 Hall	SPT50	57 (98)	1250	0	0	350.0	20.00				
96 Hall	SPT60	57 (98)	1300	0	0	500.0	30.00				
97 Hall	BHC-1500-025	125	1350	0	0	200.0	11.00				
98 Hall	BHC-1500-025	125	1500	0	0	300.0	17.00				
99 Hall	Mini-SPT	76	1600	0	0	50.0	3.00				
100 Hall	Mini MIT (M100)	76	1600	0	0	1350.0	83.00				
101 Hall	SPT-100	76	1600	0	0	300-700	15.00				
102 Hall	BHT-HD-600	72	1700	0	0	45.00	<2.2				
103 Hall	Texas Tech	77	3300	0	0	26-30 k	10000.00				
104 Hall	TAL D55 D100	73		ERR	ERR	>10 k					
105 Hall	SPT M100 M140	73		ERR	ERR	>10 k					
106 Hall		77		ERR	ERR	200.0					
107 Hall	SPT 140	56		ERR	ERR						
108 Hall ?	Fakel	56	3200	ERR	ERR	2.3 k	100.00				
109 Hybrid	HTP/PE	11	269	1310	3457						
110 Hybrid	N2O/HTP/PE	11	259	780	1982						
111 Ion	NASA Lewis	57 (97)	1760-2650	ERR	ERR	100-300	3.60	10.90			
112 Ion	Keldysh Russia	57 (78)	2500-3500	ERR	ERR	150-500	6.00	19.00			
113 Ion	JPL	57 (127)	2500-3900	ERR	ERR	500-900	12.00	31.00			
114 Ion	Keldysh Russia	57 (78)	3100-3700	ERR	ERR	50-140	1.00	5.00			
115 Ion	Hughes	57 (128)	2585	0	0	439.0	17.80				
116 Ion	Comets	51	2906	0	0	1.63 k	23.30				
117 Ion	DASA	57 (80/132)	3000	0	0	240-600	5.00	15.00			
118 Ion		80	3710	0	0	3.45 k	153.00				
119 Ion - Xe	BBM1-MK1-1	80	3518	0	0						
120 Ion - Xe	BBM1-MK1-2	80	3518	0	0						
121 Ion	Xe, Kr	19	800-1600	ERR	ERR						
122 Ion	Xe, Kr	19	1500-5000	ERR	ERR						
123 Microwave		129	730-1330	ERR	0	80.0					
124 Microwave		81		ERR	0	20-30	0.50				
125 Microwave		81		ERR	0	1k	10.00				
126 Monoprop	Hydrazine	82	200-223	1010	2180	12.9-15.4	320.00	1000.00	14-43 mNs	27-28	
127 Monoprop	Hydrazine	57 (79)	210-220	1010	2150	0.3	900.00		0.33	537.00	
128 Monoprop	Hydrazine	57 (79)	213-224	1010	2150		2200.00		0.33	767.00	
129 Monoprop	Hydrazine	57 (79)	226-229	1010	2217		4450.00		0.33	767.00	
130 Monoprop	Hydrazine	83	175	1010	1734		20.00	< 50			
131 Monoprop	Hydrazine	57 (100)	220	1010	2180		5000.00		0.82	15.2 L	
132 Monoprop	Hydrazine	84	222	1010	2200	9.6	250.00		23000	0.376	

Technology	Prop	Ref.	Isp (s)	Density	p-Isp (Ns/mr)	P (W)	Fmin (mN)	Fmax (mN)	Ibit (uN-s)	M (kg)	V (cm^3)
133 Monoprop	Hydrazine	57	223	1010	2210		1000.00			.27-.28	
134 Monoprop	Hydrazine	57 (99)	226	1010	2239		900.00			0.33	470.00
135 Monoprop	Hydrazine	57 (99)	230	1010	2279		4450.00			0.38	653.00
136 Monoprop	Hydrazine	57 (100)	230	1010	2279		18000.00			0.41	20.3L
137 Monoprop	HAN - LPXM46	114	232	1435	3272						
138 Monoprop	Hydrazine	84	234	1010	2318	9.6	1000.00		70000	0.376	
139 Monoprop	HAN - 20% H2O	85	255	1435			3590				
140 Monoprop	HAN - 15% H2O	85	262	1435			3688				
141 Monoprop	HAN - 15% H2O	85	273	1435			3843				
142 Monoprop	H2O2 85-92%	115	179	1347	2365		13345.00			23.89	
143 Monoprop	H2O2 85-82%	115	179	1347	2365		28689.00			46.46	
144 Monoprop	Hydrazine	83	150	1010	1486	5.0	20.00			50-100	
145 Monoprop	HAN/Glycine	86	247	1500	3635						
146 Monoprop	HAN/Glycine	86	225	1400	3090						
147 Monoprop	HAN/Glycine	86	204	1400	2802						
148 Monoprop	HAN/TEAN	86	247	1400	3392						
149 Monoprop	HAN/EAN	86	1400	0							
150 Monoprop	HAN/TmeAN	86	1300	0							
151 Monoprop	HAN/TEAN	85	253	1430	3548						
152 Monoprop	HAN/TEAN	85	259	1450	3690						
153 Monoprop	HAN/DEHAN	85	263	1390	3581						
154 Monoprop	HAN	85	230-280	ERR	ERR						
155 Monoprop	H2O2	63	165	1390	2250		2000.00			200000 mN	
156 Monoprop	Hydrazine	63	227	1010	2249		1000.00			100000 mN	
157 Monoprop	HAN/TEAN	63	253	0	0		400.00			500000.00	
158 Monoprop	N2O	101	206	745	1506						
159 Monoprop	Hydrazine	19	220	1010	2180	9.0	187.00	1121.00	4.45 mN	0.33	542.00
160 Monoprop	Hydrazine	19	220	1010	2180	12.0	890.00	2001.70	71.2 mN	0.319	666.00
161 Monoprop	Hydrazine	19	220	1010	2180	9.0	1334.00	5338.00	84.5 mN	0.33	666.00
162 Monoprop	Hydrazine	19	220	1010	2180	14.0	9786.00	22241.00	334 mN	0.68	2509.00
163 Monoprop	Hydrazine	19	232	1010	2299	27.0		266689.00	1156 mN	0.47	817.90
164 Monoprop	Hydrazine	19	228	1010	2259	10.0	16458.00	355586.00	503 mN	0.39	652.00
165 Monoprop	Hydrazine	19	225	1010	2229	45.0	40034.00	111206.00	979 mN	0.41	841.00
166 Monoprop	Hydrazine	19	220	1010	2180	50.0	48930.00	177929.00	3158 mN	0.88	3284.00
167 Monoprop	Hydrazine	19	228	1010	2259	60.0	71172.00	231308.00	2447 mN	0.88	6503.00
168 Monoprop	Hydrazine	19	229	1010	2269	58.0	346961.00	653889.00	266689mN	1.9	15448.00
169 Monoprop	Hydrazine	19	231	1010	2289	30.0	222411.00	489304.00	5338mN	1.86	2164.00
170 Monoprop	JW Temary	21	283	709	1967						
171 PPT	LES-6	102	200-590	ERR	1.85 (J)		26				
172 PPT	EOS-1	116	650-1400	ERR	12-70		60-860	5.09			
173 PPT	General Specs	68	650-1400	ERR	ERR		2.00	10-1000	2.5		
174 PPT	Japan Lab	102	423	0	0	23.9 J		469			
175 PPT	SMS	102	450	0	0	8.4 J		133			
176 PPT		68	500	0	0	12.5	0.14	70	3.8		

	Technology	Prop	Ref.	Isp (s)	Density	p-Isp (Ns/ltr)	P (W)	Fmin (mN)	Fmax (mN)	Ibit (uN-s)	M (kg)	V (cm^3)
177	PPT	MIT Lab	102	600	0	0	20 J				454	
178	PPT	II PPT-3 Lab	102	600	0	0	30.4 J				450	
179	PPT	TIP-II(NOVA)	102	850	0	0	20 J				375	7.55
180	PPT	China Lab	102	990	0	0	23.9 J				448	
181	PPT	LES-8/9	102	1000	0	0	20 J				267-352	8.08
182	PPT	NIPD-3	102	1130	0	0	750 J				2250	
183	PPT	Primex-NASA	102	1136	0	0	7.5 J				737	
184	PPT	Millipound	102	1210	0	0	43 J				22300	
185	PPT	MIT Lab	102	2580	0	0	100 J				227	
186	PPT	Teflon	130		ERR	ERR	100.0				6.00	50-1000
187	PPT LES 8/9	Princeton	87		ERR	ERR	25.0				285	
188	PPT-UPPT	TechSat 21	77		ERR	ERR						9-11.9
189	UPPT		102		ERR	ERR	1-20	0.00	0.03	2	0.5	
190	UPPT	Edwards	88		ERR	ERR	6-20	0.03	0.10		0.6	
191	PPT	Princeton	89	300-600	ERR	ERR	1-20	0.05	0.90	300-3500		
192	UPPT	DAWGSTAR	20	500	0	0	6.5				65	3.8
193	PPT	Primex	19		ERR	ERR	10-100	0.00	0.67			
194	Resistojet	N2O	113	127	745	928	100.0	125.00				1.24
195	Resistojet	H2O	113	152	1000	1491	100.0	45.00				3997.75
196	Resistojet	H2O	113	182	1000	1785	600.0	270.00				1.24
197	Resistojet	N2O	113	182	745	1330	600.0	270.00				3997.75
198	Resistojet	H2O	63	331	1000	3247	6000/N	10.00				1.24
199	Resistojet	H2O	103	224	1000	2197						3997.75
200	Resistojet	Hydrazine	19	290	1010	2873	350-510	178.00	334.00	2224	0.82	1049.00
201	Resistojet	Hydrazine	19	304	1010	3012	610-830	356.00	498.00	90 mN	0.85	887.00
202	Resistojet	H2O) CH4, CO2	19	180-700	ERR	ERR	250-700	445.00	1779.00			
203	Solid	Marc 4D	57 (131)	199	0	0	159000.00				0.34	530.00
204	Solid	STAR 5A	57 (104)	250	0	0	169000.00				4.7	11946.00
205	Solid	Carboranes	63	75	1380	1015	2000/N					
206	Solid	Sublex-A	63	75	690	508	2000/N	0.01	1.00			
207	Solid	Photochemical	63	130	1346	1717						
208	Solid	Photochemical	63	130	1390	1773						
209	Solid	Decompose	63	262	1860	4781	100/N					
210	Solid	H2O	63	75	1000	736						10000.00
211	Solid	Camphor	63	75	990	728						10.00
212	Solid	Acetamide	63	75	1159	853						10.00
213	Solid	Naphthalene	63	75	1025	754						10.00
214	Solid	Biphenyl	63	75	886	637						10.00
215	Solid	NSMP-NASA	105	280	0	0					445000.00	
216	Warm Gas	H2/O2 w/ Inert	57 (90)	70-140	ERR	ERR						
217	Warm Gas	Tridyne	57 (106)		ERR	ERR						
218	Warm Gas	Tridyne	63	138	206	279	10/N	10.00	10000.00			
219	Warm Gas	Tridyne	63	138	0	0					40.00	

APPENDIX B

```

# 3NH3 + 2N2O + _H2O
# (a) Rocket problem with infinite-area combustor (rocket iac by default).

# (b) NH3(g) (300 K) : N2O(g) (300 K)
# Both are in thermo.lib so that the enthalpies and "exploded" formulas
# do not need to be given.
# (c) The oxidant-to-fuel ratio is automatically determined.
# (d) The chamber pressure is 0.01,0.1,1,10,30,60 bars.
# (e) Calculations are with equilibrium and frozen flow.
# (f) One subsonic area ratio (subar=2), and seven supersonic area
# ratios (supar=2,3,4,5,6,7,8,9,10,11,12,13).

```

```

problem rocket equilibrium
case=8 p,bar=0.01,0.1,1,10,30,60
supar=2,3,4,5,6,7,8,9,10,11,12,13
eql frozen nfz=2
    reactants

```

```

fuel = NH3    moles = 2.    t(k)=300
oxid = N2O   moles = 3.      t(k)=300
oxid = H2O   moles = 2.5     t(k)=300
! 'only' dataset:

```

```

only Ar C CO CO2 H H2 H2O HNO HO2 HNO2 HNO3 N NH
NO N2 N2O3 O O2 OH O3 N2O NH3
! 'output' dataset:
output siunits transport trace=1.e-15
! 'end' dataset
    end

```

APPENDIX C

%% Viscous data for common/stable experimentally friendly gases

% Visc Matrix, Rows 1:Air 2:CO2 3:CO 4:He 5:H2 6:O2 7:N2
% Columns 1:MW 2:T=200K 3:T=300K 4:T=400K

Avogadro = 6.023E26;
D_molecule = 3.7E-10;
sigma = sqrt(2)*pi*D_molecule^2;
gamma = 1.4;

T = [200 300 400];
MW = [28.65; 44; 28; 2; 2; 32; 28];
Visc = [123.5 184.6 230.1; 1 149 190; 127 175 218; 150 199 243; ...
68.1 89.6 108.2; 147.5 207.2 258.2; 129.2 178.2 220.4];

Visc = Visc * 1E-7;

[n_gas,n_T]=size(Visc);

%% Program to compute whether or not a Re and Kn Number combination
%% is available for experimental use in the laboratory corresponding
%% to output from the NH3/NO2
%% output

stablegasdata
eratio = 50;
micro_Pc = [2 5 10 20 30];
Re_exact = [311 485 677 949 1156];
Kn_exact = [0.0024135 0.0015569 0.0011158 0.00079914 0.0065687];
Re_max = [250 600 725 1000 1200];
Re_min = [350 400 625 900 1100];
Kn_max = .002;
Kn_min = .0005;
Vol=2;
T_room=273;
mach=4.6;

[x,max]=size(micro_Pc);

for loop_ct = 1:max,

Output = 0;

```

Output_mflow = 0;
% Pressure in Pa
Pc_start = 0;
Pc_step = 10000;
Pc_end = 150000;

% Throat Diameter
Dt_start = 5E-4;
Dt_step = 5E-4;
Dt_end = 5E-3;

D_throat = Dt_start;

ct = 1;

while D_throat <= Dt_end,
for gas_ct = 1:n_gas,
for T_ct = 1:n_T,
Pc = Pc_start;

while Pc <= Pc_end,
Pbar = Pc/1E5;
Pc=Pc+Pc_step;

R = 8314.41/MW(gas_ct,1);
T_throat(1,ct) = T(1,T_ct)/(1+(gamma-1)/2);
P_throat(1,ct) = Pc/(1+(gamma-1)/2)^(gamma/(gamma-1));
rho_throat(1,ct) = P_throat(1,ct)/R/T_throat(1,ct);

Re=rho_throat(1,ct)*sqrt(gamma*R*T_throat(1,ct))*D_throat...
/Visc(gas_ct,T_ct);
Kn=MW(gas_ct,1)/sigma/D_throat/rho_throat(1,ct)/Avogadro;

if Re <= Re_max(1,loop_ct),
  if Re >= Re_min(1,loop_ct),
    %if Kn <= Kn_max,
    %if Kn >= Kn_min,
    Output(ct,1)=gas_ct;
    Output(ct,2)=D_throat;
    Output(ct,3)=Pc;
  end;
end;
end;
end;

```

```

Output(ct,4)=T(1,T_ct);
Output(ct,5)=rho_throat(1,ct);
Output(ct,6)=Re;
Output(ct,7)=Kn;
Output_mflow(ct,1)=gas_ct;
Output_mflow(ct,2)=D_throat;
Output_mflow(ct,3)=Pc;
Output_mflow(ct,4)=T(1,T_ct);
Output_mflow(ct,5)=Pc/(1+(gamma-1)*mach^2/2)^(gamma/...
(gamma-1)); %Pe
Output_mflow(ct,6)=D_throat^2*pi/4*Pc/sqrt(gamma*R*...
T(1,T_ct))*(gamma*(2/(gamma+1))^...
((gamma+1)/2/(gamma-1))); %mdot
Output_mflow(ct,7)=Output_mflow(ct,6)*R*T_room/Vol;
%Pdot
Output_mflow(ct,8)=Output_mflow(ct,5)/Output_mflow(ct,7);
% time
ct=ct+1;
end
end
%end
%end

end
end
end

D_throat = D_throat + Dt_step;

end

s=sprintf('Micronozzle Pc = %d bar, Re_exact = %d, Kn_exact = %0.5g',...
,micro_Pc(1,loop_ct),...
Re_exact(1,loop_ct),Kn_exact(1,loop_ct));
disp(s)
format short g
s=sprintf('1:Air 2:CO2 3:CO 4:He 5:H2 6:O2 7:N2');
disp(s)
s=sprintf('      Gas   D_throat    Pc      Temp_t ...
rho_t     Re_t     Kn_t');
disp(s)
disp(Output)
s=sprintf(' ');

```

```

disp(s)
s=sprintf('1:Air 2:CO2 3:CO 4:He 5:H2 6:O2 7:N2');
disp(s)
s=sprintf('      Gas   D_throat    Pc      Tc      ...
            Pe       mdot     Pdot    time');
disp(s)
disp(Output_mflow)
s=sprintf(' ');
disp(s)

end

%% Program to select specific Re and Kn Numbers from
%% Upscale_stable output matrix

diary 6Jul01SelectOutput

Re_max = 1000;
Re_min = 100;
Kn_max = .005;
Kn_min = .0005;

[n,m]=size(Output);
ct_select = 1;
ct=1;

while ct <= n,
if Output(ct,6) <= Re_max,
    if Output(ct,6) >= Re_min,
        if Output(ct,7) <= Kn_max,
            if Output(ct,7) >= Kn_min,
                ct
                Output_select(ct_select,1)=Output(ct,1);
                Output_select(ct_select,2)=Output(ct,2);
                Output_select(ct_select,3)=Output(ct,3);
                Output_select(ct_select,4)=Output(ct,4);
                Output_select(ct_select,5)=Output(ct,5);
                Output_select(ct_select,6)=Output(ct,6);
                Output_select(ct_select,7)=Output(ct,7);
                ct_select=ct_select+1;
            end
        end
    end
end
end
end

```

```
ct=ct+1;
end

format short g
s=sprintf('1:Air 2:CO2 3:CO 4:He 5:H2 6:O2 7:N2');
disp(s)
s=sprintf(' Gas D_throat Pc Temp ...
            rho Re Kn');
disp(s)
disp(Output_select)

diary off
```

APPENDIX D

%% Program to compute the grid points necessary for GRIDALL and
 %% INCA CFD Runs of a 3D block nozzle

% Inputs

% p1 = upper throat, p2 = lower throat [p1=(-)p2],
 %% p3 = upper exit, p4 = lower exit [p3=(-)p4]

```
p1_x = 6.60;
p1_y = 0.25;
p2_y = -0.25;
angle = [20 30]; % in degrees
e_ratio = [3 5 10 15 20 25 50 75 100];
```

% Calculations

```
angle_rad = angle*pi/180;
[n_angle,m_angle]=size(angle);
[n_eratio,m_eratio]=size(e_ratio);
ct_angle = 1;
ct_eratio = 1;

ct=1;
while ct_eratio <= m_eratio,
    ct_angle = 1;
    while ct_angle <= m_angle,
        Dt = p1_y-p2_y;
        De = e_ratio(1,ct_eratio)*Dt;
        p3_y = De/2;
        Le = p3_y-p1_y;
        Lx = Le/tan(angle_rad(1,ct_angle));
        p3_x = p1_x+Lx;
        Output(ct,1)=e_ratio(1,ct_eratio);
        Output(ct,2)=angle(1,ct_angle);
        Output(ct,3)=p3_x;
        Output(ct,4)=p3_y;
        ct_angle = ct_angle + 1;
        ct=ct+1;
    end
    ct_eratio = ct_eratio + 1;
end
```

```
% Output
format short g
s=sprintf('Upper nozzle point coordinates for GRIDALL');
disp(s)
s=sprintf(' ');
disp(s);
s=sprintf('      Eratio      Angle      x          y');
disp(s)
disp(Output);
```

APPENDIX E

```
$ RUN.CONTROL
    DEBUG = 'OFF'
$ END

$ DATA.CONTROL
DIMENSIONALITY      = 'THREE.DIMENSION'
NUMBER.OF.POINTS    = 20,
NUMBER.OF.LINES      = 36,
NUMBER.OF.SURFACES   = 21,
NUMBER.OF.BLOCKS     = 4,
SCHEMEUSED.SURFACE  = 'ALGEBRAIC.ONLY',
MESH.FILE FORMAT    = 'PLOT3D.ASCII'
OUTEDGE.FILE        = 'ON'
OUTSURF.FILE        = 'ON'
OUTMESH.FILE        = 'ON'
OUTCONV.FILE        = 'ON'
IMESH.FILE          = 'ON'
MESH.SCALE.FACTOR   = 1.98E-4,
$ END

$ POINT.DATA
POINT.ID   = 1,
XYZ.VALUE = 5.5 1.5 0
$ END
$ POINT.DATA
POINT.ID   = 2,
XYZ.VALUE = 5.5 0 0
$ END
$ POINT.DATA
POINT.ID   = 3,
XYZ.VALUE = 6.60 0.25 0
$ END
$ POINT.DATA
POINT.ID   = 4,
XYZ.VALUE = 6.60 0 0
$ END
$ POINT.DATA
POINT.ID   = 5,
XYZ.VALUE = 10.497 2.5 0
$ END
$ POINT.DATA
```

```
POINT.ID    = 6,  
XYZ.VALUE = 10.497 0 0  
$ END  
$ POINT.DATA  
POINT.ID    = 7,  
XYZ.VALUE = 5.5 1.5 2.5  
$ END  
$ POINT.DATA  
POINT.ID    = 8,  
XYZ.VALUE = 5.5 0 2.5  
$ END  
$ POINT.DATA  
POINT.ID    = 9,  
XYZ.VALUE = 6.60 0.25 2.5  
$ END  
$ POINT.DATA  
POINT.ID    = 10,  
XYZ.VALUE = 6.60 0 2.5  
$ END  
$ POINT.DATA  
POINT.ID    = 11,  
XYZ.VALUE = 10.497 2.5 2.5  
$ END  
$ POINT.DATA  
POINT.ID    = 12,  
XYZ.VALUE = 10.497 0 2.5  
$ END  
$ POINT.DATA  
POINT.ID    = 13,  
XYZ.VALUE = 11.5 0 0  
$ END  
$ POINT.DATA  
POINT.ID    = 14,  
XYZ.VALUE = 11.5 2.5 0  
$ END  
$ POINT.DATA  
POINT.ID    = 15,  
XYZ.VALUE = 11.5 0 2.5  
$ END  
$ POINT.DATA  
POINT.ID    = 16,  
XYZ.VALUE = 11.5 2.5 2.5  
$ END  
$ POINT.DATA
```

```
POINT.ID      = 17,
XYZ.VALUE = 4.5 0 0
$ END
$ POINT.DATA
POINT.ID      = 18,
XYZ.VALUE = 4.5 1.5 0
$ END
$ POINT.DATA
POINT.ID      = 19,
XYZ.VALUE = 4.5 0 2.5
$ END
$ POINT.DATA
POINT.ID      = 20,
XYZ.VALUE = 4.5 1.5 2.5
$ END

$ LINE.DATA
LINE.ID          = 1,
NUMBER.OF.POINTS    = 2,
POINT.ID.VALUE     = 1,2,
NUMBER.OF.GRID.POINTS   = 25,
DISTRIBUTION.OPTION  = 'ONE.SIDE.EXponential.STRETCHING',
FIRST.SPACING      = 0.05,
$ END
$ LINE.DATA
LINE.ID          = 2,
NUMBER.OF.POINTS    = 2,
POINT.ID.VALUE     = 3,4,
NUMBER.OF.GRID.POINTS   = 25,
DISTRIBUTION.OPTION  = 'ONE.SIDE.EXponential.STRETCHING',
FIRST.SPACING      = 0.001,
$ END

$ LINE.DATA
LINE.ID          = 3,
NUMBER.OF.POINTS    = 2,
POINT.ID.VALUE     = 5,6,
NUMBER.OF.GRID.POINTS   = 25,
DISTRIBUTION.OPTION  = 'ONE.SIDE.EXponential.STRETCHING',
FIRST.SPACING      = 0.05,
$ END
$ LINE.DATA
LINE.ID          = 4,
NUMBER.OF.POINTS    = 2,
```

```
POINT.ID.VALUE      = 7,8,
NUMBER.OF.GRID.POINTS   = 25,
DISTRIBUTION.OPTION  = 'ONE.SIDE.EXponential.STRETCHING',
FIRST.SPACING        = 0.05,
$ END
$ LINE.DATA
LINE.ID              = 5,
NUMBER.OF.POINTS    = 2,
POINT.ID.VALUE       = 9,10,
NUMBER.OF.GRID.POINTS = 25,
DISTRIBUTION.OPTION  = 'ONE.SIDE.EXponential.STRETCHING',
FIRST.SPACING        = 0.001,
$ END
$ LINE.DATA
LINE.ID              = 6,
NUMBER.OF.POINTS    = 2,
POINT.ID.VALUE       = 11,12,
NUMBER.OF.GRID.POINTS = 25,
DISTRIBUTION.OPTION  = 'ONE.SIDE.EXponential.STRETCHING',
FIRST.SPACING        = 0.05,
$ END
$ LINE.DATA
LINE.ID              = 7,
NUMBER.OF.POINTS    = 2,
POINT.ID.VALUE       = 1,3,
NUMBER.OF.GRID.POINTS = 30,
DISTRIBUTION.OPTION  = 'ONE.SIDE.EXponential.STRETCHING',
LAST.SPACING         = 0.001,
$ END
$ LINE.DATA
LINE.ID              = 8,
NUMBER.OF.POINTS    = 2,
POINT.ID.VALUE       = 2,4,
NUMBER.OF.GRID.POINTS = 30,
DISTRIBUTION.OPTION  = 'ONE.SIDE.EXponential.STRETCHING',
LAST.SPACING         = 0.001,
$ END
$ LINE.DATA
LINE.ID              = 9,
NUMBER.OF.POINTS    = 2,
POINT.ID.VALUE       = 3,5,
NUMBER.OF.GRID.POINTS = 100,
DISTRIBUTION.OPTION  = 'ONE.SIDE.EXponential.STRETCHING',
FIRST.SPACING        = 0.001,
```

```
$ END
$ LINE.DATA
LINE.ID          = 10,
NUMBER.OF.POINTS = 2,
POINT.ID.VALUE   = 4,6,
NUMBER.OF.GRID.POINTS = 100,
DISTRIBUTION.OPTION = 'ONE.SIDE.EXponential.STRETCHING',
FIRST.SPACING    = 0.001,
$ END
$ LINE.DATA
LINE.ID          = 11,
NUMBER.OF.POINTS = 2,
POINT.ID.VALUE   = 7,9,
NUMBER.OF.GRID.POINTS = 30,
DISTRIBUTION.OPTION = 'ONE.SIDE.EXponential.STRETCHING',
LAST.SPACING     = 0.001,
$ END
$ LINE.DATA
LINE.ID          = 12,
NUMBER.OF.POINTS = 2,
POINT.ID.VALUE   = 8,10,
NUMBER.OF.GRID.POINTS = 30,
DISTRIBUTION.OPTION = 'ONE.SIDE.EXponential.STRETCHING',
LAST.SPACING     = 0.001,
$ END
$ LINE.DATA
LINE.ID          = 13,
NUMBER.OF.POINTS = 2,
POINT.ID.VALUE   = 9,11,
NUMBER.OF.GRID.POINTS = 100,
DISTRIBUTION.OPTION = 'ONE.SIDE.EXponential.STRETCHING',
FIRST.SPACING    = 0.001,
$ END
$ LINE.DATA
LINE.ID          = 14,
NUMBER.OF.POINTS = 2,
POINT.ID.VALUE   = 10,12,
NUMBER.OF.GRID.POINTS = 100,
DISTRIBUTION.OPTION = 'ONE.SIDE.EXponential.STRETCHING',
FIRST.SPACING    = 0.001,
$ END
$ LINE.DATA
LINE.ID          = 15,
NUMBER.OF.POINTS = 2,
```

```
POINT.ID.VALUE      = 1,7,
NUMBER.OF.GRID.POINTS    = 30,
DISTRIBUTION.OPTION  = 'ONE.SIDE.EXponential.STRETCHING',
FIRST.SPACING        = 0.002,
$ END
$ LINE.DATA
LINE.ID              = 16,
NUMBER.OF.POINTS    = 2,
POINT.ID.VALUE      = 2,8,
NUMBER.OF.GRID.POINTS    = 30,
DISTRIBUTION.OPTION  = 'ONE.SIDE.EXponential.STRETCHING',
FIRST.SPACING        = 0.002,
$ END
$ LINE.DATA
LINE.ID              = 17,
NUMBER.OF.POINTS    = 2,
POINT.ID.VALUE      = 3,9,
NUMBER.OF.GRID.POINTS    = 30,
DISTRIBUTION.OPTION  = 'ONE.SIDE.EXponential.STRETCHING',
FIRST.SPACING        = 0.002,
$ END
$ LINE.DATA
LINE.ID              = 18,
NUMBER.OF.POINTS    = 2,
POINT.ID.VALUE      = 4,10,
NUMBER.OF.GRID.POINTS    = 30,
DISTRIBUTION.OPTION  = 'ONE.SIDE.EXponential.STRETCHING',
FIRST.SPACING        = 0.002,
$ END
$ LINE.DATA
LINE.ID              = 19,
NUMBER.OF.POINTS    = 2,
POINT.ID.VALUE      = 5,11,
NUMBER.OF.GRID.POINTS    = 30,
DISTRIBUTION.OPTION  = 'ONE.SIDE.EXponential.STRETCHING',
FIRST.SPACING        = 0.002,
$ END
$ LINE.DATA
LINE.ID              = 20,
NUMBER.OF.POINTS    = 2,
POINT.ID.VALUE      = 6,12,
NUMBER.OF.GRID.POINTS    = 30,
DISTRIBUTION.OPTION  = 'ONE.SIDE.EXponential.STRETCHING',
FIRST.SPACING        = 0.002,
```

```

$ END
$ LINE.DATA
LINE.ID          = 21,
NUMBER.OF.POINTS = 2,
POINT.ID.VALUE   = 13,14,
NUMBER.OF.GRID.POINTS = 25,
DISTRIBUTION.OPTION = 'ONE.SIDE.EXponential.STRETCHING',
LAST.SPACING     = 0.05,
$ END
$ LINE.DATA
LINE.ID          = 22,
NUMBER.OF.POINTS = 2,
POINT.ID.VALUE   = 15,16,
NUMBER.OF.GRID.POINTS = 25,
DISTRIBUTION.OPTION = 'ONE.SIDE.EXponential.STRETCHING',
LAST.SPACING     = 0.05,
$ END
$ LINE.DATA
LINE.ID          = 23,
NUMBER.OF.POINTS = 2,
POINT.ID.VALUE   = 13,15,
NUMBER.OF.GRID.POINTS = 30,
DISTRIBUTION.OPTION = 'ONE.SIDE.EXponential.STRETCHING',
FIRST.SPACING    = 0.002,
$ END
$ LINE.DATA
LINE.ID          = 24,
NUMBER.OF.POINTS = 2,
POINT.ID.VALUE   = 14,16,
NUMBER.OF.GRID.POINTS = 30,
DISTRIBUTION.OPTION = 'ONE.SIDE.EXponential.STRETCHING',
FIRST.SPACING    = 0.002,
$ END
$ LINE.DATA
LINE.ID          = 25,
NUMBER.OF.POINTS = 2,
POINT.ID.VALUE   = 6,13,
NUMBER.OF.GRID.POINTS = 5,
DISTRIBUTION.OPTION = 'EVEN.SPACING',
FIRST.SPACING    = 0.025,
$ END
$ LINE.DATA
LINE.ID          = 26,
NUMBER.OF.POINTS = 2,

```

```
POINT.ID.VALUE      = 5,14,
NUMBER.OF.GRID.POINTS    = 5,
DISTRIBUTION.OPTION  = 'EVEN.SPACING',
FIRST.SPACING        = 0.025,
$ END
$ LINE.DATA
LINE.ID              = 27,
NUMBER.OF.POINTS    = 2,
POINT.ID.VALUE      = 12,15,
NUMBER.OF.GRID.POINTS  = 5,
DISTRIBUTION.OPTION  = 'EVEN.SPACING',
FIRST.SPACING        = 0.025,
$ END
$ LINE.DATA
LINE.ID              = 28,
NUMBER.OF.POINTS    = 2,
POINT.ID.VALUE      = 11,16,
NUMBER.OF.GRID.POINTS  = 5,
DISTRIBUTION.OPTION  = 'EVEN.SPACING',
FIRST.SPACING        = 0.025,
$ END
$ LINE.DATA
LINE.ID              = 29,
NUMBER.OF.POINTS    = 2,
POINT.ID.VALUE      = 17,18,
NUMBER.OF.GRID.POINTS  = 25,
DISTRIBUTION.OPTION  = 'ONE.SIDE.EXponential.STRETCHING',
LAST.SPACING         = 0.05,
$ END
$ LINE.DATA
LINE.ID              = 30,
NUMBER.OF.POINTS    = 2,
POINT.ID.VALUE      = 19,20,
NUMBER.OF.GRID.POINTS  = 25,
DISTRIBUTION.OPTION  = 'ONE.SIDE.EXponential.STRETCHING',
LAST.SPACING         = 0.05,
$ END
$ LINE.DATA
LINE.ID              = 31,
NUMBER.OF.POINTS    = 2,
POINT.ID.VALUE      = 17,19,
NUMBER.OF.GRID.POINTS  = 30,
DISTRIBUTION.OPTION  = 'ONE.SIDE.EXponential.STRETCHING',
FIRST.SPACING        = 0.002,
```

```
$ END
$ LINE.DATA
LINE.ID          = 32,
NUMBER.OF.POINTS = 2,
POINT.ID.VALUE   = 18,20,
NUMBER.OF.GRID.POINTS = 30,
DISTRIBUTION.OPTION = 'ONE.SIDE.EXponential.STRETCHING',
FIRST.SPACING    = 0.002,
$ END
$ LINE.DATA
LINE.ID          = 33,
NUMBER.OF.POINTS = 2,
POINT.ID.VALUE   = 8,19,
NUMBER.OF.GRID.POINTS = 4,
DISTRIBUTION.OPTION = 'EVEN.SPACING',
LAST.SPACING     = 0.025,
$ END
$ LINE.DATA
LINE.ID          = 34,
NUMBER.OF.POINTS = 2,
POINT.ID.VALUE   = 7,20,
NUMBER.OF.GRID.POINTS = 4,
DISTRIBUTION.OPTION = 'EVEN.SPACING',
LAST.SPACING     = 0.025,
$ END
$ LINE.DATA
LINE.ID          = 35,
NUMBER.OF.POINTS = 2,
POINT.ID.VALUE   = 2,17,
NUMBER.OF.GRID.POINTS = 4,
DISTRIBUTION.OPTION = 'EVEN.SPACING',
LAST.SPACING     = 0.025,
$ END
$ LINE.DATA
LINE.ID          = 36,
NUMBER.OF.POINTS = 2,
POINT.ID.VALUE   = 1,18,
NUMBER.OF.GRID.POINTS = 4,
DISTRIBUTION.OPTION = 'EVEN.SPACING',
LAST.SPACING     = 0.025,
$ END

$ SURFACE.DATA
SURFACE.ID      = 1,
```

```
I_MINUS.LINE.ID      = 8,  
I_PLUS.LINE.ID       = 7,  
J_MINUS.LINE.ID     = 1,  
J_PLUS.LINE.ID      = 2,  
$ END  
$ SURFACE.DATA  
SURFACE.ID          = 2,  
I_MINUS.LINE.ID     = 10,  
I_PLUS.LINE.ID       = 9,  
J_MINUS.LINE.ID     = 2,  
J_PLUS.LINE.ID      = 3,  
$ END  
$ SURFACE.DATA  
SURFACE.ID          = 3,  
I_MINUS.LINE.ID     = 12,  
I_PLUS.LINE.ID       = 11,  
J_MINUS.LINE.ID     = 4,  
J_PLUS.LINE.ID      = 5,  
$ END  
$ SURFACE.DATA  
SURFACE.ID          = 4,  
I_MINUS.LINE.ID     = 14,  
I_PLUS.LINE.ID       = 13 ,  
J_MINUS.LINE.ID     = 5,  
J_PLUS.LINE.ID      = 6,  
$ END  
$ SURFACE.DATA  
SURFACE.ID          = 5,  
I_MINUS.LINE.ID     = 16,  
I_PLUS.LINE.ID       = 15,  
J_MINUS.LINE.ID     = 1,  
J_PLUS.LINE.ID      = 4,  
$ END  
$ SURFACE.DATA  
SURFACE.ID          = 6,  
I_MINUS.LINE.ID     = 16,  
I_PLUS.LINE.ID       = 18,  
J_MINUS.LINE.ID     = 8,  
J_PLUS.LINE.ID      = 12,  
$ END  
$ SURFACE.DATA  
SURFACE.ID          = 7,  
I_MINUS.LINE.ID     = 15,  
I_PLUS.LINE.ID       = 17,
```

```
J_MINUS.LINE.ID      = 7,  
J_PLUS.LINE.ID       = 11,  
$ END  
$ SURFACE.DATA  
SURFACE.ID          = 8,  
I_MINUS.LINE.ID     = 18,  
I_PLUS.LINE.ID      = 17,  
J_MINUS.LINE.ID     = 2,  
J_PLUS.LINE.ID      = 5,  
$ END  
$ SURFACE.DATA  
SURFACE.ID          = 9,  
I_MINUS.LINE.ID     = 18,  
I_PLUS.LINE.ID      = 20,  
J_MINUS.LINE.ID     = 10,  
J_PLUS.LINE.ID      = 14,  
$ END  
$ SURFACE.DATA  
SURFACE.ID          = 10,  
I_MINUS.LINE.ID     = 17,  
I_PLUS.LINE.ID      = 19,  
J_MINUS.LINE.ID     = 9,  
J_PLUS.LINE.ID      = 13,  
$ END  
$ SURFACE.DATA  
SURFACE.ID          = 11,  
I_MINUS.LINE.ID     = 20,  
I_PLUS.LINE.ID      = 19,  
J_MINUS.LINE.ID     = 3,  
J_PLUS.LINE.ID      = 6,  
$ END  
$ SURFACE.DATA  
SURFACE.ID          = 12,  
I_MINUS.LINE.ID     = 25,  
I_PLUS.LINE.ID      = 26,  
J_MINUS.LINE.ID     = 3,  
J_PLUS.LINE.ID      = 21,  
$ END  
$ SURFACE.DATA  
SURFACE.ID          = 13,  
I_MINUS.LINE.ID     = 27,  
I_PLUS.LINE.ID      = 28,  
J_MINUS.LINE.ID     = 6,  
J_PLUS.LINE.ID      = 22,
```

```
$ END
$ SURFACE.DATA
SURFACE.ID      = 14,
I_MINUS.LINE.ID = 20,
I_PLUS.LINE.ID  = 23,
J_MINUS.LINE.ID = 25,
J_PLUS.LINE.ID  = 27,
$ END
$ SURFACE.DATA
SURFACE.ID      = 15,
I_MINUS.LINE.ID = 19,
I_PLUS.LINE.ID  = 24,
J_MINUS.LINE.ID = 26,
J_PLUS.LINE.ID  = 28,
$ END
$ SURFACE.DATA
SURFACE.ID      = 16,
I_MINUS.LINE.ID = 23,
I_PLUS.LINE.ID  = 24,
J_MINUS.LINE.ID = 21,
J_PLUS.LINE.ID  = 22,
$ END
$ SURFACE.DATA
SURFACE.ID      = 17,
I_MINUS.LINE.ID = 31,
I_PLUS.LINE.ID  = 32,
J_MINUS.LINE.ID = 29,
J_PLUS.LINE.ID  = 30,
$ END
$ SURFACE.DATA
SURFACE.ID      = 18,
I_MINUS.LINE.ID = 31,
I_PLUS.LINE.ID  = 16,
J_MINUS.LINE.ID = 35,
J_PLUS.LINE.ID  = 33,
$ END
$ SURFACE.DATA
SURFACE.ID      = 19,
I_MINUS.LINE.ID = 32,
I_PLUS.LINE.ID  = 15,
J_MINUS.LINE.ID = 36,
J_PLUS.LINE.ID  = 34,
$ END
$ SURFACE.DATA
```

```
SURFACE.ID      = 20,  
I_MINUS.LINE.ID = 35,  
I_PLUS.LINE.ID  = 36,  
J_MINUS.LINE.ID = 29,  
J_PLUS.LINE.ID  = 1,  
$ END  
$ SURFACE.DATA  
SURFACE.ID      = 21,  
I_MINUS.LINE.ID = 33,  
I_PLUS.LINE.ID  = 34,  
J_MINUS.LINE.ID = 30,  
J_PLUS.LINE.ID  = 4,  
$ END  
  
$ BLOCK.DATA  
BLOCK.ID         = 1,  
NUMBER.OF.I.POINTS = 30,  
NUMBER.OF.J.POINTS = 25,  
NUMBER.OF.K.POINTS = 30,  
I_MINUS.SURF.ID  = 5,  
I_PLUS.SURF.ID   = 8,  
J_MINUS.SURF.ID  = 6,  
J_PLUS.SURF.ID   = 7,  
K_MINUS.SURF.ID  = 1,  
K_PLUS.SURF.ID   = 3,  
$ END  
$ BLOCK.DATA  
BLOCK.ID         = 2,  
NUMBER.OF.I.POINTS = 100,  
NUMBER.OF.J.POINTS = 25,  
NUMBER.OF.K.POINTS = 30,  
I_MINUS.SURF.ID  = 8,  
I_PLUS.SURF.ID   = 11,  
J_MINUS.SURF.ID  = 9,  
J_PLUS.SURF.ID   = 10,  
K_MINUS.SURF.ID  = 2,  
K_PLUS.SURF.ID   = 4,  
$ END  
$ BLOCK.DATA  
BLOCK.ID         = 3,  
NUMBER.OF.I.POINTS = 5,  
NUMBER.OF.J.POINTS = 25,  
NUMBER.OF.K.POINTS = 30,  
I_MINUS.SURF.ID  = 11,
```

```
I.PLUS.SURF.ID      = 16,  
J_MINUS.SURF.ID     = 14,  
J.PLUS.SURF.ID      = 15,  
K_MINUS.SURF.ID     = 12,  
K.PLUS.SURF.ID      = 13,  
$ END  
$ BLOCK.DATA  
BLOCK.ID            = 4,  
NUMBER.OF.I.POINTS   = 4,  
NUMBER.OF.J.POINTS   = 25,  
NUMBER.OF.K.POINTS   = 30,  
I_MINUS.SURF.ID      = 17,  
I.PLUS.SURF.ID       = 5,  
J_MINUS.SURF.ID      = 18,  
J.PLUS.SURF.ID       = 19,  
K_MINUS.SURF.ID      = 20,  
K.PLUS.SURF.ID       = 21,  
$ END
```

APPENDIX F

```

clear all

num_of_files = 2;

ct_data = 1;
ct_id = 1;
symm = 2; % number of symmetry axes from computations

% Choose Setup
setup = 1; % compare datafiles of same geometry
% setup = 2; % compare 2 datafiles of different geometries

%%% Read in data files
while ct_data <= num_of_files,

    clear Output ReOutput KnOutput

    % Display data file being analyzed
    s=sprintf('ct_data = %d',ct_data);
    disp(s)

    if ct_data == 1,
        FIsp=dlmread('../id55/FISPit5000.dat');
        diary on
        diary ../id55/FISPit5000Output
        id_num = 1;
    end

    if ct_data == 2,
        FIsp=dlmread('../id84/FISPitid84.dat');
        diary on
        diary ../id84/FISPitid84Output
        id_num = 1; % change this value to 2 if geometry different
                    % than ct_data = 1
    end

    if ct_data == 3,
        FIsp=dlmread('../id63/FISPit8000.dat');
        diary on
        diary ../id63/FISPit8000Output
    end

```

```

if ct_data == 4,
    FIsp=dlmread('..../id54/FISPit8000.dat');
    diary on
    diary ..../id54/FISPit8000Output
end

if ct_data == 5,
    FIsp=dlmread('..../id37/FISPit10000.dat');
    diary on
    diary ..../id37/FISPit10000Output
end

%% Read in file should be an 8xm matrix with the following column values:
%% 1:x 2:y 3:z 4:U(m/s) 5:P(N/m2) 6:T(K) 7:rho(kg/m3) 8:mach

[n_f,m_f]=size(FIsp); % Size of data files

begin_x=FIsp(1,1); % axial position of bottom-throat midpoint value,
% used to determine # of axial points
Dxt = begin_x;
cont = 0; % used to stop on data line which represents the next
% y-increment
% therefore indicating the number of axial grid points
ct = 2;

cell_y = 0; % set to zero because starts counting on first y line
cell_z = 1; % set to one because starts counting on second x/y plane
track_z = 0; % initial z-value
track_z_max = 0;

while cont == 0,
    if FIsp(ct,1)==begin_x, % when axial value count restarts again at
        % the throat, this loop ends
        ct_lg = ct;
        ct_end = ct-1; % actual nozzle exit value 1 iteration
        % before
        end_x = FIsp(ct-1,1); % end_x = x-position value at nozzle exit
        cont = 1;
    end
    ct = ct+1;
end

cell_x = ct_end; % number of axial grid points

```

```

for ct = 1:n_f,
    if (Flsp(ct,1)==begin_x) & (Flsp(ct,3)==0), % each time increments
        % in y-direction indicates
        % a y-grid point
        cell_y = cell_y + 1;
    end
    if Flsp(ct,3)>track_z_max, % each time z-plane increases indicates
        % increase in z-grid point
        cell_z = cell_z + 1;
        track_z = Flsp(ct,3);
        track_z_max = track_z*1.001; % when z-plane value increases by %
        % 100.1, indicates increase in
        % z-grid point
    end
end

Cells = cell_z*cell_y; % # of total cross-sectional cells

% Calculate dimensions of gridall zone (should correspond to input values)

x_max=0;
y_max=0;
z_max=0;
x_throat=begin_x;
y_throat=0;

for ct_add = 1:n_f,
    x = Flsp(ct_add,1);
    y = Flsp(ct_add,2);
    z = Flsp(ct_add,3);
    if (z == 0) & (y > y_max), % finds max y-value of exit plane
        % used for half-angle, expansion
        % ratio calcs
        y_max = y;
    end
    if (z == 0) & (x > x_max), % finds x-value of exit plane
        % used for half-angle, expansion
        % ratio calcs
        x_max = x;
    end
    if (z == 0) & (x == x_throat) & (y > y_throat),
        % finds max y-value of throat
        % used for half-angle, expansion ratio calcs
        y_throat = y;

```

```

    end
    if z > z_max, % finds maximum z-value, used for aspect ratio calcs
        z_max = z;
    end
end

Dt = y_throat*2; % total throat diameter
Rt = z_max/Dt; % half aspect ratio
if symm == 2,
    Rt = Rt*2; % total aspect ratio
end

Dz = Rt*Dt; % height of nozzle
eratio_comp = y_max/y_throat; % eratio calcs
angle = (atan((y_max-y_throat)/(x_max-x_throat)))*180/pi;
    % half-angle calc

ct_loop = 0;
ct_cell = cell_x*(cell_y-1)*(cell_z-1);
    % total number of cells to be analyzed
    % cell_x <> 1 bx looking at each cross section
ct_total = 0;

C0 = 4.6017E-7; % viscosity coefficients from CEA code and tecplot fit
C1 = 5.9156E-8;
C2 = -2.1120E-11;
C3 = 6.1332E-15;
C4 = -7.1555E-19;

if cluster == 1, % cluster = 1 indicated non-uniform mesh spacing

    plane_xy = cell_x*cell_y;
    plane_yz = cell_y*cell_z;
    ct = 0;

    % Calculate mdot_total for each x value (eratio) and Ae_eratio
    %% 1:x 2:y 3:z 4:U(m/s) 5:P(N/m2) 6:T(K) 7:rho(kg/m3) 8:mach

    for x = 1:cell_x,
        Dy = tan(angle*pi/180)*(FIsp(x,1)-Dxt)+Dt/2; % symmetry Dy
        Dy_Re = 2*Dy; % full nozzle Dy
        if Dy_Re > Dz, % used to calculate minimum physical dimension

```

```

% for Re and Kn number calcs
D_Re = Dz;
else
    D_Re = Dy_Re;
end

A_full = Dy_Re*Dz; % full nozzle area
A_symm = A_full/4; % symmetry nozzle area
eratio(x,1) = Dy/(Dt/2); % expansion ratio at this cross section

mdot_total = 0;
plane_area = 0;
Isp = 0;
F = 0;
m_flux = 0;
P_face = 0;

% calculate mass flux and area
for z = 1:(cell_z-1),
    for y = 1:(cell_y-1),
        ct = ct + 1;

        ct_loop = ct_loop + 1;
        ct_total = ct_total + 1;

        % display number of cells left to be analyzed of entire
block
        if ct_loop == 1000,
            ct_remain = ct_cell-ct_total;
            s=sprintf('ct_data = %d; ct = %d; Remain = %d',...
            ct_data,ct_total,ct_remain);
            disp(s)
            ct_loop = 0;
        end

        LB = (z-1)*plane_xy+x+(cell_x*(y-1)); % lower-left point
        RB = LB+cell_x; % lower-right point
        LU = LB+plane_xy; % upper-left point
        RU = RB+plane_xy; % upper-right point
        U = (FIsp(LB,4)+FIsp(RB,4)+FIsp(LU,4)+FIsp(RU,4))/4;
        % average velocity
        P = (FIsp(LB,5)+FIsp(RB,5)+FIsp(LU,5)+FIsp(RU,5))/4;
        % average pressure
        T = (FIsp(LB,6)+FIsp(RB,6)+FIsp(LU,6)+FIsp(RU,6))/4;

```

```

% average temperature
rho = (FIsp(LB,7)+FIsp(RB,7)+FIsp(LU,7)+FIsp(RU,7))/4;
% average density
mach =
(FIsp(LB,8)+FIsp(RB,8)+FIsp(LU,8)+FIsp(RU,8))/4;
% average mach #
y_area = FIsp(RB,2)-FIsp(LB,2); % cell y-distance
z_area = FIsp(LU,3)-FIsp(LB,3); % cell z-distance
cell_area = y_area*z_area; % cell area
plane_area = plane_area + cell_area;
% summation of cell areas for total plane area
mdot = rho*cell_area*U; % cell mass flux
mdot_total = mdot_total + mdot;
% summation of cell mass flux for total mass flux

end % y-increment

end % z-increment

plane_area = 0;
T_wt = 0;
P_wt = 0;
R_wt = 0;
U_wt = 0;

% Using precalculated total mass flux / area,
% determine thrust and Isp of given cross-section
for z = 1:(cell_z-1),
  for y = 1:(cell_y-1),
    LB = (z-1)*plane_xy+x+(cell_x*(y-1));
    RB = LB+cell_x;
    LU = LB+plane_xy;
    RU = RB+plane_xy;
    U = (FIsp(LB,4)+FIsp(RB,4)+FIsp(LU,4)+FIsp(RU,4))/4;
    P = (FIsp(LB,5)+FIsp(RB,5)+FIsp(LU,5)+FIsp(RU,5))/4;
    rho = (FIsp(LB,7)+FIsp(RB,7)+FIsp(LU,7)+FIsp(RU,7))/4;
    T = (FIsp(LB,6)+FIsp(RB,6)+FIsp(LU,6)+FIsp(RU,6))/4;
    y_area = FIsp(RB,2)-FIsp(LB,2);
    z_area = FIsp(LU,3)-FIsp(LB,3);
    cell_area = y_area*z_area;
    plane_area = plane_area + cell_area;
    if (z == cell_z-1) & (y == 1), % nozzle centerline
      mew_cntr = C0+C1*T+C2*T^2+C3*T^3+C4*T^4;
      Re_cntr = rho*U*D_Re/mew_cntr;
    end
  end
end

```

```

Kn_cntr = 23/6.023E26/sqrt(2)/pi/3.7E-
10^2/D_Re/rho;
elseif (z == cell_z-1) & (y == cell_y-1),
% sidewall centerline
mew_sidewall = C0+C1*T+C2*T^2+C3*T^3+C4*T^4;
Re_sidewall = rho*U*D_Re/mew_sidewall;
Kn_sidewall = 23/6.023E26/sqrt(2)/pi/3.7E-10^2/D_Re/rho;
elseif (z == 1) & (y == 1), % endwall centerline
mew_endwall = C0+C1*T+C2*T^2+C3*T^3+C4*T^4;
Re_endwall = rho*U*D_Re/mew_endwall;
Kn_endwall = 23/6.023E26/sqrt(2)/pi/3.7E-10^2/D_Re/rho;
elseif (z == 1) & (y == cell_y-1), % nozzle corner
mew_corner = C0+C1*T+C2*T^2+C3*T^3+C4*T^4;
Re_corner = rho*U*D_Re/mew_corner;
Kn_corner = 23/6.023E26/sqrt(2)/pi/3.7E-10^2/D_Re/rho;
end

mdot = rho*cell_area*U; % mass flux of respective cell
P_loop = P*cell_area;
% Pressure and mass flux components of Force calcs
m_loop = mdot*U;
F_loop = mdot*U+P*cell_area;
Isp = Isp+F_loop/mdot/9.81*mdot/mdot_total;
% mass-flux weighted average for Isp
P_face = P_face+P_loop; % summation of pressure term
m_flux = m_flux+m_loop; % summation of mass flux
F = F+F_loop; % summation of cross-sectional force

end % y-incrememnt
end % z-increment

actual_plane_area = eratio(x,1)*Dt^2*Rt/4; % symmetry plane area

Ae_mdot(x,1)=x;
Ae_mdot(x,2)=eratio(x,1);
Ae_mdot(x,3)=mdot_total; % total mass flux of 1/4 area
Ae_mdot(x,4)=plane_area; % summation plane area
Ae_mdot(x,5)=actual_plane_area; % expected plane area based on eratio

F=F*4; % Calculated force for entire nozzle

Output(x,1)=x;
Output(x,2)=eratio(x,1);
Output(x,3)=F;

```

```

Output(x,4)=Isp;
Output(x,5)=m_flux;
Output(x,6)=P_face;

ReOutput(x,1) = eratio(x,1);
ReOutput(x,2) = Re_cntr;
ReOutput(x,3) = Re_sidewall;
ReOutput(x,4) = Re_endwall;
ReOutput(x,5) = Re_corner;

KnOutput(x,1) = eratio(x,1);
KnOutput(x,2) = Kn_cntr;
KnOutput(x,3) = Kn_sidewall;
KnOutput(x,4) = Kn_endwall;
KnOutput(x,5) = Kn_corner;

% Each data file assigned to own matrix
if ct_data == 1,
    Graph1(x,1)=eratio(x,1);
    Graph1(x,2)=F;
    Graph1(x,3)=Isp;
    Graph1(x,4)=m_flux;
    Graph1(x,5)=P_face;
end

if ct_data == 2,
    Graph2(x,1)=eratio(x,1);
    Graph2(x,2)=F;
    Graph2(x,3)=Isp;
    Graph2(x,4)=m_flux;
    Graph2(x,5)=P_face;
end

if ct_data == 3,
    Graph3(x,1)=eratio(x,1);
    Graph3(x,2)=F;
    Graph3(x,3)=Isp;
    Graph3(x,4)=m_flux;
    Graph3(x,5)=P_face;
end

if ct_data == 4,
    Graph4(x,1)=eratio(x,1);
    Graph4(x,2)=F;

```

```

Graph4(x,3)=Isp;
Graph4(x,4)=m_flux;
Graph4(x,5)=P_face;
end

if ct_data == 5,
    Graph5(x,1)=eratio(x,1);
    Graph5(x,2)=F;
    Graph5(x,3)=Isp;
    Graph5(x,4)=m_flux;
    Graph5(x,5)=P_face;
end

end % plane loop, increment to next axial grid point

ct_remain = ct_cell-ct_total;
s=sprintf('cell_total = %d; ct = %d; Remain = %d',ct_cell,ct_total,ct_remain);
disp(s)

end % cluster == 1;

%% Ideal thrust and Isp Calculations from CEA output
% Datafile
dataceanh3

% Calculations
[n_data,m_data]=size(eratio_cea);

Stop = 1;
for ct = 1:m_data,
    if (eratio_cea(1,ct) >= eratio(ct_end,1)) & (Stop == 1),
        ct_cea = ct;
        Stop = 0;
    end
end

if Stop == 1,
    ct_cea = m_data;
end

At = Dt^2*Rt;
for ct = 1:ct_cea,
    rhov2P_cea(1,ct) = rho_cea(1,ct)*(son_vel_cea(1,ct)*...

```

```

mach_cea(1,ct))^2+P_cea(1,ct);
Ae(1,ct)      = At*eratio_cea(1,ct);
mdot_cea(1,ct) = rho_cea(1,ct)*(son_vel_cea(1,ct)*...
                         mach_cea(1,ct))*Ae(1,ct);
F_cea(1,ct)    = rhov2P_cea(1,ct)*Ae(1,ct);
Isp_cea(1,ct)  = F_cea(1,ct)/rho_cea(1,ct)/Ae(1,ct)/son_vel_cea(1,ct)...
                         /mach_cea(1,ct)/9.81;

if id_num == 1,
    Graph1_cea(ct,1)=eratio_cea(1,ct);
    Graph1_cea(ct,2)=F_cea(1,ct);
    Graph1_cea(ct,3)=Isp_cea(1,ct);
    Graph1_cea(ct,4)=mdot_cea(1,ct);
end
if id_num == 2,
% only used if geometries are different
% from one datafile to the next
    Graph2_cea(ct,1)=eratio_cea(1,ct);
    Graph2_cea(ct,2)=F_cea(1,ct);
    Graph2_cea(ct,3)=Isp_cea(1,ct);
    Graph2_cea(ct,4)=mdot_cea(1,ct);
end
end

if id_num == 1,
    Output_ideal=Graph1_cea;
end
if id_num == 2,
    Output_ideal=Graph2_cea;
end

blank=sprintf(' ');

s=sprintf('INCA/Matlab Micronozzle Computational Results');
disp(s)
Case=sprintf('ID#= %d: Angle= %0.3g: Rt= %0.3g: D= %0.3g m: Eratio= %0.3g',...
    ,id_num,angle,Rt,D,eratio_comp);
disp(Case)
CellPrint=sprintf('Cells : x=%d y=%d z=%d : Exit Plane = %d', ...
    cell_x, cell_y, cell_z, Cells);
disp(CellPrint)
s=sprintf(' ');
disp(s)

```

```

format short g

s=sprintf('    eratio      F_ideal      Isp_ideal      mdot_ideal');
disp(s)
disp(Output_ideal)
disp(blank)

if cluster == 0,
    cluster=sprintf('      X      Dy      eratio      Ae_symm
Ae_cell      mdot_total');
else
    cluster=sprintf('      X      Eratio      mdot_total      plane_area      Actual_area');
end
disp(cluster)
disp(Ae_mdot)

format short g
s=sprintf('      x      eratio      F      Isp      mass_flux      Pressure_term');
disp(s)
disp(Output)

s=sprintf('Reynolds #');
disp(s)
s=sprintf('    eratio      center      sidewall      endwall      corner');
disp(s)
disp(ReOutput)
disp(blank)

s=sprintf('Knudsen #');
disp(s)
s=sprintf('    eratio      center      sidewall      endwall      corner');
disp(s)
disp(KnOutput)
disp(blank)

ct_data = ct_data + 1;

diary off

end %end of ct_data loop for comparison files

% Figures
case_title = sprintf('ID28 Check on Convergence Criteria');
fig_ct = 1;

```

```

if setup == 1,
fig_ct = 1;

figure(fig_ct)
plot(Graph1(:,1),Graph1(:,2),'rx')
hold on
plot(Graph2(:,1),Graph2(:,2),'g*')
hold on
%plot(Graph3(:,1),Graph3(:,2),'bo')
hold on
%plot(Graph4(:,1),Graph4(:,2),'ms')
hold on
%plot(Graph5(:,1),Graph5(:,2),'kd')
hold on
plot(Graph1_cea(:,1),Graph1_cea(:,2),'r-')
hold off
xlabel('Eratio')
ylabel('Thrust (N)')
legend('Rt=10','Rt=1','ideal')
title(case_title)

fig_ct = fig_ct+1;

figure(fig_ct)
plot(Graph1(:,1),Graph1(:,3),'rx')
hold on
plot(Graph2(:,1),Graph2(:,3),'g*')
hold on
%plot(Graph3(:,1),Graph3(:,3),'bo')
hold on
%plot(Graph4(:,1),Graph4(:,3),'ms')
hold on
%plot(Graph5(:,1),Graph5(:,3),'kd')
hold on
plot(Graph1_cea(:,1),Graph1_cea(:,3),'r-')
hold off
legend('Rt=10','Rt=1','ideal')
xlabel('Eratio')
ylabel('Isp (sec)')
title(case_title)

fig_ct=fig_ct+1;

```

```
end

if setup == 2,
    fig_ct = 1;

    figure(fig_ct)
    plot(Graph1(:,1),Graph1(:,2),'rx')
    hold on
    plot(Graph2(:,1),Graph2(:,2),'b*')
    hold on
    plot(Graph1_cea(:,1),Graph1_cea(:,2),'r-')
    hold on
    plot(Graph2_cea(:,1),Graph2_cea(:,2),'b-')
    hold off
    xlabel('Eratio')
    ylabel('Thrust (N)')
    title(case_title)
    legend('id45','id46')
    fig_ct = fig_ct+1;

    figure(fig_ct)
    plot(Graph1(:,1),Graph1(:,3),'rx')
    hold on
    plot(Graph2(:,1),Graph2(:,3),'b*')
    hold on
    plot(Graph1_cea(:,1),Graph1_cea(:,3),'r-')
    hold on
    plot(Graph2_cea(:,1),Graph2_cea(:,3),'b-')
    hold off
    xlabel('Eratio')
    ylabel('Isp (sec)')
    title(case_title)
    legend('id45','id46')

    fig_ct=fig_ct+1;

end
```

APPENDIX G

id	test case #		Re_t_id	Re# ideal @ throat		F_ideal	ideal thrust
Tc	chamber temp (K)		Re_f	Re# computed @ throat		F_comp	computed thrust
Rt	aspect ratio		Kn_t_id	Kn# ideal @ throat		n_F	thrust efficiency
Dt_pre	design throat diameter		Kn_t	Kn# computed @ throat		lsp_ideal	ideal specific impulse
SF	scale factor		Re_e_id	Re# ideal @ exit		lsp_comp	computed specific impulse
ArQ	1/4 throat area		Re_e	Re# computed @ exit		n_lsp	specific impulse efficiency
Dt_pst	check throat diameter		Kn_e_id	Kn# ideal @ exit		mf_ideal	ideal mass flux
ysw	y+ value sidewall		Kn_e	Kn# computed @ exit		mf_comp	computed mass flux
yew	y+ value endwall					n_mf	mass flux efficiency

id	Tc	Rt	Dt pre	SF	ArQ	Dt pst	ysw	yew	Re_t_id	Re# ideal @ throat	Re_f_id	Re# computed @ throat	Kn_t_id	Kn# ideal @ throat	F_ideal	ideal thrust
114	3000	10	12.38	2.476E-05	3.8316E-09	12.38	0.4	0.2	253	240	441	609	0.0030	0.004		
115	3000	10	24.76	4.952E-05	1.5326E-08	24.76	0.55	0.35	505	447	881	1128	0.0015	0.002		
116	3000	10	49.53	9.906E-05	6.1331E-08	49.53	0.75	0.65	1011	949	1763	2151	0.0007	0.001		
117	3000	10	74.39	0.00014488	1.3801E-07	74.30	0.9	0.9	1516	1420	2644	3165	0.0005	0.0009		
118	3000	10	99.05	0.0001981	2.4502E-07	99.00	1.1	1	2021	1889	3523	4171	0.0004	0.0007		
119	2500	10	10.01	2.002E-05	2.5050E-09	10.01	0.37	0.19	249	233	441	588	0.0031	0.004		
120	2500	10	20.02	4.004E-05	1.0020E-08	20.02	0.54	0.34	498	462	882	1090	0.0015	0.003		
121	2500	10	40.05	0.0000801	4.0100E-08	40.05	0.74	0.61	997	918	1764	2076	0.0008	0.001		
122	2500	10	60.07	0.0001201	9.0210E-08	60.07	0.9	0.9	1495	1374	2646	3053	0.0005	0.001		
123	2500	10	80.09	0.0001602	1.6036E-07	80.09	1.1	1	1993	1829	3528	4026	0.0004	0.0007		
124	2000	10	7.94	1.588E-05	1.5761E-09	7.94	0.45	0.39	259	238	495	16	0.0031	0.005		
125	2000	10	15.88	3.176E-05	6.3044E-09	15.88	0.55	0.35	518	473	989	1156	0.0015	0.003		
126	2000	10	31.76	6.352E-05	2.5217E-08	31.76	0.75	0.65	1035	941	1978	2203	0.0008	0.001		
127	2000	10	47.65	0.0000953	5.6763E-08	47.65	0.91	0.9	1553	1408	2968	3247	0.0005	0.001		
128	2000	10	63.53	0.0001271	1.0097E-07	63.55	1	1	2072	1875	3958	4166	0.0004	0.0008		
129	1500	10	5.62	1.124E-05	7.8961E-10	5.62	0.4	0.2	267	238	579	665	0.0032	0.004		
130	1500	10	11.24	2.248E-05	3.1584E-09	11.24	0.54	0.36	533	473	1158	1247	0.0016	0.003		
131	1500	10	22.47	4.494E-05	1.2623E-08	22.47	0.76	0.65	1066	940	2315	2381	0.0008	0.002		
132	1500	10	33.71	6.742E-05	2.8409E-08	33.71	0.9	0.9	1600	1407	3473	3507	0.0005	0.001		
133	1500	10	44.94	8.988E-05	5.0490E-08	44.94	1.04	1.14	2133	1873	4629	4648	0.0004	0.0008		
134	1000	10	3.03	6.06E-06	2.2952E-10	3.03	0.4	0.2	253	212	647	683	0.0040	0.006		
135	1000	10	6.07	1.214E-05	9.2112E-10	6.07	0.54	0.35	506	420	1296	1272	0.0020	0.004		
136	1000	10	12.14	2.428E-05	3.6845E-09	12.14	0.75	0.62	1013	836	2592	2425	0.0010	0.002		

id	Kn_e_id	Kn_e	F_ideal	F_comp	n_F	lsp_ideal	lsp_comp	n_lsp	mf_ideal	mf_comp	n_mf
114	0.0072	0.03	7.83	6.5	0.830	282.1	252.1	0.894	7.07E-07	5.921E-07	0.837
115	0.0036	0.01	31.32	26.7	0.853	282.1	258.6	0.917	2.83E-06	2.636E-06	0.932
116	0.0018	0.007	125.33	109.3	0.872	282.1	263.2	0.933	1.13E-05	1.059E-05	0.935
117	0.0012	0.005	282.02	248.1	0.880	282.1	265.2	0.940	2.55E-05	2.390E-05	0.938
118	0.0009	0.004	500.69	442.7	0.884	282.1	266.3	0.944	4.52E-05	4.236E-05	0.936
119	0.0073	0.03	5.15	4.22	0.819	262.4	239	0.911	5E-07	4.494E-07	0.898
120	0.0036	0.02	20.61	17.5	0.849	262.4	245.3	0.935	2E-06	1.815E-06	0.907
121	0.0018	0.008	82.48	71.5	0.867	262.4	249.7	0.951	8.01E-06	7.298E-06	0.911
122	0.0012	0.005	185.56	162.3	0.875	262.4	251.6	0.959	1.8E-05	1.644E-05	0.912
123	0.0009	0.004	329.86	290	0.879	262.4	252.7	0.963	3.2E-05	2.924E-05	0.913
124	0.0075	0.03	3.24	2.66	0.821	236.6	216.7	0.916	3.49E-07	3.122E-07	0.895
125	0.0037	0.02	12.96	10.98	0.847	236.6	222.2	0.939	1.4E-06	1.259E-06	0.902
126	0.0019	0.008	51.82	44.8	0.864	236.6	226	0.955	5.58E-06	5.057E-06	0.906
127	0.0012	0.006	116.65	101.8	0.873	236.6	227.6	0.962	1.26E-05	1.140E-05	0.907
128	0.0009	0.004	207.50	182	0.877	236.6	228.6	0.966	2.23E-05	2.029E-05	0.908
129	0.0075	0.04	1.61	1.33	0.826	202.3	188.3	0.931	2.03E-07	1.793E-07	0.884
130	0.0038	0.02	6.44	5.49	0.853	202.3	192.7	0.953	8.11E-07	7.255E-07	0.894
131	0.0019	0.01	25.73	22.4	0.870	202.3	195.8	0.968	3.24E-06	2.911E-06	0.898
132	0.0013	0.006	57.91	50.8	0.877	202.3	197.2	0.975	7.3E-06	6.560E-06	0.899
133	0.0009	0.004	102.93	90.6	0.880	202.3	198	0.979	1.3E-05	1.166E-05	0.899
134	0.0090	0.05	0.46	0.3804	0.821	163.6	152.6	0.933	7.222E-08	6.352E-08	0.880
135	0.0045	0.03	1.86	1.58	0.850	163.6	156.2	0.955	2.9E-07	2.578E-07	0.890
136	0.0023	0.01	7.44	6.45	0.867	163.6	158.5	0.969	1.16E-06	1.036E-06	0.894

<u>Id</u>	<u>Tc</u>	<u>Rt</u>	<u>Dt</u>	<u>pre</u>	<u>SF</u>	<u>ArQ</u>	<u>Dt</u>	<u>pst</u>	<u>ysw</u>	<u>yew</u>	<u>Re</u>	<u>t</u>	<u>Re</u>	<u>s</u>	<u>id</u>	<u>Re</u>	<u>e</u>	<u>Kn</u>	<u>t</u>	<u>Kn</u>	<u>t</u>
137	1000	10	18.21	3.642E-05	8.2901E-09	18.21	0.9	1519	1251	3889	3562	0.0007	0.001								
138	1000	10	24.28	4.856E-05	1.4733E-08	24.28	2.2	1	2025	1655	5184	4876	0.0005	0.001							
139	1000	10	24.28	4.856E-05	1.4733E-08	24.28	2.5	1	2025	1664	5184	4287	0.0005	0.01							
140	2000	10	63.53	0.0001271	1.0097E-07	63.55	1.5	0.6	2072	1872	3958	3930	0.0004	0.0007							
141	3000	10	24.76	4.952E-05	1.5326E-08	24.76	0.51	0.85	505	475	881	1071	0.0015	0.002							
142	3000	10	49.53	9.906E-05	6.1337E-08	49.53	0.8	1.5	1011	947	1763	2005	0.0007	0.001							
143	3000	10	74.29	0.0001486	1.3861E-07	74.46	0.9	2	1520	1418	2650	2923	0.0005	0.0008							
144	3000	10	99.05	0.0001981	2.4503E-07	99.00	1.1	2.5	2021	1886	3523	3829	0.0004	0.0006							
145	3000	10	99.05	0.0001981	2.4503E-07	99.00	1	0.6	2021	1890	3523	4182	0.0004	0.0007							
146	3000	10	99.05	0.0001981	2.4502E-07	99.00	1	0.65	2021	1886	3523	3859	0.0004	0.0006							
147	3000	10	99.05	0.0001981	2.4503E-07	99.00	1.1	1	2021	1887	3523	4168	0.0004	0.0007							
148	3000	1	309	0.000618	2.3932E-07	309.40	0.8	1.1	6315	5817	1101	1348	0.0001	0.0002							
149	3000	1	309	0.000618	2.3932E-07	309.40	0.75	1.15	6315	5870	1101	1491	0.0001	0.0002							
150	3000	1	309	0.000618	2.3932E-07	309.40	0.7	1.1	6315	5871	1101	1523	0.0001	0.0002							
151	3000	5	138	0.000276	2.3943E-07	138.40	0.8	1.1	2825	2607	2463	2792	0.0003	0.0004							
152	3000	5	138	0.000276	2.3943E-07	138.40	7	0.8	2825	2631	2463	3159	0.0003	0.0004							
153	3000	5	138	0.000276	2.3943E-07	138.40	0.6	0.7	2825	2629	2463	3321	0.0003	0.0005							
154	3000	5	138	0.000276	2.3943E-07	138.40			2825	2628	2463	3361	0.0003	0.0005							
155	2500	10	98.7	0.0001974	2.4354E-07	98.70	1	1.3	2457	2262	4348	4947	0.0003	0.0006							
156	2500	5	139.6	0.0002792	2.4360E-07	139.60	0.8	0.95	3474	3173	3075	3736	0.0002	0.0004							
157	2500	1	312.1	0.0006242	2.4352E-07	312.10	0.85	1.4	7768	7081	1375	1767	0.0001	0.0002							
158	2000	10	98.7	0.0001974	2.4354E-07	98.70	1.2	1.6	3217	2907	6147	6405	0.0002	0.0005							
159	2000	5	139.6	0.0002792	2.4360E-07	139.60	1.2	0.92	4550	4096	4347	4776	0.0002	0.0004							
160	2000	1	312.2	0.0006244	2.4367E-07	312.20	1	1.7	10176	9139	1944	2240	0.0001	0.0002							
161	3000	5	24.6	0.0000492	7.5860E-09	24.64	0.3	0.2	503	473	438	672	0.0015	0.002							
162	3000	1	77.9	0.0001558	1.5171E-08	77.90	0.4	0.35	1590	1489	277	379	0.0005	0.0008							
163	2500	10	24.55	0.0000491	1.5074E-08	17.36	0.6	0.4	432	565	765	1614	0.0018	0.002							
164	2500	5	34.72	6.944E-05	1.5073E-08	34.73	0.45	0.3	864	795	765	1053	0.0009	0.002							
165	2500	1	77.64	0.0001553	1.5074E-08	77.65	0.45	0.45	1933	1775	342	455	0.0004	0.0008							
166	2000	10	24.56	4.912E-05	1.5080E-08	24.56	0.7	0.5	801	729	1530	1697	0.0010	0.002							
167	2000	5	34.73	6.946E-05	1.5077E-08	34.73	0.5	0.355	1132	1025	1082	1326	0.0007	0.001							
168	2000	1	77.66	0.0001553	1.5074E-08	77.65	0.5	0.55	2531	2288	484	618	0.0003	0.0006							
169	3000	5	34.8	0.0000696	1.5173E-08	34.84	0.4	0.3	711	667	620	908	0.0011	0.002							

<u>Id</u>	<u>Kn_e_id</u>	<u>Kn_e</u>	<u>F_ideal</u>	<u>F_comp</u>	<u>n_F</u>	<u>Isp_Ideal</u>	<u>Isp_comp</u>	<u>n_Isp</u>	<u>Isp</u>	<u>n_comp</u>	<u>mf_Ideal</u>	<u>mf_comp</u>	<u>n_mf</u>
137	0.0015	0.008	16.74	14.6	0.872	163.6	159.4	0.974	2.61E-06	2.338E-06	0.897		
138	0.0011	0.007	29.74	25.4	0.854	163.6	158.5	0.969	4.63E-06	4.087E-06	0.882		
139	0.0011	0.005	29.74	25.6	0.861	163.6	158.6	0.969	4.63E-06	4.118E-06	0.889		
140	0.0009	0.003	207.50	178.8	0.862	236.6	226.2	0.956	2.23E-05	2.014E-05	0.901		
141	0.0036	0.01	31.32	26.2	0.837	282.1	256.2	0.908	2.83E-06	2.606E-06	0.921		
142	0.0018	0.005	125.34	107.3	0.856	282.1	260.4	0.923	1.13E-05	1.049E-05	0.926		
143	0.0012	0.004	283.25	243.5	0.860	282.1	262.4	0.930	2.56E-05	2.365E-05	0.924		
144	0.0009	0.003	500.71	434.5	0.868	282.1	263.4	0.934	4.52E-05	4.200E-05	0.928		
145	0.0009	0.003	500.71	442.3	0.883	282.1	266.3	0.944	4.52E-05	4.233E-05	0.936		
146	0.0009	0.003	500.69	434	0.867	282.1	263.3	0.933	4.52E-05	4.201E-05	0.929		
147	0.0009	0.004	500.71	442.8	0.884	282.1	266.9	0.946	4.52E-05	4.228E-05	0.935		
148	0.0029	0.006	489.04	384.8	0.787	282.1	250.4	0.888	4.42E-05	3.916E-05	0.886		
149	0.0029	0.008	489.04	396.2	0.810	282.1	254.5	0.902	4.42E-05	3.967E-05	0.898		
150	0.0029	0.08	489.04	398.1	0.814	282.1	255.4	0.905	4.42E-05	3.973E-05	0.899		
151	0.0013	0.004	489.27	414.7	0.848	282.1	260.9	0.925	4.42E-05	4.051E-05	0.917		
152	0.0013	0.005	489.27	426.5	0.872	282.1	264.5	0.938	4.42E-05	4.109E-05	0.930		
153	0.0013	0.005	489.27	427.9	0.875	282.1	265.4	0.941	4.42E-05	4.109E-05	0.930		
154	0.0013	0.006	489.27	428.1	0.875	282.1	265.7	0.942	4.42E-05	4.107E-05	0.929		
155	0.0007	0.003	500.95	441.6	0.882	262.4	253	0.964	4.86E-05	4.448E-05	0.914		
156	0.0010	0.004	501.08	436.2	0.871	262.4	251.6	0.959	4.87E-05	4.418E-05	0.908		
157	0.0023	0.007	500.91	406.9	0.872	262.4	243	0.926	4.86E-05	4.267E-05	0.877		
158	0.0006	0.003	500.49	441.6	0.882	236.6	229.9	0.972	5.39E-05	4.895E-05	0.908		
159	0.0009	0.003	500.62	436.2	0.871	236.6	228.4	0.965	5.39E-05	4.867E-05	0.903		
160	0.0019	0.006	500.76	410.6	0.820	236.6	221.6	0.937	5.39E-05	4.724E-05	0.876		
161	0.0072	0.03	15.50	12.7	0.819	282.1	252.9	0.897	1.4E-06	1.283E-06	0.916		
162	0.0114	0.03	31.00	22.8	0.735	282.1	236.8	0.839	2.8E-06	2.452E-06	0.875		
163	0.0042	0.01	31.01	26.5	0.855	262.4	246.7	0.940	3.01E-06	2.740E-06	0.910		
164	0.0042	0.02	31.01	26	0.839	262.4	244.4	0.931	3.01E-06	2.708E-06	0.899		
165	0.0094	0.02	31.01	23	0.742	262.4	227.7	0.868	3.01E-06	2.570E-06	0.854		
166	0.0024	0.01	30.99	26.6	0.858	236.6	224.7	0.950	3.34E-06	3.021E-06	0.905		
167	0.0034	0.01	30.98	26.1	0.842	236.6	222.7	0.941	3.34E-06	2.990E-06	0.896		
168	0.0077	0.02	30.98	23.5	0.759	236.6	209.3	0.885	3.34E-06	2.861E-06	0.857		
169	0.0051	0.02	31.01	25.9	0.835	282.1	255.9	0.907	2.8E-06	2.583E-06	0.922		

<u>Id</u>	<u>Tc</u>	<u>Rt</u>	<u>Dt_pre</u>	<u>SF</u>	<u>ArQ</u>	<u>Dt_ps</u>	<u>ysw</u>	<u>yew</u>	<u>Re_t_id</u>	<u>Re_t</u>	<u>Re_e_id</u>	<u>Re_e</u>	<u>Kn_t_id</u>	<u>Kn_t</u>
170	3000	10	24.76	4.952E-05	1.5326E-08	24.76	0.54	0.9	505	477	881	1118	0.0015	0.002
171	3000	10	49.53	9.906E-05	6.1331E-08	49.53	0.8	1.5	1011	949	1763	2137	0.0007	0.001
172	3000	10	74.29	0.0001486	1.3801E-07	74.30	0.9	2	1516	1420	2644	3147	0.0005	0.0009
173	3000	10	99.05	0.0001981	2.4502E-07	99.00	1	2.5	2021	1889	3523	4151	0.0004	0.007
174	3000	10	99.05	0.0001981	2.4503E-07	99.00	1	0.6	2021	1890	3523	4182	0.0004	0.0007
175	3000	1	309	0.000618	2.3932E-07	309.40	0.9	1.15	6315	5871	1101	1512	0.0001	0.0002
176	3000	15	81	0.000162	2.4604E-07	81		0.5	1653	1537	2883	3055	0.0005	0.0008
177	3000	15	81	0.000162	2.4604E-07	81	0.55	0.55	1653	1542		3326	0.0008	
178	3000	15	81	0.000162	2.4604E-07	81	0.45	0.45	1653	1542		3413	0.0008	
179	3000	15	20	0.00004	1.5000E-08	81	0.3	0.15	408	345	712	893	0.002	0.0008

APPENDIX H

```

$ RUN.CONTROL
STARTING.STEP      = 0,
ENDING.STEP        = 5000,
CONVERGENCE.LEVEL.PRINT.FREQ = 10,
SCRPATH           = '',
INPUT.FILE FORMAT = 'VERSION.2'
WRITE.RESTART.FILE = 'YES'
RESTART.FILE.WRITE.FREQ = 100,
$ END

$ INCA.SETUP
TITLE              = 'ID118:Re2000:IMESH55(Cluster:30/100/25/25)'
NUMBER.OF.ZONES    = 4,
MESH.FILE FORMAT = 'PLOT3D.ASCII',
SOLVERS.ENABLED    = 'NS.3D',
DEBUG.FLAGS(2)     = 0, 0, 0,
PLOT.FILE.PATH     = './id118',
RESTART.FILE.PATH   = './id118',
FIELD.TECPLOT3D.FORMAT = 'BINARY',
SURFACE.TECPLOT.FORMAT = 'BINARY',
$ END

$ NSIC.UNIFORM.FLOW
LABEL   = 'ENTRANCE'
NUMBER.OF.BLOCKS = 1,
X.VELOCITY.COMP = 100,
PRESSURE        = 30E5,
TEMPERATURE     = 3000,
SPECIES.MASS.FRACTIONS = .41 .59,
$ END
$ NSIC.UNIFORM.FLOW
LABEL   = 'CONVERGENCE'
NUMBER.OF.BLOCKS = 1,
X.VELOCITY.COMP = 1000,
PRESSURE        = 20E5,
TEMPERATURE     = 2500,
SPECIES.MASS.FRACTIONS = .41 .59,
$ END
$ NSIC.UNIFORM.FLOW
LABEL   = 'DIVERGENCE'
NUMBER.OF.BLOCKS = 1,
X.VELOCITY.COMP = 2000,

```

```

PRESSURE      = 10E4,
TEMPERATURE   = 1000,
SPECIES.MASS.FRACTIONS = .42 .56,
$ END
$ NSIC.UNIFORM.FLOW
LABEL        = 'EXIT IC'
NUMBER.OF.BLOCKS = 1,
X.VELOCITY.COMP = 2000,
PRESSURE     = 5E3,
TEMPERATURE   = 1000,
SPECIES.MASS.FRACTIONS = .42 .56,
$ END

$ NSBC.SUBSONIC.INFLOW
LABEL        = 'ENTRANCE INFLOW',
STAGNATION.PRESSURE = 30E5,
STAGNATION.TEMPERATURE = 3000,
U DIRECTION.COSINE = 1,
SPECIES.MASS.FRACTIONS = .41 .59,
$ END
$ NSBC.NO.SLIP.WALL
LABEL        = 'ADIABATIC.WALL',
THERMAL.BC    = 'ADIABATIC',
$ END

$ NSBC.SUPERSONIC.OUTFLOW
LABEL        = 'EXIT OUTFLOW',
$ END
$ NSBC.SUBSONIC.INFLOW
LABEL        = 'EXIT FREESTREAM',
STAGNATION.TEMPERATURE = 300,
$ END
$ NSBC.FREE.SLIP.WALL
LABEL        = 'EXIT FREESLIP',
$ END
$ NSBC.MIXED.INFLOW.OUTFLOW
LABEL        = 'MIXED',
STAGNATION.PRESSURE = 30E5,
STAGNATION.TEMPERATURE = 3000,
U.DIRECTION.COSINE = 1,
OUTFLOW.PRESSURE = 30E5,
SPECIES.MASS.FRACTIONS = .41 .59,
$ END
$ NSBC.SYMMETRY.PLANE

```

```

LABEL          = 'SYMMETRY',
$ END

$ ZONE.SETUP
ZONE.NUMBER      = 1,
INITIALIZATION.OPTION = 'RESTART.FILE',
NUMBER.OF.INTERNAL.I.CELLS = 29,
NUMBER.OF.INTERNAL.J.CELLS = 24,
NUMBER.OF.INTERNAL.K.CELLS = 29,
INITIAL.CONDITION.LABEL = 'CONVERGENCE',
BC.LABEL.ON.J.PLUS.FACE = 'ADIABATIC.WALL',
BC.LABEL.ON.J_MINUS.FACE = 'SYMMETRY',
BC.LABEL.ON.K.PLUS.FACE = 'SYMMETRY',
BC.LABEL.ON.K_MINUS.FACE = 'ADIABATIC.WALL',
NUMBER.OFINTRZN.PATCHES = 2,
$ END
$ INTRZN.PATCH.SETUP
INTRZN.PATCH.TYPE = 'FULL.FACE.AUTO',
DONOR.ZONE      = 2,
HOST.ZONE.FACE   = 'I.PLUS.FACE',
DONOR.ZONE.FACE   = 'I_MINUS.FACE',
$ END
$ INTRZN.PATCH.SETUP
INTRZN.PATCH.TYPE = 'FULL.FACE.AUTO',
DONOR.ZONE      = 4,
HOST.ZONE.FACE   = 'I_MINUS.FACE',
DONOR.ZONE.FACE   = 'I.PLUS.FACE',
$ END
$ ZONE.SETUP
ZONE.NUMBER      = 2,
INITIALIZATION.OPTION = 'RESTART.FILE',
NUMBER.OF.INTERNAL.I.CELLS = 99,
NUMBER.OF.INTERNAL.J.CELLS = 24,
NUMBER.OF.INTERNAL.K.CELLS = 29,
INITIAL.CONDITION.LABEL = 'DIVERGENCE',
BC.LABEL.ON.J.PLUS.FACE = 'ADIABATIC.WALL',
BC.LABEL.ON.J_MINUS.FACE = 'SYMMETRY',
BC.LABEL.ON.K.PLUS.FACE = 'SYMMETRY',
BC.LABEL.ON.K_MINUS.FACE = 'ADIABATIC.WALL',
NUMBER.OFINTRZN.PATCHES = 2,
$ END
$ INTRZN.PATCH.SETUP
INTRZN.PATCH.TYPE = 'FULL.FACE.AUTO',

```

```

DONOR.ZONE      = 1,
HOST.ZONE.FACE   = 'I_MINUS.FACE',
DONOR.ZONE.FACE   = 'I_PLUS.FACE',
$ END
$ INTRZN.PATCH.SETUP
INTRZN.PATCH.TYPE = 'FULL.FACE.AUTO',
DONOR.ZONE      = 3,
HOST.ZONE.FACE   = 'I_PLUS.FACE',
DONOR.ZONE.FACE   = 'I_MINUS.FACE',
$ END
$ ZONE.SETUP
ZONE.NUMBER      = 3,
INITIALIZATION.OPTION   = 'RESTART.FILE',
NUMBER.OF.INTERNAL.I.CELLS = 4,
NUMBER.OF.INTERNAL.J.CELLS = 24,
NUMBER.OF.INTERNAL.K.CELLS = 29,
INITIAL.CONDITION.LABEL  = 'EXIT IC',
BC.LABEL.ON.J.PLUS.FACE  = 'EXIT OUTFLOW',
BC.LABEL.ON.J_MINUS.FACE = 'SYMMETRY',
BC.LABEL.ON.I.PLUS.FACE  = 'EXIT OUTFLOW',
BC.LABEL.ON.K.PLUS.FACE  = 'SYMMETRY',
BC.LABEL.ON.K_MINUS.FACE = 'EXIT OUTFLOW',
NUMBER.OFINTRZN.PATCHES = 1,
$ END
$ INTRZN.PATCH.SETUP
INTRZN.PATCH.TYPE = 'FULL.FACE.AUTO',
DONOR.ZONE      = 2,
HOST.ZONE.FACE   = 'I_MINUS.FACE',
DONOR.ZONE.FACE   = 'I_PLUS.FACE',
$ END
$ ZONE.SETUP
ZONE.NUMBER      = 4,
INITIALIZATION.OPTION   = 'RESTART.FILE',
NUMBER.OF.INTERNAL.I.CELLS = 3,
NUMBER.OF.INTERNAL.J.CELLS = 24,
NUMBER.OF.INTERNAL.K.CELLS = 29,
INITIAL.CONDITION.LABEL  = 'ENTRANCE',
BC.LABEL.ON.J.PLUS.FACE  = 'ADIABATIC.WALL',
BC.LABEL.ON.J_MINUS.FACE = 'SYMMETRY',
BC.LABEL.ON.I_MINUS.FACE = 'MIXED',
BC.LABEL.ON.K.PLUS.FACE  = 'SYMMETRY',
BC.LABEL.ON.K_MINUS.FACE = 'ADIABATIC.WALL',
NUMBER.OFINTRZN.PATCHES = 1,
$ END

```

```

$ INTRZN.PATCH.SETUP
INTRZN.PATCH.TYPE = 'FULL.FACE.AUTO',
DONOR.ZONE        = 1,
HOST.ZONE.FACE    = 'I.PLUS.FACE',
DONOR.ZONE.FACE   = 'I_MINUS.FACE',
$ END

$ TECPLOTINTERFACE.SETUP
AUTO.TECPLOT.LAUNCH = 'ON',
MESSAGE.QUEUE.KEY = 2,
$ END

$ OUTPUT.SCHEDULE.SETUP
ZONE.NUMBER = 4,
OUTPUT.TYPE = 'SURFACE.TECPLOT'
IJK.INDEX.ORDER = 'KIJ',
I.BEGIN = 3,     I.END = 6,     I.INCREMENT = 1,
J.BEGIN = 26,    J.END = 26,    J.INCREMENT = 1,
K.BEGIN = 3,     K.END = 31,    K.INCREMENT = 1,
STEP.TIME-BEGIN=1, STEP.TIME.END=20000, STEP.TIMEINCREMENT=500,
$ END
$ OUTPUT.SCHEDULE.SETUP
ZONE.NUMBER = 4,
OUTPUT.TYPE = 'SURFACE.TECPLOT'
IJK.INDEX.ORDER = 'IJK',
I.BEGIN = 3,     I.END = 6,     I.INCREMENT = 1,
J.BEGIN = 3,     J.END = 26,    J.INCREMENT = 1,
K.BEGIN = 3,     K.END = 3,    K.INCREMENT = 1,
STEP.TIME-BEGIN=1, STEP.TIME.END=20000, STEP.TIMEINCREMENT=500,
$ END
$ OUTPUT.SCHEDULE.SETUP
ZONE.NUMBER = 1,
OUTPUT.TYPE = 'SURFACE.TECPLOT'
IJK.INDEX.ORDER = 'KIJ',
I.BEGIN = 3,     I.END = 31,    I.INCREMENT = 1,
J.BEGIN = 26,    J.END = 26,    J.INCREMENT = 1,
K.BEGIN = 3,     K.END = 31,    K.INCREMENT = 1,
STEP.TIME-BEGIN=1, STEP.TIME.END=20000, STEP.TIMEINCREMENT=500,
$ END
$ OUTPUT.SCHEDULE.SETUP
ZONE.NUMBER = 1,
OUTPUT.TYPE = 'SURFACE.TECPLOT'
IJK.INDEX.ORDER = 'IJK',
I.BEGIN = 3,     I.END = 31,    I.INCREMENT = 1,

```

```
J.BEGIN = 3,      J.END = 26,  J.INCREMENT = 1,  
K.BEGIN = 3,      K.END = 3,   K.INCREMENT = 1,  
STEP.TIME-BEGIN=1, STEP.TIME-END=20000, STEP.TIME.INCREMENT=500,  
$ END  
$ OUTPUT.SCHEDULE.SETUP  
ZONE.NUMBER = 2,  
OUTPUT.TYPE = 'SURFACE.TECPLOT'  
IJK.INDEX.ORDER = 'KIJ',  
I.BEGIN = 3,      I.END = 101, I.INCREMENT = 1,  
J.BEGIN = 26,     J.END = 26,   J.INCREMENT = 1,  
K.BEGIN = 3,      K.END = 31,   K.INCREMENT = 1,  
STEP.TIME-BEGIN=1, STEP.TIME-END=20000, STEP.TIME.INCREMENT=500,  
$ END  
$ OUTPUT.SCHEDULE.SETUP  
ZONE.NUMBER = 2,  
OUTPUT.TYPE = 'SURFACE.TECPLOT'  
IJK.INDEX.ORDER = 'IJK',  
I.BEGIN = 3,      I.END = 101, I.INCREMENT = 1,  
J.BEGIN = 3,      J.END = 26,   J.INCREMENT = 1,  
K.BEGIN = 3,      K.END = 3,    K.INCREMENT = 1,  
STEP.TIME-BEGIN=1, STEP.TIME-END=20000, STEP.TIME.INCREMENT=500,  
$ END  
$ OUTPUT.SCHEDULE.SETUP  
ZONE.NUMBER = 1,  
OUTPUT.TYPE = 'FIELD.TECPLOT3D'  
STEP.TIME-BEGIN=500, STEP.TIME-END=20000,  
STEP.TIME.INCREMENT=500,  
$ END  
$ OUTPUT.SCHEDULE.SETUP  
ZONE.NUMBER = 2,  
OUTPUT.TYPE = 'FIELD.TECPLOT3D'  
STEP.TIME-BEGIN=500, STEP.TIME-END=20000,  
STEP.TIME.INCREMENT=500,  
$ END  
$ OUTPUT.SCHEDULE.SETUP  
ZONE.NUMBER = 3,  
OUTPUT.TYPE = 'FIELD.TECPLOT3D'  
STEP.TIME-BEGIN=500, STEP.TIME-END=20000,  
STEP.TIME.INCREMENT=500,  
$ END  
$ OUTPUT.SCHEDULE.SETUP  
ZONE.NUMBER = 4,  
OUTPUT.TYPE = 'FIELD.TECPLOT3D'
```

STEP.TIME-BEGIN=500, STEP.TIME-END=20000,
 STEP.TIME.INCREMENT=500,
 \$ END

\$ CHEM.SETUP
 CHEMISTRY.MODEL = 'NO.REACTION'
 NUMBER.OF.SPECIES = 2,
 LOWER.MIN.TEMP = 200,
 LOWER.MAX.TEMP = 1000,
 MIDDLE.MAX.TEMP = 6000,
 \$ END

\$ CHEM.SPECIES

SPECIE.NUMBER = 1,
 SPECIE.NAME = 'WATER'
 SPECIE.FORMULA = 'H2O1',
 SPECIE.TYPE = 'POLYATOMIC-3',
 SPECIE.MOLECULAR.WEIGHT = 18,
 BLOTTNERS.VISC.COEFS(1) = -.0973084,
 BLOTTNERS.VISC.COEFS(2) = 2.33417,
 BLOTTNERS.VISC.COEFS(3) = -19.3834,
 THERMO.COEFS.MIDDLE(1) = 2.67703787,
 THERMO.COEFS.MIDDLE(2) = 2.9718329E-3,
 THERMO.COEFS.MIDDLE(3) = -7.7376969E-7,
 THERMO.COEFS.MIDDLE(4) = 9.44336689E-11,
 THERMO.COEFS.MIDDLE(5) = -4.26900959E-15,
 THERMO.COEFS.MIDDLE(6) = -2.98858938E4,
 THERMO.COEFS.MIDDLE(7) = 6.88255571,
 THERMO.COEFS.LOWER(1) = 4.19864056,
 THERMO.COEFS.LOWER(2) = -2.3643410E-3,
 THERMO.COEFS.LOWER(3) = 6.52040211E-6,
 THERMO.COEFS.LOWER(4) = -5.48797062E-9,
 THERMO.COEFS.LOWER(5) = 1.77197819E-12,
 THERMO.COEFS.LOWER(6) = -3.02937267E4,
 THERMO.COEFS.LOWER(7) = -8.49032208E-1,

\$ END

\$ CHEM.SPECIES

SPECIE.NUMBER = 2,
 SPECIE.NAME = 'NITROGEN'
 SPECIE.FORMULA = 'N2',
 SPECIE.TYPE = 'DIATOMIC',
 SPECIE.MOLECULAR.WEIGHT = 28,
 BLOTTNERS.VISC.COEFS(1) = .0492125,
 BLOTTNERS.VISC.COEFS(2) = -.0321068,

BLOTTNERS.VISC.COEFS(3) = -9.93812,
 THERMO.COEFS.MIDDLE(1) = 2.95257626,
 THERMO.COEFS.MIDDLE(2) = 1.39690057E-3,
 THERMO.COEFS.MIDDLE(3) = -4.92631691E-7,
 THERMO.COEFS.MIDDLE(4) = 7.86010367E-11,
 THERMO.COEFS.MIDDLE(5) = -4.60755321E-15,
 THERMO.COEFS.MIDDLE(6) = -9.23948645E2,
 THERMO.COEFS.MIDDLE(7) = 5.87189252,
 THERMO.COEFS.LOWER(1) = 3.53100528,
 THERMO.COEFS.LOWER(2) = -1.23660987E-4,
 THERMO.COEFS.LOWER(3) = -5.0299437E-7,
 THERMO.COEFS.LOWER(4) = 2.43530612E-9,
 THERMO.COEFS.LOWER(5) = -1.40881235E-12,
 THERMO.COEFS.LOWER(6) = -1.04697628E3,
 THERMO.COEFS.LOWER(7) = 2.96747468,

\$ END

\$ INTEGRATION.SETUP

ZONE.NUMBER = 2,
 ZONE.FACE = 'I.PLUS.FACE',
 INTEGRATION.VARIABLES = 'FORCE',
 J-BEGIN = 1,
 J-END = 7,
 K-BEGIN = 1,
 K-END = 3,
 STEP.TIME.BEGIN = 1,
 STEP.TIME.END = 20000,
 STEP.TIMEINCREMENT = 50,

\$ END

\$ INTEGRATION.SETUP

ZONE.NUMBER = 2,
 ZONE.FACE = 'I.PLUS.FACE',
 INTEGRATION.VARIABLES = 'MASS',
 J-BEGIN = 1,
 J-END = 7,
 K-BEGIN = 1,
 K-END = 3,
 STEP.TIME.BEGIN = 1,
 STEP.TIME.END = 20000,
 STEP.TIMEINCREMENT = 50,

\$ END

\$ INTEGRATION.SETUP

ZONE.NUMBER = 3,
 ZONE.FACE = 'I.PLUS.FACE',

```

INTEGRATION.VARIABLES      = 'FORCE',
J.BEGIN                   = 1,
J.END                     = 7,
K.BEGIN                   = 1,
K.END                     = 3,
STEP.TIME-BEGIN           = 1,
STEP.TIME-END             = 20000,
STEP.TIME.INCREMENT       = 50,
$ END

$ INTEGRATION.SETUP
ZONE.NUMBER               = 3,
ZONE.FACE                 = 'I.PLUS.FACE',
INTEGRATION.VARIABLES     = 'MASS',
J.BEGIN                   = 1,
J.END                     = 7,
K.BEGIN                   = 1,
K.END                     = 3,
STEP.TIME-BEGIN           = 1,
STEP.TIME-END             = 20000,
STEP.TIME.INCREMENT       = 50,
$ END

$ NS.GENERAL
IMPLICIT.MODE   = 'LU.SGS',
FLUX.FUNCTION.TYPE = 'ROE',
TIME.STEP.MODE = 'UNIFORM.TIME.STEP'
TIME.STEP.RELAX.FACTOR = .5,
THERMODYNAMIC.MODEL = 'THERMALLY.PERFECT.SPECIES'
VISCOSITY.MODEL    = 'BLOTTNER.WILKES.SPECIES'
CONDUCTIVITY.MODEL = 'EUCKEN.WILKES.SPECIES'
FLUX.LIMITER.TYPE = 'BOTH'
G.S.RELAX.FACTOR = 1.5,
FLUX.PHI.I          = 1,
FLUX.PHI.J          = 1,
FLUX.PHI.K          = 1,
$ END

$ NS.ZONE
ZONE.NUMBER=1
CFLM-BEGIN=500, CFLM-MAXIMUM=800, CFLM-FACTOR=1.05,
$ END
$ NS.ZONE
ZONE.NUMBER=2
CFLM-BEGIN=500, CFLM-MAXIMUM=800, CFLM-FACTOR=1.05,

```

```
$ END
$ NS.ZONE
  ZONE.NUMBER=3
  CFLM.BEGIN=500, CFLM.MAXIMUM=800, CFLM.FACTOR=1.05,
$ END
$ NS.ZONE
  ZONE.NUMBER=4
  CFLM.BEGIN=500, CFLM.MAXIMUM=800, CFLM.FACTOR=1.05,
$ END
```